Karlsruher Institut für Technologie

UNIVERSIDAD NACIONAL DE SAN MARTÍN

Combined Detection of Muons and Radio Emission of Cosmic-Ray Air Showers

Zur Erlangung des akademischen Grades eines
DOKTORS DER NATURWISSENSCHAFTEN
bei der KIT-Fakultät für Physik des

Karlsruher Institut für Technologie (KIT)
und der
Universidad Nacional de San Martín (UNSAM)

genehmigte
DISSERTATION
von

Dipl. Phys. Ewa Marlen Holt
aus Achim

Tag der mündlichen Prüfung: 20. April 2018

Referent:	Prof. Dr. Dr. h.c. Johannes Blümer Karlsruher Institut für Technologie
Korreferent:	Prof. Dr. Alberto Etchegoyen Universidad National de San Martín
Betreuer:	Priv. Doz. Dr. Frank G. Schröder Karlsruher Institut für Technologie

UNIVERSIDAD NACIONAL DE SAN MARTÍN

Karlsruher Institut für Technologie

Combined Detection of Muons and Radio Emission of Cosmic-Ray Air Showers

Tesis presentada para optar por el título de
DOCTOR EN ASTROFÍSICA
del Instituto de Tecnología "Prof. Jorge A. Sábato" de la

Universidad Nacional de San Martín (UNSAM)
y del
Karlsruher Institut für Technologie (KIT)

por

Dipl. Phys. Ewa Marlen Holt
de Achim, Alemania

Fecha de la defensa oral: 20 de abril de 2018

Director:	Prof. Dr. Dr. h.c. Johannes Blümer Karlsruher Institut für Technologie
Co-director:	Prof. Dr. Alberto Etchegoyen Universidad National de San Martín
Colaborador:	Priv. Doz. Dr. Frank G. Schröder Karlsruher Institut für Technologie

Combined Detection of Muons and Radio Emission of Cosmic-Ray Air Showers

Cosmic rays have been a subject of study since their discovery more than 100 years ago. However, open questions remain about the origin of the ultra-high energy cosmic rays until today. To find answers, accurate measurements of the mass composition with large statistics are essential. Ultra-high energy cosmic rays can only be measured indirectly via extensive air showers they produce in the Earth's atmosphere. The ratio of the muonic and the electromagnetic component of these showers is correlated to the mass of the primary cosmic rays. These shower particles can be measured with extended particle detectors at the ground. In addition, the electromagnetic component can be measured via its radio emission produced in the atmosphere. At the Pierre Auger Observatory in Argentina, this hybrid detection is realized by the Muon Detector of AMIGA and the Radio Detector AERA, which are installed as engineering arrays in addition to the main Surface Detector and the Fluorescence Detector, and measure cosmic rays above an energy of $10^{17.5}$ eV.

In this thesis, a novel technique is developed to estimate the mass of the primary cosmic rays by combining these muon and radio measurements. The new mass estimator is studied using Monte Carlo simulations of air showers and then tested experimentally based on data of AMIGA and AERA. The main results are:

- The ratio of the muon density ρ_μ^{600}, determined at a distance of 600 m to the shower axis, and the strength of the radio emission, measured by the square root of the radiation energy $S_{\mathrm{RD}}^{\rho_\theta}$, is indeed sensitive to the mass of the primary particle.

- The mass composition derived from the combination of AMIGA and AERA measurements is compatible to composition measurements by the depth of the shower maximum X_{max} of the Fluorescence Detector of Auger.

- Air-shower simulations show that the muon-radio mass estimator can have higher separation power of light and heavy particles than established methods using X_{max} for showers arriving from all zenith angles, and to methods using solely particle measurements for inclined showers above 40°. Since these inclined showers can be measured with sparse radio arrays, the combination of radio and muon detectors shows great potential for the application at a large scale, e.g. by equipping the Surface Detector stations of the Pierre Auger Observatory with radio antennas.

Gemeinsame Detektion von Myonen und Radioemission ausgedehnter Luftschauer Kosmischer Strahlung

Kosmische Strahlung fasziniert die Wissenschaft, seit sie vor mehr als 100 Jahren entdeckt wurde. Jedoch konnte bis heute der Ursprung der ultrahochenergetischen Kosmischen Strahlung nicht geklärt werden. Zur Untersuchung des Ursprungs dieser kosmischen Teilchen sind präzise Messungen ihrer Massenkomposition mit hoher Statistik unerlässlich. Die ultrahochenergetische Kosmische Strahlung lässt sich nur indirekt durch ausgedehnte Luftschauer messen, die durch Wechselwirkungen der kosmischen Teilchen mit der Erdatmosphäre induziert werden. Dabei korreliert das Verhältnis der myonischen und der elektromagnetischen Komponente dieser Schauer mit der Masse des primären kosmischen Teilchens. Die Teilchen des Schauers können mithilfe von ausgedehnten Detektorfeldern am Boden gemessen werden. Die elektromagnetische Komponente kann zusätzlich anhand der von ihr in der Atmosphäre erzeugten Radioemission gemessen werden. Diese hybride Messmethode ist am Pierre-Auger-Observatorium in Argentinien realisiert. Dort wird die myonische Komponente von den Myondetektoren von AMIGA und die Radioemission von AERA gemessen. AMIGA und AERA sind dort zusätzlich zu den Wasser-Cherenkov-Detektoren und Fluoreszenzdetektoren installiert und messen Kosmische Strahlung oberhalb einer Energie von $10^{17.5}$ eV.

In dieser Dissertation wird eine neuartige Technik zur Abschätzung der Masse des Primärteilchens eines Luftschauers durch die Kombination von Myon- und Radiomessungen entwickelt. Der neuartige Massenschätzer wird mithilfe von Monte-Carlo-Simulationen ausgedehnter Luftschauer untersucht und daraufhin anhand von Messdaten von AMIGA und AERA experimentell überprüft. Die wichtigsten Ergebnisse sind:

- Das Verhältnis der Myondichte ρ_μ^{600} bei einer Distanz von 600 m zur Schauerachse und der Stärke der Radioemission, durch die Wurzel der Strahlungsenergie $S_{\mathrm{RD}}^{\rho_\theta}$ gemessen, ist mit der Masse des Primärteilchen korreliert.

- Die Massenkomposition, die mithilfe der Kombination von AMIGA- and AERA-Messungen ermittelt wurde, ist kompatibel mit der Massenkomposition, die durch Messungen des Schauermaximums, X_{max}, mit dem Fluoreszenzdetektor von Auger ermittelt wurde.

- Durch Luftschauersimulationen konnte gezeigt werden, dass der Myon-Radio-Massenschätzer eine vergleichbare Massensensitivität wie etablierte Massenschätzer besitzt. Insbesondere zeigt der neuartige Massenschätzer für alle Zenitwinkel eine größere Massensensitivität als X_{max}. Für geneigte Schauer ($\theta > 40°$) ist die Massensensitivität ebenfalls stärker als für Massenschätzer, die die Teilchenanzahl am Boden verwenden. Da diese geneigten Luftschauer mit Antennenfeldern mit großem Abstand zwischen den Radioantennen gemessen werden können, zeigt der Myon-Radio-Massenschätzer ein großes Potential für die Anwendung in großskaligen Experimenten. Eine mögliche Anwendung ist die Kombination der Wasser-Cherenkov-Detektoren des Pierre-Auger Observatoriums mit Radioantennen.

Detección Combinada de Muones y Emisión de Radio de Cascadas Atmosféricas Extensas de Rayos Cósmicos

Los rayos cósmicos han sido objeto de estudio desde su descubrimiento hace mas de 100 años. Sin embargo, algunas cuestiones acerca del origen de los rayos cósmicos de ultra alta energía permanecen abiertas hasta nuestros días. Para encontrar respuestas, es esencial medir la composición de masa con mucha precisión y con gran estadística. Los rayos cósmicos de ultra alta energía solamente pueden ser medidos indirectamente a través de las cascadas atmosféricas extensas generadas por ellos en la atmósfera terrestre. La relación entre la componente muónica y electromagnética de la cascada de partículas está correlacionada con la masa del rayo cósmico primario. Estas partículas secundarias pueden ser medidas con un arreglo de detectores extendido en la superficie terrestre. Además, la componente electromagnética puede ser medida por la emisión de radio que inducen en la atmósfera. En el Observatorio Pierre Auger, en Argentina, esta forma de detección híbrida es realizada usando el detector de muones de AMIGA y el detector de radio AERA que han sido instalados como arreglos de ingeniería adicionales al Detector de Superficie y el Detector de Fluorescencia. AMIGA y AERA miden rayos cósmicos con energía superior a $10^{17.5}$ eV.

En esta tesis se desarrolla una técnica novedosa para estimar la masa del rayo cósmico primario, que combina la medición de los muones y la emisión de radio. Este nuevo estimador de masa es estudiado usando simulaciones de Monte Carlo de cascadas atmosféricas y luego es verificado experimentalmente con datos de AMIGA y AERA. Los resultados principales son:

- La razón de la densidad de muones ρ_{μ}^{600}, determinada a una distancia de 600 m del eje de la cascada, y el tamaño de la emisión de radio, medida por la raíz cuadrada de la energía de radiación $S_{\mathrm{RD}}^{\rho_\theta}$, efectivamente es sensible a la masa del rayo cósmico primario.

- La composición de masa determinada por la combinación de las mediciones de AMIGA y AERA es compatible con la composición de masa determinada con las mediciónes de la profundidad atmosférica del máximo de las cascadas X_{max} realizadas con los telescopios de fluorescencia de Auger.

- Ha sido demostrado por simulaciones de cascadas atmosféricas, que el estimador de masa puede tener más poder de separación entre partículas ligeras y pesadas comparado con los métodos tradicionales que usan X_{max} para todos los ángulos cenitales y también con los métodos que usan las partículas secundarias para cascadas inclinadas ($\theta > 40°$). Dado que las cascadas inclinadas pueden ser medidas con arreglos de antenas de radio de gran espaciamiento, la combinación de detectores de muones y de radio muestra mucho potencial en su utilización a gran escala. Una posibilidad puede ser instalar antenas de radio con cada detector Cherenkov en el Observatorio Pierre Auger.

Contents

CHAPTER 1

Introduction

More than 100 years ago Viktor Hess discovered that the Earth is bombarded by a constant flux of energetic particles - the cosmic rays. These particles originate from outside of our solar system and have energies from 10^9 eV up to more than 10^{20} eV. Their acceleration can be explained by processes at the shock fronts of supernova remnants in our galaxy at least up to energies of $\approx 10^{14}$ eV. However, until today the origin of the cosmic rays above these energies is still unknown and a large field of research. Recently, the Pierre Auger Collaboration found observational evidence, that cosmic rays around 10^{19} eV originate from outside of our galaxy [1], but the processes accelerating particles to such high energies are still not understood. Different features of the energy spectrum of cosmic rays such as changes in the slope reveal information about these processes. In particular, the mass composition plays an important role in understanding these features. A changing mass composition around these features indicates a change in the acceleration processes or sources of these cosmic rays. Furthermore, most of the propagation processes cosmic rays undergo on their way through space are mass dependent due to magnetic deflection or particle interactions. In this thesis, a new method for the determination of the mass composition of ultra-high energy cosmic rays is developed.

Cosmic rays with energies above 10^{14} eV are measured indirectly via extensive air showers induced in the Earth's atmosphere. These air showers mainly consist of photons, electrons and muons with a small fraction of hadrons such as pions, kaons and rhos. The properties of the primary cosmic rays such as energy, mass and arrival direction, are reconstructed from observables of these showers. The mass can be estimated from the ratio of the muonic and the electromagnetic component. The particles are measured with detectors spread over a detection area at the ground. In addition, the electromagnetic component can be measured via its radio emission or fluorescence light in the atmosphere. However, at large zenith angles most of the electromagnetic particles are absorbed in the atmosphere when the shower reaches the ground. Furthermore, the fluorescence light can only be observed in dark moonless nights with clear atmosphere. Therefore, measuring the electromagnetic component via the radio emission has a great potential especially for large zenith angles, as shown in this thesis. An introduction to the theory of cosmic rays, extensive air showers and radio emission is given in Chapter 2.

The Pierre Auger Observatory in Mendoza, Argentina, is dedicated to measure cosmic rays up to the highest energies. It comprises various complementary detector systems such as a Surface Detector (SD) built of 1660 water-Cherenkov detectors, and a fluorescence detector (FD) made of 27 telescopes, measuring air-shower events in coincidence. The Surface detector spans an area of 3000 km^2. In an enhancement area of 23.5 km^2 the AMIGA (Auger Muons and Infill for the Ground Array) and AERA (Auger Engineering Radio Array) detectors, and special fluorescence telescopes are co-located, measuring cosmic rays down to energies of $10^{17.5}$ eV. AMIGA features water-Cherenkov detectors distributed over a denser grid compared to the rest of the Surface Detector, as well as buried scintillators for the muonic component of air showers (Muon Detector, MD). AERA comprises antennas to measure the radio emission (Radio Detector, RD). Hence, this area features ideal circumstances to investigate the combination of muons and radio emission for mass estimation. An overview of the Pierre Auger Observatory is given in Chapter 3.

Air-shower simulations are used to investigate the mass sensitivity of muon and radio observables for different primary energies and zenith angles. For this, various simulation libraries have been computed with the simulation tools CORSIKA and CoREAS. A combined analysis of AMIGA and AERA data is performed for the first time, for which the data as well as the analysis software are processed and adjusted. For this, a standard analysis pipeline is established for the combined reconstruction of shower observables. The simulation libraries, the processing of the data and the analysis pipeline is described in Chapter 4.

Using the simulations, different shower observables of the muonic and electromagnetic shower component are investigated on their mass sensitivity, without any measurement uncertainties and detector effects, in Chapter 5. For inclined showers, the mass sensitivity of the electron number at the ground diminishes. In contrast, the combination of the muon number and the strength of the radio emission shows an approximately constant mass sensitivity, which makes it superior for inclined showers.

These findings are tested for a realistic measurement scenario, adding simulated detector responses of AMIGA and AERA and measured radio background to the air-shower simulations. Thereby, the influence of the detection and reconstruction technique is estimated, which adds uncertainties to the observables. However, this only slightly reduces the mass separability, which is still sufficient for mass composition studies. A set of quality cuts is established, yielding high quality events for further analysis. The procedure and the results on the mass sensitivity are described in Chapter 6.

Finally, the elaborated analysis is applied to coincident events of AMIGA and AERA in Chapter 7. More than 3 years of combined measured data have been available for the analysis. The results are compared to X_{max} measurements of the Fluorescence Detector, which offers a complementary mass estimator for comparison.

In general, important improvements of the radio analysis were achieved within this thesis, such as studies on possible biases of the reconstructed radiation energy, which is described in Appendix C.

CHAPTER 2

Cosmic rays

Contents

Charged particles originating from beyond our solar system reach the Earth with almost constant flux. These so called cosmic rays (CRs) comprise to 99 % of fully ionized atoms and to 1 % of electrons and positrons. Some definitions of cosmic rays include as well neutral particles such as photons, neutrinos and neutrons that together only make up a tiny fraction of the total flux.

Cosmic rays are subject of investigation for over 100 years. At the beginning of the 20th century, scientists discovered a continuous ionization of the air. At first it was believed that this ionization originates from radioactivity in the Earth' crust. To prove this, Theodor Wulf measured the ionization of the air with an electrometer at ground and at the top of the Eiffeltower [2]. He found a decrease of the radiation with increasing altitude, but not a complete disappearance as expected for a solely terrestrial origin. In 1912, Viktor Hess conducted several balloon flights up to 5300 m height and discovered that the radiation increases again above 1400 m a.s.l [3, 4]. He concluded, that "a radiation of very high penetrating power, impinging onto the atmosphere from above" must be the reason. Kolhörster confirmed this observation in 1913 with additional balloon flights in higher altitudes and with improved electrometers [5]. He demonstrated in 1929 together with Bothe that the cosmic rays are, at least partly, charged particles [6]. For the discovery of the cosmic rays Hess was awarded the Nobel prize in 1936.

Pierre Auger later found that the radiation measured close to and at ground is not the primary cosmic rays themselves.When traversing the Earth's atmosphere, cosmic rays interact with air molecules producing a cascade of high energetic secondary particles. These particles can be spread over a wide lateral distance. In 1939, Pierre Auger measured them in coincidence in a distance between the detectors of up to 300 m and discovered extensive cosmic-ray air showers (EAS) [7].

The energy of cosmic rays reaches up to the highest energies ever measured for subatomic particles. Therefore, especially in the early years, particle physics was mainly studied with cosmic rays. Several new particles were discovered, e.g. the positron in 1932, the muon in 1936, and the pion in 1947. Nowadays, the reach of human-made particle accelerators still is only several orders of magnitude below the upper end of the cosmic ray energy spectrum.

Cosmic rays are produced and accelerated in astrophysical sites of high energy density. On their way to Earth, they undergo interactions, e.g. with galactic and intergalactic magnetic fields and the cosmic microwave background. Hence, they are messengers of the Universe. Properties of the cosmic-ray flux such as the mass composition, the energy spectrum and the distribution of arrival directions reveal information about processes in their sources. Most of these processes are not completely understood and still are being studied by scientists all around the globe. A recent review of the progress in high-energy cosmic ray physics can be found in [8].

Since cosmic rays interact with the Earth's atmosphere, direct measurements are not possible at ground. Instead, air-borne and space-based experiments facilitate direct measurements of primary cosmic rays and their properties up to energies of 10^{14} eV. The cosmic ray flux decreases with energy and for higher energies larger detection areas than achievable for satellites are essential to measure with sufficient

statistics. This is only practical at ground via the measurement of EAS.

A method for more accurate measurements of cosmic rays of ultra-high energies is subject to study in this thesis. In this chapter, an overview about the main properties such as mass, energy and arrival direction and the origin of cosmic rays is given. Furthermore, a description of the physics and different detection techniques of extensive air showers is given. In particular the detection of the radio emission emitted by air showers is discussed in detail.

2.1 Origin of cosmic rays

Cosmic rays reaching Earth carry information about their origin and processes they undergo on their way to us. The energies to which those particles are accelerated depend on the corresponding acceleration processes, and the charge and mass of the particle. Hence, we can learn about such processes from the shape of the energy spectrum of the cosmic ray flux and the change of the mass composition over energy. The cosmic rays are deflected at galactic and intergalactic magnetic fields and lose information about the location of their acceleration source. Only for very high energies or nearby sources, the deflection is small and the cosmic rays point back to their sources.

2.1.1 Energy spectrum

The flux of cosmic rays decreases towards higher energies. The energies reach from around 10^9 eV to the highest energies measured so far at a few 10^{20} eV. Whereas about 1000 particles with energies of 10^9 eV traverse each m^2 per second on average, only one particle with an energy of around 10^{18} eV appears in each square kilometer per year. The spectrum peaks at 20 GeV and below this energy the cosmic ray flux is suppressed by heliospheric magnetic fields produced by the solar wind [10]. The cosmic rays get deflected at these fields before reaching Earth.

For higher energies, the energy spectrum follows a approximately power law:

$$\frac{dN}{dE\, d\Omega\, dA\, dt} \propto E^{-\gamma} \quad , \tag{2.1}$$

with the number of particles N per energy E, solid angle Ω, area A and time t. The energy spectrum comprises various features at which the spectral index γ changes such as a steepening at the knee, the second knee and the heavy knee, a flattening at the light ankle and the ankle and a cutoff at the highest energies (see Fig. 2.1).

At the knee at around $3-5 \times 10^{15}$ eV the spectral index increases from $\gamma = 2.7$ to $\gamma = 3.1$. The KASCADE experiment showed that this steepening of the all-particle spectrum occurs due to a sharp decline of the contribution of light cosmic rays ($Z <$ 6, e.g. protons and helium nuclei) [12, 13]. However, the flux of heavy cosmic rays (Z > 13. likely dominated by iron nuclei with $Z = 26$) also sharply decreases at a higher energy of around $(8.3 \pm 0.8) \times 10^{16}$ eV with a spectral index of $\gamma = 3.24 \pm 0.05$, which is

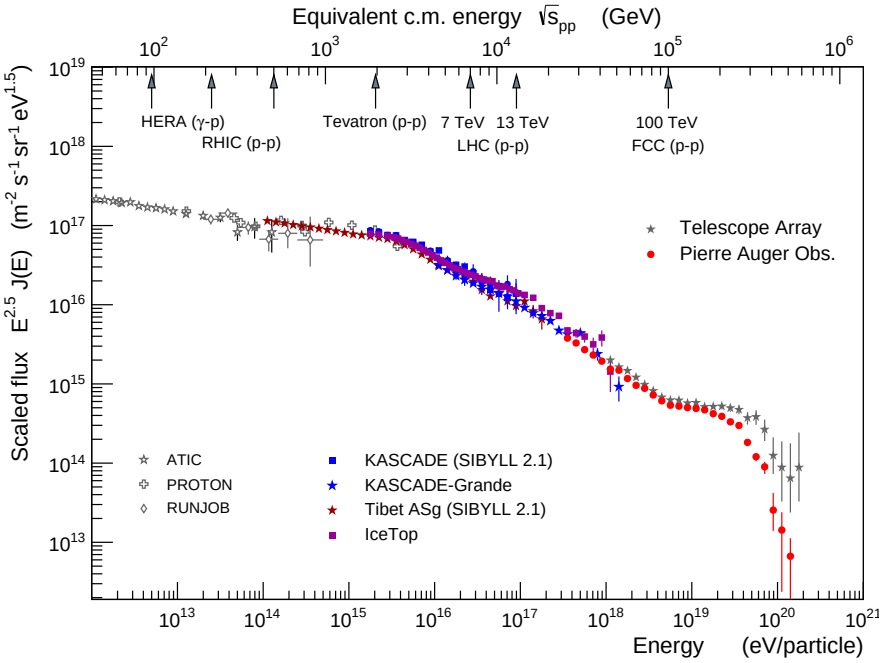

Figure 2.1: Cosmic-ray energy spectrum measured by various air-shower experiments. The flux is scaled with $E^{2.5}$ to reveal the features of the spectrum such as knee, heavy knee and/or second knee, ankle and cutoff. The figure is taken and updated from [9].

called the heavy knee [14] (see Fig. 2.2). Other experiments measured a second knee of the all-particle spectrum at a higher energy of about 3×10^{17} eV with a spectral index of $\gamma = 3.2$ above this energy [15, 16]. When taking all systematic uncertainties into account, it is unlikely but not excluded, that the second knee and the heavy knee coincide.

The ankle, a flattening of the spectrum, appears at an energy of around 5×10^{18} eV, where the all-particle spectral index changes to $\gamma = 2.6-2.8$ [17, 18]. Furthermore, KASCADE-Grande measured a flattening of the energy spectrum of the light component at 10^{17} eV [19] to $\gamma = 2.79 \pm 0.08$, thus a light ankle (see Fig. 2.2). The flux of this light component is consistent with the flux at the ankle in the all particle spectrum. At around 4×10^{19} eV a cutoff of the spectrum is observed [17, 20].

The origin of these features in the energy spectrum is still unknown and subject of various astrophysical models (see e.g. [21] for the knee, [22]). The changes in the spectral index can be caused by a changing source population or a maximum energy of acceleration processes in certain source types such as Supernovae. Alternatively, rigidity dependent propagation effects of cosmic rays might change the shape of the spectrum measured at Earth compared to the spectrum at the sources. An extragalactic origin of ultra-high energy cosmic rays above 8×10^{18} eV was recently measured by the Pierre Auger Observatory [1] and a transition from galactic to extragalactic cosmic rays is expected between the light ankle and the all-particle ankle, which entails a changing source population. Earlier explanations considered also new particle

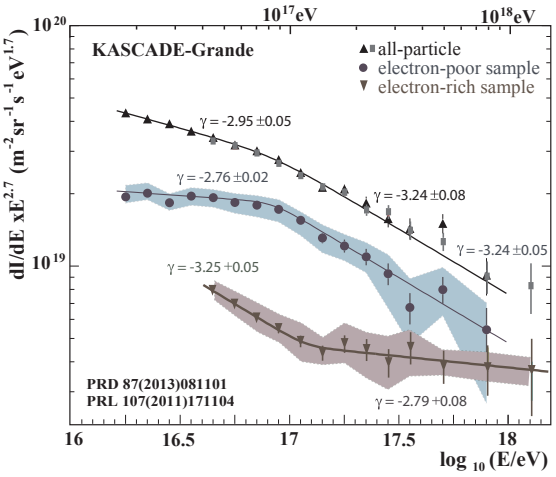

Figure 2.2: Energy spectrum for light and heavy component around the second knee and / or heavy knee [11]. The spectrum is split between the light cosmic rays, which induce EAS rich in electrons, and heavy cosmic rays with a poor electron content in the EAS. The spectrum of the light component features a decrease of the slope at 10^{17} eV, the light ankle. At 8×10^{16} eV the heavy component features an increase of the slope, the heavy knee.

processes appearing at the features, which seems unlikely, since the LHC confirmed the standard model up to center of mass energy of 13 TeV, which corresponds to a cosmic-ray energy of about 10^{17} eV for protons. Accurate measurements of the mass composition around the features is of mayor importance to distinguish between various models.

There are two explanations for the cutoff. The Greisen-Zatsepin-Kuzmin (GZK) effect [23, 24] explains the cutoff with interactions of protons or nuclei with the cosmic microwave background (CMB) above a certain threshold energy of ~7×10^{19} eV (see Section 2.1.5 for details). The protons or nuclei lose energy at each of such interactions until they reach below the threshold energy. Thus, particles with higher energies must originate in nearby regions of the Universe ($\lesssim 100$ Mpc). An alternative scenario for the cutoff is, that the maximum energies are reached to which the sources can accelerate cosmic rays. Currently, the Pierre Auger Observatory is upgraded to measure the mass composition of cosmic rays of the highest energies to distinguish between the different scenarios [25] (see Section 3.5).

2.1.2 Elemental composition

Cosmic rays are composed mainly by nuclei of elements up to iron. The fraction of the different elements changes with energy due to energy-dependent acceleration and propagation processes. Thus, measuring the mass composition as a function of energy can constrain models for these processes. Especially for the understanding of the various features of the energy spectrum such as the knee, heavy / second knee, light ankle, ankle, and cutoff and additional possible fine structures, it is of

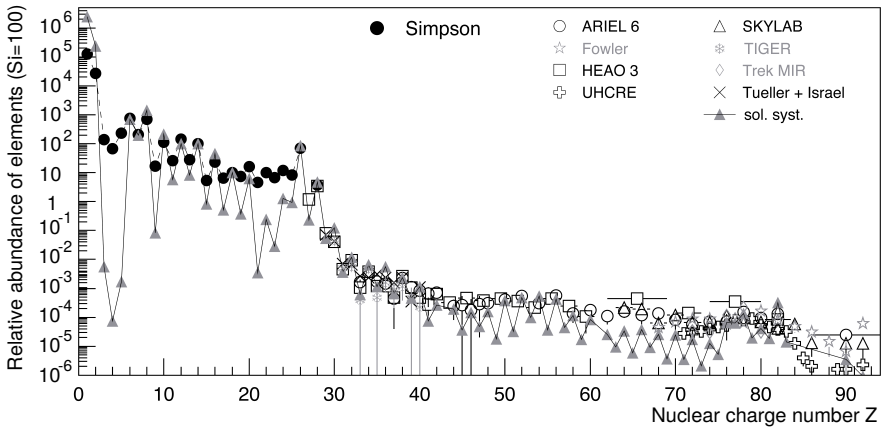

Figure 2.3: Nuclear abundance of cosmic rays at around 1 GeV per nucleon measured in air-borne and space-based experiments. Figure taken from Blümer, Engel, and Hörandel [26]. Higher fractions of Li, Be and B and of the elements just below Fe in the cosmic rays compared to the abundance in the solar system occur due to spallation of C, O and Fe.

key importance to measure the elemental composition in the energy ranges around these features. Correlated changes in the energy spectrum and the mass composition such as a gradual change in the mean mass can hint to rigidity dependent processes in the propagation or acceleration. In addition, unfolding the energy spectrum for different elemental groups has shown that the features are different for heavy and light cosmic rays.

Up to energies of 10^{14} eV the mass of cosmic rays is measured directly in air-borne or space-based experiments above the atmosphere. The relative nuclear abundance of low-energy cosmic rays around 1 GeV per nucleon is shown and compared to the abundance in the solar system in Fig. 2.3. It follows the nuclear abundance in the solar system with some exceptions. The main components of cosmic rays at this energy are hydrogen and helium with a fraction of ~85 % and ~10 %, respectively. The solar system contains a higher fraction of hydrogen and helium which are the main elements the sun is composed of. In the cosmic ray flux higher abundances of lithium, beryllium and boron and of several elements just below iron are observed. These light elements are produced only to a very small extent in nucleosyntheses in stars. Instead, they are formed in spallation processes of the more abundant elements carbon and oxygen or iron during propagation through space and, thus, they are more abundant in cosmic rays than in the solar system.

Cosmic rays of higher energies are measured indirectly via extensive air showers. The reconstruction of the primary cosmic-ray properties from the secondary particles is based on Monte Carlo simulations of air showers using different hadronic interaction models (see Section 2.2.3). Thus, the interpretation is sensitive to uncertainties of these models. In addition, the development of air showers fluctuates statistically. This uncertainties do not allow for a mass measurement of individual

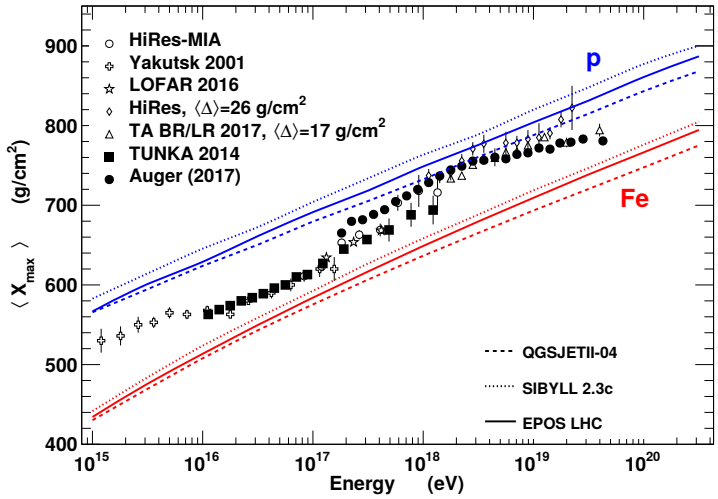

Figure 2.4: Mean $X_{\max}$ measured by cosmic-ray air showers The atmospheric depth of the maximum number of secondary particles $X_{\max}$ is correlated to the mass of the primary cosmic rays. Shown is the mean $X_{\max}$ measured by non-imaging Cherenkov and by fluorescence detectors compared to predictions from different hadronic models for proton and iron showers. Telescope Array (TA) and HiRes data are corrected for detector effects by the given Δ. Figure is provided by Pierog [27]. The distribution shows a gradual increase of the average mass towards the heavy knee at 10^{17} eV, followed by a gradual decrease up to a predominantly light composition at the ankle at 5×10^{18} eV. At higher energies, the mean mass increases again.

cosmic rays, but of a mean logarithmic mass of the cosmic ray flux:

$$\langle \ln A \rangle = \sum r_i \ln A_i \tag{2.2}$$

with the relative fraction r_i of the element with the atomic mass number A_i. This quantity can be derived from different composition sensitive air-shower parameters such as the ratio of secondary muons and electrons at the ground or the atmospheric depth of the maximum number of secondary particles $X_{\max}$, as discussed later (Section 2.2.2).

In Fig. 2.4 results for $\langle X_{\max} \rangle$ measurements of various air shower experiments are shown together with the predictions for proton and iron of different hadronic models. The change of $\langle X_{\max} \rangle$ from 10^{15} eV to 10^{17} eV is compatible to a gradual increase of the average mass. With modern particle accelerators such as the LHC the hadronic interactions are well surveyed up to energies of around $\sim 10^{15}$ eV by experiments specialized to the parameter space of interactions in air showers (e.g. NA61-SHINE [28] at the CERN SPS or CASTOR at LHC [29, 30]). Hence, the systematic uncertainties of the models are small. In addition, unknown particle processes are disfavored to appear at the energies of accelerator measurements. Measurements from KASCADE-Grande of the energy spectrum separately for light and heavy parti-

cles show a consecutive cutoff of the flux for the different mass groups (heavy knee at 8×10^{16} eV) [14]. This leads to interpretations of the knee as a rigidity dependent leakage of galactic cosmic rays from the galaxy and/or a rigidity dependent maximum energy of galactic sources.

The average mass decreases again towards 10^{18} eV, resulting in a predominantly light composition at the ankle. One explanation is a transition from galactic sources to different types of extragalactic sources with higher maximum energies and different mass compositions. Particles with higher energies can escape the magnetic fields of their host galaxy and enter the Milky Way. The energy spectrum is increasingly dominated by these extragalactic cosmic rays as the maximum energies of galactic sources are reached. The dip-model explains the flatter spectrum above the ankle with interactions of protons with photons of the CMB, resulting in a production of an e^+e^- pair [31, 32]. This scenario favors a nearly pure proton composition above 10^{18} eV. However, the Pierre Auger Collaboration recently published measurements indicating a mixed composition at the ankle [33], disfavoring the dip-model as sole explanation for the ankle.

At the highest energies the current measurement results are not conclusive yet due to systematic uncertainties of the hadronic models and very small statistics. Auger measured a change towards a mixed composition [34], HiRes and Telescope Array (TA) measured $\langle X_{\mathrm{max}} \rangle$ compatible with a light composition, but not excluding a significant fraction of helium and CNO nuclei. However, at around 10^{20} eV no measurements of $\langle X_{\mathrm{max}} \rangle$ are available so far. To answer the remaining questions about the mass composition and with it the origin of ultra-high energy cosmic rays (UHECRs), the Pierre Auger Observatory is currently upgraded for better separated measurements of the muonic and electromagnetic component of the shower as well as for larger statistics in the $\langle X_{\mathrm{max}} \rangle$ measurements (see Section 3.5).

2.1.3 Anisotropies of the arrival directions

To identify sources of cosmic rays, anisotropies in the arrival directions can be compared to locations of known astrophysical objects possibly acting as point sources or cluster regions of sources of different types. However, cosmic rays get deflected in galactic and intergalactic magnetic fields during their propagation through space. Hence, their arrival directions do not necessarily point back to the location of their sources. The strength of the deflection is rigidity dependent, and less charged ($\equiv$ lighter) cosmic rays with higher momentum are less bent from their original direction. Therefore, anisotropies are expected in the flux of the ultra-high energy cosmic rays in the direction of strong emitters which are located nearby within a distance of tens of Mpc. A separate analysis of arrival directions of light and heavy cosmic rays will enhance the search for single sources, which makes composition measurements in this energy regime crucial.

Possible source candidates of cosmic rays are jets of Active Galactic Nuclei (AGNs), i.e. supermassive black holes in the center of galaxies, and starburst galaxies (SBGs), i.e. galaxies with intense star formation. The Pierre Auger Collaboration compared

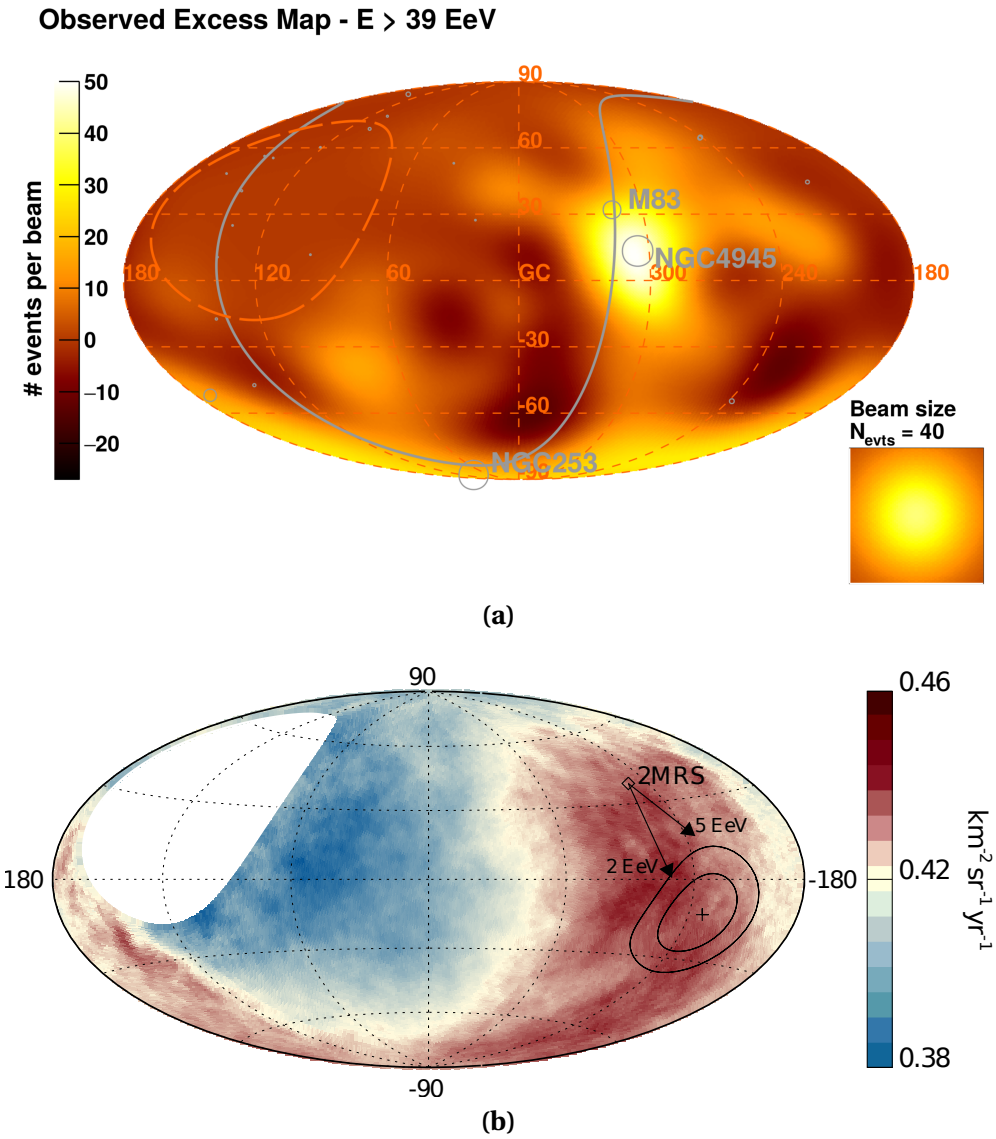

Figure 2.5: Intermediate- and large-scale anisotropies in the arrival directions of cosmic rays Both sky maps are drawn in galactic coordinates, so that the galactic center is in the origin. **(a)** Observed excess map of cosmic rays above $E \leq 3.9 \times 10^{19}$ eV measured from the Pierre Auger Collaboration compared with the locations of starburst galaxies from the Fermi-LAT catalog. The grey circles indicate the locations of SBGs. The orange dashed line delimits the field of view of the experiment. The grey solid line shows the Super-Galactic Plane. The figure is taken from [35]. **(b)** Sky map of the average cosmic-ray flux of energies $E \leq 8 \times 10^{18}$ eV smoothed out in 45° radii. The cross indicates the direction of the observed dipole and the surrounding contours the 68 % and 95 % confidence level regions. The figure is taken from Aab [1].

the arrival directions of measured events above an energy of 3.9×10^{19} eV with the locations of SBGs from the Fermi-LAT catalog (gamma-ray measurements) [35]. A deviation from isotropy was found at an angular scale of 13° with a significance of $4.0\,\sigma$, showing the most intense clustering of cosmic rays from the direction of the starburst galaxy NGC 4945, M 83 and NGC 253 (see Fig. 2.5a). However, no individual source is identified with sufficient significance. Comparisons with the locations of AGNs found in the Swift-BAT NASA mission (X-ray observations) and closer than 80 Mpc with the arrival directions of cosmic rays above 6×10^{19} eV showed a weaker correlation with a significance of $2.7\,\sigma$ on a 7° angular scale, dominantly in the direction of Centaurus A (see Fig. 2.6b), the closest radio-loud AGN in 4 Mpc distance. The Telescope Array Experiment found indications for a hot-spot in intermediate-scale searches (angular window of 20° radius) at 139° in right ascension and 45° in declination with a global significance of $3.74\,\sigma$ [36].

Recently, the Pierre Auger Collaboration found a dipolar structure at large scales of 45° radius for ultra-high energy cosmic rays above 8×10^{18} eV [1]. It has an amplitude of $6.5^{+1.3}_{-0.9}$ % pointing to (100 ± 10)° in right ascension and -24^{+12}_{-13} ° in declination with a significance of $5.2\,\sigma$(see Fig. 2.5b). The maximum of this dipole lies about 125° from the galactic center and therefore indicates an extragalactic origin of cosmic rays above 8×10^{18} eV. The anisotropic distribution of the extragalactic cosmic rays can be explained by an anisotropic distribution of sources (e.g. galaxies) or alternatively by a dominant foreground source combined with diffusion through intergalactic magnetic fields. In any case, the anisotropy indicates that most of the cosmic rays originate from the close-by universe ($\lesssim 100$ Mpc). The location of the cosmic-ray dipole was found to be in a distance of 55° to the location of a dipole in the distribution of galaxies from the 2MRS catalog. The arrows in Fig. 2.5b indicate a possible deflection from the originating direction by galactic magnetic fields for cosmic rays of E/Z = 5×10^{18} eV or 2×10^{18} eV. This corresponds to cosmic rays of 1×10^{19} eV, assuming a mean mass between $Z \approx 1.7 - 5$ consistent with current observations and recent models for the deflection at galactic magnetic fields. Once more, more accurate measurements of the mass composition of cosmic rays at the highest energies are crucial to distinguish between multiple or single source models as explanations for the discovered dipole.

2.1.4 Sources and acceleration mechanisms

Although cosmic rays were discovered about 100 years ago, their origin is still not completely understood, especially at the highest energies. There exist various theories about the processes from which these particles gain such high energies. The most established theories predict stochastic processes in which the particles get accelerated in multiple scattering processes in magnetic fields. The acceleration process lasts as long the particle is trapped in the magnetic field. Fermi proposed the acceleration to happen at moving interstellar clouds of magnetized plasma [37], which is called second-order Fermi acceleration. The direction of motion of the cloud is random to the trajectory of the cosmic ray which leads to energy gains and

losses with a net gain. However, the acceleration process is quite inefficient and slow. On average a particle gains an energy per interaction with a cloud of

$$\Delta E/E \approx \frac{4}{3}\beta_c^2 \tag{2.3}$$

with $\beta_c = v/c << 1$ being the velocity of the cloud in units of the speed of light. An alternative process was proposed by Blandford and Ostriker [38] and is called first-order Fermi acceleration. Here, the particles are accelerated at shock fronts. Possible source candidates featuring shock fronts are supernova remnants (SNRs) [39] or jets of AGNs. The particles are trapped in the moving magnetic fields of the shocked gas. Thus, they are scattered multiple times at the shock front, gaining energy at each back-and-forth crossing. Hereby, the energy gain per back-and-forth crossing is more efficient compared to the second-order Fermi acceleration with

$$\Delta E/E \approx \frac{4}{3}\beta_s \quad , \tag{2.4}$$

where β_s is the velocity of the shocked gas and $\beta_c^2 << \beta_s$. From this mechanism we can derive an expectation for the energy spectrum discussed in Section 2.1.1 [40]. After n back-and-forth crossings the particle has an energy of

$$E_n = E_0\,(1+\xi)^n \tag{2.5}$$

with the initial energy E_0 of the particle and an energy gain of ξ. If the probability to escape from the acceleration region is given by P_{esc}, the number of particles left after n crossings is

$$N_n = N_0\,(1-P_{esc})^n$$

with the initial number of particles N_0. From this follows

$$\frac{N}{N_0} = \left(\frac{E}{E_0}\right)^{-p}, \quad \text{with } p = -\frac{\ln(1-P_{esc})}{\ln(1+\xi)} \tag{2.6}$$

and the differential energy spectrum

$$\frac{dN}{dE} \propto \left(\frac{E}{E_0}\right)^{-(p+1)} \quad . \tag{2.7}$$

Hence, the energy spectrum emitted at the sources follows a spectral index of $\gamma_{source} = -(p+1)$ which can be estimated to ≈ -2 with some additional calculations. The measured spectral index is of the same order, but differs due to energy dependent escape probabilities and energy losses from propagation effects, which will be discussed in Section 2.1.5.

To gain the highest energies observed, the particles must be trapped long enough in the source region. The Larmor radius r_L of a charged relativistic particle in a

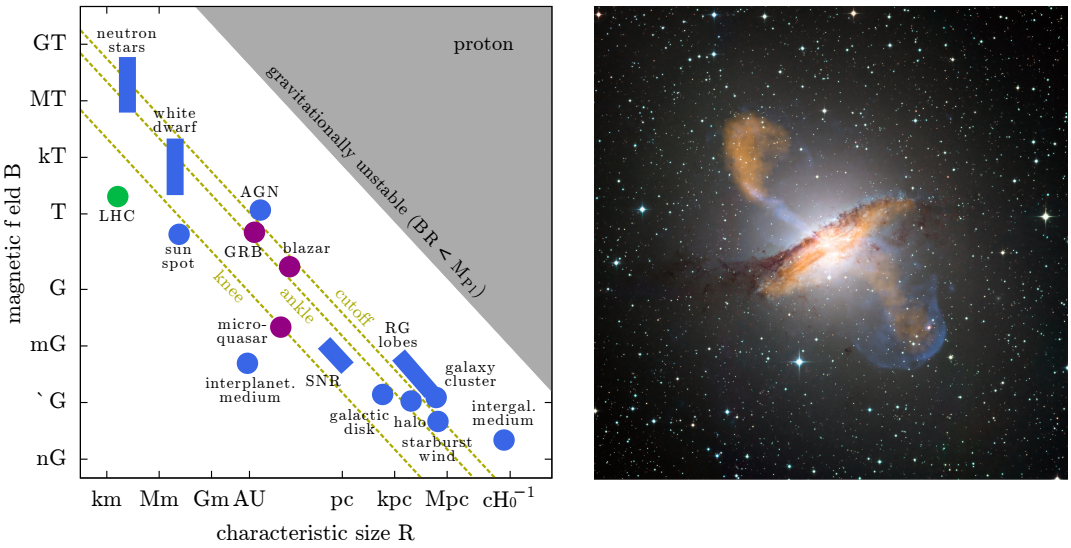

Figure 2.6: Sources of cosmic rays (a) The Hillas plot of cosmic ray source candidates (blue) with their typical size R and magnetic field B. For blazars, gamma-ray bursts and microquasars the parameters are shown in the jet frame (Doppler boosted, purple). In green, the corresponding spot for the LHC beam is shown. The yellow dashed lines show lower limits for accelerators of protons at the knee ($10^{14.5}$ eV), the ankle ($10^{18.5}$ eV) and the potential GZK-cutoff ($10^{19.6}$ eV). The gray area describes a region of gravitation instability. Figure is taken from Dova [41], initial figure from Hillas [42] **(b)** Colour composite image of Centaurus A, the closest known AGN to Earth [43]. It has relativistic jets emitted by the black hole in the center of the galaxy. The jets emit light in different frequency bands such as radio, x-ray and optical. The image was measured in optical from the Wide Field Imager (WFI) on the MPG/ESO 2.2 m telescope, in 870-micron submillimetre from LABOCA on APEX (shown in orange) and in X-ray from the Chandra X-ray Observatory (shown in blue).

magnetic field B is

$$r_L = \frac{1.08}{Z} \cdot \left(\frac{E}{10^{18}\,\text{eV}}\right) \cdot \left(\frac{B}{\mu\text{G}}\right)^{-1} \text{kpc} \tag{2.8}$$

with the energy E and the charge number Z of the particle. To be able to trap the particle, the size R of the source must be larger than $2r_L$. This leads to a maximum energy a particle can obtain in a source, which is described by the Hillas criterion [42]:

$$\left(\frac{E_{\text{max}}}{10^{18}\,\text{eV}}\right) \approx 0.54 \cdot Z \cdot \left(\frac{B}{\mu\text{G}}\right) \cdot \left(\frac{R_{\text{source}}}{\text{kpc}}\right) \cdot \beta_s \quad , \tag{2.9}$$

where β_s is the shock velocity. It puts constrains on the type of the source as well as on the composition of cosmic rays since the maximum energy is proportional to Z. Heavier particles stay longer in the acceleration region and gain more energy. This gives possible explanations for different features in the energy spectrum discussed in

Sections 2.1.1 and 2.1.2 such as knee and heavy knee as well as light ankle and ankle. In Fig. 2.6a source candidates are placed according to their corresponding magnetic field and size. The yellow dashed lines show the lower limits for the different features of the energy spectrum for the acceleration of protons. The galactic disk is located below the requirements for the energies at the ankle which is consistent with the extragalactic origin of cosmic rays above the ankle. The only possible sources for protons at the energy of the cutoff are radio galaxy lobes, galaxy clusters and neutron stars. Exceptions may be sources which move relativistically in the host-galaxy frame such as gamma-ray bursts (GRBs) and jets from AGNs since the maximum energy is increased due to a Doppler boost. However, a heavier composition is observed at the cutoff and no evidence for protons above $10^{19.2}$ eV was found so far [44]. Heavier particles (≡ higher charge) could be accelerated up to the cutoff by sources with smaller size or magnetic field as needed for protons.

Most of the source candidates not only produce cosmic rays but as well emit light at different wavelengths and neutrinos. Multimessenger searches are combining measurements of cosmic rays, photons, neutrinos and other possible signals such as gravitational waves [45, 46]. They are the key for the understanding of the most energetic processes in the Universe. As example the AGN Centaurus A is shown in Fig. 2.6b as observed in different wavelength regions.

2.1.5 Propagation

Leaving the source region, cosmic rays travel astronomical distances until they reach Earth. They are exposed to different processes and interactions on their way. The resulting energy spectrum and composition of the cosmic rays at Earth is therefore modified from the one injected from the sources. The particles undergo inelastic scattering at interstellar medium and especially at higher energies they interact with photons from the CMB as well as from the extragalactic background light (EBL) at infrared, optical and ultra-violet wavelengths. In addition, the composition changes due to radioactive decay and due to the generation of secondary particles as a result of spallation processes. Theoretical assumptions of the propagation for galactic cosmic rays indicate a steepening of the spectral index of the energy spectrum by 0.6 – 0.7. With measurements of the boron-to-carbon ratio (see Fig. 2.3), from balloon and satellite experiments this diffusion coefficient δ is determined to (-0.6) – (-0.4) in the GeV to TeV range [47]. Together with the result from Eq. (2.7) this leads to a spectral index of $\gamma = -(p+1) + \delta \approx -2.6$ which is in very good agreement with the measurements up to the knee (see Section 2.1.1).

The charged particles get deflected by galactic and intergalactic magnetic fields. The average magnetic field strength in the Milky Way is measured to be a few μG, and in other spiral galaxies and their halos it is of the same order of magnitude of ~1 – 40 μG. For a galaxy of the size of the Milky Way, these fields confine particles of up to ~10^{17} eV inside the galaxy they are generated in. Hence, measured cosmic rays up to this energy originate primarily inside the Milky Way. Intergalactic magnetic fields are presumably in the order of 1 – 100 nG [48]. For sources in a distance of

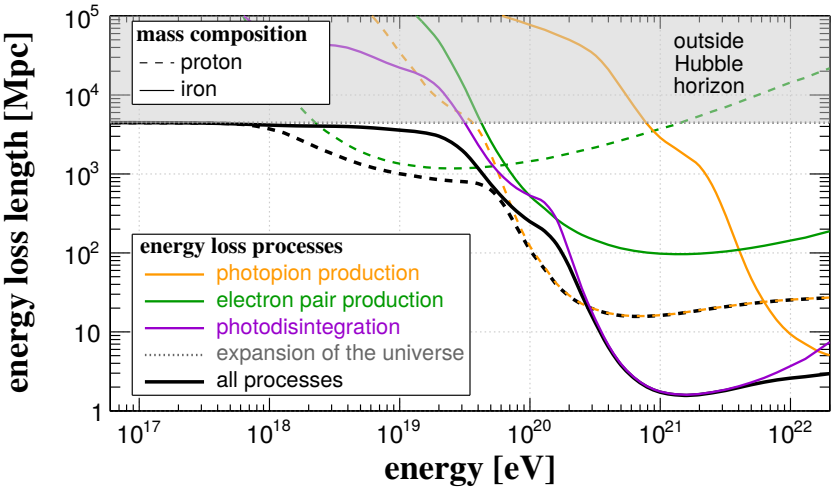

Figure 2.7: Energy loss length of propagation processes for proton (dashed lines) and iron (solid lines). The CMB and infrared extragalactic-background-light photon background are taken from Kneiske et al. [50]. Figure is taken from Alves Batista et al. [51].

several 10 Mpc the trajectories of the particles are strongly influenced by these fields and thus are the energy spectra and arrival direction distributions [49].

Cosmic rays with the highest energies suffer energy losses from the expansion of the Universe, from pair production, and from pion production after interactions with background photons. The contribution of extragalactic-background-light photons is negligible above energies of 10^{18} eV and the interactions mainly occur with the CMB photons. The production of an electron-positron pair at an interaction of a cosmic nucleus N with a photon

$$N + \gamma_{\mathrm{CMB}} \longrightarrow N + e^- + e^+ \tag{2.10}$$

has a threshold energy of $\sim 10^{18}$ eV per nucleon and is the dominant energy-loss process in this energy regime [52, 53]. The pion production by cosmic-ray protons has its threshold energy at $\sim 7 \times 10^{19}$ eV and is an extremely efficient process above this energy. In the so called Greisen-Zatsepin-Kuzmin (GZK) effect [23, 24] the protons are excited to a delta resonance, resulting in pion production:

$$p + \gamma_{\mathrm{CMB}} \longrightarrow \Delta^+(1232\,\mathrm{MeV}) \longrightarrow p + \pi^0 \tag{2.11}$$

$$\longrightarrow n + \pi^+ \tag{2.12}$$

The protons lose energy at each of such interactions until they reach an energy below the threshold energy. Hence, particles with higher energies than the threshold energy must originate in nearby regions of the Universe, from sources within the GZK sphere

of 75 – 150 Mpc radius. The pions and neutrons further decay to

$$\pi^0 \longrightarrow \gamma + \gamma \tag{2.13}$$
$$n \longrightarrow p + e^- + \overline{\nu}_e \tag{2.14}$$
$$\pi^+ \longrightarrow \mu^+ + \nu_\mu \tag{2.15}$$
$$\hookrightarrow \quad e^+ + \nu_e + \overline{\nu}_\mu \tag{2.16}$$

These secondary photons and neutrinos are essential for multimessenger studies.

Nuclei heavier than a proton lose energy and nucleons via different photodisintegration processes [54]. A CMB photon is absorbed by the nucleus, resulting in an excited state which immediately decays to a lighter nucleus and a subatomic particle such as proton, neutron, α-particle or a second nucleus. The threshold energies and cross-sections differ with the process and the atomic number A. For iron nuclei the cutoff energy is of the same order as the GZK energy for protons. In Fig. 2.7 the energy loss length for different interaction processes is shown for proton and iron.

2.2 Cosmic-ray induced air showers

The energy spectrum of cosmic rays in Fig. 2.1 shows that the flux decreases towards higher energies. To gain significant statistics for studying cosmic rays above 10^{14} eV, a large fiducial area of the experiments is essential. This is only feasible at ground. The cosmic rays interact with the Earth's atmosphere before reaching ground and release cascades of followup interactions. Hence, they can only be measured indirectly via the secondary particles produced in these extensive air showers (EAS). In fact, the high multiplicity of the secondary particles enables efficient measurements with widely spread detectors.

To interpret the measurements towards the properties of the primary cosmic ray, they are compared to simulations of EAS. For the simulations, a detailed understanding of the processes in EAS is crucial to minimize the systematic uncertainties in the interpretation of cosmic-ray data. Whereas the electromagnetic interactions in showers are well understood, there still remain challenges in the understanding of hadronic interactions at the highest energies.

2.2.1 Physics of extensive air showers

Extensive air showers contain different secondary particle types which are categorized in an electromagnetic ($e^\pm, \gamma$), muonic ($\mu^\pm$) and hadronic ($\pi^\pm, \pi^0, K^\pm, K^0, \rho^\pm, \rho^0$, baryons and other mesons) component. Primary electrons, positrons and photons induce nearly pure electromagnetic showers. A basic qualitative description of the development of an electromagnetic EAS is given by the Heitler-model [56, 57] (see Fig. 2.8 left panel). It describes the shower with two dominant processes occurring in the field of atomic nuclei of the atmosphere: radiation of a photon in form of bremsstrahlung by electrons and positrons and electron-positron pair production

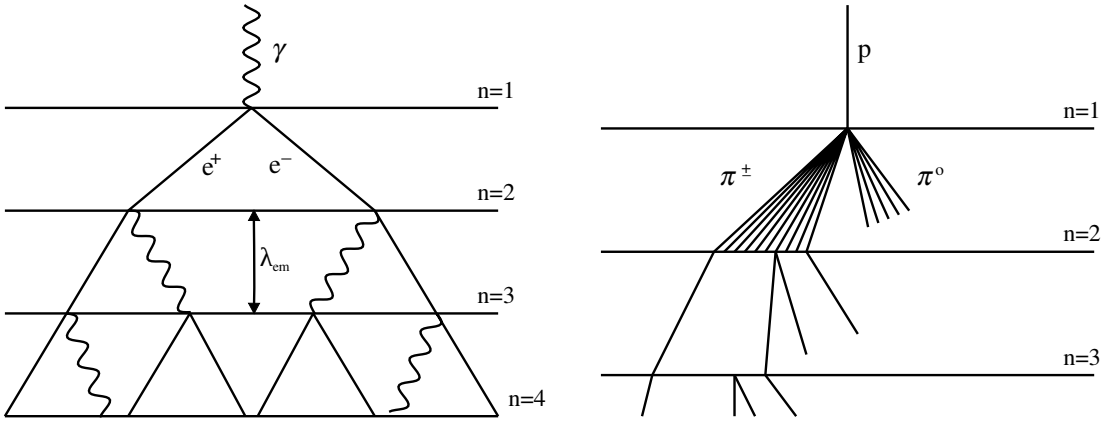

Figure 2.8: Heitler-model of extensive air showers Schematic view of an extensive air shower induced by a photon (left panel, electromagnetic shower) and a proton (right panel, hadronic shower). In the electromagnetic shower the particle number doubles after one generation n, i.e. after traversing a depth of λ_{em}. Photons create electron-positron pairs. Electrons and positrons emit bremsstrahlung. In the hadronic shower the particle multiplicity is higher and in first order π^+, π^- and π^0 are produced in equal parts. Charged pions re-interact after a mean depth of λ_{had}. Neutral pions decay into photons, yielding electromagnetic sub-showers as shown in the left panel. Not all pion trajectories are shown here for simplicity. Sketches are not to scale. Figure is modified from Matthews [55]

by photons. Both interactions take place after the same characteristic length of $\lambda_{\mathrm{pair}} = \lambda_r = \lambda_{\mathrm{em}} \approx 36.62\,\mathrm{g\,cm^{-2}}$ [1] in air. Each of these interactions of a particle with energy E leads to two new particles with equal energy $E/2$. At an atmospheric depth $X = n \cdot \lambda_{\mathrm{em}}$, after n generations of interactions the number of produced particles N_n and their energy E_n are

$$N_n = 2^n = 2^{X/\lambda_{\mathrm{em}}} \quad , \tag{2.17}$$

$$E_n = \frac{E_0}{N_n} = \frac{E_0}{2^{X/\lambda_{\mathrm{em}}}} \quad . \tag{2.18}$$

Furthermore, the electrons suffer ionization-energy losses. The particle-multiplication process continues as long as the radiation-energy loss dominates over the ionization-energy loss. At a critical energy of $E_c \approx 84\,\mathrm{MeV}$ the two energy losses are equal and the maximum number of particles is reached:

$$X_{\mathrm{max}}^{\mathrm{em}} = \lambda_{\mathrm{em}} \ln\left(\frac{E_0}{E_c}\right) \quad . \tag{2.19}$$

[1] Atmospheric lengths are corrected for the height dependent density and therefore in units of column density [$\mathrm{g\,cm^{-2}}$]

This shows that $X_{\max}$ depends on the primary energy, which is described by the elongation rate

$$\Lambda = \frac{d\langle X_{\max}\rangle}{d\ln E} \quad . \tag{2.20}$$

For the more abundant primary nuclei the Heitler-model was extended to describe hadron-induced showers by the Heitler-Matthews model [55]. It assumes, that in each interaction of a hadron with energy E with an air molecule a number of N_{tot} particles (in this model only pions) with the energy E/N_{tot} are produced (see Fig. 2.8 right panel). Positive, negative and neutral pions are produced in equal parts, which leads to two third of charged (N_{ch}) and one third of neutral pions. The neutral pions decay immediately into photons ($\pi^0 \to \gamma\gamma$), which further interact to electromagnetic sub-showers. The charged pions interact again with the air after a mean interaction length λ_{had} ($\approx 120\,\text{g}\,\text{cm}^{-2}$ for pions). Furthermore, below a distinct decay energy E_{dec} ($\approx 30\,\text{GeV}$ for pions) the probability of further interactions is lower than the decay probability, i.e. the pions decay into a muon and an (anti-)neutrino ($\pi^{\pm} \to \mu^{\pm} + \nu_{\mu}/\overline{\nu}_{\mu}$). The energy contained in the hadronic and electromagnetic component after n generations is

$$E_{\text{had}} = \left(\frac{2}{3}\right)^n E_0 \quad , \qquad E_{\text{em}} = \left[1 - \left(\frac{2}{3}\right)^n\right] E_0 \quad . \tag{2.21}$$

Solving this equations for a typical number of $n = 6$ generations of a shower reaching ground, that was induced by a particle of 10^{18} eV, shows that ~90 % of the energy is contained in the electromagnetic component. Therefore, the energy of the electromagnetic component (sometimes called calorimetric energy) is used as estimator of the primary energy. The depth of the shower maximum of a hadron-induced shower is dominated by the electromagnetic sub-showers produced in the hadronic interaction with the largest inelasticity (≡ largest multiplicity of secondary particles). Assuming this to be the first interaction (which is true in most cases), leads to

$$\left\langle X_{\max}^{\text{had}} \right\rangle \approx \lambda_{\text{had}} + \lambda_{\text{em}} \ln\left(\frac{E_0}{2N_{\text{tot}}E_c}\right) \quad , \tag{2.22}$$

which is subject to shower-to-shower fluctuations due to statistical fluctuations in the hadronic interactions e.g. the elasticity of the first interaction. The factor 2 takes into account that each π^0 decays into two photons. The number of particles in the shower can be separately derived for electrons and muons. In Fig. 2.9 the average number of hadrons, muons, electrons and photons along the shower development are shown for proton-induced showers with an energy of 10^{19} eV, calculated by Monte Carlo simulations with the CORSIKA code [58]. The number of electrons can be calculated from Eq. (2.17) as the number of particles in the electromagnetic sub-showers. The number of muons follows from the number of charged pions N_{ch} which decay when reaching the energy E_{dec} after n generations of interactions:

$$E_n = E_{\text{dec}} = \frac{E_0}{(N_{\text{tot}})^n} \tag{2.23}$$

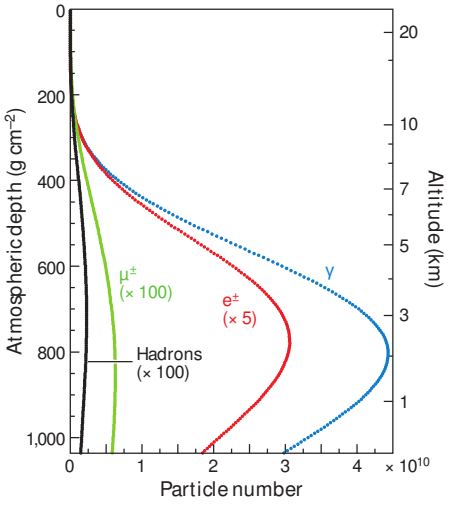

Figure 2.9: Longitudinal shower profile Average number of different secondary particle types along the shower development for proton-induced showers with 10^{19} eV energy. Simulations calculated with the CORSIKA code. Figure is taken from [9].

$$\Rightarrow N_\mu = N_{\text{ch}}^n = \left(\frac{E_0}{E_{\text{dec}}}\right)^\alpha \qquad \text{with} \qquad \alpha = \frac{\ln N_{\text{ch}}}{\ln N_{\text{tot}}} = \frac{\ln \frac{2}{3} N_{\text{tot}}}{\ln N_{\text{tot}}} \approx 0.85 \tag{2.24}$$

Hence, the number of muons depends on the primary energy E_0, the air density (through E_{dec}) and the particle multiplicities N_{tot} and N_{ch}.

The Heitler- and the Heitler-Matthews model do not describe all details of the particle interactions, although they describe qualitatively the most important features of air showers quite accurately. Therefore, the fraction of charged particles of 2/3 of the total number of particles and thereby the value of α only approximates reality. More detailed calculations of the interactions are performed with Monte Carlo simulation codes, including not only pions, but as well kaons, ρ's and other mesons. Furthermore, the models do not consider statistically distributed inelasticities of the interactions which can only be accounted for in Monte Carlo simulations. As a result, α was predicted by (older) air shower simulations to be $0.88-0.92$ [59]. A fit to the simulation set used in this thesis results in $\alpha = 0.923$ which is slightly higher than these predictions (see Section 5.1.1). For more details on the simulation codes, see Sections 2.2.3 and 4.1.

2.2.2 Air-shower observables sensitive to the mass of the primary particle

The Heitler-Matthews model can be extended to heavier nuclei based on simple assumptions. The binding energy between the nucleons is negligible compared to the typical first interaction energies. Therefore, a shower induced by a nucleus with energy E and A nucleons can be seen as A parallel showers with each an energy of E/A. This superposition model leads to dependencies on the primary mass of

the shower maximum $\langle X_{\max} \rangle$ and the ratio between the number of electrons and positrons N_e and the number of muons N_μ.

Depth of the shower maximum

Applying the superposition model to Eq. (2.22) leads to

$$\left\langle X^A_{\max}(E) \right\rangle = \left\langle X^p_{\max}(E/A) \right\rangle = \left\langle X^p_{\max}(E) \right\rangle - \lambda_{\mathrm{em}} \ln A \quad . \tag{2.25}$$

Hence, iron-induced showers reach their maximum on average $80-100\,\mathrm{g\,cm^{-2}}$ higher in the atmosphere than proton-induced showers (label 'p'). Due to shower-to-shower fluctuations of $X_{\max}$ and a small flux of cosmic rays at high energies, $\ln A$ cannot be determined for single events with sufficient accuracy. Instead, an average shower maximum is measured, which for a mixed composition with fractions f_i of nuclei with mass A_i is given by

$$\langle X_{\max} \rangle = \sum_i f_i \left\langle X^{A_i}_{\max} \right\rangle = \left\langle X^p_{\max} \right\rangle - \Lambda_p \langle \ln A \rangle \quad , \tag{2.26}$$

where Λ_p is the elongation rate Λ of proton

$$\Lambda = \frac{d < X_{\max} >}{d \ln E} \quad . \tag{2.27}$$

In Fig. 2.10a the distribution of $\langle X_{\max} \rangle$ over the calorimetric energy of air-shower simulations for proton and iron is shown. The calorimetric energy does not fluctuate much and provides a good estimator for the energy of the primary particle. The shower-to-shower fluctuations from $\langle X_{\max} \rangle$ are of the order of the mean difference between proton and iron, which makes them overlap. However, this fluctuations serve as an additional mass estimator, since they are much larger for protons than for iron nuclei. Measurements of the mean logarithmic mass $\langle X_{\max} \rangle$ are shown in Fig. 2.4 and discussed in Section 2.1.2.

Ratio of electrons and muons

Another mass estimator for cosmic rays is the number ratio of muons and electrons in the shower. They are measured, e.g., as particle densities with detectors at ground. The number of muons at ground for a nucleus with atomic number A can be derived from Eq. (2.24) to

$$N^A_\mu(E) = A \cdot \left(\frac{E/A}{E_{\mathrm{dec}}} \right)^\alpha = A^{1-\alpha} \cdot N^p_\mu(E) \propto A^{0.1} \quad , \tag{2.28}$$

where the label 'p' denotes a proton-induced shower. Hence, showers induced by heavier primaries feature more muons. Since the muons rarely interact with the atmosphere, this is valid for all atmospheric heights below the muon maximum, which is reached at $E_n = E_{\mathrm{dec}}$. The energy of the primary particle is shared between

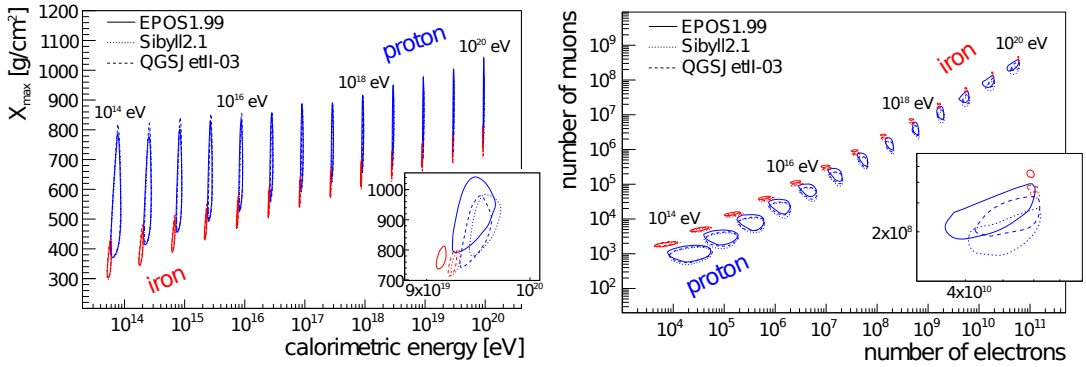

Figure 2.10: Air-shower observables as mass estimators Both figures are taken from [60] **(a)** $X_{\max}$ relative to the calorimetric energy of simulated showers with vertical zenith angle. The regions framed by the contour lines include 90% of the showers. Values for proton showers are subject of higher shower-to-shower fluctuations as for iron. The calorimetric energy fluctuates only sparsely which enables a good estimation of the primary energy. **(b)** Electron number vs. muon number shown for simulated showers with vertical zenith angle and primary proton and iron at an observation level of 800 g cm^{-2}.

the different components of the shower:

$$E_0 = E_{\text{em}} + E_{\text{had}} \tag{2.29}$$

with $E_{\text{had}} = N_\mu \cdot E_{\text{dec}}$ after all pions reach the decay energy. The fraction of the energy in the electromagnetic component is given by

$$f = \frac{E_{\text{em}}}{E_0} = \frac{E_0 - N_\mu \cdot E_{\text{dec}}}{E_0} = 1 - \left(\frac{E_0}{E_{\text{dec}} \cdot A}\right)^{\alpha-1} \quad . \tag{2.30}$$

The number of electrons at the shower maximum, where they reach the critical energy E_c (see Eq. (2.19)), is given by

$$N^A_{\text{em,max}}(E_{\text{em}}) = A \cdot N^p_{\text{em,max}}(E_{\text{em}}/A) = A \cdot \left(\frac{E_{\text{em}}/A}{E_c}\right) = N^p_{\text{em,max}}(E_{\text{em}}) \quad . \tag{2.31}$$

Since the energy of the electromagnetic component is $E_{\text{em}} = f \cdot E_0$ and the energy E_0 of the particle inducing the subshower changes with $1/A$ in the superposition model, $N^A_{\text{em,max}}(E_{\text{em}})$ depends indirectly on the primary mass. Substituting Eq. (2.30) into Eq. (2.31) and applying some numerical approximations as in [15] leads to

$$N^A_{\text{em,max}}(E_0) \approx 5.95 \cdot 10 \cdot A^{-0.046} \cdot \left(\frac{E_0}{\text{PeV}}\right)^{1.046} \quad . \tag{2.32}$$

Here, absorption in the atmosphere is not taken into account, so that $N_{\mathrm{em,max}}$ is only valid at X_{max} and the number of electrons at ground has to be corrected by

$$N_{\mathrm{e,ground}} \approx N_{\mathrm{em,max}} \exp\left(-\frac{-\Delta X}{\lambda_a}\right) \tag{2.33}$$

with the attenuation length $\lambda_a \approx 60\,\mathrm{g\,cm^{-2}}$ and a distance between the shower maximum and the detector of $\Delta X = X_{\mathrm{ground}}/\cos\theta - X_{\mathrm{max}}$. Showers initiated by heavier particles reach their maximum higher in the atmosphere than proton-initiated showers, so that ΔX is larger and the shower is further developed when reaching ground. This leads to an additional mass sensitivity of the number of electrons at ground. Alternatively, the number of electrons at X_{max} can be measured via the radio emission (see Section 2.3). The bulk of this emission is induced by the electromagnetic particles at the shower maximum X_{max} which makes the amplitude of the radio signal a good estimator on the number of these particles.

While the sum of the electron and muon numbers is a measure for the primary energy, the ratio of these numbers is related to the mass. It can be derived for the shower maximum from Eqs. (2.28) and (2.32):

$$\frac{N_e}{\mathrm{N}_\mu} \approx 35.1 \cdot \left(\frac{E_0}{\mathrm{PeV}\cdot A}\right)^{0.15} \quad . \tag{2.34}$$

This ratio is based on the simplified assumptions of the Heitler-Matthews model. The average number of electrons vs. the number of muons at an observation altitude of $800\,\mathrm{g\,cm^{-2}}$, calculated by simulations of vertical air showers, are shown in Fig. 2.10b. As in the case of X_{max}, proton showers are subject to higher shower-to-shower fluctuations. Since the simulations were performed at a fixed altitude of the detector, the attenuation effect of the electrons is visible indirectly. At lower energies the shower maximum has a larger distance to the detector, resulting in a larger attenuation and a more prominent difference between the number of electrons in proton and iron showers.

2.2.3 Hadronic interaction models

For a more quantitative description of extensive air showers, detailed simulations of particle interactions in showers are calculated. Different models exist for the hadronic multiparticle productions occurring in hadronic showers. The basis for all these models is quantum chromodynamics (QCD). However, pertubative QCD is not applicable for particle-production processes at high energies and in interactions with a small momentum transfer ('soft interactions'). Instead, phenomenological interaction models are used to describe these processes.

Measurements of particle accelerators provide important information constraining the hadronic interaction models. The Large Hadron Collider (LHC) recently measured proton-proton interactions up to a center of mass energy of $\sqrt{s} = 13\,\mathrm{TeV}$ which is equivalent to $\sim 10^{17}$ eV in the laboratory system. Experiments like NA61-SHINE

[28] at the CERN SPS or CASTOR at LHC [29, 30] are dedicated to measure data relevant for particle-productions in EAS, i.e. interaction in the forward direction of the beam with a small momentum transfer. However, for the highest cosmic-rays up to 10^{20} eV, the center of mass energies of the first interactions ($\sqrt{s} \approx 400\,\text{TeV}$ for a proton) are beyond the accelerator energies and the models are based on theory-guided extrapolations.

The recent versions of the most commonly used models are QGSJETII-4 [61], EPOS-LHC [62] and Sibyll 2.3 / Sibyll 2.3c [63]. A description of the approaches of the different models and a comparison between them can be found in [64]. Recently, the Pierre Auger Collaboration published results which show that the number of muons is measured to about 30 – 80 % larger as predicted in hadronic models [65] (QGSJETII-4, EPOS-LHC, Sibyll 2.1). The analysis was independent of uncertainties of the absolute energy scale. Thus, the results indicate an inaccurate description of the hadronic interactions. Albeit, the newest release of Sibyll 2.3 predicts an increased number of muons due to an enhanced treatment of meson interactions (ρ^0). However, the discrepancies in the absolute number of muons has no mayor influence on the mass separation power between light and heavy primary particles, albeit on the interpretation of the absolute scale of the mean mass, as later shown in Chapters 5 and 7. The predictions for the electromagnetic part of air showers agree within measurement uncertainties with results from the experiments and the differences in the models are negligible for the calculation of the radio emission. Therefore, only QGSJETII-4 will be used in simulation studies in this thesis.

2.2.4 Detection of extensive air showers

Air showers can be measured with different detection techniques (see Fig. 2.11 for an overview). Particle detectors at the ground measure directly the secondary particles, but only take a 'snapshot' of the air shower at the moment it arrives at the ground. More indirect techniques detect electromagnetic emission induced by the secondary particles when traversing the atmosphere such as fluorescence light, Cherenkov light and radio emission. These techniques detect signals coming from different stages of the shower, observing its longitudinal development. At the highest energies various techniques are combined to hybrid experiments to gain complementary information about the air shower and to minimize the dependence on hadronic interaction models and systematic uncertainties therein. In particular, the combined measurements of the muons at ground and the radio emission induced by the electromagnetic shower component, as conducted in this thesis, provide complementary information on the air shower.

Particle detection

The extensive lateral distribution of air showers at ground requires arrays of particle detectors distributed over large areas. At the same time, air showers of cosmic rays above 10^{18} eV can be measured even with a kilometer spacing between the detectors. The lower energy threshold of the experiment is defined by the size of the detectors

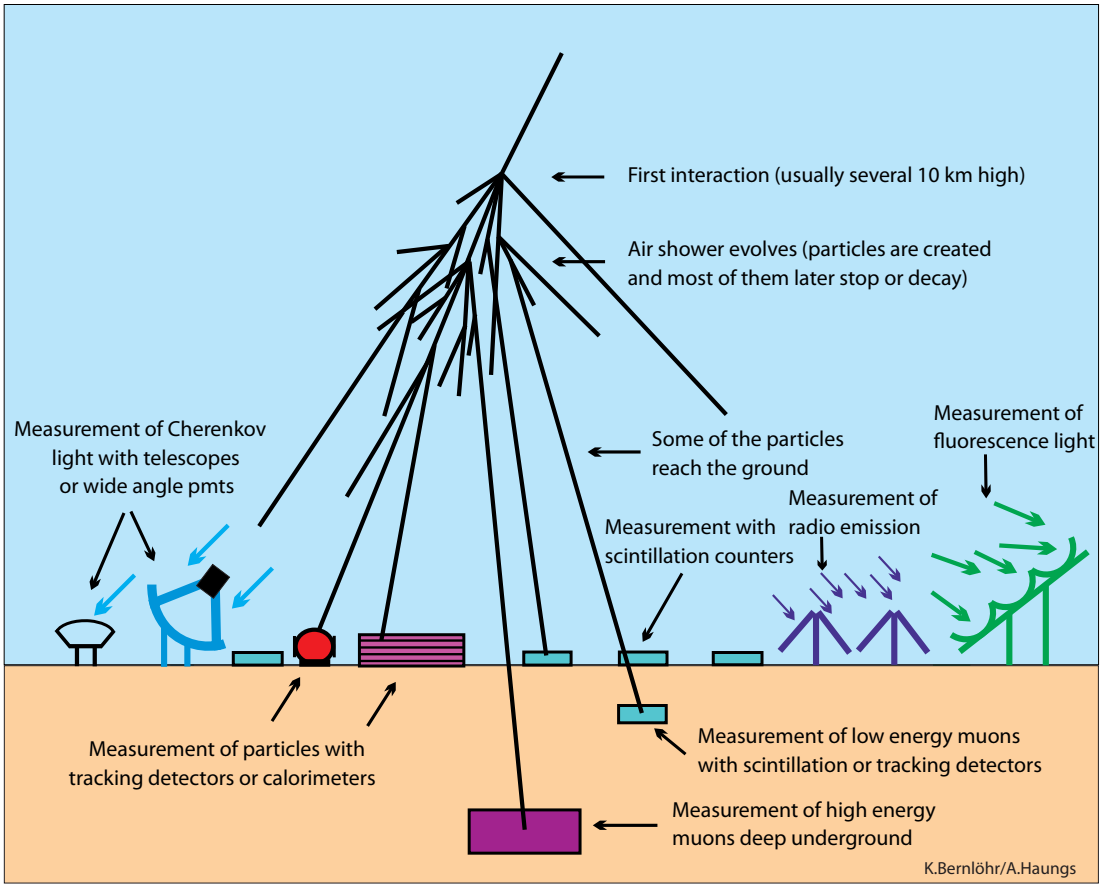

Figure 2.11: Air shower detection techniques schematic overview [66]

and the distance between the detectors (due to the width of the lateral distribution) The upper energy threshold is statistically limited by the overall size of the area (due to a decreasing flux of cosmic rays). Particle detectors widely used are water-Cherenkov tanks (e.g. at the The Pierre Auger Observatory (see Section 3.1, [67]), at HAWK [68] or at IceTop filled with clear ice [69]) or scintillators (e.g. at AMIGA (see Section 3.3, [70]), KASCADE(-Grande) [71], Tunka-Grande [72], AGASA [73] and Telescope Array [74]). They bring the advantage of detecting almost independent on weather and day-/night-effects and have an operation time of up to 100 %.

The secondary shower particles travel with relativistic speed in a disc of $\mathcal{O}(1\,\mathrm{m})$ thickness. The arrival direction of a primary cosmic-ray is measured via the residuals of the arrival time of the shower disc in the different stations. The overall number of particles in the shower and the width of the lateral distribution depend on the primary energy. To estimate the primary mass, a separate measurement of the muonic and the electromagnetic shower component is essential. This can be realized e.g. by placing detectors above and below an electron-shielding such as lead plates or several meters of soil as used in the AMIGA Muon Detector at the Pierre Auger Observatory (see Section 3.3). The amount and density of the material above the detectors

defines the energy threshold for muons, since the penetration depth depends on the energy of the particles. Measurements of the hadronic component of the shower provide additional information on the primary mass and energy and for the test of hadronic interaction models. For that purpose the KASCADE experiment installed a hadronic calorimeter in the center of its detection array [75]. Furthermore, the shower maximum $X_{\max}$ can be inferred from characteristics of the time profiles, i.e. the rise time, of Cherenkov light peaks in water-Cherenkov tanks, as recently shown by the Pierre Auger Collaboration [76].

Fluorescence light in the atmosphere

The charged secondary particles excite nitrogen molecules when traversing the atmosphere. The nitrogen emits light in a characteristic wavelength in ultraviolet when decaying back to ground state. This fluorescence light is emitted isotropically so that it can be observed from all directions, e.g. with a mirror telescope. The mirror projects the light on a photomultiplier (PMT) camera, where the passing by shower is seen as a trace along the camera. The intensity of the light is directly proportional to the energy deposit of the shower in the atmosphere and hence the number of electromagnetic particles. The intensity profile along the trace shows the longitudinal development of the shower as a function of slant atmospheric depth. Fitting a longitudinal profile, the shower maximum $X_{\max}$ can be reconstructed and hence the primary mass estimated. The integral over the profile is proportional to the calorimetric energy in the shower which corresponds to the primary energy despite the missing energy contained in the (several orders of magnitude smaller) muonic component. The energy threshold of this measurement technique is at around 10^{17} eV as the light yield from less energetic showers is too weak to be detected by the PMTs, and the shower maximum is too high in the atmosphere so that the light gets more attenuated on the longer way. A typical field of view of such a telescope is $1-30°$ in elevation. The disadvantage of this technique is that it relies on a clear and cloudless atmosphere, since the light gets scattered and attenuated by aerosols. Because of the small light yield, highly sensitive PMTs are used, which can only be operated in dark, moonless nights. This limitations lead to an operational time of only ~15 %. The pioneering experiments using fluorescence telescopes were Fly's Eye and its successor HiRes [77]. The largest experiments using this techniques are currently the Pierre Auger Observatory [67] (see Section 3.2) on the southern hemisphere and the Telescope Array on the northern hemisphere [78]. Both experiments operate the fluorescence telescopes in hybrid mode with particle detectors. Future experiments such as JEM-EUSO [79] and KLYPVE/TUS [80] aim for an observation of the fluorescence light from space with a very wide field of view telescope to study extreme-energy cosmic rays (EECRs) beyond the GZK-cutoff.

Cherenkov light in the atmosphere

When the charged secondary particles traverse the atmosphere with a velocity larger than the speed of light in the medium air, they induce Cherenkov light emission.

This emission is beamed in a forward cone around the direction of the particle inducing it. Hence, a detector has to be aligned to the arrival direction of the primary particle or has to feature a wide field of view. Experiments such as H.E.S.S. [81], MAGIC [82], or VERITAS [83], and the future CTA [84] are using a mirror telescope similar to the fluorescence technique, so called imaging atmospheric Cherenkov telescopes (IACT), which can be aligned to regions of interest at the sky. They focus on the measurement of air showers induced by high energy gamma-rays from cosmic sources. The Tunka-133 experiment [85] with its successor TAIGA [86] is using wide angle PMTs, covering a large fraction of the sky, to measure air showers induced by cosmic rays and gamma-rays. However, it features a higher energy threshold than imaging telescopes. Cherenkov telescopes have the same constrains for clear moonless nights as the fluorescence technique.

2.3 Radio emission from extensive air showers

In 1962, Askar'yan postulated a coherent radiation in the MHz range, induced by the electrons and positrons of the electromagnetic component of air showers [87]. Three years later, a radiation induced by air showers was first measured by Jelley et al. [88]. Kahn and Lerche [89] predicted, that the radiation is correlated to the angle between the shower axis[2] and the Earth magnetic field. However, the research of this radiation was confined by analog antenna techniques, in contrast to other detection techniques for EAS. Therefore, this measurement approach was not followed further for various decades. In the 2000's, when digital radio techniques and signal processing advanced, measurements of air-shower radio emission were revived. Since then various digital radio experiments have measured the radio emission of EAS successfully, and meanwhile the emission mechanisms are well understood. A general overview of radio emission and detection techniques is given in [90] and[91].

The radio emission shows a similar lateral extension as Cherenkov-light at the ground. This makes a detection with an array of radio antennas feasible. Since the atmosphere is transparent for MHz radiation, the propagation of the radio emission is almost independent on atmospheric conditions, leading to an operational time of nearly 100 %. This is an advantage compared to the fluorescence and Cherenkov techniques. Only during thunderstorms or heavy rain clouds, the radio signal is disturbed by strong electromagnetic fields in the atmosphere. However, this enables to study weather phenomenons with radio experiments [92, 93].

Further background to radio experiments are the radio emission of the Galactic plane, man-made broad- and narrowband radio-frequency interferences (RFI) from electrical equipment (generators, transformers) or broadcasting, where the latter can be avoided by an appropriate choice of the bandwidth. RFI pulses can have a similar characteristic as cosmic-ray radio pulses, which makes self-triggering on the radio signal challenging. However, self-triggering has been successfully applied in unpopulated regions by the RAUGER [94], TREND [95] and ARIANNA [96] experiments.

[2] axis along the arrival direction of the primary particle

Current radio arrays measure cosmic rays above a primary energy of around 10^{17} eV. However, the detection efficiency and the energy threshold depends on the arrival direction of the primary particles, and the bandwidth and the spacing of the antennas. In [97] it was shown, that the energy threshold can be reduced by an order of magnitude with a proper choice of the bandwidth. Furthermore, the local geomagnetic field and the observation level of the experiment determine features of the emitted radio emission.

Radio emission measurements are complementary to other measurement techniques of air showers and provide additional information on the primary cosmic-rays. Therefore, radio antenna arrays are often combined with particle detectors, which provide a trigger for the radio antennas. Examples for cosmic-ray radio experiments are the LOPES experiment in Karlsruhe, Germany [98], which was collocated with the KASCADE-Grande experiment, Tunka-Rex in Siberia [99], which is collocated with the TAIGA experiment, and AERA at the Pierre Auger Observatory in Argentina (see Section 3.4). The LOFAR experiment located in Europe, features a dense array of antennas, which makes very accurate and detailed radio measurement of air showers possible [100]. In addition, various experiments aim at the detection of ultra-high energy extraterrestrial neutrinos, such as ARIANNA on the Ross Ice Shelf [96], ARA at the South Pole [101] and the future large scale experiment GRAND [102].

2.3.1 Emission mechanisms

The radio emission originates from the superposition of various emission mechanisms. The two dominant mechanisms are the geomagnetic effect and the Askaryan effect, which produce in average 80 – 90 % and 10 – 20 % of the emission, respectively. Other proposed mechanisms could not be proven experimentally, yet, and are expected to be at least an order of magnitude weaker in the common observation frequencies of MHz to GHz. These are in particular: bremsstrahlung of the electrons from ionized atmospheric molecules [103, 104, 105], synchrotron radiation of the electron in the shower due to curved trajectories in the Earth magnetic field and transition radiation when the shower enters the ground (sudden death) [106, 107]. In the following, the two dominant mechanisms are discussed in more detail.

Geomagnetic effect

The electrons and positrons in the shower get deflected at the Earth magnetic field in opposite directions by the Lorentz force (see Fig. 2.12 left panel). This charge separation corresponds to a drift current transverse to the direction of the shower. Along the shower development, the number of particles changes and thus the strength of the drift current changes with time. The resulting Hertz dipole induces radio emission. The radio emission is linearly polarized perpendicular to the direction of the Earth magnetic field [89, 108]. The variation of the current changes its sign at the shower maximum, which results in a bipolar shape of the radio pulse in the antennas at the ground. The amplitude depends on the strength of the Lorentz force and hence on the local strength of the geomagnetic field $\sin\alpha$, where α is the angle between the

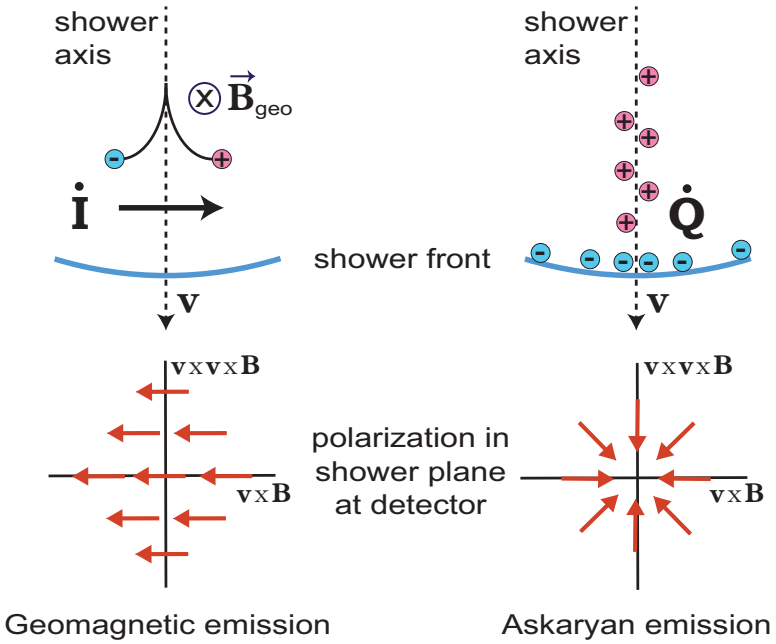

Figure 2.12: Radio emission mechanisms Schematic illustration of the two dominant radio emission mechanisms and the resulting polarization [91].

shower axis and the Earth magnetic field. Therefore, the threshold and efficiency of the detection depends on the arrival direction of the shower [109].

Askaryan effect

Atmospheric molecules get ionized by high energy photons of the shower and the liberated relativistic electrons join the shower. Furthermore, shower positrons annihilate with electrons of atmospheric atoms. In total, the shower front gains a negative charge excess and a positively ionized plasma is created behind the shower (see Fig. 2.12 right panel). This corresponds to a current along the shower axis whose strength varies with the shower development [87]. This induces radio emission, which is radially polarized around the shower axis [110]. Due to interference of the geomagnetic (linearly polarized) and the Askaryan emission (radial polarized), the strength of the total emission is distributed asymmetrically around the shower axis with the maximum slightly off the axis [111] (see Fig. 2.14).

The fraction of Askaryan emission and the geomagnetic emission of the total radio emission depends predominantly on the angle to the Lorentz force, which defined the strength of the geomagnetic emission. In addition, it depends on the distance to the shower axis, the shower inclination, and the height of the shower maximum. The fraction of the Askaryan emission was measured recently by various radio experiments to be between 3 – 20 %, depending on the observation level of the experiment and the parameters mentioned above [110, 112, 113].

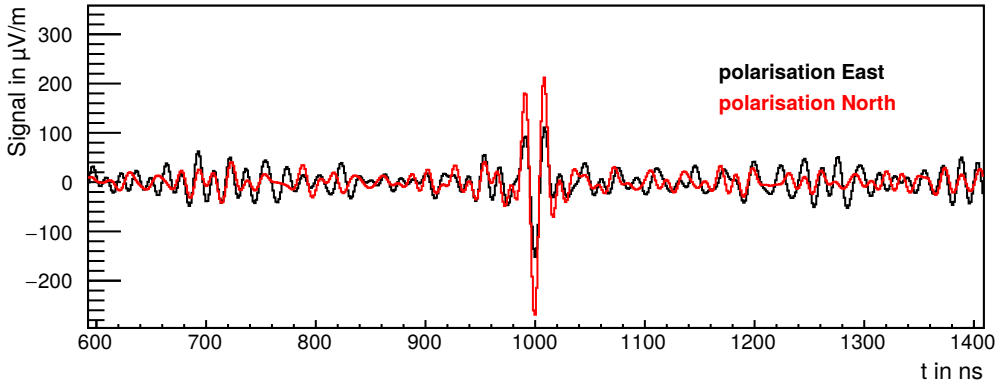

Figure 2.13: Example radio pulse as detected in an antenna station of AERA, comprising two antennas aligned in the east-west and north-south direction. The antennas are sensitive in the bandwidth of 30 – 80 MHz.

2.3.2 General features of the radio emission

Electromagnetic radiation is coherent, if the wavelength is larger than the emission region. The particle front of an air shower is typically ~1 m thick, which produces amplified radio emission in frequencies of up to various 100 MHz. The width of a radio pulse in an antenna depends on the distance to the shower axis and to the shower maximum and is in the order of 10 ns (near) and 100 ns (far). However, the measured pulse shape in an antenna varies with its bandwidth. A typical radio pulse for a bandwidth of 30 – 80 MHz is shown in Fig. 2.13, as measured from the AERA experiment in the north-south and east-west polarization.

The radiation is emitted in forward direction. The propagation speed of the produced radio waves depend on the refractive index as $c_{\text{air}} = c/n_{\text{air}}$. The refractive index changes with the atmospheric height due to a changing density and humidity. At a characteristic angle around the shower axis, the Cherenkov angle $\theta_{\text{Ch}} \approx \arccos 1/n$ ($\approx 1°$ in air), the radio emitting particles travel with the same speed than the already produced radio waves, which results in a coherent emission, and, thus, in an amplification of the radio signal to much larger frequencies up to several GHz. The maximum amplification appears at the so called Cherenkov ring, which typically has a radius of ~100 m around the shower axis in the shower plane (see Fig. 2.14), although it depends on the distance from the observer to the emission region (shower maximum). This ring particularly becomes more pronounced at frequencies higher than 100 MHz.

The radio emission is predominantly produced at the atmospheric depth featuring the maximum number of shower particles, the shower maximum X_{max}. For inclined showers, the shower maximum is at higher altitudes and the shower maximum is extended compared to vertical showers due to a slower development of the shower in the less dense atmosphere. This causes a slightly stronger radio emission for inclined showers. The total emission is distributed over a larger lateral area for inclined showers due to geometric projection effects dependent on the angle between the

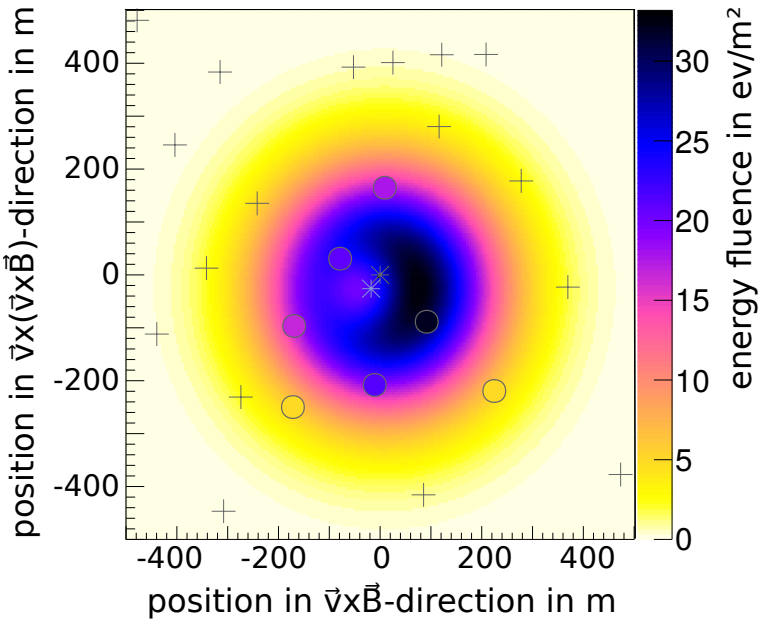

Figure 2.14: Two-dimensional lateral distribution of the radio emission in the plane perpendicular to the shower axis of the energy fluence contained in the radio emission, for an example event measured by AERA. The x-axis is chosen to be in the direction of the Lorentz force $v \times B$ and the y-axis is aligned to $v \times v \times B$.

shower axis and the antenna array plane. Hence, inclined showers can be detected with sparse antenna arrays due to the large footprints at the ground. However, they feature a smaller signal density at the ground, which increases the energy threshold for the detection.

A typical radio footprint is shown in Fig. 2.14. It shows an asymmetric bean like shape and a maximum at the Cherenkov ring. The asymmetry is caused by the interference of the geomagnetic and the Askaryan emission.

2.3.3 Reconstruction of cosmic-ray properties from the radio signal

The radio emission features information on the primary particle properties. The arrival direction can be estimated by the distribution of the arrival times in the different antennas of the array. Here, the knowledge of the shape of the wavefront of the radio emission is essential for an accuracy of better than 1 – 2°. Measurements of various experiments as well as simulation studies showed that the wavefront shape is approximately hyperbolic [114, 115]. With this, an accuracy of better that 0.5° is reached for the reconstruction of the arrival direction [116, 117].

The primary energy can be reconstructed from the energy contained in the radio emission, the radiation energy. The amplitude of the radio emission correlates lin-

early and the radiation energy quadratically with the number of electromagnetic particles in the shower, which follows from the coherence of the radio emission. This electromagnetic particles make up the bulk of the shower, and the energy contained in the electromagnetic shower component is correlated to the primary energy. Therefore, the radiation energy scales quadratically with the primary energy. The total radiation energy can be determined by integrating over the footprint, in the plane perpendicular to the shower axis, as done in the AERA experiment with an energy resolution of 14 % [118]. Alternatively, the primary energy can be reconstructed from the one-dimensional lateral distribution, when correcting for the asymmetry caused by the superposition of the geomagnetic and Askaryan emission, as done in the Tunka-Rex experiment with a precision of 15 % [119].

The mass of the primary particle is correlated to X_{max}. Since the bulk of the radio emission is radiated around X_{max} and the radiation is forward beamed, the width and the steepness of the footprint are observables for the distance to X_{max} and hence for the mass. Hence, the mass can be reconstructed from the width of the lateral distribution in th plane perpendicular to the shower axis or from the opening angle of the hyperbolic wavefront. So far, an accuracy of around $40\,\mathrm{g\,cm^{-2}}$ has been reached with sparse radio arrays such as Tunka-Rex and AERA [119, 120], and around $20\,\mathrm{g\,cm^{-2}}$ with dense radio arrays such as LOFAR [121]. Moreover, the mass of the primary particle can be estimated by combined measurements of the radio emission and the muons at the ground. This technique is developed in this thesis.

CHAPTER 3

The Pierre Auger Observatory

Contents

The Pierre Auger Observatory [67] is the world's largest observatory for cosmic rays. It is dedicated to measure the origin, properties and interactions of cosmic rays above 10^{17} eV up to the highest energies above 10^{20} eV with high statistics. The observatory is designed as a hybrid detector measuring cosmic-ray air showers with different complementary detection techniques. In a part of the observatory, muon detectors are collocated to radio antennas, which makes it a perfect environment to test the combined detection of muons and radio emission. The observatory was started to be built in 2002 and completed in 2008. The first air-shower data was recorded in 2004. Scientists from 16 countries work together in the Pierre Auger Collaboration.

The Observatory is located in the province of Mendoza in western Argentina, next to the city of Malargüe. The Surface Detector Array (SD) spans an area of 3000 km^2. The whole area is relatively flat with altitudes of 1340 – 1610 m above sea level and a mean altitude of ~1400 m. This corresponds to an atmospheric overburden of ~875 $\mathrm{g\,cm}^{-2}$, which is just beyond the mean shower maximum of vertical air showers of the highest energies. The entire array is overlooked by the Fluorescence Detector (FD) consisting of telescopes at four sites at the perimeter of the array. In the west of the array the so called enhancements area with a size of 23.5 km^2 is located. Here, the particle detector AMIGA, the radio antenna array

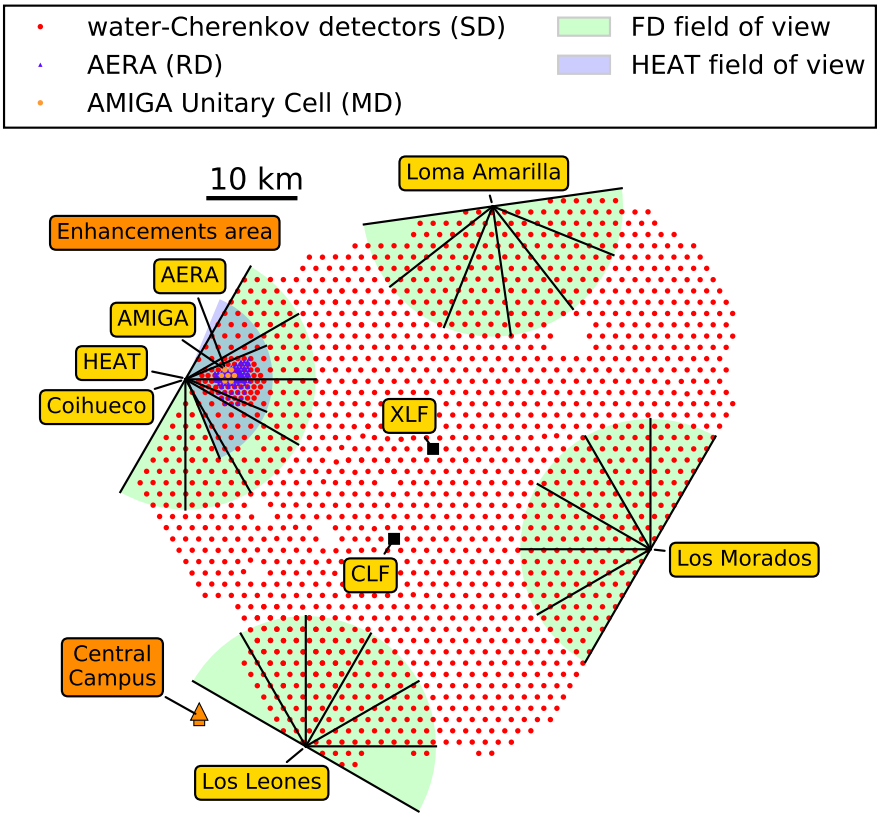

Figure 3.1: Map of the Pierre Auger Observatory The Surface Detector (SD) array comprises water-Cherenkov detectors on a grid of 1500 m spacing. It spans an area of 3000 km^2. The array is overlooked by the Fluorescence Detector (FD), which is located at four telescope sites at the perimeter of the array. Close to the Coihueco site, the enhancements area is located, including the high elevation telescopes HEAT, the infilled area of water-Cherenkov detectors and buried muon scintillators (MD) of AMIGA and the radio antenna array AERA (RD). For a zoom in the enhancements area see Fig. 3.4.

AERA, and the tilted fluorescence detector HEAT are co-located to detect cosmic rays down to energies of 10^{17} eV in coincidence. In Fig. 3.1 a map of the Observatory with its different detector components and the central campus in Malargüe is shown. In this chapter an overview of the different detector components of the Observatory is given.

3.1 The Surface Detector Array

The Surface Detector Array comprises 1660 water-Cherenkov detectors distributed on a triangular grid of 1500 m distance to the nearest neighbors [122] in the main array and 750 m distance in the enhancements area (see Section 3.3). It detects the secondary particles of air-showers reaching the ground, providing a snapshot of the shower at the time of arrival. The relativistic shower particles produce Cherenkov

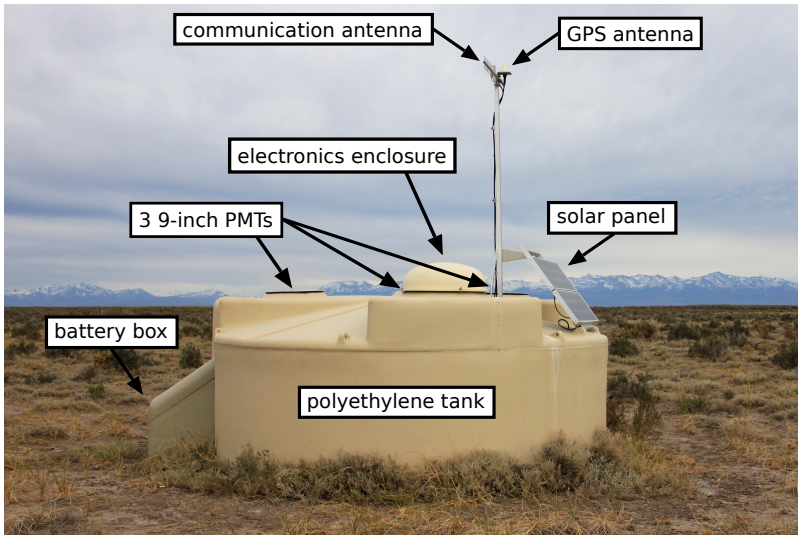

Figure 3.2: Surface Detector station

light when traversing the water volume of the detectors. The detectors are sensitive to the muons and charged electromagnetic particles of the shower, as well as to high energy photons which convert into electron-positron pairs in the water.

The spacing defines the detection efficiency at the trigger-level, for which coincident detection in at least three neighboring stations is required. Full efficiency is reached for energies above $10^{18.5}$ eV in the main array, which is almost independent of the type of the primary particle. Naturally, the quality of the measurements improves with increasing energy. The 3-dimensional design of the detectors lead to a uniform exposure up to large zenith angles. The detector has an up-time of nearly 100 % and is practically independent on weather conditions.

Each Surface Detector station includes a water tank of 3.6 m diameter and 1.2 m height, filled with 12 m^3 of ultra-pure water. The tanks are made of polyethylene resin with a sealed liner inside. The inner surface of the liner diffusely reflects the Cherenkov light. Three photomultiplier tubes each with 9-inch diameter are installed at the surface of the liner with a downwards orientation to measure the Cherenkov light. Each station works autonomously. It is powered by two solar panels installed on the top of the tank. The energy produced by the panels is stored by a battery placed at the side of the tank. The electronics is accommodated in a hatch at the top of the tank and includes a processor, a power controller, a GPS receiver, and a radio transmitter for communication with the central data-acquisition system (CDAS). The signals are recorded in flash analog-to-digital converters (FADC) and calibrated by the local electronics in each station [123]. The high voltage of each PMT is adjusted to match the average event rate of all PMTs of the tank. The GPS receiver measures the position of the station with an accuracy of better than 1 m, which is sufficient for a good reconstruction of the shower parameters. A picture of a Surface Detector station is shown in Fig. 3.2.

The Cherenkov light is measured in units of vertical equivalent muons (VEM) -

the signal a muon produces when it traverses the tank vertically. The shower is reconstructed by converting the signals in the different stations into units of VEM. The measured time structure of this signals is translated into particle densities at the ground. The primary arrival direction is reconstructed by the signal times in the individual stations. The energy is estimated by fitting a lateral distribution function to the particle densities measured in the different stations. The particle density at 1000 m distance S(1000) serves as an energy estimator. It is calibrated based on Fluorescence Detector measurements from hybridly detected events, since the FD features direct energy measurements. The energy spectrum is then determined with the Surface Detector featuring larger statistics than the FD due to the large up-time. The combined energy estimation has a systematic scale uncertainty of 14 % [67].

3.2 The Fluorescence Detector

The Fluorescence Detector [124] measures the longitudinal shower profile via the amount of fluorescence light induced by the shower passing through the atmosphere. The ultraviolet light is emitted by atmospheric nitrogen, which is excited predominantly by the electromagnetic shower particles. The detector consists of four telescope buildings at the perimeter of the array, each containing six fluorescence telescopes. Each telescope has a field of view of 30° × 30° in azimuth and elevation with a minimum elevation of 1.5° above the horizon. The telescopes are arranged such that they cover an azimuth angle of 180° at each side, facing inwards the Surface Detector Array. In that way every shower event above 10^{19} eV arriving within the array is recorded by at least one telescope. At one site named Coihueco, three additional telescopes are installed in tiltable buildings to elevate the field of view by up to 29° above the horizon, i.e. from 29° to 59° elevation (High Elevation Auger Telescopes - HEAT). They are capable to observe air showers of cosmic rays with an energy down to $\sim 10^{17}$ eV, which develop higher in the atmosphere. The Fluorescence Detector can only be operated during dark moonless nights and clear weather, which leads to a duty cycle of ~15 %. It always measures in hybrid mode with the Surface Detector Array and timing synchronization by GPS enables simultaneous measurements of the same air showers.

The telescopes are installed in closed, clean and climate controlled rooms. The fluorescence light enters through an aperture system compound of a circular diaphragm of 1.1 m radius, which is covered by a UV bandpass filter reducing the background. The light is focused onto a curved focal plane by a segmented spherical mirror of 13 m^2 surface. On the focal plane a camera, consisting of 440 (22 x 20) hexagonal PMT pixels, is installed. The pixels are separated by Winston cones to collect the light onto the PMTs. Each pixel has a field of view of 1.5°. The electronics of the camera are located below the camera mounting in order not to disturb the light inciding onto the mirror. In front of the aperture an annular lens corrects for spherical and coma aberration. The aperture is closed automatically by shutters during daylight, when moonlight falls in the field of view, and during bad weather conditions (rain, high wind speed, etc.) to protect for damage caused by intensive light incidence, water or

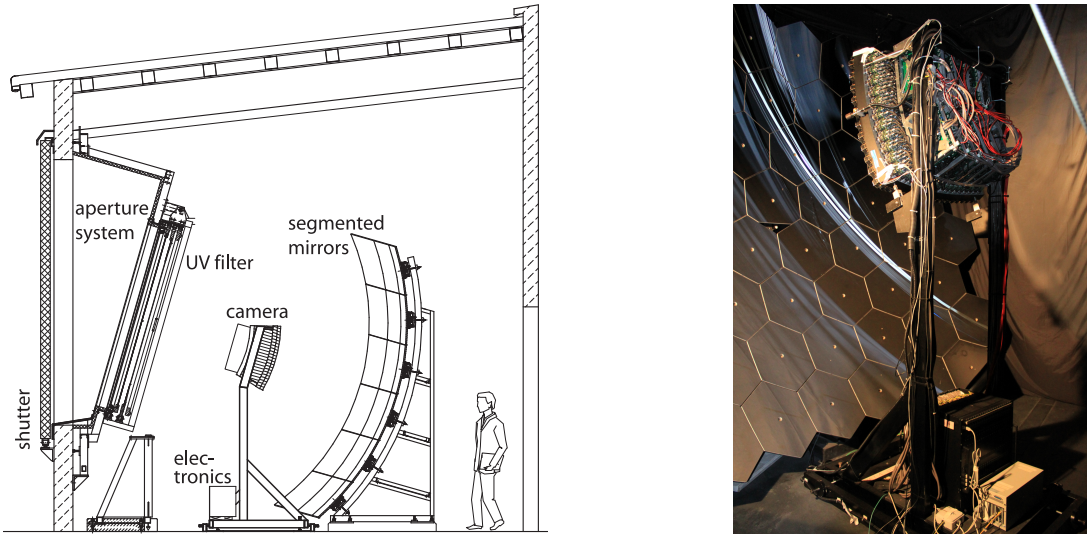

Figure 3.3: Fluorescence telescope (a) Schematic view [124] **(b)** Mirror and camera

wind. In case of a malfunction of the shutters an emergency curtain drops in front of the aperture. A schematic view of the different components is shown in Fig. 3.3a, and a photo of the mirror and the back of the camera is shown in Fig. 3.3b.

Since the atmosphere is not completely clear, the fluorescence light is attenuated and scattered on the way from the shower to the telescopes. Thereby, the atmospheric conditions vary over time and over the array of the Observatory. The changing aerosol properties are most influential to the attenuation of the light. For a correct interpretation of the measured data, the atmospheric conditions are monitored during measurements of the Fluorescence Detector. Collimated UV laser pulses are directed into the atmosphere from the Central Laser Facility (CLF) [125] and the eXtreme Laser Facility (XLF), both located close to the center of the array. The scattered light of the laser shots is then detected by the telescopes and gives information about the aerosol properties in the line of sight. The measured laser data is used additionally to check the performance and alignment of the telescopes as well as to determine time offsets to the Surface Detector. In addition, there is a lidar station, a ground-based weather station, and a cloud camera at each telescope site to monitor the atmospheric conditions and cloud coverage close to the telescope. Furthermore, data from the Global Data Assimilation System (GDAS) [126] are used as additional information on the atmospheric conditions. Still, the atmospheric properties remain one of the largest systematic uncertainties, in particular for the energy measurements.

A shower passing the atmosphere is detected in the telescope cameras as a trace of light. The shower is then reconstructed from the measured light distribution in the camera as a function of time. The full longitudinal shower profile is estimated by fitting a Gaisser-Hillas function to the light distribution [127]. The intensity of the fluorescence light is proportional to the energy deposit of the electromagnetic

shower particles. Thus, the total calorimetric energy of the shower is measured via the integral over the shower profile. To estimate the primary cosmic-ray energy, the calorimetric energy is corrected for the "invisible" energy which is carried away by high energy muons and neutrinos [128]. This energy estimator is used to calibrate the Surface Detector energy estimator S(1000). The maximum of the shower profile corresponds to the shower maximum, whose atmospheric depth X_{max} is the best statistical estimator for the primary cosmic-ray mass. The precision of a single site at around 10^{19} eV is ~10 % and 20 g cm^{-2} for the energy estimator and for X_{max}, respectively. Stereo measurements in more than one telescope are used for cross-checks of atmospheric corrections and of the detector resolution.

3.3 The Auger Muons and Infill for the Ground Array (AMIGA)

In 6 km distance to the FD site Coihueco, the Auger Muons and Infill for the Ground Array (AMIGA) is located [70]. Its main objectives are to measure cosmic rays at lower energies than the main array of the Observatory and to measure another composition-sensitive observable by directly detecting the muonic component of the air showers. In addition, separate measurements of the muonic component enable to study hadronic interactions. AMIGA is co-located with the other low-energy enhancements HEAT and AERA (see Fig. 3.4) and detects air-showers in coincidence with them. At lower energies the particle footprints of the air-showers are smaller, which demands a smaller spacing of the detectors. Therefore, The Surface Detector of AMIGA comprises 61 water-Cherenkov detectors in a denser array with 750 m spacing on an area of 23.5 km^2. Each of these water-Cherenkov detectors will be combined with buried plastic scintillators to measure muons (Muon Detector - MD)[1]. Since March 2015 seven SD stations are already fully equipped with such underground muon detectors. With the reduced spacing AMIGA reaches full detection efficiency at 3×10^{17} eV for air showers with zenith angles smaller than 55° [129]. In a part of the array, seven Surface Detector stations are installed in a hexagon, called AERAlet, with a spacing of 433 m to measure events below 3×10^{17} eV. In addition, this hexagon serves as a trigger for these low energy events for AERA. Although the array is smaller compared to the main SD, AMIGA gains sufficient statistics for the energy range between the second knee and the ankle due to the larger cosmic-ray flux. AMIGA is operated with the same duty cycle as the Surface Detector of nearly 100 %.

3.3.1 The scintillator module design of the Muon Detector

At each detector station scintillator modules will be buried at a depth of 2.3 m in soil with an average local density of (2.38 ± 0.05) g cm^{-3} (see Fig. 3.5a). This corresponds to a vertical mass of ~550 g cm^{-2} and about 15 radiation length of electromagnetic

[1] In the internal language of the Pierre Auger Collaboration AMIGA often referred only to the Muon Detector of AMIGA and the Surface Detector of AMIGA is called 'Infill'.

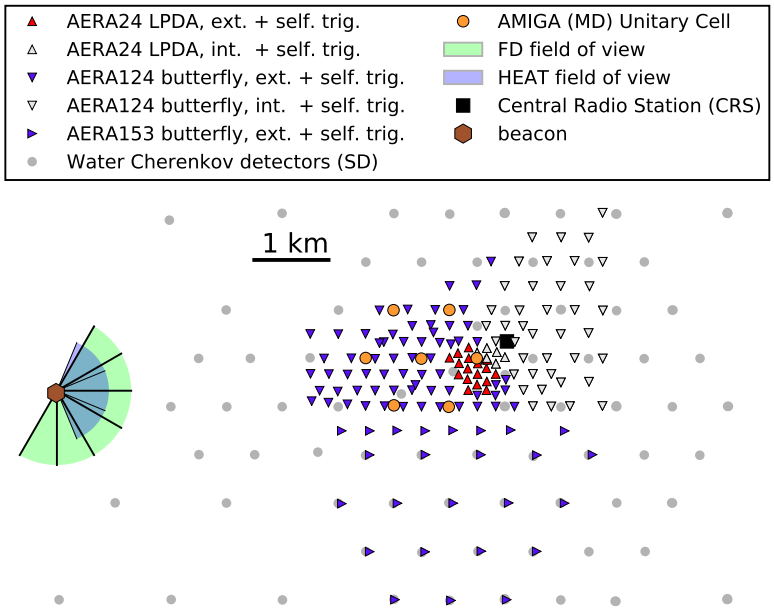

Figure 3.4: Map of the low-energy enhancements area The enhancements area is dedicated to the detection of low-energy cosmic rays above $10^{17.5}$ eV. It comprises the high elevation telescopes HEAT, the infilled Surface Detector stations of AMIGA with a spacing of 750 m, the AMIGA Unitary Cell containing prototype muon detectors under ground, and the radio antennas of AERA. AERA was build in three deployment phases and contains two different types of antennas, which are triggered externally from the SD and FD as well as self-triggered on the radio signal and internally triggered by build-in scintillators. A beacon at the site of the Coihueco fluorescence telescope building transmits continuous sine waves for the time calibration of the radio antennas. The Central Radio Station (CRS) connects the LPDA and the internally triggered butterfly antenna stations to the central DAQ.

particles. Thus, the soil shields the electromagnetic component of the shower and all muons below an energy of about 1 GeV. The scintillators cover an area of 30 m^2 which is segmented into two modules of 10 m^2 and two modules of 5 m^2. The modules are buried in at least 5 m distance from the water-Cherenkov tank to avoid shadowing effects. They are placed in an L-shape to reduce systematic uncertainties on the azimuth angle due to inclined muons. The acquisition electronics is installed locally at each scintillator module and maintainable via an access tube filled with soil bags. It is powered by an additional solar panel and battery, located at the water-Cherenkov tank. The data is sent to the central data acquisition system of the observatory via an additional antenna based on WiFi 802.11g standard.

Prototypes of muon detectors were deployed at seven infilled Surface Detector stations in a hexagon (see Fig. 3.5b). This so called Unitary Cell is fully operational since March 2015. It is dedicated to track down and resolve possible engineering issues and to finalize the design for the entire AMIGA array. A second set of scintillator modules was installed at two stations to investigate the accuracy of the muon-counting

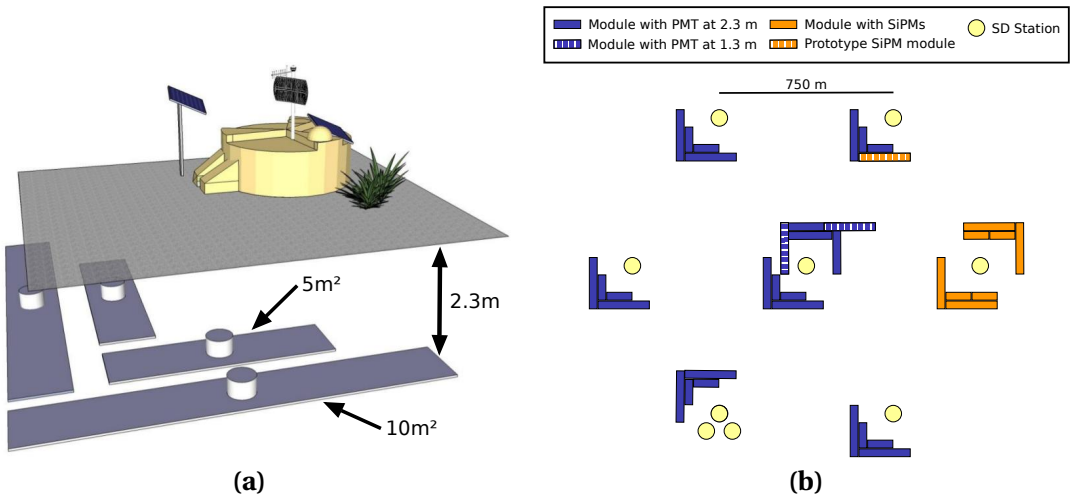

Figure 3.5: AMIGA station design (a) Each AMIGA station comprises of a water-Cherenkov detector and buried scintillator modules at 2.3 m depth forming the Muon Detector. **(b)** In the Unitary Cell prototype muon detectors are installed to investigate the final design of the whole AMIGA array (distances not to scale in the figure). Two scintillators are buried at a smaller depth of 1.3 m to investigate the shielding potential of the local soil. Twin detectors are installed at two stations to measure the counting precision of the muon detectors. The scintillators at one station are equipped with silicon photomultiplier (SiPMs) instead of normal PMTs to test their performance.

technique related to the detector design and to measure the counting fluctuations. At the center of the hexagon two additional modules of 10 m^2 area were installed at a shallower depth of 1.3 m equivalent to ~310 $g\,cm^{-3}$ vertical mass to analyze the shielding power of the local soil. It was shown that the shallower depth of 1.3 m is insufficient, because the muon counting is biased by the contamination by electromagnetic particles. Furthermore, the energy threshold for muons is decreased, which reduces the mass discrimination power due to larger shower-to-shower fluctuations for low energy muons [130].

Each scintillator module is segmented into 64 scintillator strips with a width of 4.1 cm, a height of 1.0 cm and a length of 4 m and 2 m at the 10 m^2 and 5 m^2 modules, respectively. A schematic view of a scintillator strip is shown in Fig. 3.6. The scintillator is made of polystyrene, doped with fluor and each strip is wrapped with a thin reflective layer of titanium dioxide (TiO_2) for light tightness. Since the scintillator material has an attenuation length of ~(5.5 ± 0.5) cm, the light is transported to a PMT via an optical fiber. The wavelength shifting fiber with a diameter of 1.2 mm is glued into a 2.0 mm groove with an optical cement. To avoid photon losses, the groove is covered with a reflective aluminum foil. 32 scintillator strips are placed at each half of the module. The fibers are connected to a multi-anode PMT with 64 channels via an optical connector at the center of the module. At one station the PMTs are replaced with Silicon photomultipliers (SiPMs) to investigate their

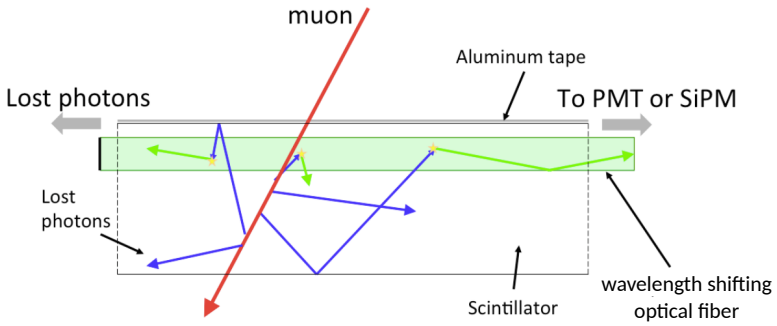

Figure 3.6: Schematic view of scintillation process A muon crossing the scintillator deposits energy which is emitted in form of photons. The photons are carried directly or via reflection at the walls of the scintillator to a wavelength shifting fiber. The fiber transports the light to a PMT or SiPM connected at the end of the fiber. Photons transported to the other end of the fiber are lost for the detection. Figure is taken from [70].

performance and uncertainties on the muon-counting compared to the PMTs [131]. The whole module is sealed into a light- and water-tight Polyvinyl Chloride (PVC) casing, including a dome in the center accommodating the acquisition electronics with a removable cover for maintenance access. A photo of a scintillator module in the laboratory is shown in Fig. 3.7.

The electronics of each module is separated into two units, the surface and the underground electronics. The underground electronics comprises of the PMT, the analog front-end, a digital board and a micro-controller board. The digital board includes an FADC to digitize the signal, a discriminator, a Field Programmable Gate Array (FPGA) and a local memory. The FPGA samples the digitized signal with a rate of 3.125 ns and pushes it to a ring buffer in case of a trigger from the SD. The micro-controller board interfaces via cables with the surface electronics to transmit data and regulates the power coming from the photovoltaic system. The surface electronics is located at the water-Cherenkov tank and interfaces with the SD electronics for triggering and for muon data transfer. It includes as well a network switch for communication with the modules, a transmitter for wireless communication to the central data-acquisition system (CDAS) and a power regulator for the photovoltaic system.

3.3.2 Muon counting technique

The muons are counted with a 1-bit strategy. The discriminator digitizes the analog signal to "1" or "0" depending on a configured threshold of the pulse height (see Fig. 3.8). Thereby "1" and "0" correspond to a signal existent or absent in a bin with a fixed length in time (3.125 ns depending on the length of the scintillator), respectively. A muon is counted if certain patterns of "1"s are found in a time window of 8 bins, i.e. 25 ns. This counting technique is very robust since it does not require detailed

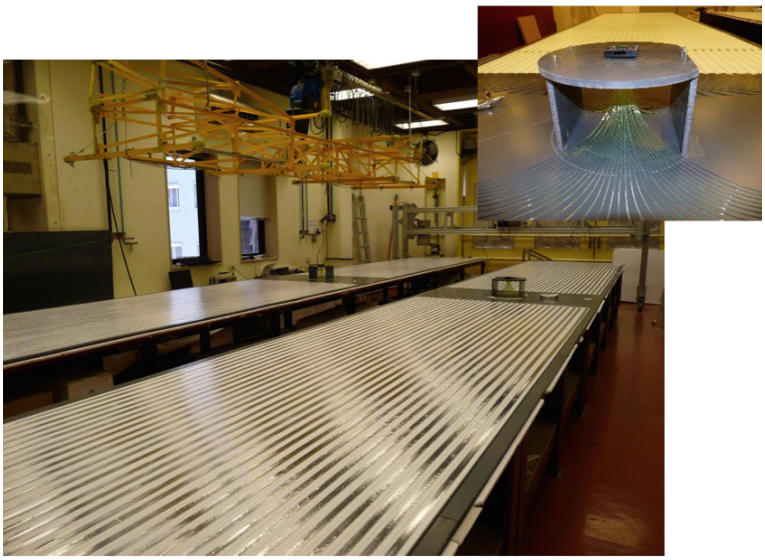

Figure 3.7: AMIGA module in the laboratory A module during production in the laboratory. The inset photo shows the fiber routing to the optical connector. Figure is taken from [70].

knowledge about the signal shape and intensity and does not rely on deconvolution of an integrated signal. Furthermore, it is only minimally dependent on the gain of the PTMs and its fluctuations, on the point of impact of the muon, on the light attenuation along the fiber to the PMT, and on Poissonian fluctuations of the number of single photoelectrons (SPEs) per arriving muon. However, a fine segmentation, an appropriate adjustment of the discrimination threshold and the size of the bins and the time window as well as a proper counting strategy are essential to avoid under- and over-counting of muons. If multiple muons pass the same scintillator strip in a time difference smaller than the length of the time window, they may not be counted separately. This pile-up effect is minimized by choosing a short time window. Albeit, the time window is chosen long enough to avoid that a single muon produces light in two consecutive time windows. The cross-talk between the PMT channels was measured to be less than 1 % [133]. To minimize false-positive signals from cross-talk, a counting strategy is chosen that always requires more than one non-consecutive "1" to count a muon. i.e. patterns of "1X1" with X = "1" or "0". An inclined muon arriving in a large relative azimuth angle to the scintillator strips may cross two neighboring strips and be counted as two muons. This so called clipping-corner effect is minimized by choosing a large width of the strips compared to the height. In addition, the over-counting bias arising from this effect is corrected depending on the zenith and relative azimuth angle during shower reconstruction [134, 135]. Further counting uncertainties arise from electronics noise, shower-to-shower fluctuations and electromagnetic punch-through. The counting strategies applied later during the shower reconstruction are explained in Section 4.3.3.

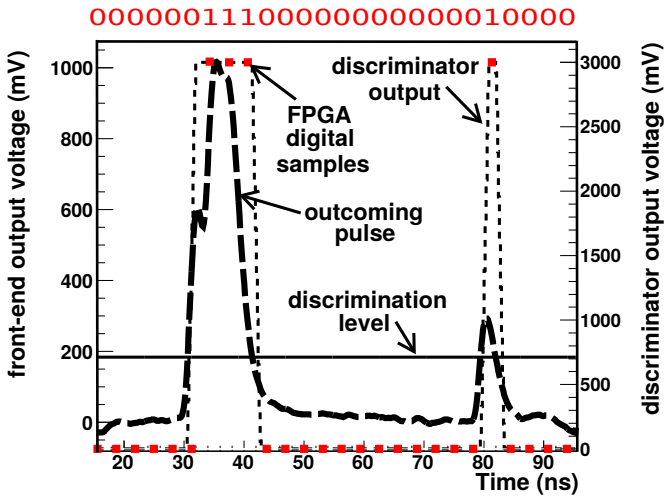

Figure 3.8: Discrimination of a muon signal Example of an analog signal of a channel [132]. The discriminator digitizes the analog pulse to "1" and "0" depending on a given threshold of the output voltage (here 180 mV). The size of the time window of the digital samples is chosen to 3.125 ns to avoid a bias due to cross-talk between the channels.

3.4 The Auger Engineering Radio Array (AERA)

The Auger Engineering Radio Array (AERA) measures the radio emission induced by air-shower particles in the atmosphere. As an engineering array it is dedicated to study the principles of the radio detection technique, i.e. to improve the understanding of the radio emission mechanisms, to develop and test hardware for the detection and software for the reconstruction of shower observables [136]. Finally, the properties of cosmic rays such as energy, mass and arrival direction between the second knee and the ankle are investigated with AERA. In short, the main goal is to make the radio technique applicable to large-scale arrays.

AERA is located in the enhancements area of the Observatory and measures cosmic rays with energies above $\sim 10^{17}$ eV in coincidence with the FD and AMIGA. It spans an area of 17 km^2 with 153 radio detector stations (RDS). They measure the radio emission in the frequency range of 30 – 80 MHz. AERA is triggered externally by the Surface Detector and Fluorescence Detector, and uses a build-in trigger mechanism for self-triggering [137]. In addition, 46 stations contain a small build-in scintillator for internal particle triggering. AERA features a duty cycle of nearly 100 %. The measurements are only disturbed by heavy atmospheric electric field which emerge from heavy rain clouds and thunderstorms over the array [92, 138].

AERA was deployed in three phases and completed in March 2015, i.e. roughly when the AMIGA Unitary Cell became fully operational. In September 2010, 24 radio detection stations equipped with logarithmic periodic dipole antennas (LPDAs) [139] were deployed on a triangular grid with a spacing of 144 m, covering an area of 0.4 km^2 (AERA24). Based on the experience from AERA24, 100 additional stations

with a different type of antennas, butterfly antennas [140], were deployed in May 2013 forming AERA124. The design of the hardware and electronics as well as trigger concepts were updated and the stations were distributed with a larger spacing of partly 250 m and partly 375 m to test radio detection with sparser arrays. With the enlarged area of 6 km^2, AERA detects several thousand cosmic-ray evens per year. In March 2015, 25 additional stations were build on an even sparser grid of 750 m spacing. Altogether, the complete array forms AERA153 with an area of 17 km^2. The large spacing aims to detect inclined air showers with a zenith angle above 60°. The lateral distribution of the radio emission becomes larger for inclined air showers, which was measured with AERA124 [141]. This enables measurements with a large spacing between the antennas. In addition, R&D stations were installed to test different antenna designs such as tripole antennas for the detection of the vertical polarized vector component of the radio emission [142], a low-frequency antenna and SALLA antennas [143, 139] also used in Tunka-Rex [144] to test a cost-effective design for a future large-scale radio array at the Auger site. The array design with the different phases and antenna types is shown in Fig. 3.4.

In this thesis, data from the externally triggered stations of AERA124 from June 2013 on and of AERA153 from March 2015 until October 2016 are analyzed together with AMIGA data. The AMIGA Unitary Cell overlaps with a part of AERA24 with LPDAs and a part of AERA124 with butterfly antennas. Hence, different antenna types are combined in the analysis, which introduces systematic uncertainties to the results.

3.4.1 Station design of the Radio Detector

Each station of the Radio Detector works autonomously and comprises an antenna mounted on a metal pole, local electronics, a GPS antenna for timing, a solar power system, a communication unit and a fence to protect from cattle and other animals. The detector stations of the LPDA and butterfly antennas feature a slightly different station design.

The LPDA used in AERA24 is built of half wave dipoles with increasing length. This yields an approximately constant gain over the full bandwidth, which is defined by the lengths of the shortest and the longest dipole. Each antenna station features two perpendicular LPDAs aligned to the Earth's magnetic field at AERA and perpendicular to it for polarization measurements of the radio emission. The antenna is most sensitive to signals from the zenith, and the gain is nearly independent of the ground conditions. It has dimensions of 4 m × 4 m × 3.5 m and is installed on a metal pole. Its electric footpoint is located at the top at around 4.5 m above the ground. The signal is guided via a coaxial cable to a low-noise amplifier (LNA) located at the bottom of the antenna. A photo of an LPDA is shown in Fig. 3.9a.

The expensive design and the complicated deployment of the LPDA led to the decision to deploy the rest of AERA with butterfly antennas. This type of antenna was first used in the CODALEMA experiment [145]. The butterfly antenna is build of two triangular arms made of 6 mm aluminum rods. Its design is simpler than the LPDA and, thus, cheaper and easier to deploy. To measure the different polarizations as for

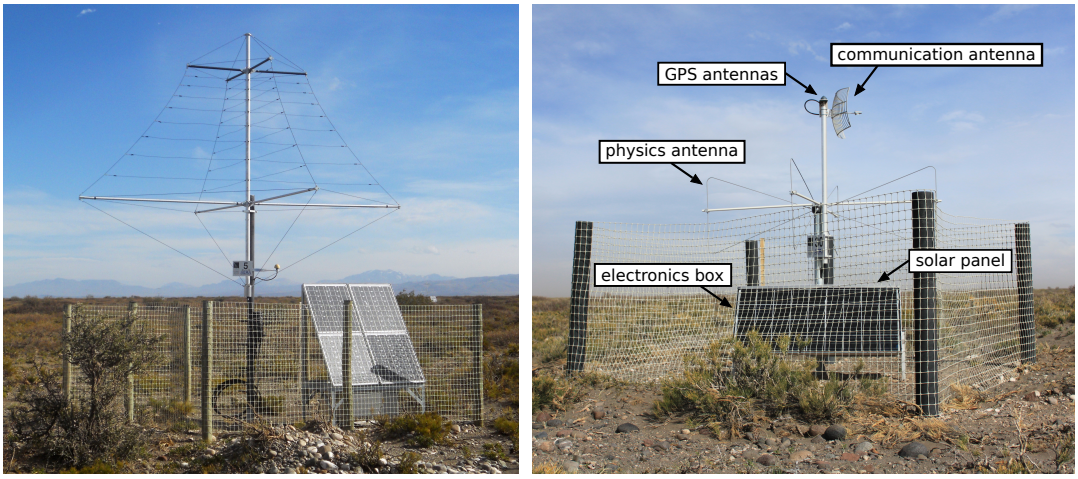

(a) **(b)**

Figure 3.9: AERA stations with two different antenna types (a) Logarithmic periodic dipole antenna (LPDA) **(b)** Butterfly antenna

the LPDAs, two antennas are combined perpendicularly aligned in the north-south and east-west directions, respectively. To support against oscillation and binding caused by heavy wind, fiberglass compounds are attached to the antenna arms. The butterfly antenna is 2 m × 2 m × 1 m in dimension and installed on a metal pole with the center at ~1.6 m above the ground. The signal of the two dipoles is directly fed into an LNA placed at the center of the antenna. The antenna design takes advantage of the reflection of the radio signal at the ground. The direct and the reflected wave interfere constructively which enhances the gain of the antenna. However, this improvement makes the antenna gain more sensitive to ground conditions and the station design, i.e., the shape of the metal box below the antenna containing the electronics impacts the antenna properties. Thus, the butterfly antennas feature larger systematic measurement uncertainties than the LPDAs. A photo of a butterfly antenna is shown in Fig. 3.9b including explanations to the different station components.

The local electronics consists of the aforementioned LNA and a so called digitizer. The LNA amplifies the signal. Then, the signal is sent to the digitizer located inside of a metal box. The digitizer features a slightly different design for the externally and internally triggered antennas. In the digitizer, the signal is further amplified and filtered by a filter-amplifier board to the design frequency range of 30 – 80 MHz. Then the signal is digitized using an flash analog-to-digital converter (FADC) with a sampling rate of 180 MHz and 12 bits depth in the externally triggered stations and a sampling rate of 200 MHz and 14 bits depth in the internally triggered stations, respectively. An FPGA is used to evaluate a trigger decision via pulse shape parameters of the digital signal and to store the signal in a local memory in the form of voltage traces.

A GPS receiver at the antenna pole provides a timestamp for the measurements

with an accuracy of 10 – 20 ns [146]. A central processing unit controls the communication with the data acquisition. In case of the LPDAs and the butterfly stations in the eastern part of AERA (internally triggered), the data is sent to a central radio station (CRS), located at the center of the AERA24 field, via fiber cables. From the CRS the data is sent to the central data acquisition (DAQ) located in the Coihueco building via a wireless link. The butterfly antenna stations in the western part of AERA (externally triggered) directly send the data to the central DAQ. The digitizer, the CPU and a battery are protected inside a water-tight box which is made of metal to shield the antenna from radio frequency interference (RFI) by the electronics. Solar panels are placed on the box which provide the power for the station together with the battery and a charge controller.

3.4.2 Calibration and differential-GPS measurements of the station positions

The measured radio signal is a convolution of the radio signal impinging the antenna and the response of the readout electronics. To obtain the radio signal independent on the detector design, the influence of all hardware components has to be removed from the measured signal. Therefore, detailed knowledge of the antenna response pattern is crucial. The antenna response of the LPDA was calibrated using an emitting reference source attached to an octocopter which was steered above the antennas [147]. This calibration campaign yielded an overall uncertainty of the amplitude of 9.4 %.

For the high-precision reconstruction of the radio wavefront [115, 113], the timing of the radio antennas has to be calibrated. The absolute timing is provided by the GPS receiver at each station. The timing synchronization between the GPS clocks is done using a "beacon" [148] which transmits sine waves in customized frequencies. The nanosecond-level accuracy of this method was confirmed by independent measurements using radio waves transmitted by commercial airplanes [146].

To achieve this timing accuracy, the positions of the antennas had to be measured with an accuracy of ~30 cm corresponding to the distance an electromagnetic wave travels in 1 ns time. This measurements were carried out in two measurement campaigns using a differential-GPS devise. In the first campaign, the positions of AERA124 were measured [149]. The measurement campaign of the 25 antenna positions deployed in March 2015 (AERA153) were part of this thesis and are described in the following.

With a differencial GPS, coordinates can be measured to sub-meter precision. The used equipment features online corrections of the travel time of the signal to the satellites which are caused by disturbances in the atmosphere. It comprises two identical GPS devices serving as a base and a rover, connected via radio. The base is placed at a reference point which is known precisely, e.g. a geodetic benchmark. The base continuously measures its position and calculates the offset to its known position. The rover is placed at the position of interest. It is connected to the base via radio and receives information about the offset, which is used to correct the

(a) **(b)** **(c)**

Figure 3.10: Measurements of the AERA antenna positions using a differencial GPS device
A reference point was created within the AERA site for the measurements of the antenna coordinates. For this, the base was located on a geodetic benchmark as shown in **(a)**. The metal pole was installed on the roof of the CRS and its position was measured with the rover as shown in **(b)**. This known position was then used as a reference point for the base. The positions of all AERA stations were then measured by placing the rover on top of the LNAs, i.e. the centers of the antennas as shown in **(c)**.

measured position. In this way, atmospheric effects at the time of the measurement are corrected.

First, a reference point was created inside the AERA field at the CRS to serve as the position for the base. This was necessary since no geodetic benchmark is close enough to AERA. Thus, the geodetic benchmark OGUA 18-086 [150, 151], which is in a distance of about 15 km to the the central radio station (CRS), served to create a reference point at the CRS. For this, the base was positioned at the geodetic benchmark as shown in Fig. 3.10a. The rover was installed on a metal rod on the roof of the CRS (see Fig. 3.10b) and its position was measured in connection to the base. The UTM coordinates (WGS84) were measured to:

zone	19H
east	451401.053
north	6114803.350
altitude	1558.385 m

This position can be used as a reference point by placing the base on the metal rod.

Using this reference point, the antenna positions of the 25 butterfly antennas deployed in March 2015 were measured. For this, the rover was placed on the center of the antenna, directly above the LNA as shown in Fig. 3.10c (here elevated to

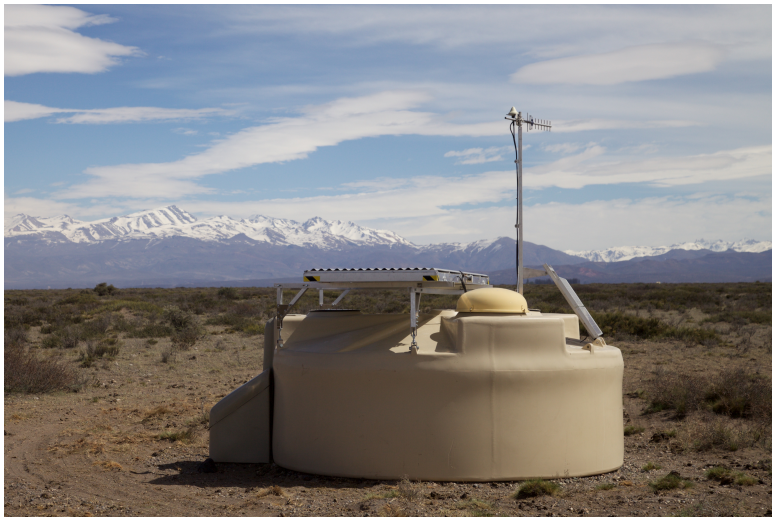

Figure 3.11: Surface Scintillator Detector station of AugerPrime All Surface Detector stations will be equipped with a plastic scintillator bar on top to enhance separate measurements of the electromagnetic and muonic shower component.

establish a better connection to the base). The measured altitude was later corrected for the distance to the LNA.

In addition, the positions of 5 stations of AERA124 were measured using the created reference point and compared to the measurements of the former campaign. An offset of −0.109 m to the east, −0.044 m to the south and −0.664 m on the altitude was found. The positions of AERA124 were corrected for this offset to avoid a relative offset between the antenna positions.

3.5 AugerPrime - the Upgrade of the Pierre Auger Observatory

Currently the Pierre Auger Observatory is being upgraded for a better mass separability and overall performance for the remaining operation time until 2025 [25]. The aim is to measure for each event the ratio between the electromagnetic and the muonic component up to the highest energies. This will allow for detailed investigations on the origin of the flux suppression at the end of the energy spectrum. It will enable the differentiation between energy loss processes during propagation of the cosmic rays and the maximum-energy scenario of the cosmic-ray sources (see Sections 2.1.1 and 2.1.2). In addition, it will enable an estimation of the proton content in the cosmic-ray flux at the highest energies, which can be used to estimate the secondary flux of neutrinos and γ-rays produced in proton energy-loss processes. Furthermore, hadronic multiparticle interactions in air-showers will be investigated in energy ranges exceeding the maximum energy of man-made particle-accelerator experiments. This will help to reduce the systematic uncertainties of hadronic interaction

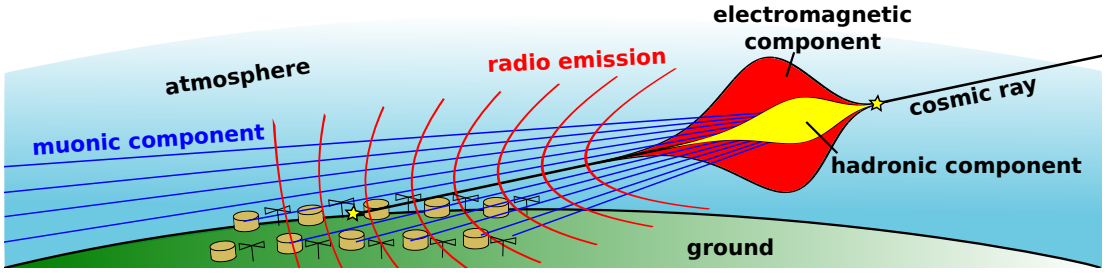

Figure 3.12: Schematic view of an inclined air shower When the shower reaches the ground, the electromagnetic component is completely absorbed in the atmosphere. Solely muons reach the ground and can be detected by particle detectors. The radio emission is induced by the charged electromagnetic component and can be detected from radio antennas at the ground.

models used for air-shower simulations.

To increase the mass separability of the Surface Detector, each water-Cherenkov detector will be equipped with a plastic scintillator on top, forming the Surface Scintillator Detector (SSD) (see Fig. 3.11). The design of the scintillators is inspired by the MD scintillator detectors. The water-Cherenkov detectors and the scintillators feature different responses to electromagnetic particles and muons. The two signals are deconvolved to determine the particle numbers. For the calibration of the SSD and for fine-tuning of the method, all 61 stations of AMIGA will be equipped with underground muon detectors. The electronics of the SD undergoes a major upgrade to be capable of processing both SD and SSD data, and to improve the data quality and the capabilities for the trigger logic, processing, calibration and monitoring. This will likely improve the X_{max} resolution of SD, although this needs experimental verification. In addition, the duty cycle of the Fluorescence Detector will be increased by ~50 % by operating during higher night-sky brightness with a reduced PMT gain by lowering the high voltage.

For the next improvement after the current upgrade, investigations are ongoing to equip every Surface Detector station also with a radio antenna. This will increase the zenith angle range for separate measurements of the electromagnetic and muonic component. The effective detection area of the SSD for inclined events gets small. Inclined showers travel a larger distance through the atmosphere and reach the ground at a later development state (see Fig. 3.12). For inclinations of $\theta \geq 60°$ almost only muons reach the ground. These muons are detected by the water-Cherenkov detectors, which are sensitive to inclined shower due to their 3-dimensional design. The footprint of the radio emission grows to diameters in the kilometer range [141], which enables the detection with a sparse array of 1500 m spacing. Thus, the combination of the SD with radio antennas allows for separate measurements of the muonic and electromagnetic shower components. The mass separability for the combination of muon and radio detectors is investigated in this thesis, for less inclined showers detected with the existing AERA and AMIGA Unitary Cell stations.

CHAPTER 4

Tools and data processing

Contents

The first combined analysis of AERA and AMIGA data was performed using several software tools, which were developed and adjusted for the purposes of the different steps in the analysis chain. Detailed investigations of the shower observables measured by the different detector types and a combination of them for mass-composition studies were performed using various simulation libraries. These libraries were generated with the air-shower simulation tool CORSIKA [58] and its

extension for the radio emission CoREAS [152]. Measured data was processed from the raw output format of CORSIKA to combined files comprising coincident events of the different detector types. Both the simulations and the measured data were investigated using the analysis software framework of the Pierre Auger Collaboration Offline [153]. For this purpose, a combined analysis pipeline of AMIGA (Surface Detector and Muon Detector) and AERA data was developed.

4.1 Air-shower simulations

Monte Carlo simulations of cosmic-ray induced air showers were produced with the tool CORSIKA. For the analysis of shower observables measurable with the AMIGA Surface and Muon Detectors, CORSIKA delivers information about the lateral particle number distribution at the altitude of the detector. This information is provided separately for different particles types, e.g. the number of muons above a certain energy threshold which are counted in the MD. For the analysis of the radio emission measurable with AERA, the radio simulation code CoREAS was used. Different simulation sets were produced for a systematic analysis of the capabilities of a combined analysis of AERA and AMIGA for mass-composition studies.

4.1.1 Simulations of extensive air showers with CORSIKA

CORSIKA (**CO**smic **R**ay **SI**mulations for **KA**SCADE) is a Monte Carlo program to simulate the evolution of extensive air showers induced by cosmic rays in the atmosphere [58]. It was initially developed to predict the average values and fluctuations of shower observables for interpretation of the measurements of the KASCADE experiment, and now has become the world's most used standard program for air-shower simulations. It simulates the showers in detail by tracking each shower particle along its trajectory through the atmosphere until it interacts with the air or decays. It takes into account all branches of possible interactions down to a branching ratio of ~1 %. In Fig. 4.1a an example shower simulated by CORSIKA is shown with tracks of different particle types. For the description of the interactions of high-energy as well as low-energy particles different hadronic models can be applied. In this thesis,the recent versions of the hadronic models QGSJETII-04 [61], EPOS-LHC [62] and Sibyll 2.3 [63] are applied for high-energy interaction. For a description of the models and their systematic uncertainties see [64]. For the modeling of low-energy interactions the interaction model FLUKA 2011.2c [155, 156] is applied.

With CORSIKA showers induced by different primary cosmic particles such as nuclei from proton to iron, photons and other particles can be simulated. The primary energy and the arrival direction can be adjusted as input variables. The arrival direction is defined by the zenith angle θ and azimuth angle φ relative to the ground plane at a configurable observation level. The strength of the Earth's magnetic field is included in the simulations, which can be adjusted to the location of the detector and the detection time. A configurable atmospheric model describes the elemental composition and the density variation with altitude. This influences the

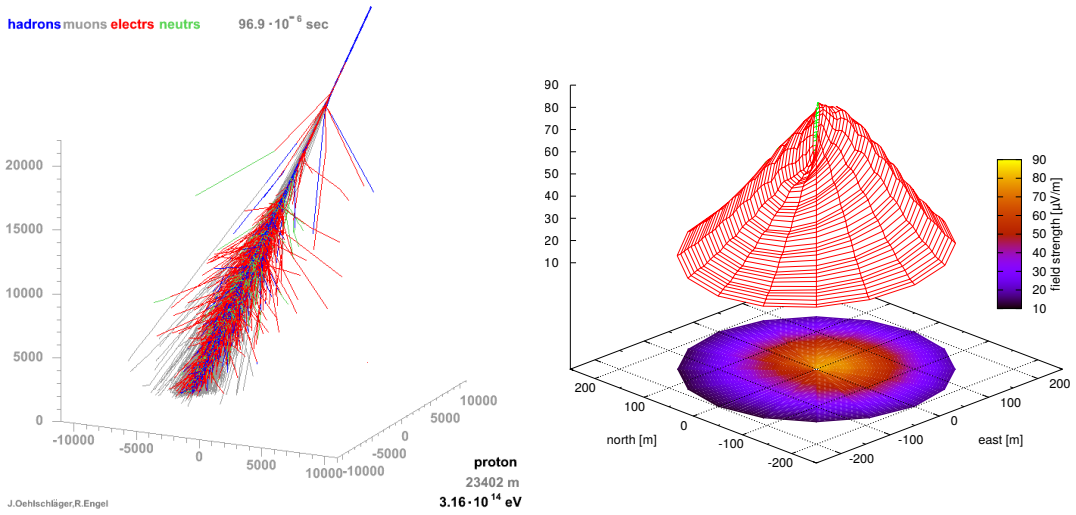

(a) **(b)**

Figure 4.1: Simulated CORSIKA and CoREAS showers **(a)** Simulated particle tracks of a proton-induced shower, calculated with CORSIKA. The different colors denote hadrons, muons, electrons and neutrons. Figure taken from [154]. **(b)** Lateral distribution of the peak radio amplitude in the 40 – 80 MHz frequency range of a vertical air-shower induced by an iron nucleus of energy 10^{17} eV. The radio emission is simulated with CoREAS at observer positions at the cross points of the red lines and interpolated to form the footprint at the bottom of the figure. The asymmetry of the footprint is caused by the superposition of the geomagnetic and Askaryan emission. Figure taken from [152].

transport of the shower particles, their interactions with air nuclei, and the refractive index for the radio waves simulated with CoREAS. Since the computational time scales with the number of particles and therefore roughly with the primary energy E_0, it becomes large for high-energy primaries. To minimize the computational time, the particles are tracked only until reaching a lower energy threshold. This threshold can be configured for hadrons, muons, electrons and photons separately and usually is set to the detection threshold of the detector of interest. Furthermore, a thinning algorithm can be applied. This algorithm follows only a randomly selected fraction of the particles below an adjustable energy threshold $\varepsilon_{\text{th}} = E/E_0$ and discards the other particles. The surviving particles are weighted accordingly to ensure energy conservation. Each particle i survives with a probability of

$$p_i = \frac{E_i}{\varepsilon_{\text{th}} \cdot E_0} \tag{4.1}$$

and, in case of survival, a weight of $\omega_i = 1/p_i$ is attributed. This algorithm leads to a constant number of followed particles in the lower-energy part of the shower instead of an exponential increase.

The parameters of the particles are stored in output files when the shower reaches

a configurable observation level. In addition, the longitudinal distribution of the number of particles and the longitudinal energy deposit in the atmosphere are stored in steps of 5 g cm^{-2} slant depth.

4.1.2 Calculation of the radio emission with CoREAS

CoREAS (**Co**rsika-based **R**adio **E**mission from **A**ir **S**howers) is a program directly implemented into CORSIKA to calculate the radio emission by extensive air showers simulated with CORSIKA [152]. It makes use of the endpoint formalism [157] to calculate the electromagnetic radiation of the charged particles. This formalism is based on classical electromagnetism. It describes the particle tracks as a series of sub-tracks. At the endpoints of these sub-tracks, discrete and instantaneous acceleration events take place. CORSIKA provides the position, time and energy of the tracked particles in the air showers at the start- and endpoints of the sub-tracks. Each acceleration event induces electromagnetic radiation, which is summed up to the total radio emission from the shower. CoREAS considers effects of the varying refractive index along the atmosphere, which leads to coherent radiation around the Cherenkov angle due to time-compression and amplification effects [158]. The radio emission calculated by CoREAS was validated to agree with measurements by various experiments such as LOPES, Lofar, Tunka-Rex and AERA [110, 159, 160, 161].

The radio emission is calculated for defined observer positions at the ground. It is provided in form of electric field traces of the east-west, north-south and vertical component. The time-series correspond to radio pulses calculated for bandwidths much larger than experimentally observed, and have to be filtered to the bandwidth of the detector of interest. Figure 4.1b shows the lateral distribution of the peak amplitudes at observer positions, filtered to a bandwidth of 40 – 80 MHz, for a simulated vertical shower of 10^{17} eV. The footprint shows an asymmetric shape which originates from the interference of the different emission mechanisms (see Section 2.3.1).

4.1.3 Air-shower simulations for the combined analysis of muons and radio emission

Different sets of simulations were calculated for a step-by-step analysis of AERA and AMIGA shower observables and for a combined analysis. An overview of the energy and geometry settings and the hadronic models applied in the different simulation sets is given in Table 4.1. The distribution of the arrival directions, shower cores and energies of the simulation sets are shown in Fig. 4.2.

To investigate the dependencies of the observables on the primary energy, the library A comprises 3000 simulations equally distributed over the energy range of $10^{17.5} - 10^{19}$ eV. The zenith angle is chosen constant at 38° (median of the solid angle of the standard SD analysis using the zenith angle range 0 – 60°) to be free from zenith angle dependencies. The observation level is chosen at 100 m below the mean altitude of the AERA field to avoid artefacts occuring in the simulated radio emission when the shower stops at the detector height.

Table 4.1: Input parameters of the different simulation libraries used in this thesis.

lib.	primary	energy	zenith	azimuth	hadronic model	#
A	proton	$10^{17.5}-10^{19}$ eV	38°	0 – 360°	QGSJETII-4	500
	iron	$10^{17.5}-10^{19}$ eV	38°	0 – 360°	QGSJETII-4	500
	proton	$10^{17.5}-10^{19}$ eV	38°	0 – 360°	Sibyll 2.3	500
	iron	$10^{17.5}-10^{19}$ eV	38°	0 – 360°	Sibyll 2.3	500
	proton	$10^{17.5}-10^{19}$ eV	38°	0 – 360°	EPOS-LHC	500
	iron	$10^{17.5}-10^{19}$ eV	38°	0 – 360°	EPOS-LHC	500
B	proton	$2\times10^{16}-4\times10^{19}$ eV	0 – 90°	0 – 360°	QGSJETII-4	5302
	iron	$2\times10^{16}-4\times10^{19}$ eV	0 – 90°	0 – 360°	QGSJETII-4	5302

The library B comprises more than 10000 simulations reproducing externally triggered events of AERA corresponding to measured showers in the time interval from the 2nd June, 2013 to the 2nd March, 2015. The reconstruction parameters of the SD are taken as input parameters for the simulations such as energy, core position and arrival direction. The distribution of the energy, core position and arrival direction represents the combined detection efficiency of SD and RD and the cosmic-ray flux as a function of these parameters. For each measured event two simulations were produced, with the primary particle being a proton and an iron nucleus.

All simulations were calculated with CORSIKA and CoREAS with the same settings for the thinning threshold $\varepsilon_{\text{th}} = E/E_0$ of $E_0 = 10^6$ eV. The Earth's magnetic field is set to a constant value of $B_x = 19.79\,\mu\text{T}$ and $B_z = -14.15\,\mu\text{T}$ for all events. The U.S. standard atmosphere is used as atmospheric model. The observation level was adjusted to 100 m below the altitude of the Auger site at the core position (on average 1452 m a.s.l. corresponding to $870\,\text{g}\,\text{cm}^{-2}$ atmospheric overburden). To investigate the mass separation power, there is an equal amount of simulations for protons and for iron nuclei as primary particles with the same input parameters. In libraries A the shower cores are all located inside the AMIGA Unitary Cell. Since the input parameters of library B are taken from events measured with AERA, the shower cores are distributed widely around the AERA detector. However, 2252 events are contained inside the Unitary Cell of AMIGA. The simulations of all libraries contain observers at all the positions of AERA24, AERA124 and AERA153 radio antennas, excluding only prototype antennas. For each simulation, antennas up to 1 km distance to the core are evaluated and taken into account in this simulation. A typical CORSIKA as well as CoREAS steering file with the common settings of all simulations used in this thesis is shown in Appendix A.

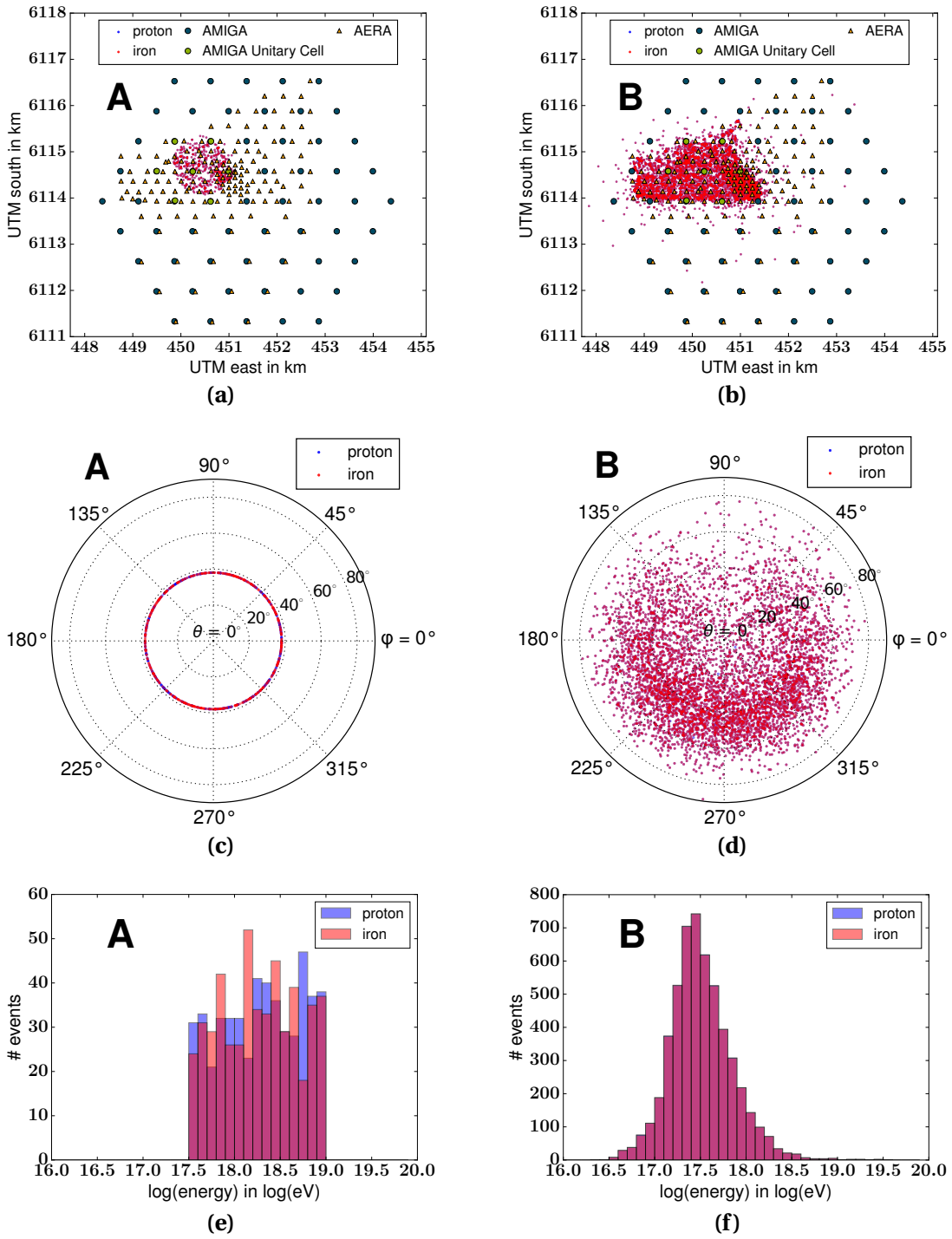

Figure 4.2: Input parameters of the different simulation libraries (a)-(b) All shower cores are inside the AMIGA Unitary Cell for library A. For the library B the input parameters are taken from measured AERA events triggered by SD. Most of the detected showers have their core inside of AERA24 and the part of AERA124 with externally triggered antennas. AERA153 was not built yet during the evaluated detection period. **(c)-(d)** The zenith angle is constant at 38° and the azimuth angle is distributed over the whole range of 0 – 360° in library A. The detected events of library B are distributed over the whole sky. The asymmetry occurs since the strength of the radio emission depends on the angle to the Earth's magnetic field. **(e)-(f)** The primary energy is distributed over the range of $10^{17.5}$ – 10^{19} eV in library A. The energy of library B is distributed according to the detector efficiency of AERA and the cosmic ray flux.

4.2 Combined processing of data measured by AERA and AMIGA

For the combined investigation of AERA and AMIGA measurements, the data has to be available in the same data format. Therefore, the data of both detectors was stored and converted to an Auger proprietary data format based on ROOT [162] and combined to joint data files, in which the coincident air-shower events detected by all the different detector types (SD, FD, MD and RD) are associated to each other.

4.2.1 Processing of AERA data

The raw data of each AERA24 station is sent via cables to the Central Radio Station, where it is bundled and sent to a central data acquisition (DAQ) inside the Coihueco FD building. The rest of the AERA stations comprise communication antennas transmitting the data. At the central DAQ, the data of all stations is combined and recorded as air-shower events in binary files of separate runs [163]. Each binary file is hierarchically structured. The file header contains information such as the run id and the event ids and the GPS time stamps of the first and last event in the file. In the body of the file, the events are stored sequentially. The header of each event contains information such as the event id, the GPS time stamp of the first triggered station and the number of participating stations. Each event has a body with the data of all participating stations. The header of each station contains hardware-dependent information, the GPS time stamp and a body with the measured ADC traces. These binary files can be directly read into the analysis framework Offline of the Pierre Auger Collaboration. However, the files are very large since they contain 999 events of multiple stations with time series of 2 ADC traces each. The data transfer of the binary files from Argentina to Europe has to be done via hard-disks due to limited bandwidths of the local wireless network of the Pierre Auger Observatory. Furthermore, the read-in of the binary files to Offline is slow.

For a faster read-in to Offline and the possibility to combine the AERA data with the data of the other detectors of the Observatory, the input-output library AERA-ROOTIOlib was written [164]. The library has a built-in application to convert the binary data into a ROOT-based file format. The ROOT format has a more flexible data structure, which enables direct access to single events for writing and reading operations. Furthermore, the data volume is reduced by 20 % and the read-in to Offline is sped up by a factor of 5. The events can be separated into different event types according to the time stamp or the trigger flag. This feature is used to produce separate files of different event types used for different purposes such as different physics analyses, monitoring and calibration. This reduces the data volume for each purpose which facilitates the data handling.

Various file types are automatically produced on a server in the Coihueco building for monitoring, in a daily or hourly period. Furthermore, the binary data files are carried to Europe via external harddrives and converted into the different file types at a computer center in Lyon (see Fig. 4.3). The Physics-data files (RdExternal)

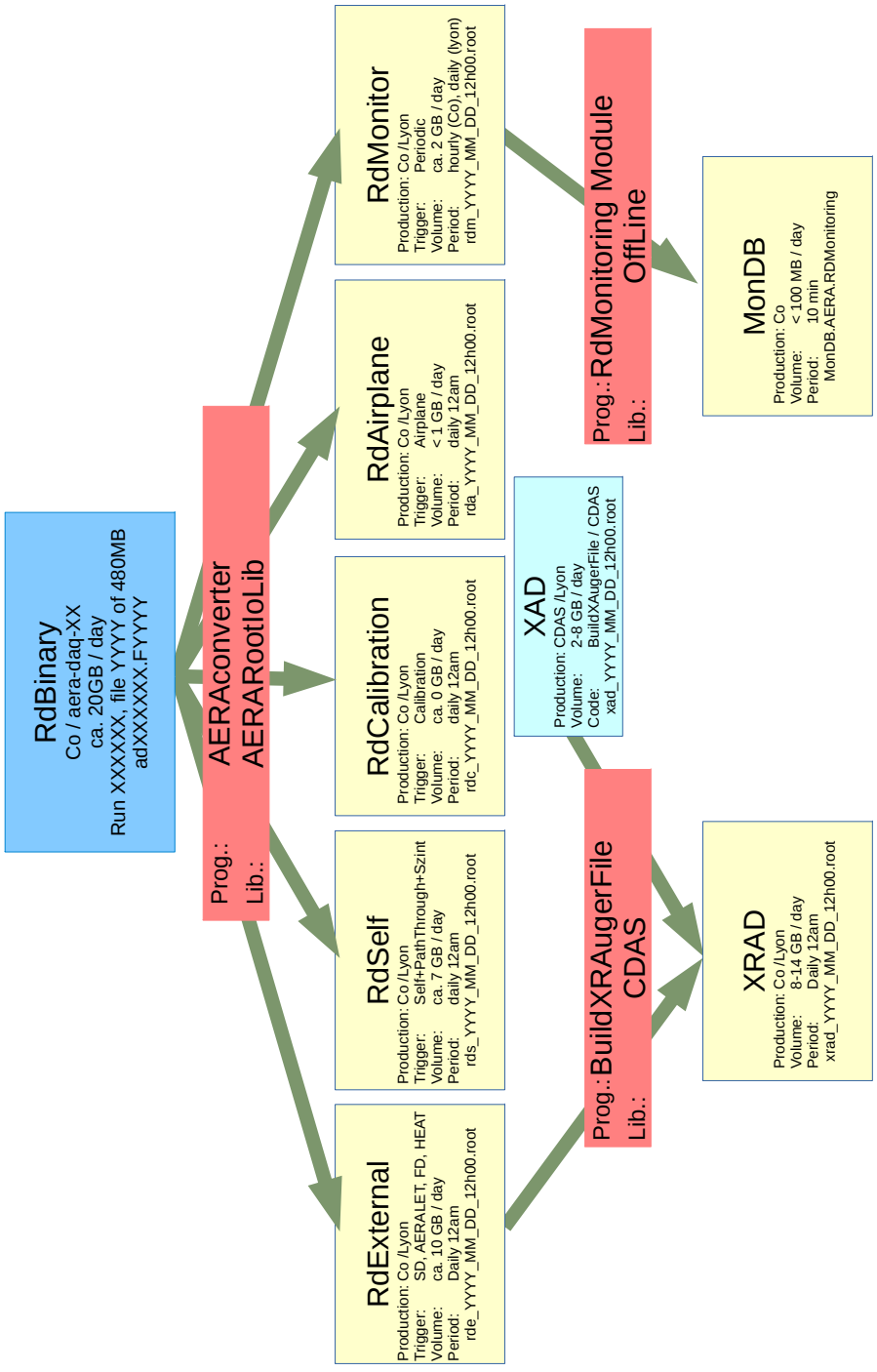

Figure 4.3: AERA data processing chain The data of the radio antennas of AERA are stored in binary files. These data is converted to a ROOT-based format and stored in separate files for different event types, sorted by the event trigger and time stamp. The physics data are combined to files containing also the coincident events of the other detector types of the Observatory (XRAD). These files are analyzed using standard applications of the software framework Offline.

contain events which are externally triggered by the SD and FD or self-triggered and are subsequently merged with files (XAD) containing MD, SD and FD data to enable hybrid analyses, as described in the following section. Around 7000 of these 'physics' radio events are detected per day, which covers a daily data volume of ~10 GB. However, only about 11 events per day feature a significant radio signal of an air shower in at least three AERA stations. Additionally a data stream with background events (RdMonitor) is produced. These background events are measured by initiating a trigger periodically, that was initiated every 10 s until July 2014 and afterwards reduced to a period of 100 s. The background events are used in this thesis to add realistic noise to air-shower simulations (see Section 4.3.2).

4.2.2 Processing of AMIGA data and low-level merging into joint data files

The raw data of the Surface Detector of AMIGA is sent via wireless TCP/IP communication to the central data acquisition system (CDAS) of the Observatory [165]. The data of the Surface Detector is recorded in daily ROOT-based files, combining the FADC traces of all stations of the 1500 m and 750 m grids participating in the air-shower event. The Surface Detector data is then merged into joint files with the data recorded by the Fluorescence Detector. Thereby, coincident events are associated by comparing the GPS seconds of the air-shower triggers. The data of the Surface Detector and the Fluorescence Detector of each coincident event is stored together as one single Auger event in a ROOT-based file, enabling hybrid analyses. To assure that all data of one night of measurements by the Fluorescence Detector are combined into the same file, the daily files include events measured from 12:00 p.m. noon to 11:59 a.m. noon the next day. These daily files have a data volume of ~500 MB.

When the Muon Detector receives a trigger from the Surface Detector, the corresponding muon event is stored in a ring buffer and is sent to the CDAS via WiFi antennas upon request [166]. There, it is stored in daily ROOT-based files in a similar form as the Surface Detector data. The files have a hierarchical structure. They contain sequentially ordered events, each containing a UTC date and time and a list of Muon Detector stations participating in the event. Each station contains a list of participating modules, which in turn contain the signal traces of the 64 channels in form of binary entries with time stamps. An average of 25 bytes of data volume is occupied per event, leading to daily files of ~4 – 5 MB size. The recorded Muon Detector events are added to the Auger event files by a similar merging procedure as with the Surface Detector and Fluorescence Detector data.

In a final step, these joint files of SD, FD and MD data are merged with the files of the AERA physics data stream. Thereby, coincident events are associated by time stamps, taking into account a trigger time delay (between the event time and the time when the trigger is established and arrived at the RD station) of ~0.137 ms for standard SD and FD triggers and ~0.01 ms for the triggers of the SD 433 m array (AERAlet). Radio events are only written to the joint file, if an SD or FD coincident event was found.

Eventually, the data of all detectors have been merged into one file and can be analyzed in combination. Thereby, for all radio events as well coincident data of the SD or the FD are contained in the same file. For this thesis, only SD and AERAlet triggered events are relevant, since only these events can contain MD data.

4.3 The Offline reconstruction tools for air-shower simulations and measured data

For the analysis of the joint data files of air-shower event candidates as well as of air-shower simulations, the analysis framework of the Pierre Auger Collaboration Offline is used. The software framework Offline is designed for the reconstruction of air-shower properties from measurements of the Pierre Auger Observatory and from air-shower simulations [153]. It comprises an interface to read the files in the ROOT-based Auger format. The analyses of measured data include a correction of the hardware response, suppression of potential background, and a reconstruction strategy individual for each detector type. For the analysis of air-shower simulations, the detector response is first applied to the simulations to mime measured data. Then the same analysis as for measured data is performed.

For the combined analysis of AMIGA and AERA, both, for air-shower simulations and for measured data, standard analysis pipelines were developed within this thesis. For this, the standard analyses pipelines of the Surface Detector, Muon Detector and Radio Detector were optimized for a hybrid analysis and combined to applications. In addition, analysis modules of the Fluorescence Detector were added to search for multi-hybrid events detected in all four detector types. The software Framework Offline and the elaborated applications are described in detail in the following.

4.3.1 The software framework Offline

Offline is the software framework for data analysis developed by the Pierre Auger Collaboration. It is written in C++ and was originally developed for the analysis of the Surface and Fluorescence Detectors, and later was enhanced for analyzing the data of the Radio Detector AERA [136] and the data of the Muon Detector of AMIGA [167]. It is able to read in various data formats such as raw Auger data, Auger-ROOT files containing data of the different detectors and files of air shower simulations produced by various simulation codes such as CORSIKA/CoREAS, Aires/ZHAires, SELFAS, EVA, CONEX and SENECA. Offline is build in a modular structure where the processing steps are separated in so called modules and executed sequentially. This enables analysis pipelines for a variety of specific purposes by arranging and configuring modules and enables the user to add own algorithms. The module sequence and input parameters for the modules are configured via steering files written in human-readable Extensible Markup Language (XML).

Offline is structured in three main parts as shown in Fig. 4.4: the detector description, the analysis pipeline and the event class. The read-only detector description

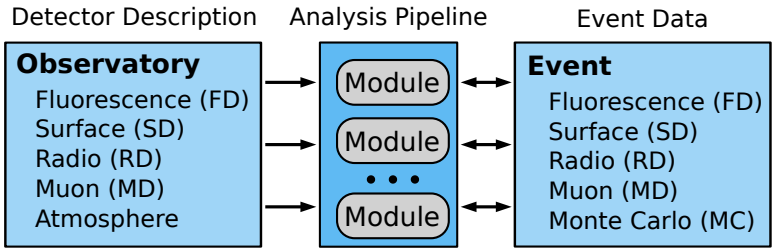

Figure 4.4: $\overline{\text{Off}}\underline{\text{line}}$ structure comprising of three main parts. The read-only detector description contains information about the configuration and performance of the different detectors. In the event class all information is stored, which varies with each event and includes the raw as well as calibrated event data and reconstructed entities. The modules contain the algorithms to perform analyses of the event data. Figure adapted from [153].

contains information about the configuration and performance of all different detector types at the Observatory. The event class comprises all information that changes for each event. This information is separated in four parts including the raw event, e.g. measured traces, the calibrated event, the reconstructed event, i.e. air shower observables, and the simulated event in case an air-shower simulation is processed. The event class is capable of converting the event data to various data formats for output. The modules contain the algorithms for analyzing the measured data e.g. for air-shower observables or for monitoring purposes. They are interfacing to each other through the event class by reading and modifying its quantities. They have read access to the detector information from the detector class.

The detector description is stored in XML files and MySQL databases [168]. Static information, such as hardware configurations and the positions of the detector stations, is stored in XML files. E.g. for the Radio Detector (RD), AERA, frequency dependent response maps of the individual hardware components (antenna, filter, amplifier, LNA) are stored. Dedicated databases provide the time dependent information for quantities varying during data taking such as hardware changes, bad periods with hardware and software problems, monitoring quantities, calibration constants and atmospheric conditions, e.g. aerosol properties and cloud coverage.

This main structure of $\overline{\text{Off}}\underline{\text{line}}$ is built on a set of utility classes for XML parsing, error logging, handling of units, mathematics manipulation, foundations classes to represent common objects such as signal traces, and unit testing. $\overline{\text{Off}}\underline{\text{line}}$ handles units in the physically correct way. Hence, the user does not need to take care of handling the units when performing operations with a quantity. Since the Observatory consists of various different instruments spread over a large area with non negligible Earth curvature and since the Fluorescence detector points in different directions, there is no preferred coordinate system in $\overline{\text{Off}}\underline{\text{line}}$. Furthermore, the geometry of an air shower is usually described in a different system than the detector geometry. This requires complicated coordinate transformations, which are handled automatically by a geometry package. The time series and e-field traces of radio pulses are stored in

so called FFT-data-containers. To provide the radio signal in the time and frequency domain, an interface is implemented which automatically performs a fast fourier transformation (FFT) of the trace or the frequency spectrum, respectively. The geomagnetic field configuration at any time and location, which is relevant for the radio emission, is stored in a class based on the data of the International Geomagnetic Reference Field (IGRF) [169]. Dedicated unit tests as well as consistency check of reconstructed quantities are provided. The tests are performed automatically on different platforms by buildbots [170] each time the code of Offline is modified to ensure the stability and maintainability of the software framework.

All external dependencies of Offline are made available in the Auger Package Environment (APE). APE automatically downloads and installs all the necessary packages, such as the open source programs ROOT for serialization [162], boost for C++ extensions [171], FFTW for fast fourier transforms [172], Geant4 for detector simulations [173], and some packages created inside the Collaboration for dedicated tasks. The latter include the software of the central data acquisition system CDAS, which handles the read and write access of the SD, FD and MD data and provides various operation tools for these data files, such as a merging tool to combine the data of these different detector types in shared files. The AERAROOTIOlib contains the tools for converting AERA raw data into ROOT based files and handles the read and write access of this data format in Offline. The FFTW package is used to transform the radio signal traces between the time and frequency domain.

The results of the different applications of Offline are written in so called Advanced Data Summary Tree (ADST) files based on ROOT. These ADST files contain the information stored in the event class and the detector description used during analysis. The ADST files can be directly analyzed with external user code. In addition, the information of interest can be extracted, e.g. to ASCII (American Standard Code for Information Interchange) files. Furthermore, Offline includes a functionality called EventBrowser to open the ADST files and display the event information such as raw measured traces or the reconstruction results of the different detector types.

4.3.2 Simulation of the detector responses

The air shower simulations produced with CORSIKA and CoREAS were used to study different parameters measurable by AERA and AMIGA, important for a combined analysis on the mass composition. To include influences on these parameters by the instruments, the detector responses on air-shower events are simulated. In particular, the responses of the Surface Detector, Muon Detector and Radio Detector are applied. The event including the finished detector simulation can be further processed in the same way as measured data. The complete analysis pipeline of the detector simulations, followed by a shower reconstruction, is shown in Appendix B and described in detail in the following.

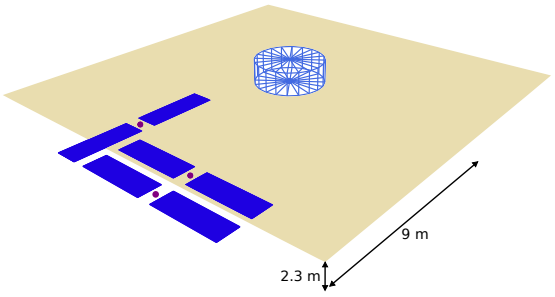

Figure 4.5: Simulated detector design of AMIGA Simulated configuration of the AMIGA stations. Three modules of 10 m^2 area each are arranged in an L-shape and buried in 2.3 m depth. This configuration is according to the final design of AMIGA. It deviates from the configuration currently deployed in the Unitary Cell, comprised of 2 scintillator modules of 10 m^2 area and 2 modules of 5 m^2 at each station (see Fig. 3.5a).

Surface Detector and Muon Detector of AMIGA

Depending on the shower core position, for each detector station it is determined which particles traverse the SD water-Cherenkov tank and the underground MD scintillators below the tank. For each tank hit by shower particles, the energy loss of each particle and its Cherenkov light emission is calculated with the aid of Geant4. In addition, the particles are propagated through the ground until the depth of the scintillator. In the next step, the responses of the PMTs and the local electronics (FADC) to the Cherenkov light are simulated and the "measured" signal traces are derived. The local trigger of the tank is simulated and a GPS time stamp created.

Then, the detector simulation of the Muon Detector follows by injecting the particles into the scintillator below the tank. Thereby, the simulated tank trigger is used for timing. The energy deposit of the injected particles is simulated, followed by the response of the fibers, multi-anode PMTs and the front-end electronics. The binary signal traces are derived by simulating the discrimination of the single-photoelectron pulses. With the simulated signal in each detector station, a global trigger is created. It uses the information of multiple stations to decide whether the event is "recorded" according to the number of stations with a signal. With this, the detector simulation is complete and the raw event structure is built for further analysis.

The AMIGA stations are located at the real positions of the infilled area of the real Observatory. They are distributed on a triangular grid with about 750 m spacing. In the simulations used in this thesis, not only the 7 SD stations of the AMIGA Unitary Cell, but all 62 SD stations of AMIGA are equipped with a water-Cherenkov tank and buried scintillators as currently under construction in Argentina (see Fig. 4.5). Three scintillator modules with an area of each 10 m^2 are buried in 2.3 m depth, which is according to the planned design for the completion of AMIGA. They are arranged in an L-shape with two parallel modules and a third perpendicular module. The center of the outer module of the two parallel ones has a distance of 9 m to the center of the water-Cherenkov tank, far enough to avoid shadowing effects from the tanks on any of the scintillators.

AERA radio antennas

The radio emission was calculated by CoREAS at observer positions fixed relative to the shower core. These observer positions were located at the corresponding positions of the AERA153 antennas in both simulation libraries described in Section 4.1.3. Based on the corresponding position, the "measured" signal in each antenna is simulated.

The electric field vector of the radio emission in air is converted to voltage traces in the two polarization channels of each antenna. In addition, the response of all hardware such as cables, filters and amplifiers is incorporated using the response pattern of the signal chain of the respective station and antenna type. This detector response is provided in form of a time dependent detector description stored in a database. The responses of the different parts of the signal chain were measured in the laboratory or in the field. The responses of the different antenna types (LPDA and butterfly) are modeled using the software NEC2 [174] including effects from the ground conditions, and adjusted to calibration measurements [147].

The derived time series is re-sampled to the sampling frequency used in the experiment and clipped to the length used for measured data. Then, the voltage traces are converted to ADC counts according to the gain of the electronics. Finally, background measured at the AERA site is added to the signals, which provides a realistic case as in the experiment. This background was measured by periodically triggering the antenna array. It contains galactic noise, RFI signals and the calibration signal transmitted by the beacon in four defined frequencies.

4.3.3 Combined reconstruction of AMIGA and AERA

The air-shower simulations including the simulations of the detector responses conform the shape of measured data. Hence, measured data and the simulations are analyzed in an analogous manner to reconstruct the shower observables from the signal in the detectors. Therefore, the signals in the different detector stations are preprocessed, calibrated and filtered according to their quality. The lateral distribution is determined via fitting a dedicated function to the processed signals for the SD, MD and RD signals. From this lateral distribution shower observables such as the arrival direction, energy and shower core can be estimated.

Reconstruction strategy for the Surface Detector data

The signals detected by the Surface Detector provide information about the arrival direction and the energy of the primary particle as well as the shower core at the ground level. To preprocess the signals in the water-Cherenkov tanks, various quality checks, e.g. of the functionality of the PMTs, and a correction for a timing offset by the electronics are applied. Then, the signals of the single SD stations are calibrated by converting them to VEMs. Stations with hardware or software malfunction are removed from the analysis. Since the Surface Detector array includes grids of various spacings (1500 m, 750 m and 433 m), the stations with signal are checked for being

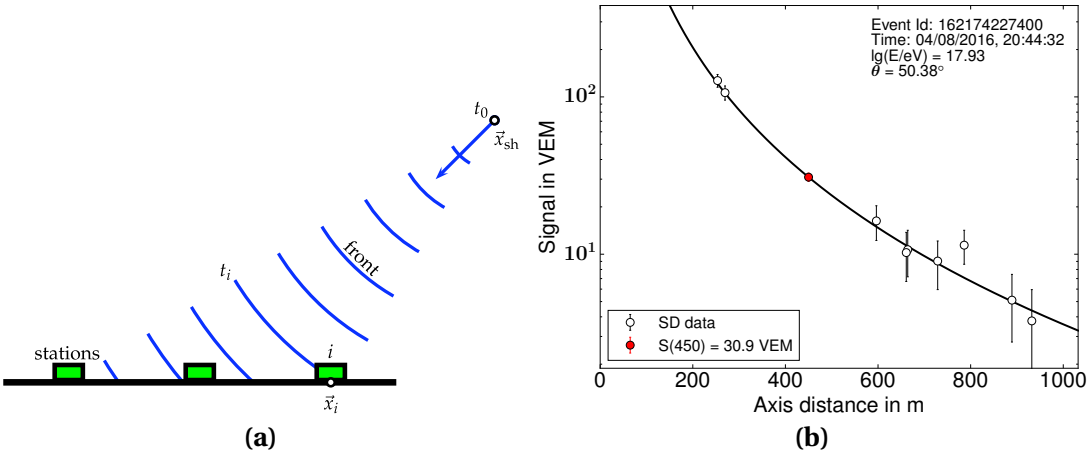

Figure 4.6: Event reconstruction of the Surface Detector (a) Direction reconstruction based on signal arrival times. The shower particles travel with a shower front of $\mathcal{O}(1\,\mathrm{m})$ thickness. The arrival direction is reconstructed by fitting a shower front model to the arrival time residuals in the detectors. Figure is taken from [67]. **(b)** Example of a lateral distribution function fitted to the signal sizes detected at different distances to the shower axis of the measured event 162174227400. The energy is reconstructed to $8.54 \pm 0.53 \pm 0.37 \cdot 10^{17}$ eV, based on $S(450) = 30.9 \pm 1.9 \pm 1.3$ VEM. The shower direction is reconstructed to a zenith of $\theta = (50.4 \pm 0.4)°$ and an azimuth of $\varphi = (318.7 \pm 0.4)°$.

in the grid of interest. With the final set of calibrated stations with signal, the event is checked of being a cosmic-ray candidate. For this, the time delay among the candidate stations has to be smaller than their distance divided by the speed of light (200 ns). In addition, the distribution of the candidate stations has to fulfill defined trigger conditions (on details of the trigger conditions see [175]). In case of a cosmic-ray candidate, a reconstruction of shower observables is performed.

First, the arrival direction is estimated using the arrival times of the shower at the position of the stations (see Fig. 4.6a). Thereby, the shape of the shower front is assumed to be a plane moving at the speed of light. The derived vector of the shower axis is used to determine the shower core by calculating the barycenter of the signals in the stations. Then, the lateral distribution of the signals is determined in the shower plane perpendicular to the shower axis. The lateral distribution is fitted by the maximum-likelihood method, which properly takes into account stations with no signal or saturated signal and includes a model for the signal uncertainties. The signal as a function of distance to the shower axis is fitted using the NKGBetaOnly function, a modified version of the Nishimura-Kamata-Greisen (NKG)-type function [176]:

$$S(r) = S\left(r_{\mathrm{opt}}\right) \cdot \left(\frac{r}{r_{\mathrm{opt}}}\right)^{\beta} \cdot \left(\frac{r + r_{\mathrm{opt}}}{r_{\mathrm{scale}} + r_{\mathrm{opt}}}\right)^{\beta} \quad . \tag{4.2}$$

r_{opt} is the optimum distance, at which the signal is minimally influenced by changes in the slope, induced by shower-to-shower fluctuations. It depends on the geometry

of the detector array, i.e. the spacing between the detectors, and equals 450 m for the infilled Surface Detector array with 750 m spacing. r_{scale} is a scale parameter, which influences the signal only at large distances. It is correlated with β and fixed to 700 m. β is a parameter governing the slope. It is fixed by default and within this thesis to

$$\begin{aligned}\beta\left(\log_{10} S\left(r_{\mathrm{opt}}\right),\theta\right) = a + b\cdot\log_{10} S\left(r_{\mathrm{opt}}\right) + \left(c + d\cdot\log_{10} S\left(r_{\mathrm{opt}}\right)\right)\cdot\sec\theta \\ + \left(e + f\cdot\log_{10} S\left(r_{\mathrm{opt}}\right)\right)\cdot\sec^2\theta\end{aligned} \tag{4.3}$$

with the fixed shape parameters $a-f$. In Fig. 4.6b the fit of the LDF of an example event is shown.

The signal at the optimum distance $S\left(r_{\mathrm{opt}}\right)$ is corrected for the zenith angle dependence and then used to estimate the primary energy. The energy scale is calibrated against accurate fluorescence light measurements of hybrid events. The estimated energy of the individual event is then corrected for attenuation of shower particles in the atmosphere, which depends on the atmospheric conditions at the time of the detection (on ADST level). In addition, the arrival direction reconstruction is enhanced by fitting a more realistic spherical shower front. The shower reconstruction of the Surface Detector event is now complete.

Reconstruction strategy for the Muon Detector data

From the signals in the buried scintillators, the muon density at a reference distance to the shower axis is determined via a fit on the lateral distribution of the signal. This muon density serves as a mass estimator in combination with the SD energy or the radiation energy reconstructed from the RD signals.

To reconstruct the muon density, first, muons detected in the single modules of the AMIGA counters are counted. A counting strategy was developed to differentiate muon signals from false signals. Thereby, the binary signal traces of each PMT pixel are scanned for distinct patterns of "1"s and "0"s, where each sample corresponds to 3.125 ns of time (see Fig. 4.7, muon patterns are shown as grey boxes). After scanning each trace, all time traces are divided into equal time windows of 8 samples (= 25 ns) and for each window the number of recognized muon patterns N_{s} in all pixels are counted. There are three main causes for false signals: cross-talk between PMT pixels, pile-up of muons, and the corner-clipping effect [134].

Cross-talk occurs by a leakage of the signal of one PMT pixel to an adjacent pixel and may occur by two effects. A photon transported by a fiber to the PMT may leak to the adjacent PMT due to the numerical aperture of the fiber. This is called optical cross-talk. Electronic cross-talk occurs, if a secondary electron from the multiplication process inside a PMT leaks to the adjacent PMT. In both cases another cascade is triggered in the adjacent PMT, resulting in an isolated single photoelectron (SPE) pulse. The signal pulse of a single photoelectron (SPE) lasts typically ~4 ns, whereas the Muon Counter electronics digitally samples the signal trace every 3.125 ns. Hence, the signal pattern produced by an isolated SPE can be a null-trace (000) (if the signal is below the discrimination threshold in all samples), an isolated one (010) or two consecutive isolated ones (0110). On the contrary, the signal of a traversing muon

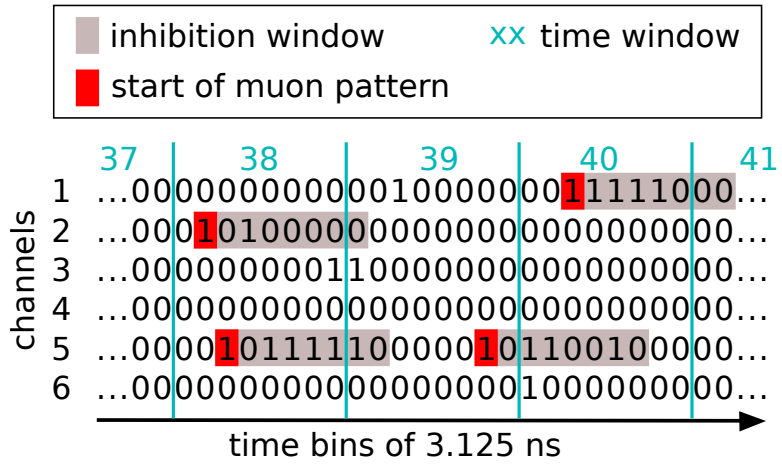

Figure 4.7: Muon counting strategy of the Muon Detector Example of binary traces of multiple channels of one scintillator module. The binary signal is generated from the analog signal by a discriminator. Each channel is then scanned for muon signal patterns of at least two non-consecutive "1"s, i.e. "1X1". Muon signal patterns appearing in the example traces are indicated in red, following an inhibition window of 8 samples indicated in grey. The number of recognized muons patterns are counted for each time window and summed over the whole time trace of 1024 samples.

are multiple SPEs. To remove cross-talk signals, only patterns of two "1s" with a gap in between, i.e. (1X1), are counted as a muon. The X in the gap can either be a "0" or a "1".

To avoid double counting of one muon, an inhibition window of 25 ns ($\hat{=}$ 8 samples) is applied from the beginning of a recognized muon pattern (shown as grey boxes in Fig. 4.7). Additional muons arriving during the inhibition window "pile-up" and are not counted (unless they deposit enough energy to form a muon pattern signal as well in the next inhibition window). This results in an under-counting bias. Therefore, the number of muons N_s in each time window is corrected to account for the under-counting bias due to this pile-up effect [177] by

$$N_s' = -N_{seg} \ln\left(1 - N_s / N_{seg}\right) \quad , \tag{4.4}$$

where $N_{seg} = 64$ is the number of segments, i.e. the number of scintillator strips in the module. The total number of muons counted along the whole time trace is calculated by

$$N_s^{tot} = -N_{seg} \sum_{i=0}^{n} \ln\left(1 - N_{s,i} / N_{seg}\right) \tag{4.5}$$

with $n = 1024$ being the number of samples in the time trace.

The reconstruction chain continues with rejecting modules, which are not of interest for the analysis, e.g. prototype stations. Then, the event is checked if it has at least three non-saturated counters with a signal. Furthermore, if the zenith angle (taken from the SD reconstruction) is larger than a configurable value (55° in this

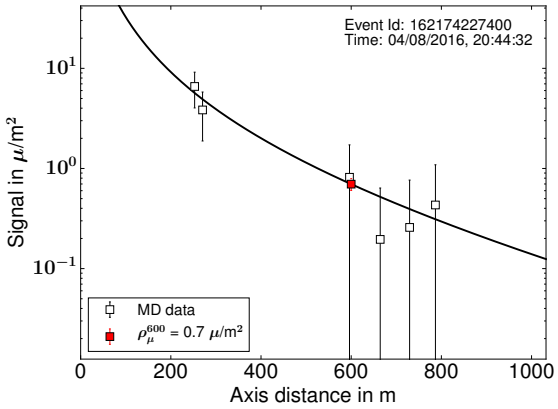

Figure 4.8: Muon lateral distribution function fitted to the muon density measured in muon counters of the same event as in Fig. 4.6b. The muon density at 600 m is reconstructed to $\rho_\mu^{600} = 0.70 \pm 0.09\,\mu/\mathrm{m}^2$. The errorbars depict the uncertainty due to Poisson fluctuations $\sqrt{N}$.

thesis), the event is rejected.

The design of the scintillator modules is done such that a muon usually only crosses one scintillator strip. But inclined muons may cross through two neighboring strips, depositing energy in both (corner-clipping effect). Depending on if the deposited energy is above or below the discrimination threshold, the muon may be counted not at all, in one of the strips or in both, resulting in a net over-counting bias. This bias depends on the zenith angle of the impinging muon and the azimuth angle relative to the direction of the scintillator strip. Hence, a zenith and azimuth angle dependent correction is applied to the number of muons [134, 135]. The values for the zenith and azimuth angle are taken from the preceding reconstruction of the Surface Detector event.

Finally, the lateral distribution of the muon density $\rho_\mu(r)$ (r is the distance to the shower axis) in the shower plane is fitted using the maximum likelihood method. The fitting function used in this procedure is adapted from the KASCADE-Grande experiment [71] and is a Nishimura-Kamata-Greisen (NKG)-type function [176]:

$$\rho_\mu(r) = \rho_\mu(r_{\mathrm{ref}}) \cdot k \cdot \left(\frac{r}{r_0}\right)^{-\alpha} \cdot \left(1 + \frac{r}{r_0}\right)^{-\beta} \cdot \left(1 + \left(\frac{r}{10 r_0}\right)^2\right)^{-\gamma} \quad , \tag{4.6}$$

where $\alpha = 1$, $\gamma = 1.85$ and $r_0 = 150\,\mathrm{m}$ are fixed and β and $\rho_\mu(r_{\mathrm{ref}})$ are fitted to the measured muon densities. Thereby, $\rho_\mu(r_{\mathrm{ref}})$ is the muon density at a reference distance of r_{ref}, which is by default set to 450 m, i.e. the same reference distance as for the SD with 750 m spacing. In this thesis, the reference distance is set to 600 m, which is evaluated the distance with the best mass separation power in Section 5.1.2. β governs the slope of the lateral distribution and is fixed to

$$\beta(\theta) = 3 - \sec\theta \tag{4.7}$$

if the number of counters with a signal is less than four and otherwise is a free parameter. k is a factor normalizing the fit parameter $\rho_\mu(r_{\text{ref}})$ to the value of the lateral distribution at the distance r_{ref}:

$$k = \left(\frac{r_{\text{ref}}}{r_0}\right)^{\alpha} \cdot \left(1 + \frac{r_{\text{ref}}}{r_0}\right)^{\beta} \cdot \left(1 + \left(\frac{r_{\text{ref}}}{10 r_0}\right)^2\right)^{\gamma} \quad . \tag{4.8}$$

An example of a muon lateral distribution function fitted to the signals in the muon detectors is shown in Fig. 4.8.

Reconstruction strategy for AERA data

From the signal traces in the radio antennas, the signal peak amplitude and the energy fluence at each station is derived. From this, the radiation energy of the event is determined performing a two-dimensional fit on the lateral distribution of the energy fluence. The radiation energy is a measure of the cosmic-ray energy. In addition, it can be used as a mass estimator in combination with the muon density at 600 m, as shown in this thesis.

To be able to determine these shower parameters, the raw signal has to be corrected for responses of each component of the detector signal chain. The detector response is unfolded using the time dependent detector description, which is as well used in the detector simulation. Each antenna station of AERA acquires data with two or three channels in the form of time traces. In this thesis, only stations with two channels, corresponding to the east-west and north-south aligned antennas, are analyzed. Various analysis steps are applied on the frequency spectrum of the signals, obtained by a fast Fourier transform on the time trace.

The raw time traces of the channels contain ADC counts, which are converted to voltage. Then, the channel responses are unfolded from the signal. A beacon transmitter installed at the FD building close to the AERA field transmits sine waves in defined frequency lines. These are used to calibrate the timing between the antennas. However, for the analysis of air showers, the beacon signals are RFI noise and therefore these frequencies are digitally suppressed in the spectrum during the analysis. In addition, a band-stop filter is applied on the spectrum to filter the signal for additional disturbances. The time traces are upsampled by adding zeros to the frequency spectrum outside of the design frequency band of the antennas. In this way, signal parameters such as peak amplitudes can be determined with a higher precision.

The corrected signals in the channels correspond to the product of the electric field in east-west and north-south direction and the vector effective length (VEL) of the antennas. The time-dependent electric-field vector $\vec{E}(t)$ of each station is reconstructed from this by unfolding the antenna response. Signal parameters for higher-level analyses such as the peak amplitude and the energy fluence are derived from the electric-field vector for the different vector components x, y and z, the magnitude of the vector, and the projection of the vector to the x-y-plane, depending on the purpose of the analysis. An example of the signal trace is given in Fig. 4.9a.

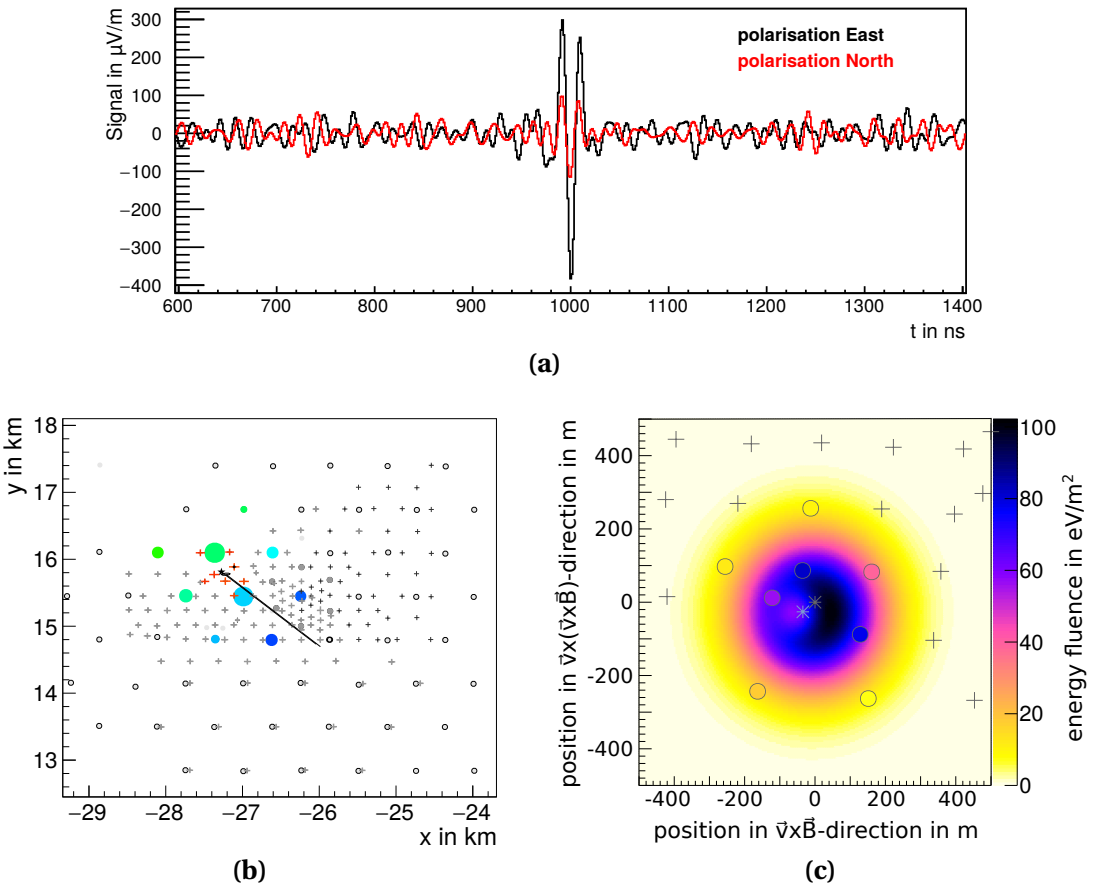

Figure 4.9: Event reconstruction of the Radio Detector of the same example event as in Fig. 4.6b **(a)** Signal trace of the north-south and east-west polarizions of the hottest antenna. **(b)** Particle and radio footprint of the shower. The size of the circles and the crosses represents the signal size in the surface detectors and the radio antennas, respectively. The color denotes the time of arrival, from early times in blue/orange to late times in green/red, respectively. Grey points and crosses represent particle detectors and radio antennas with a signal-to-noise ratio below threshold. The star denotes the reconstructed shower core, the black line the shower axis. **(c)** Two-dimensional lateral distribution reconstructed from the energy fluence measured in antennas (circles). Crosses denote stations with a signal-to-noise ratio below threshold. The stars denote the reconstructed shower core from the SD (brown) and the RD (blue) reconstruction. Figures are extracted from the Offline EventBrowser.

The signal peak amplitude of each station is reconstructed by calculating the maximum of the Hilbert envelope in a signal time window. The signal time window is determined from the event time of the corresponding SD event. The energy fluence is calculated by integrating over the Poynting vector (vector of the energy flux) in a given time window $[t_1, t_2]$ around the signal peak. The Poynting vector corresponds to the squared absolute electric-field traces. To account for noise, the energy fluence arising from noise is determined by integrating over a time window $[t_3, t_4]$ different from the signal window. This noise energy fluence is then substracted from the signal energy fluence. The energy fluence is then given in units of $\mathrm{eV\,m^{-2}}$ by

$$u = \varepsilon_0 c \left(t_{\mathrm{bin}} \sum_{t_1}^{t_2} |\vec{E}(t_i)|^2 - t_{\mathrm{bin}} \frac{t_2 - t_1}{t_4 - t_3} \sum_{t_3}^{t_4} |\vec{E}(t_i)|^2 \right) \tag{4.9}$$

with ε_0 being the vacuum permittivity, c the vacuum speed of light and t_{bin} the size of a time bin.

Using the derived arrival time, amplitude and energy fluence of the signal, false signal stations are rejected based on time residuals, on the polarization of the electric field or on the position of the station if it is outside of the radio footprint. The arrival direction and the shower core are reconstructed in a similar way as done for the Surface Detector using the time residuals in the stations (see Fig. 4.6a) and assuming a plane wave front. The lateral distribution of the energy fluence in the shower plane is fitted using a two-dimensional LDF function to account for the asymmetric shape of the radio footprint. The two-dimensional LDF function is parameterized by a superposition of two Gaussian functions by

$$u(\vec{r}) = A \left[\exp\left(\frac{-\left(\vec{r} + C_1 \vec{e}_{\vec{v}\times\vec{B}} - \vec{r}_{\mathrm{core}}\right)^2}{\sigma^2} \right) - C_0 \exp \frac{-\left(\vec{r} + C_2 \vec{e}_{\vec{v}\times\vec{B}} - \vec{r}_{\mathrm{core}}\right)^2}{\left(C_3 e^{C_4 \sigma}\right)^2} \right] \quad , \tag{4.10}$$

where A is the amplitude, σ the width of the lateral distribution, $\vec{r}_{\mathrm{core}}$ the position of the shower core, $\vec{e}_{\vec{v}\times\vec{B}}$ the unit vector in the direction of the geomagnetic Lorentz force, and C_{0-4} constants, which are parameterized using air-shower simulations [178]. The shower core is fixed to the reconstructed core from the Surface Detector in the case of less than 5 signal stations. The footprint of an example event is given in Fig. 4.9b and the two-dimensional LDF fitted to the energy fluences in antennas is shown in Fig. 4.9c. The radiation energy of the air shower is calculated by integrating the two-dimensional LDF:

$$E_{\mathrm{rad}} = \int u(\vec{r}) d^2\vec{r} \quad . \tag{4.11}$$

To obtain an energy estimation of the electromagnetic shower component, finally, zenith and azimuth dependent corrections are applied (see Eq. (5.7)).

Reconstruction strategy for Fluorescence Detector data

With the Fluorescence Detector the air showers are detected as tracks of light on pixel cameras (example in Fig. 4.10a). This light is emitted from excited nitrogen

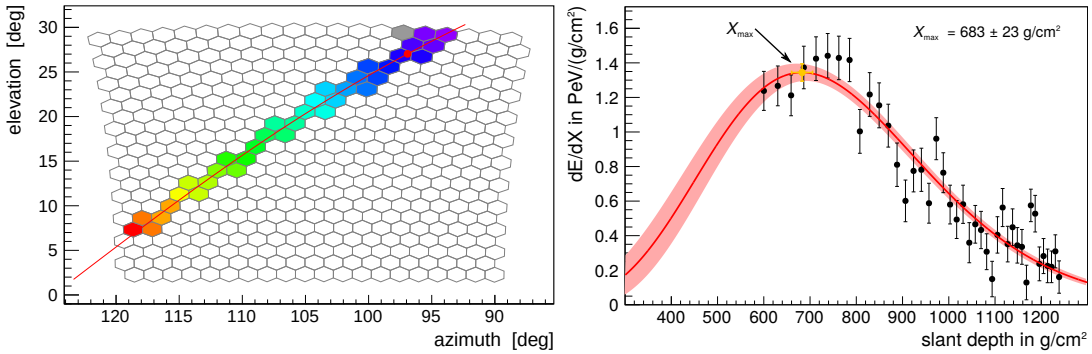

(a) **(b)**

Figure 4.10: Event reconstruction of the Fluorescence Detector of the same example event as in Fig. 4.6b. **(a)** Light trace measured in the pixel camera of one of the telescopes. The color denotes the arrival time of the light in the pixels, from early times in violet to late times in red. **(b)** Reconstructed longitudinal shower profile of the energy deposited in the atmosphere. The maximum of the profile corresponds to X_{max}, which is reconstructed to $(683 \pm 23)\,\mathrm{g\,cm^{-2}}$. Figures are extracted from the Offline EventBrowser.

along the shower in the atmosphere. The track of the air shower in the atmosphere is reconstructed from the time distribution of the light in the pixels combined with the time stamp of the shower arriving in the Surface Detector station closest to the shower core, as shown in Fig. 4.10b. The intensity of the light arriving from the different position along the shower track is fitted with a Gaisser-Hillas function to reconstruct the longitudinal shower profile. The intensity of the light is directly correlated to the energy deposited from the shower in the atmosphere and thereby with the cosmic-ray energy. It is reconstructed by integrating over the shower profile. The maximum of the shower profile corresponds to the atmospheric depth with the maximum number of secondary particles, i.e. X_{max}, which is used as a mass estimator. A detailed description of the event reconstruction can be found in [179]. In this thesis, the FD reconstruction is performed only for measured events, which by chance happen to feature FD data in addition to SD, MD, and RD data (see Section 7.1.1).

4.3.4 Multi-hybrid analysis pipeline

For the first time, a combined reconstruction procedure of simulations and data from the Surface Detector, the Muon Detector, the Radio Detector and the Fluorescence Detector (only for data) has been developed in form of a joint analysis pipeline. This enables the analysis of coincident air-shower events of all detectors at the Pierre Auger Observatory. A schematic overview of the multi-hybrid reconstruction procedure is shown in Fig. 4.11. The analysis pipelines for the event reconstruction of air-shower simulations and of measured data have been added to the current version of the Offline software in form of standard applications. The corresponding

configurations of the module sequences and the XML parameters are shown in Appendix B. These applications are used in this thesis to investigate air-shower simulations in Chapter 6 and measured data in Chapter 7.

The application for simulations, including the detector simulation and the reconstruction, consumes on average 9 minutes computational time to process one CORSIKA simulation. Thereby, simulating the muons crossing the scintillator modules of AMIGA using GEANT4 dominates the run time by 67 %. The reconstruction of the events only makes up a small percentage of the run time, so that the reconstruction of one measured event only consumes on average 13 s computational time. However, the reconstruction of the data of one day takes on average 16 h computational time in which around 4858 cosmic-ray candidate events are processed.

Although the constructed analysis pipeline already delivers high quality multi-hybrid events, various open issues remain to even enhance the event reconstruction of AMIGA and AERA. In [135], a new parametrization to the muon lateral distribution function was derived, which showed to enhance the reconstruction of the muon density at a reference distance. Furthermore, it was found that an inhibition window of the length of 7 instead of 8 samples leads to a more accurate number of counted muons in the scintillator modules. The algorithms used to reject false signal stations in the radio data were improved in [180]. Furthermore, the robustness of the two-dimensional LDF to the energy fluences in the Radio Detector stations can be validated for the case the shower core is fixed to the reconstructed SD core (events with less than 5 signal stations) This is done by varying the core position inside the uncertainty ellipse of the reconstructed SD core. Therewith, a selection on the fit quality can be performed by only accepting robust fits. Furthermore, an alternative method was developed to reconstruct the radio lateral distribution, which is based on an analytic description of the radio emission [181]. These enhancements were not yet included in the $\overline{\text{Off}}\underline{\text{line}}$ software version used in this thesis, but are available in the meantime in the current version of $\overline{\text{Off}}\underline{\text{line}}$.

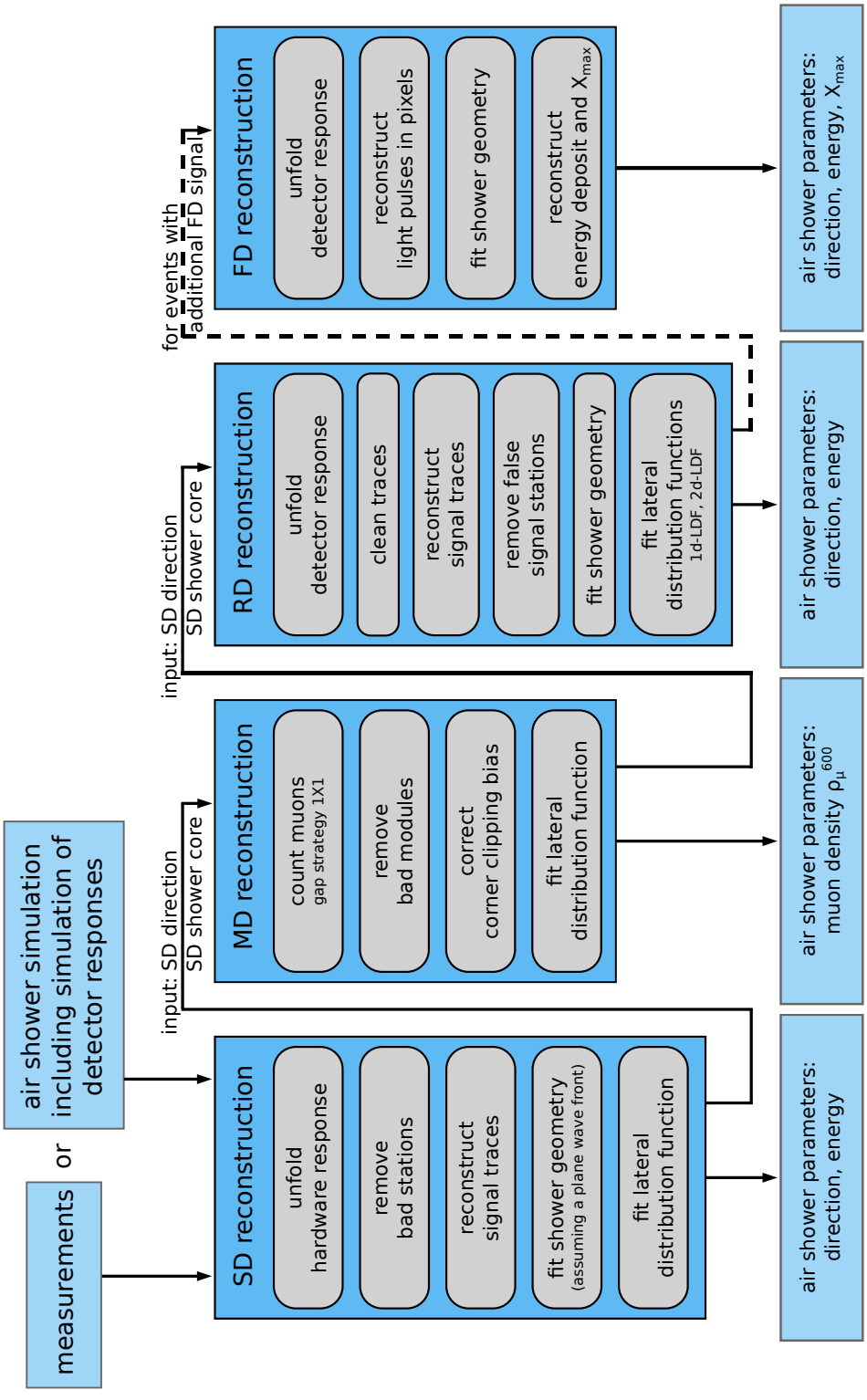

Figure 4.11: Reconstruction of an air shower by Offline including the analysis of all detector types at the Pierre Auger Observatory, i.e., the Surface Detector, Muon Detector, Radio Detector and Fluorescence Detector.

CHAPTER 5

Muons and radio emission for mass estimation

Contents

The development of the muonic and electromagnetic components in a cosmic-ray air shower depends on the mass of the primary particle (see Section 2.2.2). This can be used to estimate the primary mass by measuring the muonic and electromagnetic components of the same air shower separately. Air showers induced by heavier particles develop faster, and more muons and less electrons are produced compared to showers of light primary particles. This influences the ratio between the numbers of muons and electrons at the shower maximum and at the ground. A common method is to measure the number densities at a reference distance to the shower axis of electrons and muons at ground (e.g. in CASA-MIA [182, 183], AGASA [73], KASCADE-Grande [71]). Except for showers more inclined than 60°, the muons rarely interact or decay in the atmosphere and their number is approximately constant from the shower maximum to the ground. However, the electrons are absorbed in the atmosphere so that their number depends on the distance to the shower maximum $X_{\max}$. Especially for particles arriving at large zenith angles, the distance to the shower maximum is long and the number of electrons falls below the detection threshold. On the contrary, the radio emission is produced by the charged electromagnetic component along the shower and is not absorbed in the atmosphere. Thus, it provides information about the size of the electromagnetic component for all zenith angles. Furthermore, the width of the footprint at the ground rises with the

zenith angle [141], which makes detection possible for radio antenna arrays with a large spacing.

In this chapter, the capability of the radio emission is evaluated to serve as a mass estimator in combination with the muons at the ground. For this, different parameters such as the particles numbers and radiation energy are studied for proton- and iron-induced air showers. The mass separation power is investigated depending on the zenith angle and the primary energy. It shows that for inclined showers using the radio emission is superior compared to classical detection methods. The observables of interest are derived from air-shower simulations calculated by CORSIKA (see Section 4.1.3 for details about the simulation libraries) on an observation level of about 1550 m. To study the pure shower physics, the observables are true values independent on any detector related dependencies. In the following Chapter 6 detector effects of the AMIGA and AERA detectors are investigated.

5.1 The muonic component at ground

5.1.1 Total number of muons at the ground and at $X_{\max}$

The total number of muons of a shower when reaching the ground depends on the primary energy, as shown in Fig. 5.1a. Here, only showers with 38° zenith angle are plotted and all muons above an energy of 50 MeV are taken into account. A power law fit is performed to determine the energy dependence:

$$N_\mu(E) = a \cdot \left(\frac{E}{10^{18}\text{eV}}\right)^i \quad . \tag{5.1}$$

The fit shows that the dependency is not linear but the number of muons grows with the energy with a mean index for proton and iron primaries of 0.936 ± 0.006 for showers with a zenith angle of 38°. Repeating this fit for all zenith angles yields a slightly smaller mean index of 0.923 ± 0.003, which will be used in the following to correct for the energy dependence. The Heitler-Matthews model, a simplified model for hadronic air-showers, predicts an index of 0.85 and the different hadronic models predict values between 0.88 – 0.92 (see Section 2.2.1), which is in the uncertainty range of the fit result here. Furthermore, the fitted amplitude shows that the number of muons for showers of the same energy is about 30 % larger for iron primaries than for protons.

Muons interact much less with matter, i.e. the atmosphere, than electrons and have only negligible energy losses from bremsstrahlung due to their larger mass. The muon is an unstable particle, but its decay is only mediated by weak interaction and therefore slow with a mean lifetime of 2.2 µs. Hence, this decay only becomes important for inclined showers, where the distance from $X_{\max}$ to the ground is of the same order of the distance traveled in the lifetime. In Fig. 5.1b the true number of muons at $X_{\max}$ and at the ground are plotted. Here, the simulation set corresponding to 5302 real measured events of AERA is used with an energy range from $10^{17} - 10^{20}$ eV

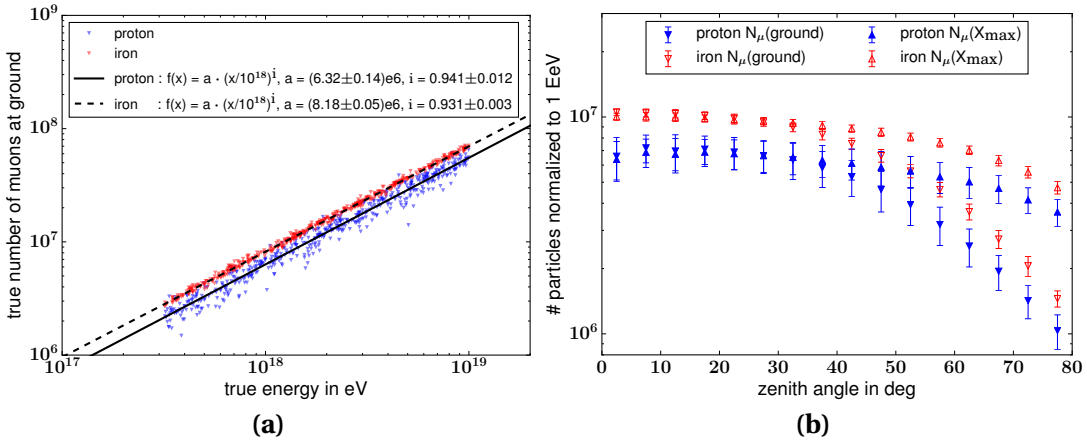

Figure 5.1: True number of muons at the ground and at $X_{\max}$ above a muon energy of 50 MeV. Both plots show a higher number of muons for iron induced showers compared to proton. **(a)** Energy dependence of the true number of muons of showers with a zenith angle of 38°. A power law fit results in a mean dependence to $N_\mu \propto E^{0.936}$. **(b)** Zenith angle dependence of the true number of muons at $X_{\max}$ and at the ground. Real measured events of AERA are simulated for proton and iron primaries, and the number of muons is normalized to an energy of 10^{18} eV. The number of muons is stable from $X_{\max}$ to the ground up to around 45°. For larger zenith angles the traveled distance becomes large and a fraction of the muons decays during the shower development.

and a zenith angle range from 0 – 80°. For each shower the number of muons is normalized to the corresponding value at an energy of 10^{18} eV, using the obtained fit results of the energy dependence. The mean number of muons of zenith angle bins of 5° width is plotted. For zenith angles up to around 45° the number of muons is stable up to the ground. For larger zenith angles a growing fraction of the muons decays before reaching the ground and even before $X_{\max}$, whereas the effect is larger for the number of muons at the ground.

The number of muons at the ground is larger for iron than for proton showers for all zenith angles. The spread (standard deviation) is larger for proton showers, which is explained by larger shower-to-shower fluctuations (see Section 2.2.2). However, the separation between proton and iron is larger than the spread, which shows the potential of the number of muons at the ground for estimation of the primary mass, provided that the primary energy is known.

The Pierre Auger Collaboration has recently shown, that the measured number of muons is about 30 – 60 % higher than predicted from air-shower simulations using hadronic interaction models [65]. This discrepancy does not influence the mass separation power. However, the absolute scale of this observable is shifted which has to be taken into account when comparing simulations to measured data.

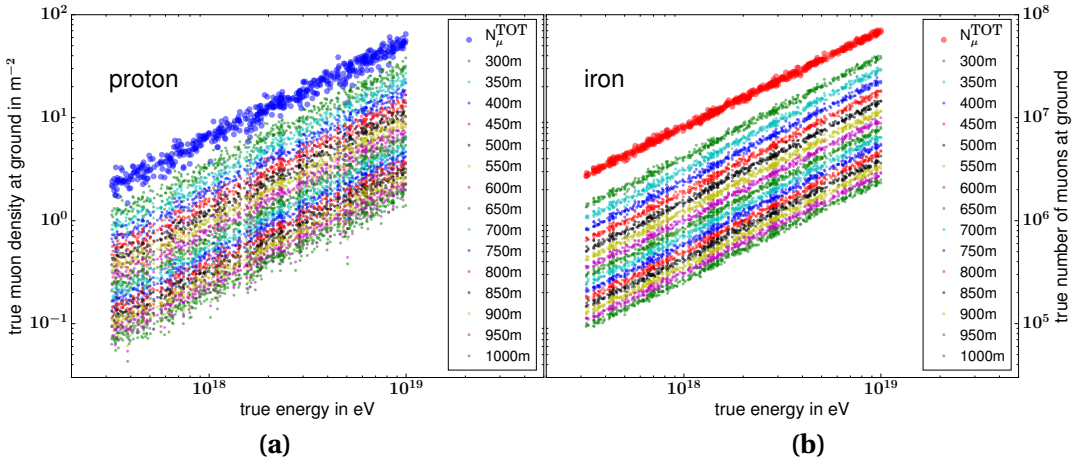

Figure 5.2: True muon density at different distances to the shower axis above a muon energy of 50 MeV for showers induced by **(a)** proton and **(b)** iron with a zenith angle of 38°. It is directly correlated to the total number of muons at the ground and shows the same energy dependence.

5.1.2 Observable: muon density at a reference distance

The particle footprint of a cosmic-ray air shower extends over several km^2 at the ground at the energies investigated here. Hence, it is rather complicated to measure its total number of muons. Instead, the number of muons is measured at different positions inside the footprint with detectors of a certain detection area. The measured muon density is fitted over the perpendicular distance to the shower axis with a lateral distribution function (LDF, see e.g. Section 4.3.3 for the LDF used in AMIGA), assuming axial symmetry, which is a good approximation except for very inclined showers. The muon density at a chosen reference distance is directly correlated to the total number of muons at the ground, as shown in Fig. 5.2. It shows the true muon density for proton (Fig. 5.2a) and iron (Fig. 5.2b) primaries at distances from 300 – 1000 m as well as the total true number of muons at the ground over the primary energy for showers with a zenith angle of 38°. The muon density has the same energy dependence as the total number of muons at the ground for all distances. Therefore, the same normalization to the energy with an index of 0.923 ± 0.003 is applied in the following.

The muon density shows a maximum separation between proton and iron showers at a certain distance, which is investigated in the following. The mean muon density over the distance to the shower axis is shown in Fig. 5.3a for showers with a zenith angle of 38°, normalized to an energy of 10^{18} eV. The muon density decreases with the distance for both proton and iron showers. Thereby, the relative difference between the mean density of proton and iron showers

$$\Delta N_{\mu,\mathrm{rel}} = \frac{N_{\mu,Fe} - N_{\mu,P}}{2\left(N_{\mu,P} + N_{\mu,Fe}\right)} \tag{5.2}$$

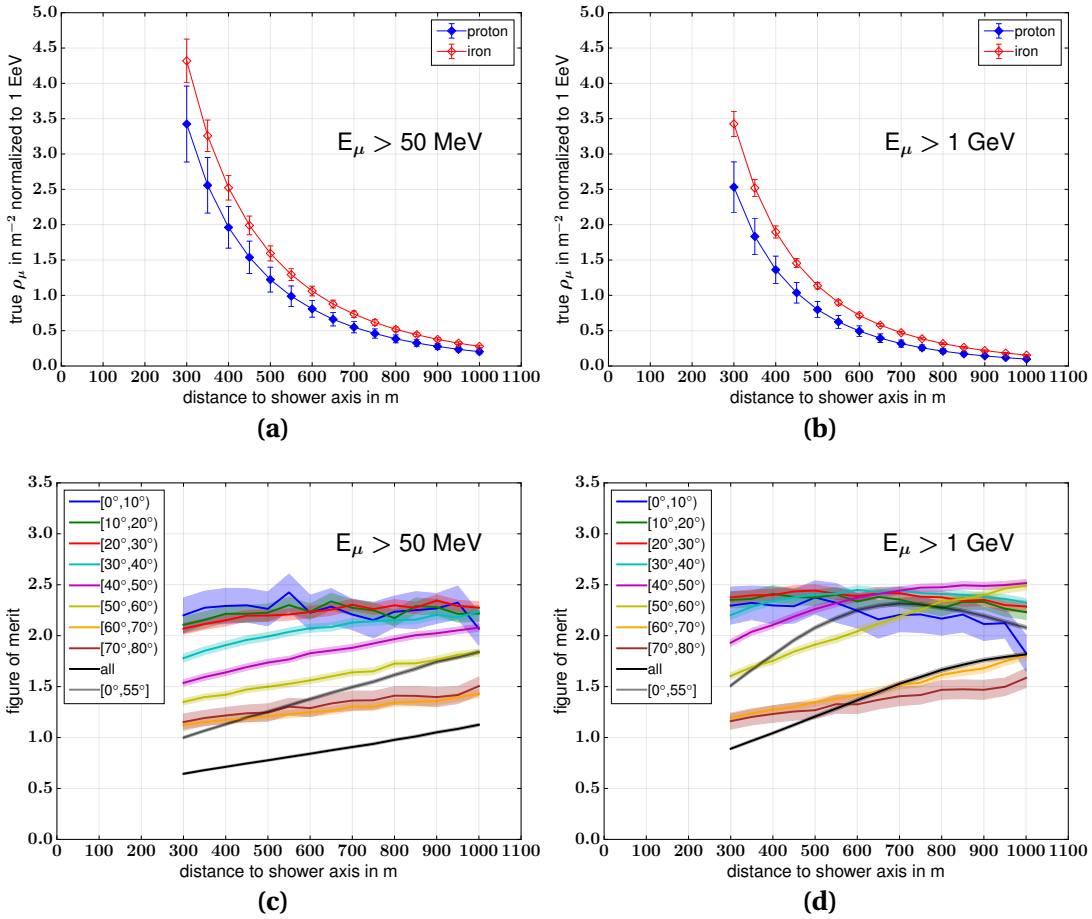

Figure 5.3: Mass separation power of the muon density at different distances to the shower axis (a)–(b) True muon density for different muon energy thresholds over the distance to the shower axis for showers with a zenith angle of 38°. The muon density decreases with the distance. Thereby, the relative difference between proton- and iron-induced showers increases, whereas the relative spread is constant. The muon density is decreased by around 25 % for a threshold of 1 GeV compared to 50 MeV. **(c)–(d)** Figure of merit for different muon energy thresholds over the distance to the shower axis for different zenith angle ranges and for combining showers at all zenith angles. For a threshold of 50 MeV the figure of merit increases continuously with the distance for zenith angles above 20°. Comparing different zenith angles, the figure of merit decreases with the zenith angle due to larger shower-to-shower fluctuations. For a higher energy threshold of the muons of 1 GeV the figure of merit is enhanced for the full zenith angle range and shows a maximum between 600 – 800 m for the range of 0 – 55°.

increases, whereas the relative spread due to shower-to-shower fluctuations

$$\sigma_{\mathrm{i,rel}} = \frac{\sigma_{\mathrm{i}}}{N_{\mathrm{i}}} \tag{5.3}$$

is constant for iron with 6 % and for proton with 14 %. Both parameters influence the capability to differentiate between proton and iron showers. As a measure for the separation power of two classes, i.e. here proton and iron, the so called figure of merit is calculated:

$$FOM = \frac{|\mu_1 - \mu_0|}{\sqrt{\sigma_0^2 + \sigma_1^2}} \quad , \tag{5.4}$$

where μ_{i} is the mean value and σ_i the standard deviation of the class, in this case 0=p, 1=Fe. The figure of merit is a valid statistical estimator for Gaussian distributions, which is given here for all true observables. Figure 5.3c shows the figure of merit for proton and iron primaries over the distance to the shower axis for showers with different zenith angles as well as for all zenith angles combined and for the zenith angle range of AMIGA of 0 – 55°. For small zenith angles below 20°, the figure of merit is constant over all distances. For more inclined showers, it increases with the distance and does not reach a maximum until 1000 m.

In addition, the energy threshold of the muons influences the density distribution depending on the lateral distance to the shower axis. The LDF and the figure of merit is shown for the standard threshold of 50 MeV used in the simulations in Figs. 5.3a and 5.3c, and for a muon energy threshold of 1 GeV, as for the scintillators of AMIGA buried in 2.3 m depth, in Figs. 5.3b and 5.3d. The LDF shows a similar shape for both thresholds, but with an around 25 % smaller muon density at all distances for a threshold of 1 GeV. The figure of merit is enhanced for zenith angles of 20 – 50° for small distances up to 700 m and for larger zenith angles at larger distances. This leads to a maximum at 700 m for the zenith angle range of 0 – 55° for a threshold of 1 GeV.

However, the muon density here is calculated from pure shower simulations and does not contain any detector uncertainties. Due to a small detection area of particle detectors, Poisson fluctuations of the number of counted muons are expected. Since the muon density decreases with the distance, it is expected that these fluctuations and consequently the measurement uncertainties increase with the distance. This influences the figure of merit differently for the different distances and gives a preference for smaller distances. Even for the true values without detector uncertainties, the density at 600 m shows only a minor decrease in the figure of merit compared to 700 m for the zenith angle range of AMIGA of 0 – 55°. Therefore, the muon density ρ_μ^{600} at a reference distance of 600 m is chosen for all following analyses.

The dependence of the muon density ρ_μ^{600} on the zenith angle is shown in Figs. 5.4a and 5.4b for a muon energy threshold of 50 MeV and 1 GeV, respectively. The muon density above an energy of 50 MeV shows the same dependence on the zenith angles as the total number of muons above this energy (see Fig. 5.1b). It is approximately constant up to a zenith angle of 50°. For larger zenith angles it decreases due to muon decays. The muon density of high energy muons above 1 GeV differs from this

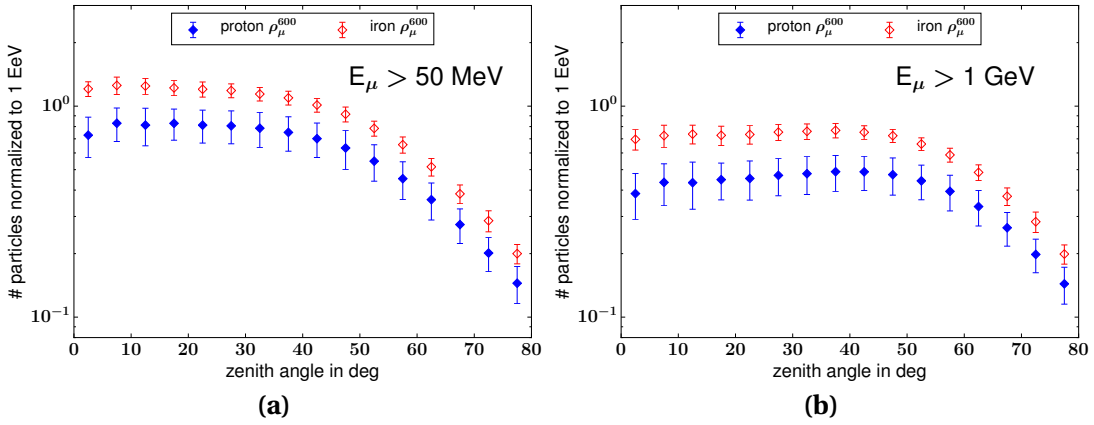

Figure 5.4: Zenith angle dependence of the muon density at 600 m for different energy thresholds of the muons. **(a)** The density of muons above an energy of 50 MeV shows the same dependence as the total number of muons above this energy (see Fig. 5.1b). It is approximately constant until 50° and increases for larger zenith angles due to muon decays. **(b)** The density of muons above an energy of 1 GeV increases for zenith angles up to 50°, which indicates that up to these zenith angles the production of high energy muons dominates. For larger zenith angles it decreases in a similar manner as when including the low energy muons.

behavior. It slightly increases for zenith angles up to 50°. This indicates that up to these zenith angles more high energy muons are produced by hadronic decays than decay. Vice versa, the for low energy muons, the decay dominates already at smaller zenith angles, which is compensated by the production of high energy muons. The muon energy threshold of the AMIGA Muon Detector is shown to be slightly below 1 GeV in Section 6.2.1, and hence features the observed increase in the energy range of AMIGA. This leads by accident to a constant ratio of the muon density with the radio emission as observed in Fig. 5.9 later in this chapter.

5.2 The electromagnetic component and the radio emission

5.2.1 Number of electrons at the ground and at $X_{\max}$

The number of electrons in an air shower can be detected by particle detectors at the ground in a similar way as the muons. However, the electrons are partly absorbed in the atmosphere on their way to the ground and suffer much larger energy losses, by e.g. bremsstrahlung, than the much heavier muons. Therefore, their number in the shower strongly depends on the distance in atmospheric depth to $X_{\max}$, which increases with the zenith angle θ roughly with $1/\cos\theta$. The number of electrons at the ground and $X_{\max}$ are plotted over the zenith angle in Fig. 5.5a. As expected,

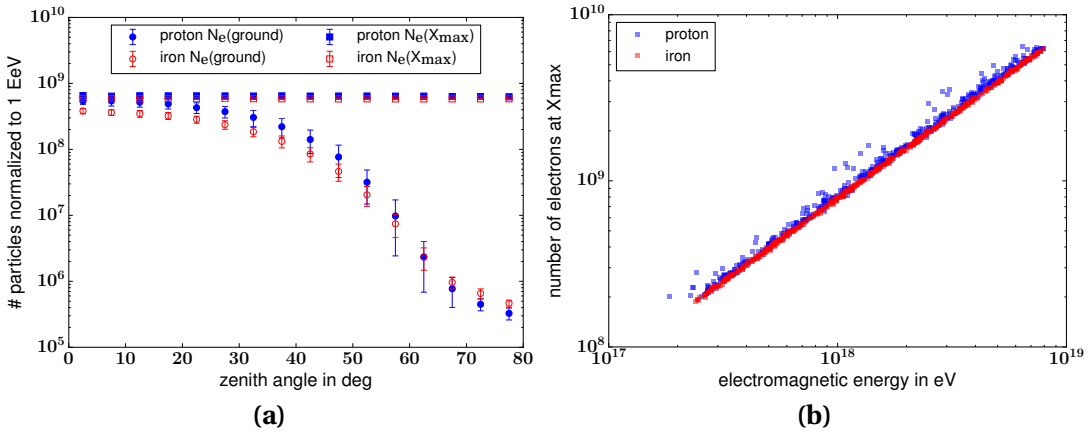

Figure 5.5: True number of electrons at $X_{\max}$ and at the ground above an energy of 250 keV. **(a)** Zenith angle dependence of the true number of electrons. The number of electrons at the ground decreases by about three orders of magnitude over the plotted zenith angle range due to absorption in the atmosphere. Proton showers contain more electrons than iron showers except for very inclined showers, where the electrons are mainly products of muon decays. On the contrary, the number of electrons at $X_{\max}$ is constant over all zenith angles and higher in proton showers. **(b)** Correlation of the number of electrons at $X_{\max}$ and the energy deposited in the atmosphere by electrons along the shower development. Shown are proton- and iron-induced showers with a zenith angle of 38°. Both particle types show the same correlation except for higher shower-to-shower fluctuations for proton.

the number at ground decreases with the zenith angle and is about three orders of magnitude smaller at an angle of 80° compared to vertical showers. This has to be corrected when using the electron number for mass separation measurements. This leads to additional uncertainties from the measurement of the arrival direction of the shower. Depending on the size and type of the particle detectors and on the observation level, the number of electrons falls below the detection threshold and only the muons are detected for very inclined showers.

Moreover, it becomes apparent that the difference between proton and iron showers becomes smaller and finally flips the direction, so that for showers more inclined than 65° iron showers contain more electrons than proton showers. The shower-to-shower fluctuations are increased around the zenith angle of the flip. In addition, the slope becomes smaller towards higher zenith angles. This observations are explained by the increasing number of muon decays into electrons (see Fig. 5.1b). Hence, these electrons are mostly created by the muonic component. Thus, for inclined showers, the number of electrons is correlated with the number of muons in the shower, which is larger for heavier primary particles. Due to this flip in the proton-iron separation, the number of electrons at ground does not provide a reliable mass estimator for inclined air showers.

On the contrary, the number of electrons at $X_{\max}$ does not depend on the zenith

angle. It is larger for proton than for iron-induced air showers and, thus, provides information about the mass of the primary particle. However, it cannot be measured directly. But the location with the largest amount of particle makes the largest contribution to the deposited energy. Thus, the number of electrons at X_{max} is directly correlated to the electromagnetic energy deposited in the atmosphere, as shown in Fig. 5.5b. This electromagnetic shower energy is larger for protons than for iron by 4.5 % for an air shower with a primary energy of 10^{18} eV, but the difference decreases at higher energies, e.g. to 3 % at 10^{19} eV [9]. It can be measured by the fluorescence light, the Cherenkov light or the radio emission produced by the shower in the atmosphere. Hence, in contrast to direct measurements of the number of electrons, indirect measurements such as by radio are expected to provide mass sensitivity for all zenith angles including very inclined showers, when combined with the size of the muon content.

5.2.2 Observable: the radiation energy of the radio emission

The radio emission of an air-shower is induced by the electromagnetic particles in the shower. Hence, the energy contained in the radio emission - the radiation energy E_{rad} - provides a calorimetric measurement of the electromagnetic shower energy E_{em}. This correlation between the radiation energy and the electromagnetic shower energy was observed at the Pierre Auger Observatory [118] and is used here to calculate the radiation energy from the shower simulations.

The radiation energy slightly depends on the arrival direction and the angle to the geomagnetic field. Corrections for these dependencies are modeled in [184] for showers with a zenith angle up to 80° and applied here. The geomagnetic fraction of the radiation energy is influenced by the magnitude of the geomagnetic field B_{Earth} as well as the angle α between the shower axis and B_{Earth}. It scales with $\sin^2\alpha$ because of the coherent nature of the radio emission. The charge excess fraction a of the radiation energy grows with the atmospheric density $\rho_{X_{\mathrm{max}}}$ at X_{max}. The atmospheric density decreases with altitude. Thus, $\rho_{X_{\mathrm{max}}}$ depends on the zenith angle and the altitude of the shower maximum X_{max}, which is generally higher in the atmosphere for showers induced by heavier particles. Furthermore, there is a second order dependence on $\rho_{X_{\mathrm{max}}}$. Whereas the radio emission depends on the geometric distance (in m), the air shower develops according to the atmospheric depth (in $\mathrm{g\,cm^{-2}}$). The ratio between the geometric distance and the atmospheric depth is higher for regions of lower atmospheric density. This leads to a slightly larger radio emission, if X_{max} is higher in the atmosphere. Therefore, the radiation energy E_{rad} is corrected for these dependencies by

$$S_{\mathrm{RD}}^{\rho_{X_{\mathrm{max}}}} = \frac{E_{\mathrm{rad}}}{a(\rho_{X_{\mathrm{max}}})^2 + \left(1 - a(\rho_{X_{\mathrm{max}}})^2\right)\cdot \sin^2\alpha} \cdot \frac{1}{\left(1 - p_0 + p_0 \cdot \exp\left[p_1 \cdot \left(\rho_{X_{\mathrm{max}}} - \langle\rho\rangle\right)\right]\right)^2} \quad , \tag{5.5}$$

where $p_0 = 0.251 \pm 0.006$ and $p_1 = -2.95 \pm 0.06\,\mathrm{m^3\,kg^{-1}}$, and $\langle\rho\rangle = 0.65\,\mathrm{kg\,m^{-3}}$ is the atmospheric density at the average $\langle X_{\mathrm{max}}\rangle = 669\,\mathrm{g\,cm^{-2}}$ for an average zenith angle of 45° and a primary energy of 10^{18} eV for a 50 %-proton / 50 %-iron composition.

The correlation of the true radiation energy S_{RD}, after normalization according to the arrival direction, with the electromagnetic shower energy E_{em} is modeled in [184] by

$$S_{\mathrm{RD}}^{\rho_{X_{\mathrm{max}}}} = A \cdot 10^7\,\mathrm{eV} \cdot \left(\frac{E_{\mathrm{em}}}{10^{18}\,\mathrm{eV}}\right)^B \tag{5.6}$$

with $A = 1.683 \pm 0.004$ and $B = 2.006 \pm 0.001$. The radiation energy used for this model was later found to be underestimated by about 11 % in the simulations used for this parametrization due to settings in the CoREAS simulations [185], which is not considered here. However, the simulations used here feature the same underestimation. Hence, the radiation energy calculated here is directly comparable to the radiation energy reconstructed including the detector response, as done in Chapter 6.

However, X_{max} is often not accessible in an experiment and in case it is measured, there are additional measurement uncertainties. Therefore, a correction dependent on the zenith angle, for which the measurement uncertainties are much smaller, is formulated based on the mean X_{max} at the respective zenith angles:

$$S_{\mathrm{RD}}^{\rho_{\theta}\prime} = \frac{E_{\mathrm{rad}}}{a(\rho_\theta)^2 + \left(1 - a(\rho_\theta)^2\right) \cdot \sin^2\alpha} \cdot \frac{1}{\left(1 - p_0 + p_0 \cdot \exp\left[p_1 \cdot \left(\rho_\theta - \langle\rho\rangle\right)\right]\right)^2} \quad . \tag{5.7}$$

In addition, another zenith angle dependent effect has to be taken into account. Depending on the observation level of a detector, the shower might not be fully developed at the time of detection. Hence, a part of the shower is clipped before the radio emission of this part is released. The magnitude of this clipping effect depends on the distance between the observer and X_{max}. The radiation energy investigated in the following is corrected for this effect by

$$S_{\mathrm{RD}}^{\rho_\theta} = \frac{S_{\mathrm{RD}}^{\rho_{\theta}\prime}}{1 - \exp\left(-8.7\,\mathrm{cm^2\,kg^{-1}}\left(D_{X_{\mathrm{max}}} + 0.29\,\mathrm{kg\,cm^{-2}}\right)^{1.89}\right)} \quad , \tag{5.8}$$

where $D_{X_{\mathrm{max}}}$ is the distance between the observer and X_{max} in $\mathrm{kg\,cm^{-2}}$.

In summary, in this work $S_{\mathrm{RD}}^{\rho_{X_{\mathrm{max}}}}$ is calculated from the electromagnetic shower energy of the full shower by Eq. (5.6). Then, E_{rad} is calculated using Eq. (5.5) and corrected for the atmospheric density depending on the zenith angle by Eq. (5.7). Finally, the radiation energy is clipped according to the observation level by Eq. (5.8) to gain $S_{\mathrm{RD}}^{\rho_\theta}$, which is investigated in the following.

The corrected radiation energy $S_{\mathrm{RD}}^{\rho_\theta}$ is plotted over the zenith angle in Fig. 5.6 after normalization to 10^{18} eV by assuming $S_{\mathrm{RD}}^{\rho_\theta} \propto E^2$ [118]. $S_{\mathrm{RD}}^{\rho_\theta}$ grows with the zenith angle, as inclined showers extend over a larger geometric distance on which the radiation energy is released. In addition, the shower-to-shower fluctuations decrease with increasing zenith angle. Proton showers release more radiation energy than iron showers due to the larger amount of electrons and positrons at X_{max}. In fact,

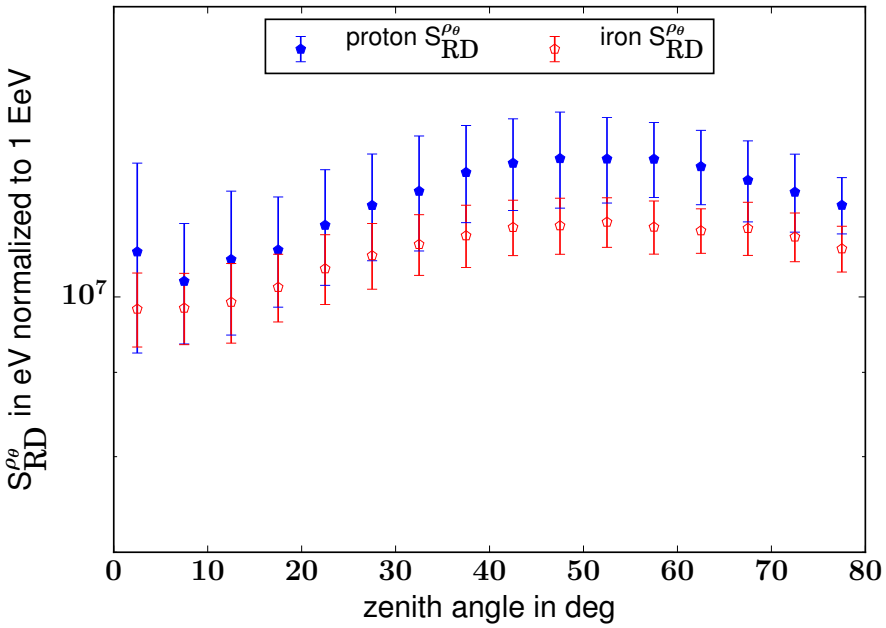

Figure 5.6: True radiation energy over the zenith angle The radiation energy is corrected for variation due to the angle between the geomagnetic field and the shower axis as well as due to the air density at the mean X_{max} at the zenith angle. Furthermore, the radiation energy is 'clipped' due to the chosen observation level in the simulations. It increases with the zenith angle up to 50°, whereas this effect is larger for proton showers. This leads to an enhanced mass sensitivity at this zenith angle.

the difference between proton and iron showers grows with the zenith angle. This is expected, since the mean free path of the shower particles grows and thus the difference between the total path lengths of all electrons and positrons. In addition, the full development of an iron shower is shorter in atmospheric depth than of a proton shower with the same primary energy. This becomes apparent, when the iron shower (A=56) is described as 56 parallel developing "proton" sub-showers with each a primary energy of $E_0/56$ (see Section 2.2.1). Each of these sub-showers develops faster than the proton shower with the primary energy E_0 and hence the whole iron shower does. Therefore, the proton shower travels a longer geometric distance on which more radiation energy is released. This effect becomes larger for more inclined showers, where the ratio between the atmospheric depth and the geometric distance becomes larger.

5.3 Mass estimation by combining observables

The relative difference between proton- and iron-induced air showers of each investigated observable is shown in Fig. 5.7. The radiation energy shows an enlarged mass sensitivity at higher zenith angles, reaching a plateau at around 50°. In contrast, the number of electrons loses its mass sensitivity at angles above 60° due to the fact

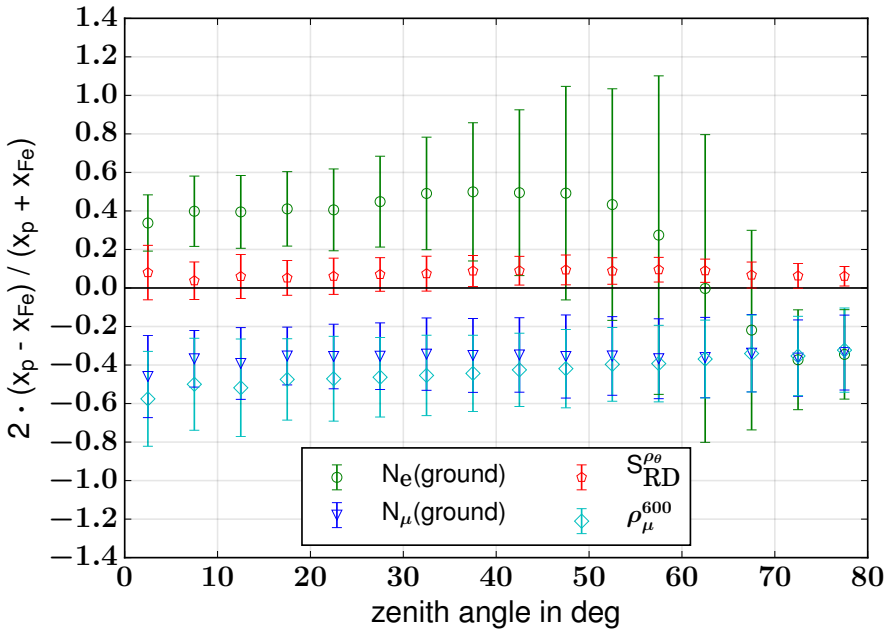

Figure 5.7: Relative difference of observables of proton and iron showers The observables of the electromagnetic shower component are larger for proton showers, whereas the observables of the muonic component are larger for iron showers. However, the number of electrons loses this mass sensitivity at zenith angles above 60°, since only electrons created by muon decay are present in the showers when arriving at the ground. In contrast, the radiation energy is relatively constant for all zenith angles. The muon observables show a slightly decreasing mass sensitivity with increasing zenith angle.

that mainly electrons originating from muon decay reach the ground. In addition, the uncertainties due to shower-to-shower fluctuations are large. The difference between proton and iron showers for the number of muons at the ground as well as for the muon density at 600 m only decreases slowly for large zenith angles. Both muon observables show the same separation.

The observables of the electromagnetic component feature higher values for proton showers (N_e only up to 60° zenith angle), the muonic observables are higher for iron. Therefore, it is expected that the mass sensitivity is enhanced by combining complementary observables. To investigate the correlation between the muon density and the radiation energy, these observables are plotted over each other in Fig. 5.8a. A power-law fit results in a correlation by an average index of 0.474. This is in accordance with the expectations, comparing to the energy correlations of the two observables of $\rho_\mu^{600} \propto E^{0.923}$ and $\sqrt{S_{\mathrm{RD}}^{\rho\theta}} \propto E$. Thus, a minor additional correlation on the energy with an index of 0.058 is applied when calculating the ratio $\rho_\mu^{600}/\sqrt{S_{\mathrm{RD}}^{\rho\theta}}$. The fit is performed for different hadronic models in Fig. 5.8b. Only minor differences between the models can be observed for both observables, whereby Sibyll 2.3 predicts slightly more muons for proton showers at small radiation energies and

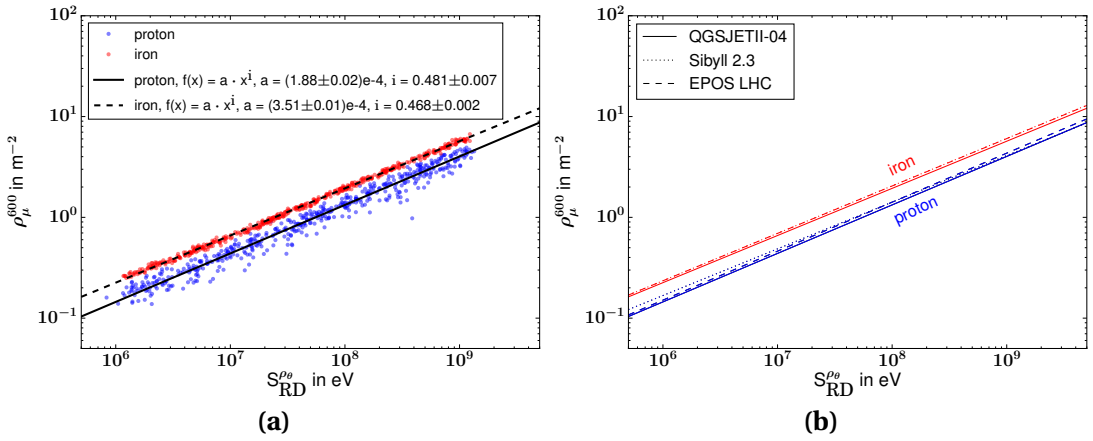

Figure 5.8: Correlation between the muon density and the radiation energy (a) A power-law fit results in a correlation in agreement with the expectation. **(b)** The fit results using different hadronic models show only minor differences in both parameters. Therefore, only QGSJETII-04 is used for all following investigations in this thesis.

EPOS-LHC at higher radiation energies. Because of the marginal difference between the models, only simulations calculated with QGSJETII-04 are used in the following.

In Fig. 5.9 the ratio between the muon density at 600 m axis distance and the square root of the radiation energy is plotted over the zenith angle. The ratio decreases at zenith angles above 50°, since the muon density decreases (see Fig. 5.1b). The separation between proton and iron showers is larger than the spread (standard deviation) of both distributions for all investigated zenith angles.

The mass separation power represented by the figure of merit is shown in Fig. 5.10 for the ratio of the muon density and the radiation energy, the ratio of the muon density and the number of electrons at the ground, the muon density, and $X_{\max}$, normalized by their dependencies on the true energy. Furthermore, all observables are normalized by correcting them for their energy dependence, whereby the true energy is exactly known from the simulations. In an experiment this is not the case, but the energy has to be measured in addition, introducing additional measurement uncertainties. If e.g. the muon density and the primary energy are measured with the same detector, their measurement uncertainties are correlated which makes a mass estimation with the ratio of them difficult. On the contrary, the measurement uncertainties become smaller if two different detectors are used for the observables whose ratio represents the mass estimator. The ratios of $\rho_\mu^{600}/\sqrt{S_{\mathrm{RD}}^{\rho_\theta}}$ and ρ_μ^{600}/N_e are shown as well without energy correction. It becomes apparent, that compared to the normalized case the mass separation power only decreases slightly for the combination with the radiation energy. Since the radiation energy is directly correlated to the primary energy, it is an energy estimator itself. In contrast, using the number of electrons without additional information about the primary energy highly decreases the merit factor, except for large zenith angles at which the electron-muon

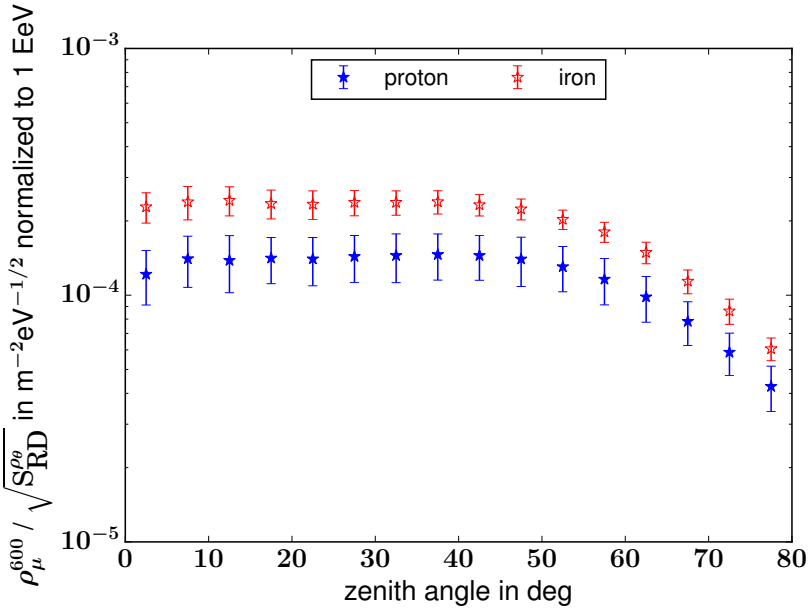

Figure 5.9: Ratio between the muon density and the square root of the radiation energy The separation of proton and iron showers exceeds the spread originating from shower-to-shower fluctuations. The ratio decreases for larger zenith angles, since the muon density decreases (see Fig. 5.1b).

ratio anyway has poor separation power. In addition, the figure of merit is overestimated for the case of detecting electromagnetic particles, since in an experiment the total number of electrons cannot be measured but instead the electron density at a reference distance, as it is done for muons as well. Thereby, the uncertainties increase slightly due to Poisson fluctuations. However, the density of electrons at a reference distance was not investigated in this thesis and therefore the total number of electrons is used.

In summary, for showers in the range of $0-35°$ zenith angle, the best measurable mass estimator is ρ_μ^{600}/N_e, if the primary energy is well known. This is the zenith angle range at which the AMIGA detector (water-Cherenkov tanks in combination with buried scintillators) has the best detection efficiency due to the larger effective area of the scintillator modules for more vertical showers. However, in an experiment the figure of merit is expected to be lower due to Poisson fluctuations when counting particles with limited detection areas. For flat detectors such as scintillators, this effect even increases with the zenith angle. On the contrary, radio measurements have the advantage to not suffer from Poisson fluctuations. Therefore, it is expected that in an experiment the mass separation power for the mass estimators $\rho_\mu^{600}/\sqrt{S_{RD}^{\rho_\theta}}$ and ρ_μ^{600}/N_e can be of the same order for vertical showers. For inclined showers the radiation energy clearly enhances the mass estimation compared to the classical method of electromagnetic particle counting. In addition, the radio emission is spread over

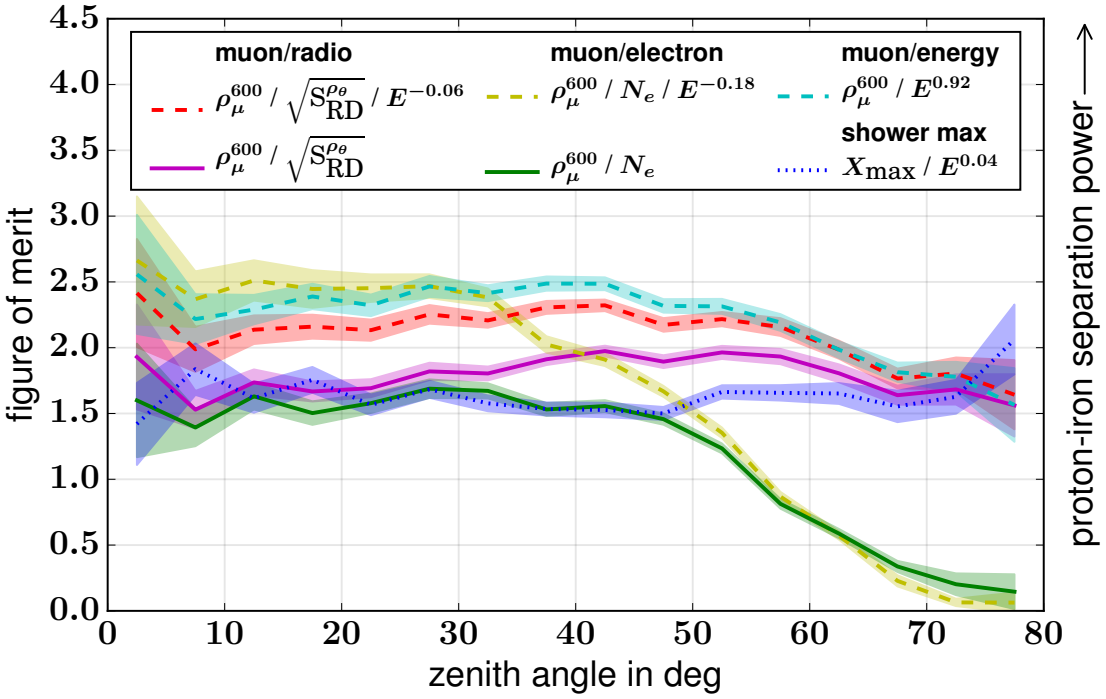

Figure 5.10: Figure of merit of the different shower observables The different mass estimators are corrected for their dependence on the primary energy, which is known for this simulations (dashed lines). In addition the uncorrected ratios are shown (solid lines). The errorbands depict the uncertainties due to shower-to-shower fluctuations. For zenith angles up to 30° the classical methods combining the muon number with the electron number or primary energy, respectively, show the largest mass separation power. This, however, decreases drastically for the combination with electrons for larger zenith angles. For more inclined showers, the mass separation power of the muon density combined with the primary energy as well as with the radiation energy are comparably strong mass estimators. The combination with the radiation energy is least affected, if no information is available on the primary energy, in particular at zenith angles above 60°.

larger distances at the ground for inclined showers, which enables detection with a large spacing between detectors and large instrumented areas become feasible. The detection efficiency of AERA increases with the zenith angle (see Fig. 7.2). Hence, combining AMIGA and AERA data, the transition region of the zenith-angle range in which the radiation energy enhances the mass sensitivity can be investigated and compared to results by the classical method using only the particle numbers. The mass separation power of X_{max} is smaller than that of $\rho_\mu^{600}/\sqrt{S_{RD}^{\rho_\theta}}$ for all zenith angles. However, X_{max} can be measured simultaneously with the same radio detectors and can serve as an independent and complementary mass estimator in combination with $\rho_\mu^{600}/\sqrt{S_{RD}^{\rho_\theta}}$.

The results shown here compare the well established and methodologically sound mass estimator using the particles numbers with a radio observable not yet tuned

for mass estimation. The first proof of principle conducted here illustrates the potential of radio emission measurements to enhance mass estimation in particular for inclined showers. Potentially, the mass sensitivity of the radio emission can even be improved by investigating other radio observables on their mass sensitivity such as the amplitude or energy fluence at a reference distance instead of the integral $\sqrt{S_{\mathrm{RD}}^{\rho_\theta}}$ over the whole footprint. Furthermore, the method of mass estimation via the ratio of the muon density and the radiation energy can be combined with the independent mass estimator X_{max}, inferred as well from the radio emission, to reduce the overall uncertainties on the mass.

CHAPTER 6

Simulation study on detection techniques and reconstruction methods

Contents

The true observables investigated in Chapter 5 derived from air shower simulations are based on pure shower physics. Their variation is due to shower-to-shower fluctuations, only. However, the reconstruction of these observables from measurements is always constrained by measurement uncertainties, which are determined by the detector system. In this chapter the influence of these measurement uncertainties on the mass separation power is investigated. Therefore, the detector responses of the water-Cherenkov detectors and the buried scintillators of AMIGA, and of the radio antennas of AERA are simulated using the Offline software framework as described in Section 4.3.2, including detector uncertainties and measured radio background at the site of the Pierre Auger Observatory. The same air-shower simulation libraries as in Chapter 5 are used. Hence, the results based on the true and the reconstructed

observables can be compared directly to study the impact of detector effects and measurement uncertainties on the mass separation power.

From the simulated signals in the detectors the muon density and the radiation energy are reconstructed as described in Section 4.3.3. The number of muons detected by each scintillator of AMIGA is counted and a lateral distribution function is fitted to these values, yielding the muon density at a reference distance of 600 m. The energy fluence detected by each AERA antenna is determined and a two-dimensional fit of the lateral distribution is used to determine the radiation energy contained in the radio signal.

In the following, suitable cuts on these reconstructed observables are investigated to obtain a high quality event set. The combined uncertainties of the measurement and the reconstruction methods are determined by comparing the true values with the reconstructed values from the detector simulations. Finally, results of this event set on the mass separation power are discussed.

6.1 Quality cuts on reconstructed events

To ensure a high quality event set, the reconstructed events are selected based on the energy and zenith angle range, at which the detectors deliver reliable measurements, and on the reconstruction quality. The reconstruction of the muon density and the radiation energy is based on fits to reconstructed values. To ensure the quality of these fits on each individual event within their measurement and reconstruction uncertainties, the following quality cuts are applied. A preselection on the SD signal is performed, which is passed by around 20 % of the events. Subsequent quality cuts on the radio signal in the single antennas and the two-dimensional fit reject another 40 % of the events. Finally, quality cuts on the MD signal reject some additional outliers, only.

6.1.1 Preselection on the Surface-Detector signal

Reconstructed observables of the Surface-Detector signal such as the arrival direction, the shower core and the primary energy are used as input values for the radio and muon reconstruction. Therefore, quality cuts are applied on these observables. The SD fit of the arrival direction requires at least 3 neighboring stations with signal, which is not true for all simulated showers. Since the infilled array with a spacing of 750 m features a 100 % detection efficiency for energies above $10^{17.5}$ eV and zenith angles below 55° [129], corresponding cuts are applied, removing two third of the events.

6.1.2 Selection on the radio signal

The reconstruction of the arrival direction from the radio signal requires a minimum of 3 radio stations with signal. A station is considered a signal station if the ratio of the squared signal S (maximum amplitude) and noise N (squared RMS of the

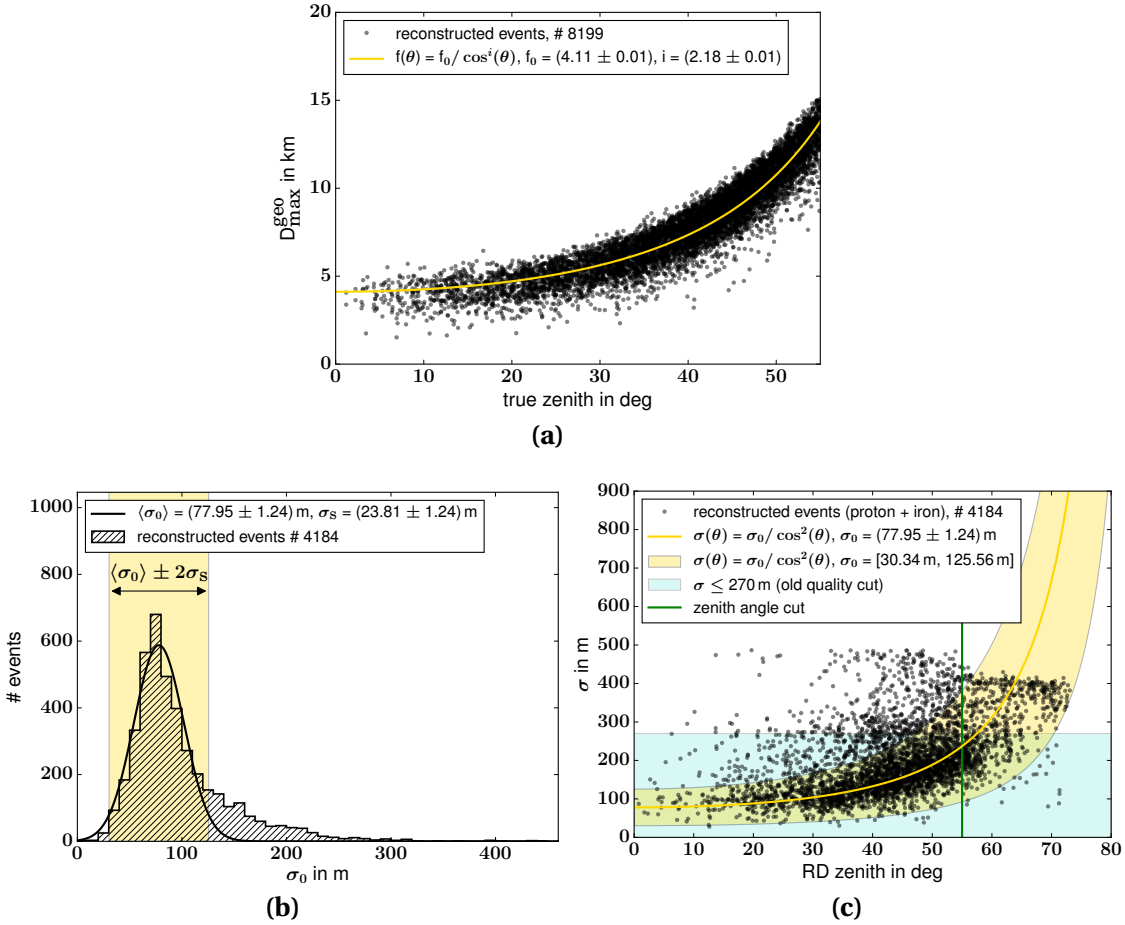

Figure 6.1: Zenith angle dependent cut on the width of the radio footprint The width of the radio footprint changes with the distance to $X_{\max}$. **(a)** The distance to $X_{\max}$ plotted over the true zenith angle for all simulated events up to 55°. The dependence on the zenith angle is fitted to $1/\cos^i\theta$ with $i = 2.18$, which is approximated to 2 for the definition of the cut on σ. **(b)** For all reconstructed events surviving former cuts (see Table 6.1, the cuts on the energy and zenith angle are not applied), the footprint width is normalized to $\theta = 0$. A Gaussian distribution is fitted to the resulting histogram of $sigma_0$. Events outside of 2 standard deviations of the Gaussian fit σ_S are discarded. **(c)** The footprint width is plotted over the zenith angle. The cut limits derived by the Gaussian fit is folded into the distribution and the resulting area of included events is shown in yellow. For comparison, the inclusion area of a zenith angle independent cut used in previous analyses is shown in blue.

field strength in a defined noise window of the signal time series) is $\frac{S^2}{N^2} \geq 10$. To validate the direction reconstruction, the directions reconstructed from the SD and the RD signal are compared. Events with an angular difference much larger than the resolution of 1° – 2°, i.e. $|\Omega_{\mathrm{SD}} - \Omega_{\mathrm{RD}}| > 5°$ are discarded.

2d-LDF fit

To reconstruct the radiation energy E_{rad} of an event, the two-dimensional LDF fit described in Eq. (4.10) is used. Therefore, only events with a converged fit contain information about the radiation energy. The fit is repeated 1000 times to validate its robustness, varying the input energy fluences of the antennas inside their uncertainties. If the fit converges less than 500 times, the event is discarded. In addition, the Chauvenet criterion is applied on the χ^2 probability p of the fit. According to this criterion, all events are considered outliers and discarded for which $p \cdot n < 0.5$, with the number of events $n = n_{\mathrm{P}} + n_{\mathrm{Fe}}$ after preselection by former cuts. For this event set, the limit on the χ^2 probability is 2.6×10^{-4}.

The parameter σ of the 2d-LDF fit is a measure of the width of the radio footprint in the plane perpendicular to the shower axis. The radio emission is emitted in a forward beamed cone, so that the width of the footprint changes with the geometric distance to the radiation source X_{max}. In Fig. 6.1a this distance $D^{\mathrm{geo}}_{\mathrm{max}}$ is plotted over the zenith angle for all simulated showers up to 55°. It changes with the zenith angle by $1/\cos^i\theta$ with $i = 2.18 \pm 0.01$, which is approximated to 2 in the following. A zenith angle dependent cut on σ is defined in the form of the function

$$\sigma(\theta) = \sigma_0 \cdot \frac{1}{\cos^2\theta} \quad , \tag{6.1}$$

where the parameter σ_0 reflects the footprint width of a shower, if it were arriving at a zenith angle of 0°. σ_0 is calculated for all reconstructed events surviving all former cuts by

$$\sigma_{0,\mathrm{rec}} = \sigma(\theta)_{\mathrm{rec}} \cdot \cos^2\theta \quad , \tag{6.2}$$

where $\sigma(\theta)_{\mathrm{rec}}$ is the reconstructed value from the two-dimensional LDF fit. For determining a cut on the allowed range of $\sigma_{0,\mathrm{rec}}$, no cut on the energy and the zenith angle is applied to avoid boundary effects. The histogram of the results is shown in Fig. 6.1b. The footprint width is expected to vary due to shower-to-shower fluctuations as well as measurement and reconstruction uncertainties. A Gaussian is fitted to the histogram, resulting in a $\langle\sigma_0\rangle = (77.95 \pm 1.24)\,\mathrm{m}$. Values not following the Gaussian distribution are expected to be results from falsely reconstructed 2d-LDF fits. Thus, a cut on twice the standard deviation $\sigma_{\mathrm{s}} = (23.81 \pm 1.24)\,\mathrm{m}^2$ is applied around $\langle\sigma_0\rangle$. These cut limits are folded into Eq. (6.1). The resulting inclusion area is shown in Fig. 6.1c in yellow together with all events and the fit for the mean σ_0 from the Gaussian fit. This cut is compared to a cut independent on the zenith angle of $\sigma \geq 270\,\mathrm{m}^2$, as used in former works [178]. A population of outlier events with a σ above 400 m is cut reliably by the combination of the defined cut and a cut on the zenith angle above 55°.

6.1.3 Selection on the muon signal

For the reconstruction of the muon density ρ_μ^{600} at the axis distance of 600 m the lateral distribution function described in Eq. (4.6) is used. Hence, only events with a converged fit are considered in the analysis. The fit results are validated in a similar way as done for the radio 2d-LDF fit by discarding events with a χ^2 probability of the fit of less than $1/[2(n_\mathrm{P} + n_\mathrm{Fe})]$, which removes about 2 % of the events.

6.1.4 Set of events after quality cuts

In Table 6.1 the applied cuts are summarized and the resulting numbers of events after each cut are shown. For 65 % of the events, the reconstruction of the shower direction and energy from the SD signal is successful. However, only 34 % of these events are in the energy and zenith angle range of interest. Another 37 % of these events are discarded mostly due to an insufficient quality of the radio 2d-LDF fit. The energy, zenith angle and direction distribution of the resulting 1478 events are shown in the Fig. 6.2. The proton and iron induced events show the same distributions and no composition bias due to any of the cuts is observed. Less events are observed from the north (azimuth angle $\varphi = 90°$) since these events arrive almost parallel to the geomagnetic field $\mathrm{B}_\mathrm{Earth}$ and the geomagnetic radio emission becomes small. This effect is already present in the initial simulation set, which reproduces real events measured by AERA (see Fig. 4.2d).

In Fig. 6.3 an example event simulated once for a proton and once for an iron nucleus as primary particle is shown. The input values are the same, i.e. corresponding to the same measured event, besides the primary particle. The same event as reconstructed from data is shown in Fig. D.3.

Table 6.1: Number of events surviving the cuts applied to the $\overline{\text{Off}}\underline{\text{line}}$ reconstruction of simulated proton and iron showers including detector uncertainties and realistic radio background.

cut	# P events	# Fe events	# shared events
simulated showers	5302	5302	5302
SD reconstruction successful	3292	3643	2971
SD reconstructed zenith angle $\leq 55°$	2903	3108	2613
SD reconstructed energy $\geq 10^{17.5}$ eV	1048	1286	964
RD reconstruction successful	845	1100	781
$\lvert\Omega_{\text{SD}} - \Omega_{\text{RD}}\rvert \leq 5°$	821	1071	749
RD 2d-LDF fit converged and robust	818	1063	745
$\chi^2_{\text{2d-LDF}}$ probability $\geq 1/[2(n_{\text{P}} + n_{\text{Fe}})]$	746	1014	655
$\sigma(\theta) = \sigma_0/\cos^2(\theta)$, $\sigma_0 = [73.8\,\text{m}^2, 23.1\,\text{m}^2]$	672	858	545
$\sigma(E_{\text{rad}})/E_{\text{rad}} \leq 1$	644	806	512
MD-LDF fit converged	644	806	512
$\chi^2_{\text{MD-LDF}}$ probability $\geq 1/[2(n_{\text{P}} + n_{\text{Fe}})]$	636	786	493
$\sigma(\rho_\mu^{600})/\rho_\mu^{600} \leq 1$	**636**	**786**	**495**

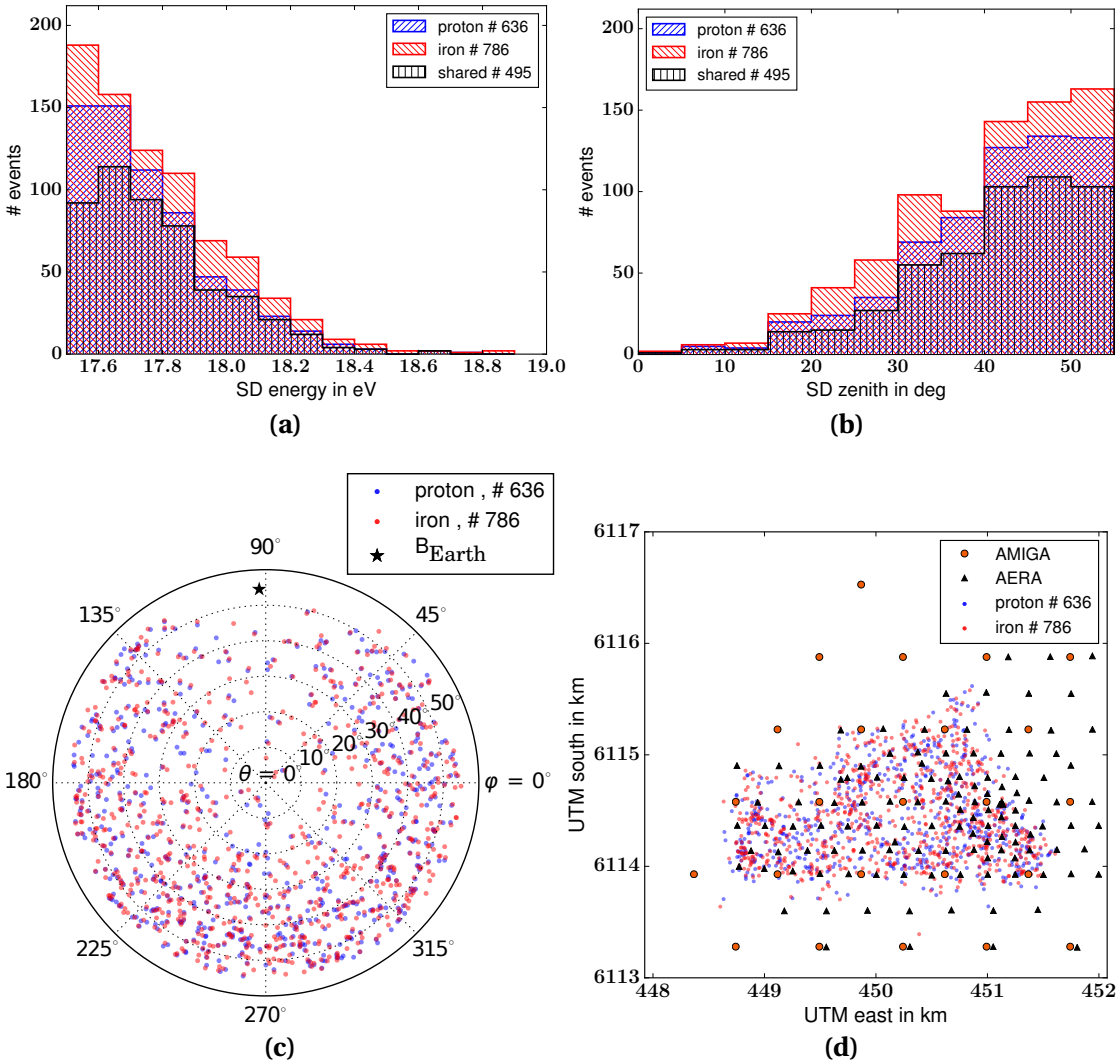

Figure 6.2: Event set surviving the quality cuts **(a)** Primary energy, **(b)** zenith angle, **(c)** arrival direction and **(d)** core distribution. All observables are reconstructed from the Surface-Detector signal. The asymmetry in the arrival directions occur due to the geomagnetic field in the north. If the arrival direction is close to parallel to B_{Earth}, the geomagnetic radio emission is small and less events pass the detection threshold.

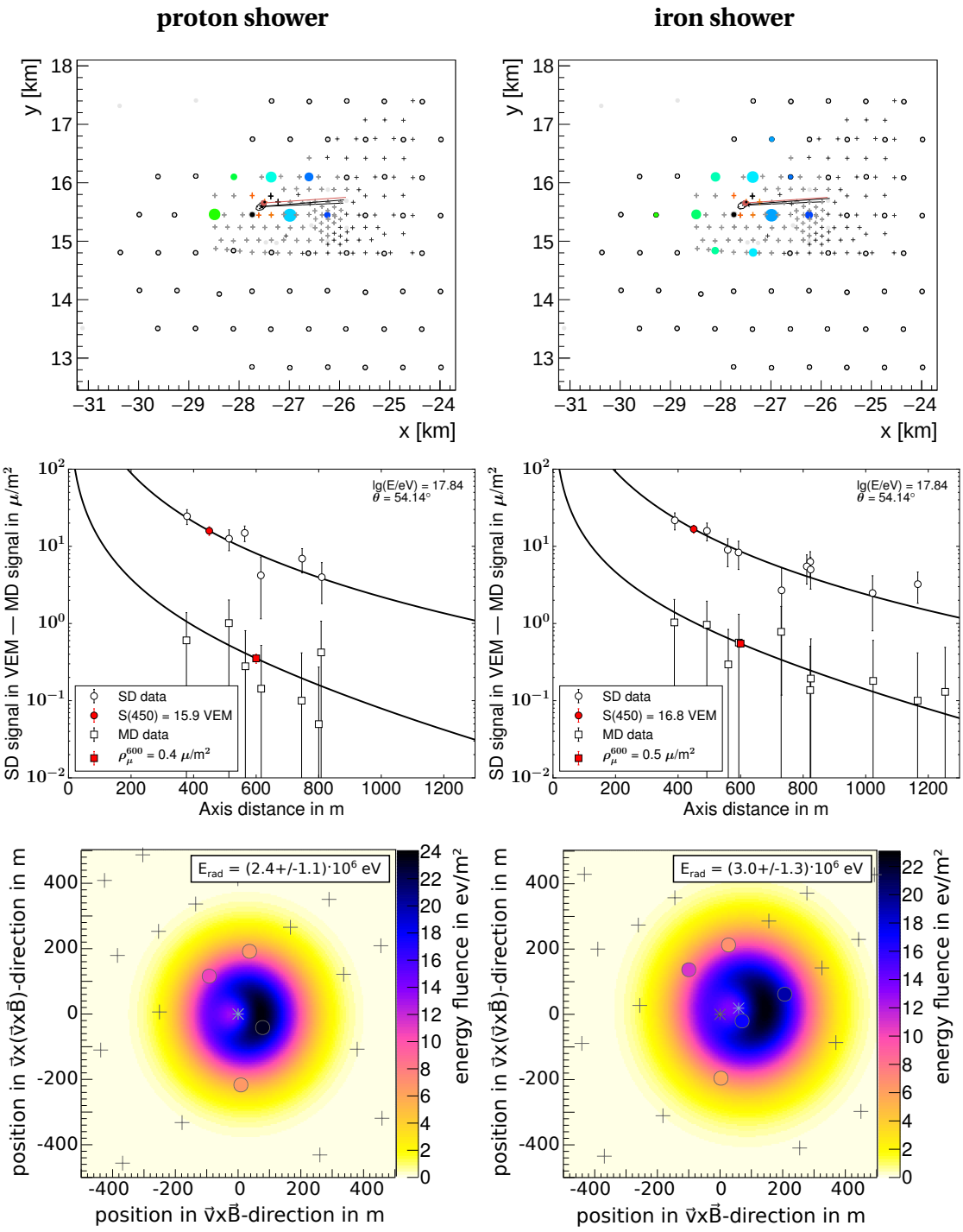

Figure 6.3: Simulated example event with proton and iron primary The proton (left panels) and iron (right panels) events are simulated with the same input values, i.e. corresponding to the same measured AERA event. **(a)-(b)** Event map of the Surface Detector stations and the Radio Detector. The size of the circles (SD) and crosses (RD) depict the signal strength, and the colors the detection time (blue/yellow = early, green/red = late). Grey and black stations don't have a signal or are rejected. **(c)-(d)** The one-dimensional LDF fit to the signal in the SD as well as in the MD. **(e)-(f)** The two-dimensional LDF fit to the energy fluence measured in the RD.

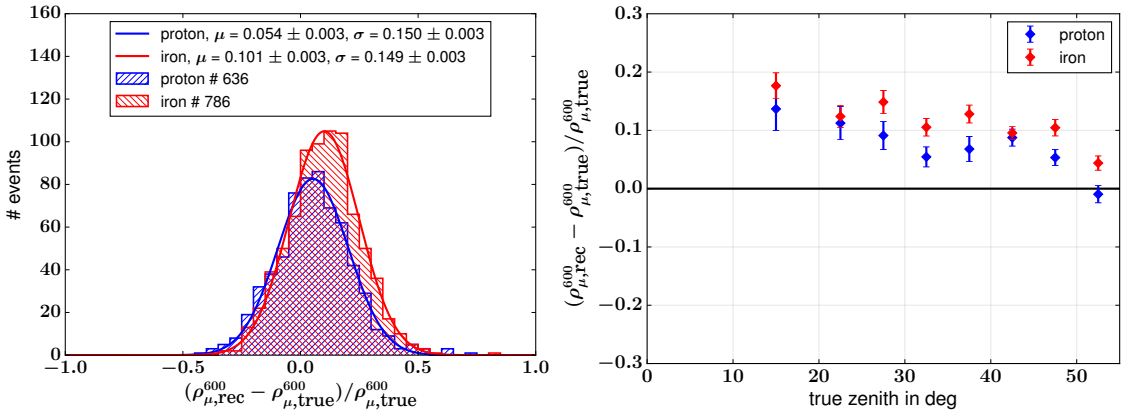

Figure 6.4: Reconstruction uncertainty of the muon density (a) The reconstructed muon density is overestimated compared to the true muon density for both, proton and iron showers. Hence, the sharp energy threshold of 1 GeV applied to the simulations when determining the true values removes slightly more muons than detected by the MD. Iron showers show a larger offset of 10 % to the true muon density than proton showers with 5 %. This indicates a larger fraction of low-energy muons in iron showers which are on average older than the proton showers, when they reach the ground. **(b)** The overestimation decreases with the zenith angle. The amount of soil the muons penetrate until reaching the buried scintillators increases with the zenith angle and thus the energy threshold of the detector is slightly higher for inclined showers. The uncertainty on the mean values is a combination of measurement and reconstruction uncertainties ($\sigma/\sqrt{N}$).

6.2 Reconstruction uncertainties

The uncertainties and possible biases on measurements under realistic conditions and on the reconstruction of the muon density, the radiation energy and the cosmic ray energy reconstructed from the Surface Detector signal are investigated. Therefore, these observables are compared to the true values derived directly from the shower simulation for those events passing all quality cuts.

6.2.1 Muon density

The relative difference between the true and the reconstructed muon density is shown in Fig. 6.4a. For the true muon density all muons above 1 GeV are considered, which corresponds to the approximate detection threshold of the buried scintillators of AMIGA. The reconstructed muon density is on average overestimated by (5.4 ± 0.3) % for proton showers and (10.1 ± 0.3) % for iron showers. However, the intrinsic bias on the zenith angle due to the corner clipping effect is already corrected. This shows that the energy threshold of the AMIGA shower is not exactly 1 GeV, but on average a bit lower. Furthermore, the energy threshold depends on the amount of soil the

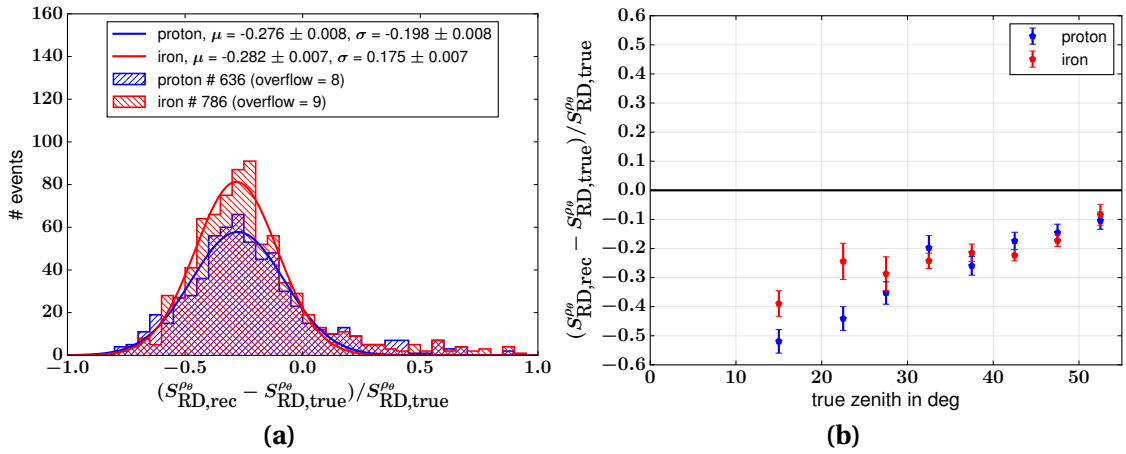

Figure 6.5: Reconstruction uncertainty of the radiation energy (a) The radiation energy is underestimated by about 28 % compared to the true radiation energy calculated from the electromagnetic shower energy. The offset is the same for proton and iron induced air showers. Hence, there is no bias on the particle type. For 17 events the offset is above a value of 1, and they are not shown here. **(b)** The offset decreases with the zenith angle. The error-bars depict the uncertainty on the mean of $\sigma/\sqrt{N}$.

muons penetrate until reaching the buried scintillator. This amount of soil increases with the zenith angle of each muon and hence on average with the zenith angle of the shower. Thus, the energy threshold increases with the shower zenith angle and the offset of the reconstructed muon density decreases, as shown in Fig. 6.4b.

Iron showers show a larger offset than proton showers for all zenith angles, which implies a detection bias on the mass of the primary particle. This indicates, that iron showers contain a larger fraction of muons below 1 GeV than proton showers. Iron showers develop earlier in the atmosphere and are older, when they arrive at the ground. Hence, more low-energy muons were created. This small composition-dependent reconstruction bias increases the mass separation power by the muon density.

The standard deviation of the relative difference between the reconstructed and the true muon densities is 15 % for both primary particle types and depicts the combined statistic uncertainty of the measurement and reconstruction of the muon density.

6.2.2 Radiation energy

The reconstructed radiation energy E_{rad} is corrected for the angle between the shower axis and the Earth's magnetic field as well as for the atmospheric density at the mean X_{max} depending on the zenith angle by Eq. (5.7). However, no correction for the clipping of the shower is applied, which is relevant for showers up to 50° zenith angle and is in the order of up to 10 % of the radiation energy. The true radiation energy $S^{\rho_\theta}_{\mathrm{RD}}$ at the ground is calculated from the electromagnetic shower energy by Eqs. (5.6)

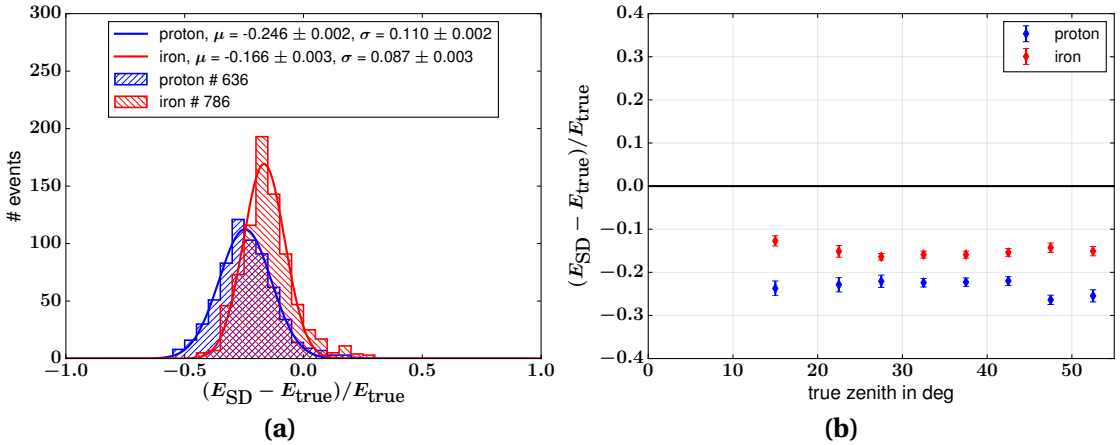

Figure 6.6: Reconstruction uncertainty of the primary energy from the SD signal **(a)** The primary energy is underestimated for both proton and iron showers due to the discrepancy of the hadronic models to measurements. For proton showers smaller energies are reconstructed since they contain less muons than iron showers, which produce the bulk of the signal in the Surface Detector. **(b)** The underestimation shows no dependence on the zenith angle. The error-bars depict the uncertainty on the mean of $\sigma/\sqrt{N}$.

to (5.8), including the effect of clipping the shower at the observation level. The relative difference between the reconstructed and the true radiation energy is shown in Fig. 6.5a. The reconstructed radiation energy is on average underestimated by about 28 % for both, proton and iron showers. The offset decreases with the zenith angle, as shown in Fig. 6.5b.It is caused by the superposition of various analysis steps during the event reconstruction, such as cutting a part of the energy contained in the signal when suppressing noise. These effects were studied and are understood, as discussed in Appendix C. The offset is the same for proton and iron and therefore does not influence the mass separation power. The standard deviation of $S_{\mathrm{RD}}^{\rho_\theta}$ is 19 %, which represents the combined statistical uncertainty on the measurement and reconstruction of the radiation energy. In particular the effect of background is included, since real measured radio background was added to the simulations. No bias on the particle type of the uncertainty and the offset is observed.

6.2.3 Cosmic-ray energy reconstructed from the Surface-Detector signal

The relative difference between the true and the reconstructed primary energy is shown in Fig. 6.6a. The reconstructed primary energy is underestimated for both proton and iron showers. This is caused by the fact, that the hadronic interaction models predict less muons than observed in the experiment (see Section 2.2.3). The Surface Detector is most sensitive to the muonic component of the shower and

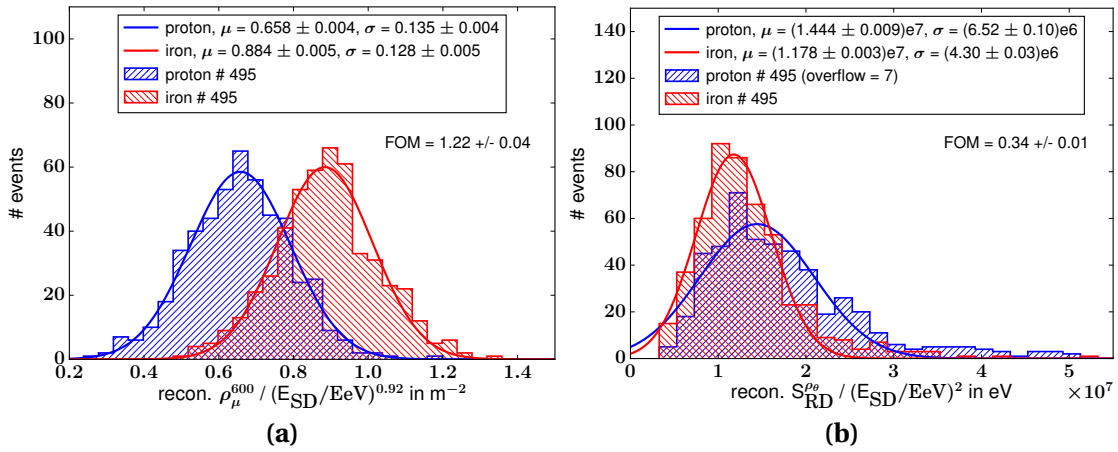

Figure 6.7: Mass separation power of reconstructed observables combined with the SD energy (a) The muon density normalized by the reconstructed primary energy from the SD signal shows a figure of merit of 1.22. As expected, the muon density is larger by about 35 % for iron showers. **(b)** The radiation energy normalized by the SD energy is larger by about 20 % for proton showers. Due to the large spread the merit factor results in only 0.34, i.e. the combination of the radiation energy and the SD energy is not suited for mass separation.

therefore affected by this discrepancy. The bias does not depend on the zenith angle, as shown in Fig. 6.6b. Moreover, the offset to the true energy is larger for protons by 8 %. This indicates a mass dependent reconstruction bias on the primary energy. Proton air showers feature less muons than iron showers of the same energy. Therefore, the signal in the detectors is smaller for proton showers, which influences the reconstruction of the primary energy. The energy is reconstructed from the signal size at a reference distance, at which this bias is minimal. However, in Fig. 6.6a it is shown that the remaining bias is not negligible. Thus, the mass separation power of the muon density is reduced, when normalized by the SD energy. The radiation energy instead, which is an estimator for the primary energy, too, does not feature a mass dependent reconstruction bias. Hence, the mass separation power of the muon density is increased when combined with the radiation energy.

6.3 Mass sensitivity of the reconstructed observables

To investigate the mass separation power of the reconstructed observables only 'shared' events, surviving the quality cuts for both a proton and an iron nucleus as primary particle, are considered in the following. The muon density and the radiation energy of these events are normalized by the primary energy reconstructed from the SD signal in Figs. 6.7a and 6.7b. For both, the correlation with the primary energy

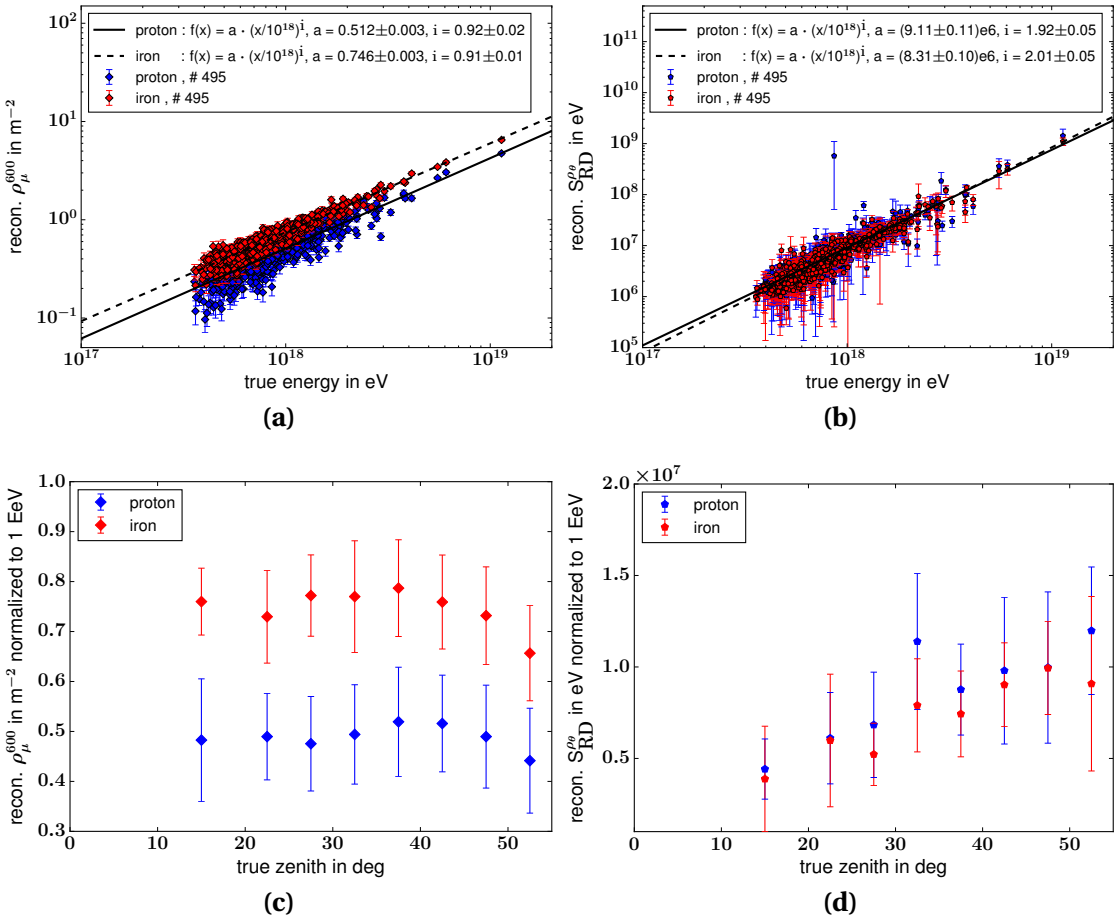

Figure 6.8: Energy and zenith angle dependence of reconstructed observables All dependencies are in accordance with the true observables investigated in Chapter 5. **(a)** The muon density grows with the energy with a mean index of 0.912 ± 0.015 in agreement with the true number of muons in Section 5.1.1. **(b)** The radiation energy shows a dependence on the energy with an index of 1.962 ± 0.053 compatible to [118]. **(c)** The muon density decreases at angles above 45° due to muon decay in the atmosphere. **(d)** The radiation energy increases with the zenith angle due to the increasing travel distance of the air shower, at which this energy is released, and due to clipping of the shower below 50°. (Error-bars depict the standard deviation to the mean.)

derived in Chapter 5 is applied for normalization, using the energy reconstructed from the SD. Combining the reconstructed muon density with the SD energy, both including measurement and reconstruction uncertainties, results in a figure of merit of 1.22 for mass separation, with a higher signal for iron showers by on average 35 %. The radiation energy shows a mass sensitivity of a figure of merit of only 0.34 with on average a 20 % higher signal for proton showers.

The energy and zenith angle dependencies of the reconstructed observables are shown in Fig. 6.8. The muon density grows with the energy with an average index for proton and iron showers of 0.912 ± 0.015 (see Fig. 6.8a), which agrees with the mean index of 0.923 ± 0.003 for the true values (see Section 5.1.1) within the uncertainties. The radiation energy shows an increase with the energy with an average index of 1.962 ± 0.053 (see Fig. 6.8b). This is in agreement with the energy dependence of the radiation energy found in AERA with an index of 1.98 ± 0.04 [118]. Hence, no energy dependent reconstruction bias can be observed for both observables. The observables were normalized according to their energy dependence and the mean values are shown over the zenith angle in Figs. 6.8c and 6.8d. The muon density is constant within the uncertainties up to a zenith angle of 45° and then decreases. This was already observed for the true values (see Fig. 5.1b) and is caused by muon decay, which has a growing impact for showers above this angle. The difference between proton and iron showers is constant over the zenith angle and larger as the standard deviations around the means. The radiation energy grows with the zenith angle, which is in accordance with the behavior observed for the true radiation energy in Fig. 5.6. This growth is mainly caused by the longer distance in units of atmospheric depth the shower travels up to the ground, at which more radiation energy is released. In addition, for showers with zenith angles up to 50°, the showers are not fully developed when reaching the ground and hence 'clipped'. No difference can be observed between proton and iron showers within the uncertainties.

To investigate the combination of these MD and RD observables, the muon density is plotted over the radiation energy in Fig. 6.9a. An orthogonal distance regression fit including reconstruction uncertainties is performed to derive the correlation between these two observables. Both proton and iron showers show a correlation compatible with the square root of the radiation energy (mean index i = 0.49), which is in accordance to the results for the true values derived in Fig. 5.8a. Therefore, the ratio of the muon density and the square root of the radiation energy is used in the following. A difference of 0.04 in the indices of the fits to the proton and iron showers indicates a decrease of the mass separation power towards higher energies for measurements at the observation level of AMIGA and AERA. However, the energy range where the proton and iron lines would cross has not been investigated in this thesis. The histogram of this ratio is shown in Fig. 6.9b. The mass separation power represented by the figure of merit results in 1.25 for the full zenith angle range of 0 – 55°.

Figure 6.10a shows the mean ratio for zenith angle bins of 5° (below 20° zenith angle the bin width is chosen to 10° due to the low number of events). The ratio shows a similar behavior than the true ratio (see Fig. 5.9). However, the ratio is larger

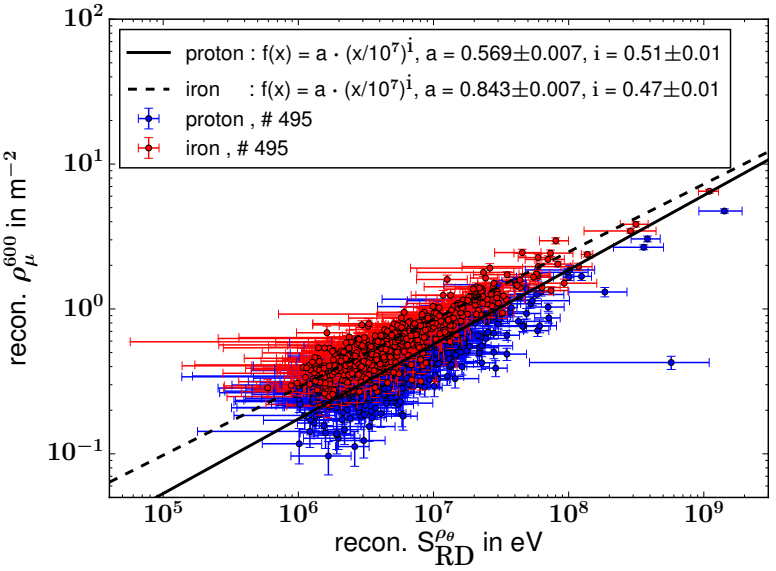

(a)

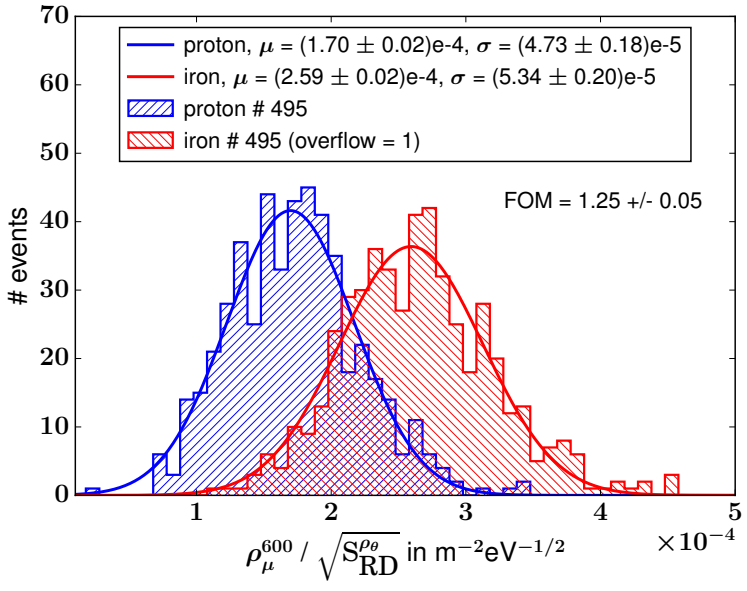

(b)

Figure 6.9: Correlation between the muon density and the radiation energy (a) Muon density plotted over the corrected radiation energy. A weighted power-law fit is performed using an orthogonal distance regression. The fit results in an index of about 0.51, which is compatible to the square root of the radiation energy. **(b)** Histogram of ratio of muon density and square root of radiation energy. The mass separation power represented by the figure of merit results in 1.25.

by about 35 percent due to the slight overestimation of the muon density and the underestimation of the radiation energy in the simulations including detector effects (see Fig. 6.4a and Fig. 6.5a). The figure of merit is determined for the different zenith angles and shown in Fig. 6.10b. For comparison, the true values for this ratio shown in Fig. 5.10 and the reconstructed muon density normalized by the SD energy are plotted in addition. As expected, the figure of merit of the true values is larger, on average by 0.5. The true values neglect the uncertainties emerging from the detection technique, the reconstruction method and the background, which reduce the figure of merit. The reconstructed muon density normalized by the SD energy features a slightly larger mass separation for vertical showers, but decreases for larger zenith angles. For angles above 40° the radiation energy exceeds the mass separation power compared to the SD energy for reconstructed values. Hence, the uncertainties on the measurements and the reconstruction of the observables have a higher impact on the mass separation power using the SD energy than the radiation energy.

This results emphasize the radiation energy as a promising alternative for mass composition studies of inclined showers compared to classical methods using the muon density normalized by the energy measured by particle detectors. In particular, the combination of the AMIGA Muon Detector with AERA shows a comparable mass sensitivity as the combination of the SD and MD of AMIGA, over the whole zenith angle range of 0 – 55°. In addition, the reconstruction of the energy by the well established Surface Detector features a bias on the primary mass, which reduces the mass sensitivity. On the contrary, the novel radio detection method by AERA features the potential to be further improved on the mass sensitivity by investigating other radio observables or enhancing the reconstruction of the radiation energy from the radio footprint.

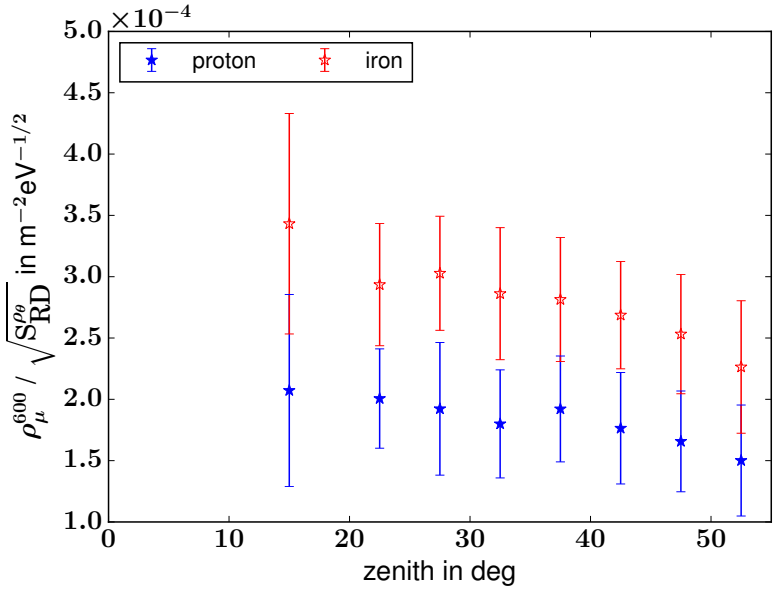

(a)

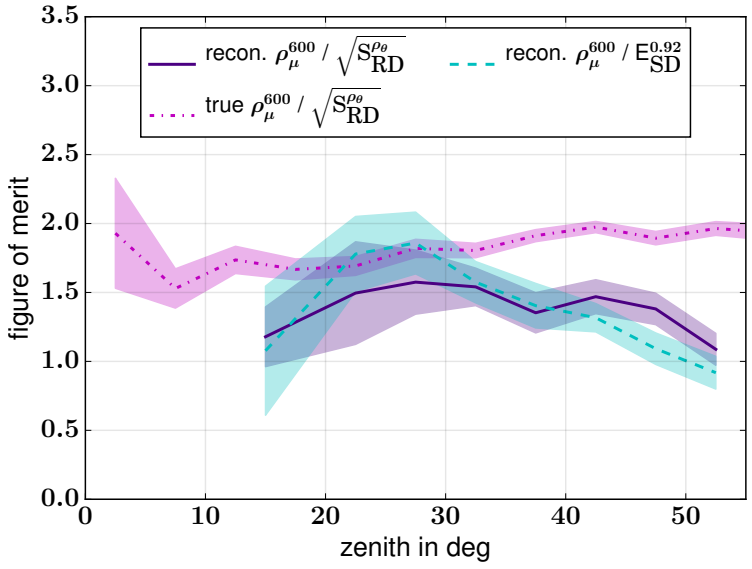

(b)

Figure 6.10: Zenith angle dependence of the ratio between the muon density and the square root of the radiation energy (a) The ratio including the detector simulation shows a similar behavior as for true values (see Fig. 5.9). However, the absolute values are larger by about 35 percent due to the reconstruction biases on the radiation energy as well as on the muon density. **(b)** The figure of merit is decreased for the reconstructed ratio of the muon density and the radiation energy by about 0.5 compared to the true values due to additional uncertainties arising from the detection technique, the reconstruction method and the added radio background. Using the SD energy instead of the radiation energy, the mass separation power is enhanced slightly at small zenith angles, but decreased towards larger zenith angles.

CHAPTER 7

Analysis of coincident AMIGA and AERA measurements

Contents

The combination of the radio emission with the size of the muonic component of air showers features a large mass separation power for all zenith angles, as shown in the simulation studies. In Chapter 5 the general mass separation power was investigated based on true observables of air-shower simulations. It was found to be approximately constant over the whole zenith angle range, which makes it superior to mass estimators based on the ratio of the number of muons and electrons, in particular at zenith angles above 40°. In fact, the mass separation power is even slightly enhanced for the zenith angle range of 35 – 55°, which coincides with the range of the largest combined efficiency of the AMIGA and AERA detectors of the Pierre Auger Observatory. In Chapter 6 this was tested by applying the detector responses of the AMIGA and AERA detectors to the simulations and adding measurement uncertainties. The mass separation power was found to be sufficient for the whole zenith angle range up to 55°, where the AMIGA detectors show a 100 % detection efficiency. Therefore, the analysis is performed on measured data of AMIGA and AERA in this chapter.

For this analysis of measurements, the same reconstruction pipeline of $\overline{\text{Off}}\underline{\text{line}}$ is applied as for the air-shower simulations (see Section 4.3.3). The events are selected by applying the quality cuts derived in Section 6.1. First, an overview of the resulting event set is given. Then, the correlation of the muon density to the radiation energy is compared to the results for proton and iron showers from the simulations. A slight trend towards a lighter composition is observed for increasing energies in the range $3 \times 10^{17} - 2 \times 10^{18}$ eV below the ankle, which is in accordance to results from the X_{max} measurements of the Fluorescence Detector of Auger. This confirms the potential of combining muons and radio for mass estimation. Based on this, more accurate mass composition measurements can be performed as soon as more statistics of the data is available.

7.1 Data set: detector configuration and event statistics

More than three years of combined data of AERA and the Surface Detector and Muon Detector of AMIGA have been analyzed, from the 2nd June, 2013 to the 17th October, 2016. Because there are engineering arrays, the configuration of both AERA and the Muon Detector of AMIGA were modified during this time period. Since the 2nd June, 2013, AERA124 is fully deployed and data is recorded of its 124 radio antenna stations. In March, 2015, another 25 radio antenna stations were deployed, building AERA153 (including as well 4 prototype stations not used in this work). The Unitary Cell of AMIGA, consisting of seven muon detectors arranged in a hexagon, was deployed in various steps and is fully equipped since March, 2015. All muon detectors are calibrated since 20th October, 2015. Therefore, the data is divided into two sets with the time periods before and after this date. The Muon Detector is triggered by the Surface Detector so that for all MD events SD data is available in addition. AERA is triggered by the SD, the FD and self-triggered. However, here, only events triggered from SD are used, for which SD data is available in addition.

The data was reconstructed using the $\overline{\text{Off}}\underline{\text{line}}$ reconstruction pipeline from Section 4.3.3, and quality cuts derived in Section 6.1 were applied. The resulting number of events recorded by the Radio Detector and the Muon Detector in combination with the Surface Detector, as well as the combination of events recorded simultaneously by all three detectors is shown in figure Fig. 7.1. Time periods without any events in one or several detector types indicate that the detectors were shut down due to maintenance work or bad weather periods. When long periods with cloudy weather appear (mainly occurring between March and May), the solar panels do not produce enough power during the day to charge the batteries for the night. In such occasions the detectors were turned off to avoid a deep discharge.

The Radio Detector measured on average 15 events per week. It measured more events than the Muon Detector (~10 per week) since it covers a larger detection area. Only MD events with the shower core inside the Unitary Cell are considered. Furthermore, the mean rate of MD events is decreased to ~8 per week for the calibrated

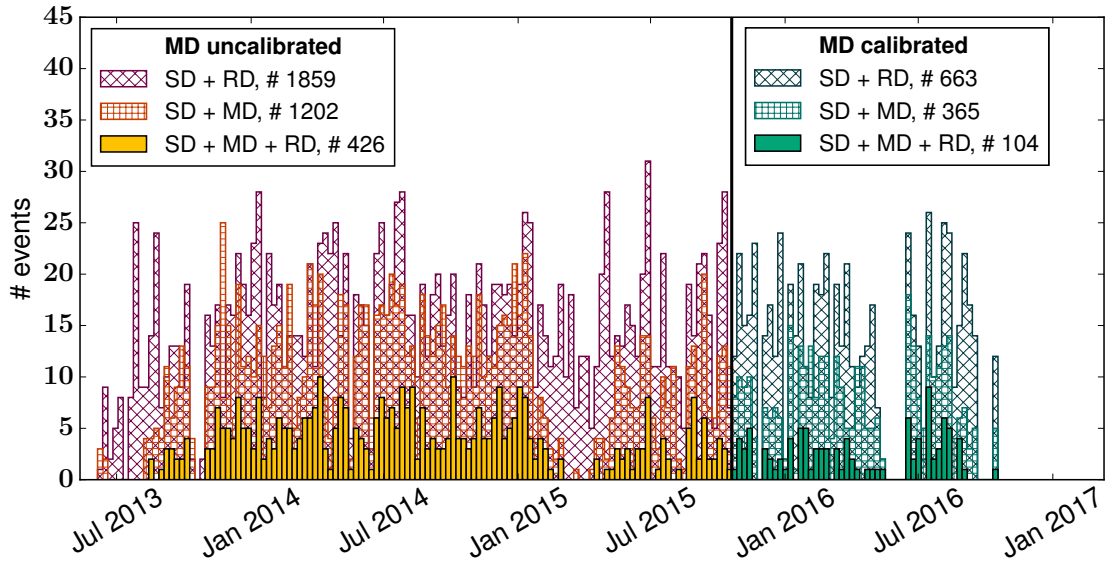

Figure 7.1: Calender of measured coincident events More than 3 years of MD and RD data has been recorded in coincidence from the 2nd June, 2013 to the 17th October, 2016. For the last 302 days (starting 20th October, 2015) the muon counters of MD were calibrated and provided high quality data. In various weeks one or several detector types were shut down due to maintenance work or bad weather periods. With the RD on average more events were measured, since it covers a larger detection area.

period. Before this period, on average 4 events were measured in coincidence with RD and MD and afterwards on average 2.5.

The distribution of the energy and the zenith angle for the events recorded before and after the Muon Detector was calibrated are shown in Fig. 7.2. The parameters are reconstructed from the SD signal. All distributions show the same behavior for both data sets. The number of events decreases with the energy due to the reduced flux of cosmic rays. Thereby, the number of RD events decrease slower. This indicates that the RD reaches its full efficiency at higher energies, so that the energy distribution can be understood as combined effect of the detector efficiency and the cosmic-ray energy spectrum. In contrast, the SD and MD reach full detection efficiency at $10^{17.5}$ eV and the energy distribution corresponds to the cosmic-ray flux. The highest energetic event, which was detected in coincidence by RD and MD, features a reconstructed primary energy of 6.1×10^{18} eV.

The detection efficiency of RD increases with the zenith angle due to the enlarged lateral distribution of the radio signal. In addition, with increasing zenith angle, the solid angle spanned by the full azimuthal range increases and thereby the cosmic-ray flux, assuming an isotropic flux over the whole sky. Therefore, the number of events increases sharply with the zenith angle for the RD. In contrast, the effective detection area of the plane scintillators of the MD decreases for more inclined showers. Therefore, the number of events peaks at around 40° and decreases for higher zenith angles. Overall, the number of coincident events increases with the zenith angle,

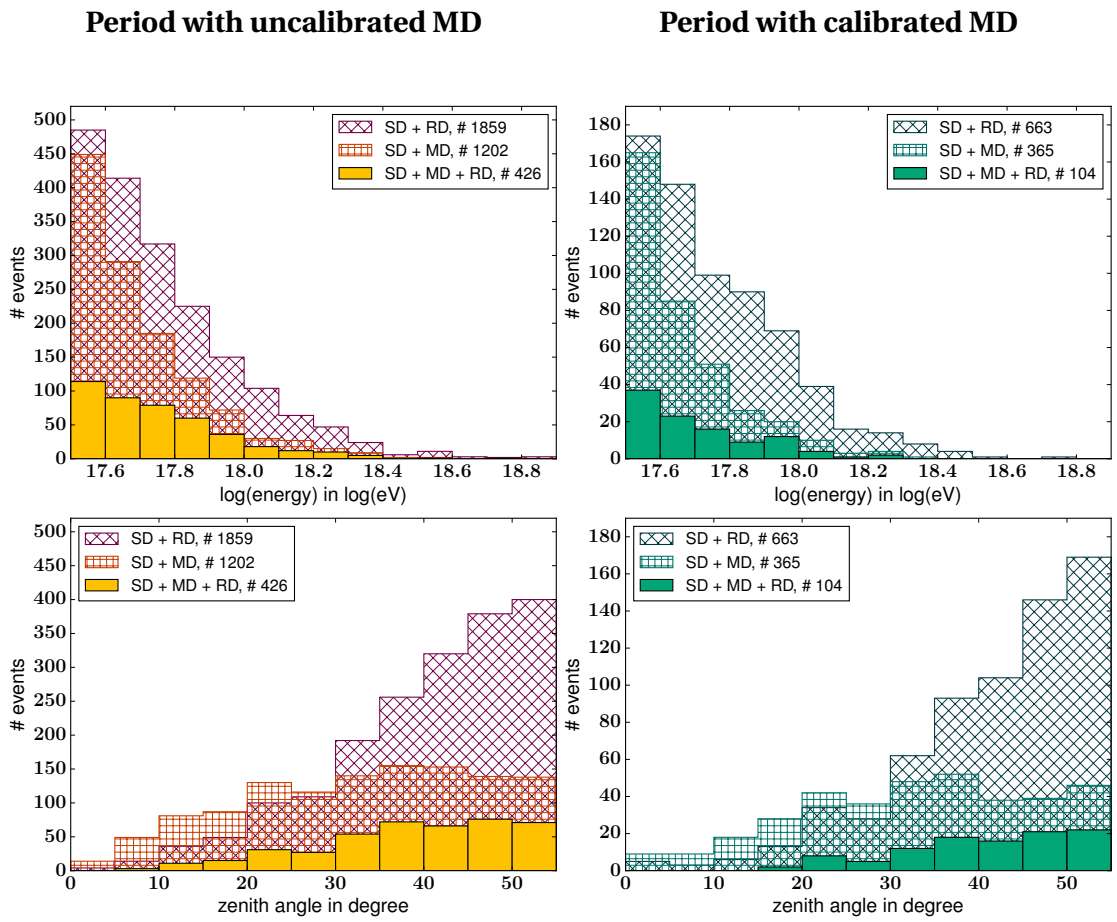

Figure 7.2: Energies and zenith angles of measured coincident events The left and right panels show the distributions for the time periods with uncalibrated and calibrated MD, respectively. The distributions of the primary energies and the zenith angles are shown, as reconstructed from the SD signal. **(a)-(b)** The number of events decreases with increasing energy due to the decreasing flux of cosmic rays. This is independent on the detector type. **(c)-(d)** AERA shows an increased efficiency for air showers with larger zenith angles due to their large radio footprint. The efficiency of the MD peaks at around 40°. Thus, about 80 % of the coincident events of MD and RD feature zenith angles between 30 – 55°.

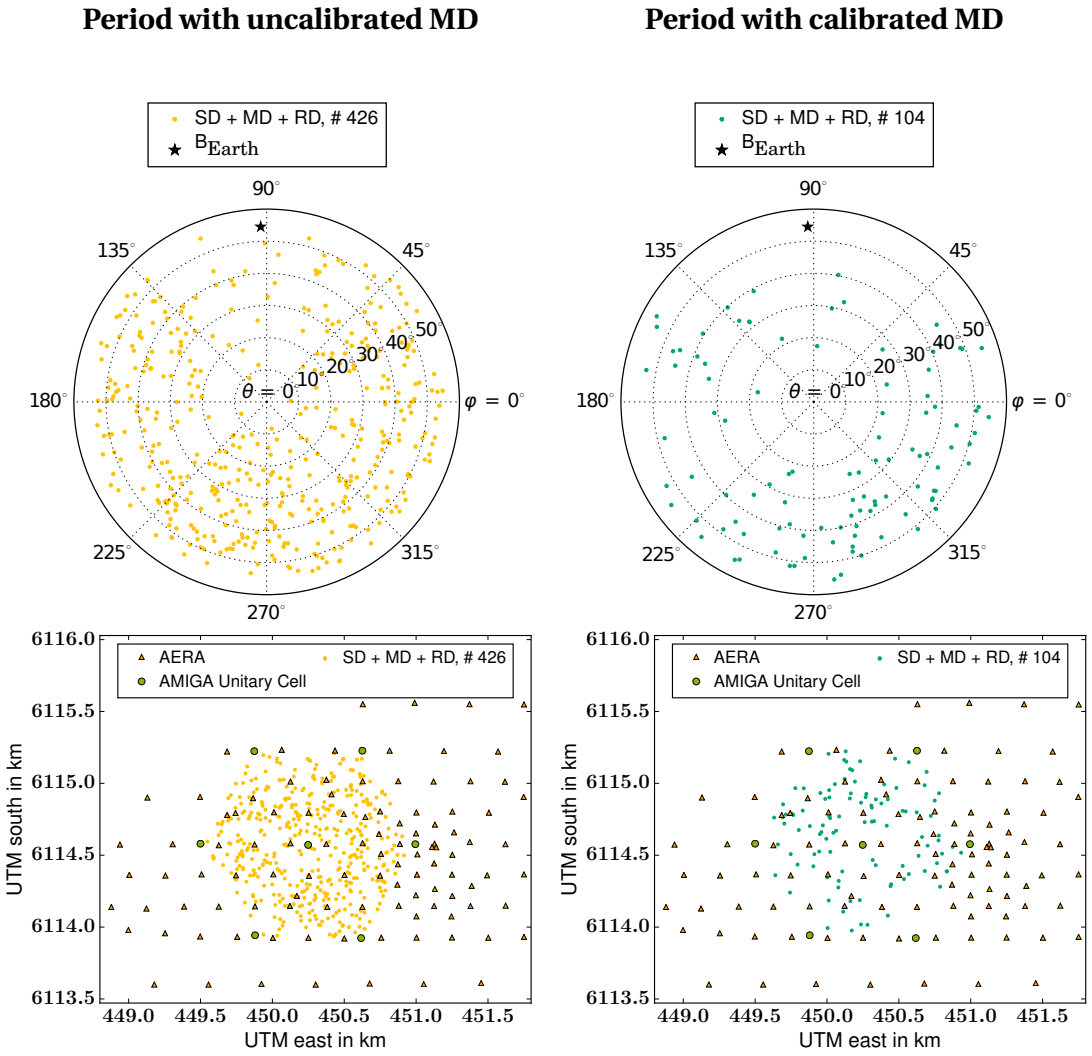

Figure 7.3: Arrival directions and shower cores of measured coincident events (e)-(f) The distribution of the arrival directions shows a north-south asymmetry due to the angular dependency of the geomagnetic radio emission. If the arrival direction is close to parallel to B_{Earth}, the geomagnetic radio emission is small and less events pass the detection threshold of AERA. **(g)-(h)** Only events with a shower core within the AMIGA Unitary Cell are considered. The shower cores are approximately equally distributed over the Unitary Cell.

however less sharply as for the RD alone. The event featuring the smallest zenith angle arrived from $\theta = 7.7°$.

The distributions of the arrival directions and the shower cores for coincident RD and MD events are shown in Fig. 7.3 for the two data sets. The arrival directions show an asymmetry with the minimum in the direction of the Earth's magnetic field. This asymmetry is caused in the geomagnetic emission of the radio signal, since the strength of the emission depends on the geomagnetic Lorentz force. Only the fraction of the motion vector of the shower particles, which is perpendicular to the magnetic field, produces emission. The shower cores are approximately equally distributed over the Unitary Cell, which excludes a locational detection bias.

7.1.1 4-fold events measured with the Surface, Muon, Radio and Fluorescence Detectors

In the reconstructed data set, a search for events measured additionally in coincidence with the Fluorescence Detector was performed. Thereby, only events up to December, 2015 are considered, until which a calibration for the Fluorescence detector is available. The standard quality cuts for the Fluorescence Detector were applied, which require that X_{max} is in the field of view of the telescope and is reconstructed with an uncertainty of less than $40\,\mathrm{g\,cm^{-2}}$ and $\chi^2/NDF < 2.5$ on the Gaisser-Hillas fit. In total 43 of such 4-fold hybrid events were measured in coincidence with all four detectors, of which only 2 events were measured after the calibration of the Muon Detector. 4-fold hybrid measurements give the unique opportunity to measure the cosmic-ray properties with various independent methods and to cross-calibrate the detector responses and shower observables. With the Fluorescence Detector, the primary mass is estimated by the shower maximum X_{max}. This independent mass estimator can be used to cross-calibrate the mass estimator using the muon density of the Muon Detector and the radiation energy of the Radio Detector. However, the statistics with calibrated data is not sufficient yet. An example for a 4-fold event of different energies and zenith angles is shown in Fig. 7.4. Additional example events are shown in Appendix D. X_{max} is reconstructed from the profile fitted to the longitudinal energy deposit of the air shower in the atmosphere.

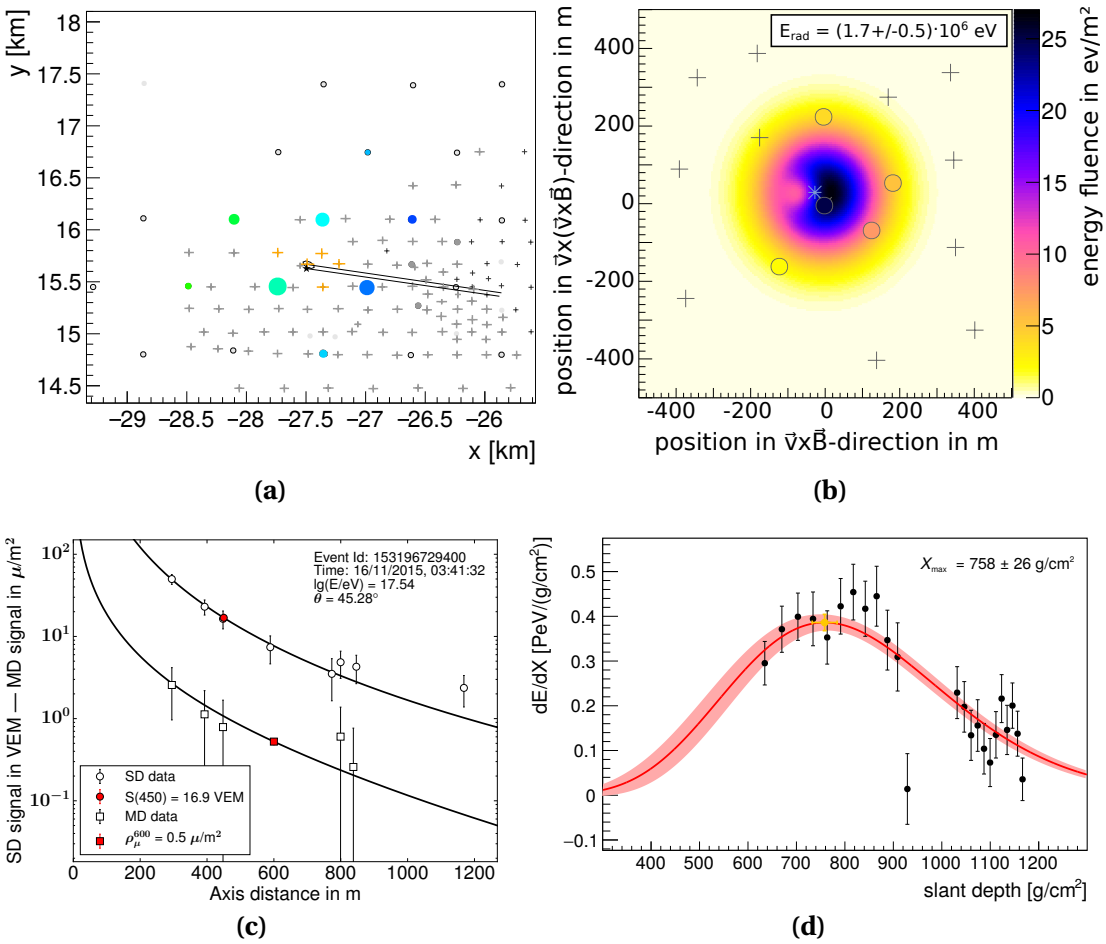

Figure 7.4: 4-fold example event The event was detected in 8 Surface Detector stations, 5 Muon Detector stations, 5 Radio Detector stations and 1 telescope (Coihueco). The arrival direction was reconstructed from the SD to a zenith angle of $\theta = (45.3 \pm 0.5)°$ and an azimuth angle of $\varphi = (350.5 \pm 0.6)°$, the primary energy to $(3.49 \pm 0.40) \times 10^{17}$ eV. The radiation energy was reconstructed from the RD signal and is corrected for the zenith angle dependence to $(1.88 \pm 0.52) \times 10^6$ eV. The shower maximum $X_{\max}$ was reconstructed to $(758 \pm 26)\,\mathrm{g\,cm^{-2}}$ from the FD signal. **(a)** SD and RD array **(b)** reconstructed two-dimensional LDF of the RD signal. **(c)** reconstructed one-dimensional LDFs to the SD and the MD signals. **(d)** Reconstructed longitudinal profile of the energy deposit of the shower in the atmosphere.

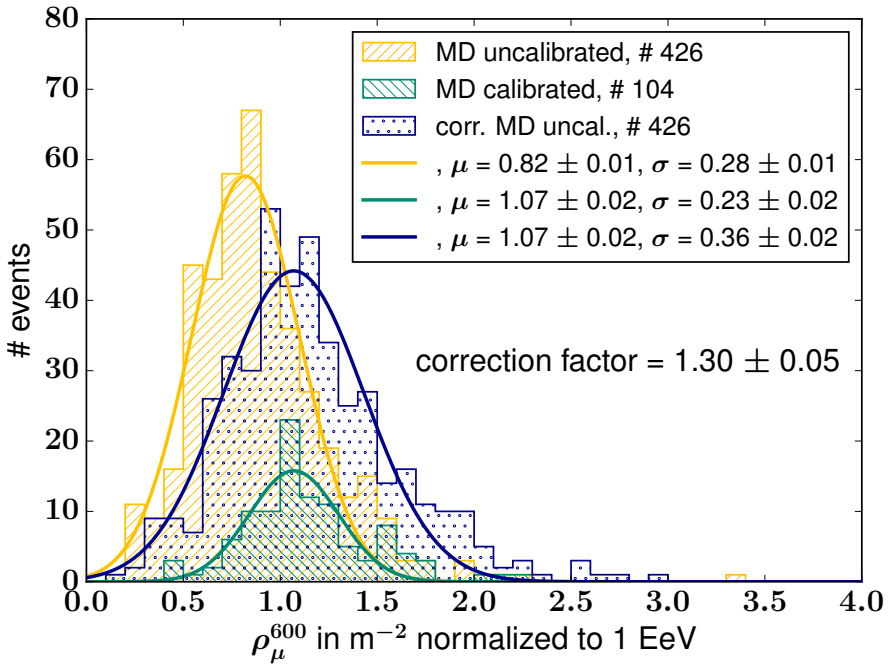

Figure 7.5: Correction of uncalibrated muon data The histograms show the muon density measured with the uncalibrated and calibrated Muon Detector, normalized to an energy of 10^{18} eV. The uncalibrated data is on average underestimated by 30 % compared to the calibrated data. The uncalibrated data is corrected for this mean offset.

7.2 Muon density measured with AMIGA

The coincident events measured by AMIGA and AERA are investigated. For these events, the muon density at a distance to the shower axis of 600 m is reconstructed by fitting a lateral distribution function to the muon signals in the MD stations, as described in Section 4.3.3. The muon density measured with the uncalibrated Muon Detector is corrected such that the absolute scale fits the calibrated data. Finally, the energy and zenith angle dependence is compared to the expectations from the simulations.

7.2.1 Correction of the uncalibrated muon data

The Muon Detector was not calibrated before the 20th October, 2015. More precisely, various calibration techniques were tested before this date, whereby, e.g., the discrimination threshold was modified. Hence, the absolute scale of the number of muons counted in the scintillator modules feature time dependent offsets to the true number of muons, which leads to an offset on the muon density at a reference distance of 600 m. In Fig. 7.5 the histograms of the muon density normalized to an energy of 10^{18} eV for events measured with the uncalibrated and calibrated Muon Detector is shown. The mean ρ_μ^{600} of the calibrated data is (30 ± 5) % larger than for the uncalibrated data. Hence, the uncalibrated data is shifted by this offset by applying

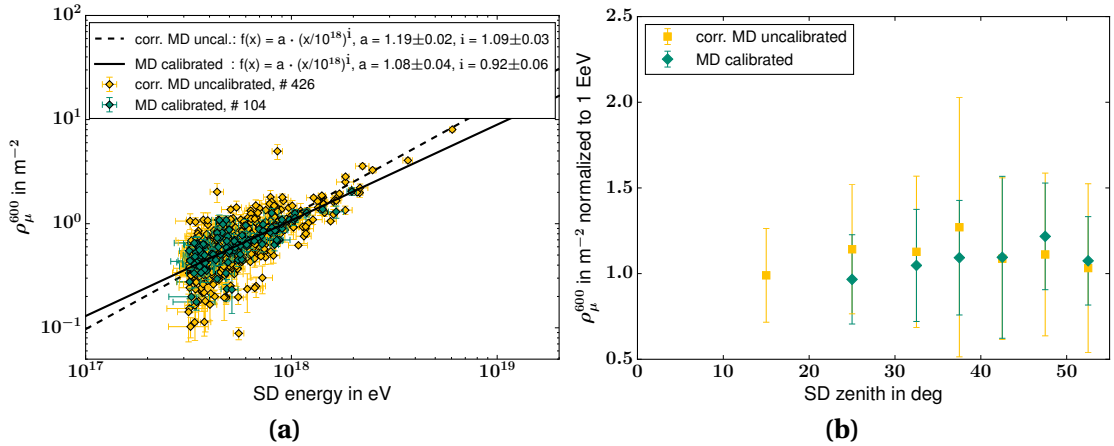

Figure 7.6: Energy and zenith angle dependence of the muon density The energy and the zenith angle are reconstructed from the Surface Detector signal. **(a)** The muon density grows with the energy with an index of 0.92 ± 0.06, in accordance to the simulation results. However, the absolute scale is larger by 71 % compared to the simulations. This indicates a known discrepancy in the predictions of the muon content from the hadronic models compared to measurements. **(b)** The muon density is normalized by the energy measured from the SD. It shows no significant dependency on the zenith angle. A decrease due to muon decay above 45° was observed in the simulations. However, the uncertainties are too large for this data set to resolve this effect, (error bars depict the standard deviation).

a correction factor of 1.3. However, the corrected uncalibrated data shows a larger spread than the calibrated data, which demonstrates the limitation of this correction method. A more accurate approach would be to correct the number of muons in each scintillator module separately. However, this would require knowledge about the offsets in the single modules, which was not available for this work. Hence, the uncalibrated data have to be interpreted with care.

7.2.2 Energy and zenith angle dependence

The distributions of the muon density at 600 m over the primary energy and the zenith angle, both reconstructed from the Surface Detector signal, are investigated. A power-law is fitted to the energy distributions by an orthogonal distance regression, taking into account the uncertainties of the observables and the reconstructed energy (see Fig. 7.6a). The muon density showed a dependency on the true primary energy of $E^{0.92}$ in the simulations, both for the true values of ρ_μ^{600} and after applying the detector response (see Section 5.1.1 and Fig. 6.8a). This dependency is confirmed with the calibrated MD data, which increases over the SD energy with an index of 0.92 ± 0.06. However, the uncalibrated data shows a larger dependency on the energy with an index of 1.09 ± 0.03. This indicates an energy-dependent systematic bias on the muon number in the uncalibrated scintillators. Therefore, no conclusions can

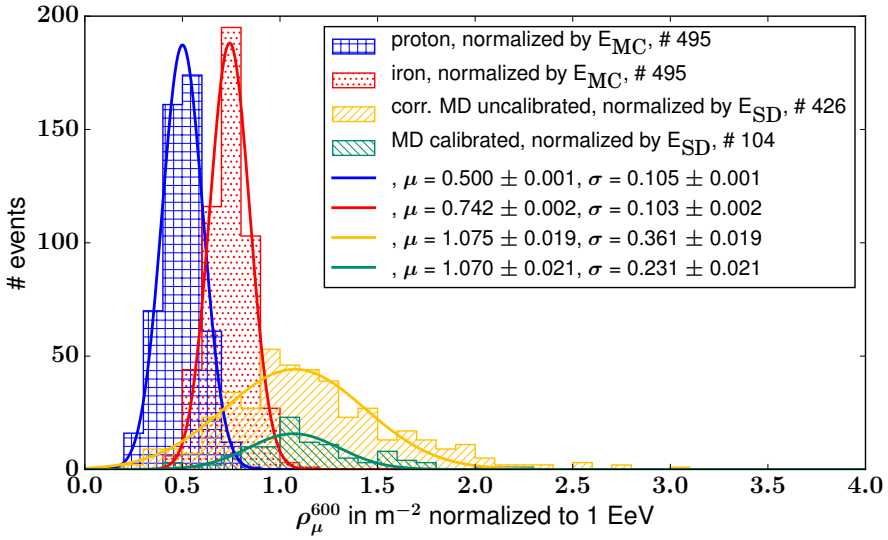

Figure 7.7: Comparison of muon density from data and from simulations The histograms show the muon density measured with the uncalibrated (corrected) and calibrated Muon Detector, as well as predicted for proton and iron showers, normalized to an energy of 10^{18} eV. The predictions are normalized by the true energy, since the SD energy from simulations is affected by the underestimation of the muons investigated here. The SD energy reconstructed for the measurements is calibrated with the FD energy scale and free of this bias. The mean muon density is underestimated by 110 % for proton and by 44 % for iron compared to the measurements.

be drawn about the mass composition from this uncalibrated data. However, in the following, this data set is still used to investigate the radiation energy, which is not affected by this bias, and it is further shown for comparison to the calibrated data set.

The muon density is normalized to an energy of 10^{18} eV, using the energy dependency derived from the simulations in Fig. 6.8a, except instead of the true energy the SD energy is used. The average normalized muon density is shown over bins of the zenith angle in Fig. 7.6b. No correlation with the zenith angle can be observed, taking into account the uncertainties due to the small size of the data set. In the simulations, a decrease above 45° could be observed. Above this angle, the travel length of the shower is in the range of the lifetime of a muon, and hence a part of the muons decay before reaching the ground. However, until 55°, the zenith angle range covered with AMIGA, the effect of the muon decay is smaller than the measurement uncertainties and than the spread of the muon density in the data sets used here. Thus, the zenith angle dependence needs to be studied later again, when larger data sets will be available.

The absolute mean value of the muon density is larger by 71 % compared to the simulations, comprising 50 % proton and 50 % iron showers, as shown in Fig. 7.7. More precisely, the absolute mean value is larger as the proton prediction by 110 % and as the iron predictions by 44 %. This is in accordance to an earlier result, that the hadronic interaction models were found to predict less muons as measured with

the Pierre Auger Observatory [65]. In particular, the model QGSJETII-04, used in the simulations in this thesis, shows a discrepancy of (61 ± 21) %, which is in the same order as the offset found here for a mixed composition. However, in [65] the underestimation has been derived for muons measured in the Surface Detector, which features a smaller energy threshold for muons of about 200 – 400 MeV compared to a threshold of about 1 GeV in the Muon Detector. Furthermore, the mass composition of the simulations used in [65] correspond to the composition measured by the Fluorescence Detector via X_{max}. Therefore, a slightly different underestimation is expected, when comparing to a composition of 50 % proton and 50 % iron showers, as done here.

7.3 Radiation energy measured with AERA

The radiation energy was reconstructed for the coincident events of AMIGA and AERA by fitting a two-dimensional lateral distribution function to the energy fluence measured in the antennas, as described in Section 4.3.3. It was corrected for a zenith angle dependence due to the atmospheric density at X_{max} (see Eq. (5.7)). For AERA, there is no need to distinguish between the two data sets, since the difference is only in the muon signal in the MD, which does not influence the radio signal. The energy and zenith angle dependence of the radiation energy is investigated using the energy and zenith angle reconstructed from the Surface Detector signal. In this way, the dependencies are studied using observables measured independently from the radio signal, which itself is sensitive to the primary particle and the arrival direction of the shower. A new parametrization is derived to estimate the primary energy from the radiation energy, which includes the correction on the zenith angle dependence.

7.3.1 Dependency on the primary energy

In Section 6.2.3 it was shown that the primary energy reconstructed from the Surface Detector signal features a bias on the mass of the primary particle, while the radiation energy does not. The signal in the SD is primarily produced by the muonic component of the shower, which is larger for showers induced by heavier primary particles. Thus, the SD energy slightly overestimates the primary energy for heavy particles and underestimates it for light particles. Therefore, it is not ideal to use the SD energy for the mass composition studies conducted in this chapter. Instead, the energy of the primary particle is derived from the energy estimator of the radio signal, the radiation energy.

The radiation energy was corrected for the dependency on the angle to the Earth's magnetic field and the zenith angle dependence arising from the atmospheric density at X_{max} (see [184], Eq. (5.7)). On the contrary, in [118] the correlation with the energy was derived for AERA events measured in coincidence with the Surface Detector, using only a simplified correction on the angle to the Earth's magnetic field α by dividing by $\sin^2 \alpha$, but no correction on the zenith angle. Therefore, when using an enhanced correction as done in this thesis, the correlation to the energy has to be

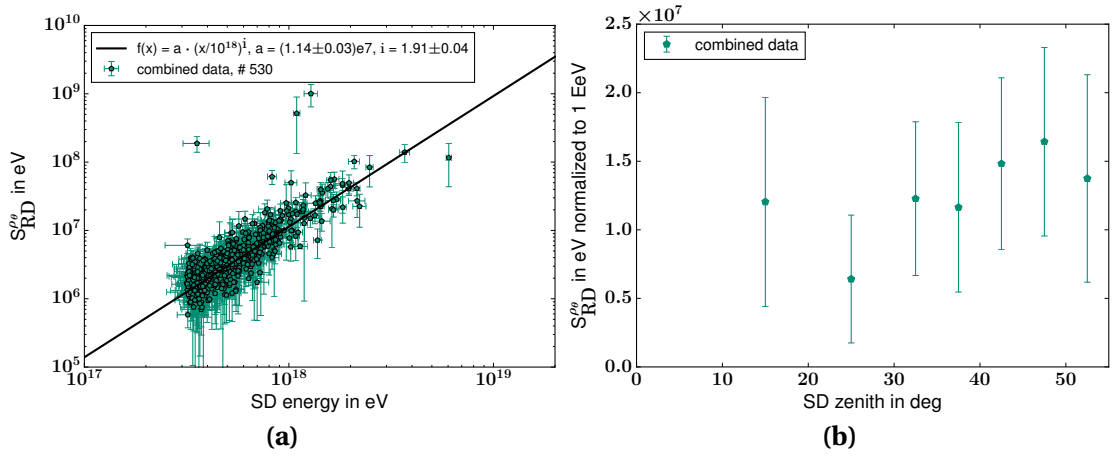

Figure 7.8: Energy and zenith angle dependency of the radiation energy The energy and the zenith angle are reconstructed from the Surface Detector signal. **(a)** The correlation of the radiation energy is parameterized by a power-law fit and is used to determine the primary energy from the radiation energy. **(b)** No significant correlation to the zenith angle can be observed for the zenith angle range of the data set, (error bars depict the standard deviation).

newly parametrized. For this, the correlation to the SD energy is used. Thereby, the overall correlation is still influenced by the mass bias on the SD energy, depending on the mass composition of the data set. However, the event-by-event mass bias is minimized when using the radio energy instead of the SD energy.

The radiation energy is shown over the SD primary energy in Fig. 7.8a. A power-law is fitted to the distribution, using an orthogonal distance regression, which takes the uncertainties on the radiation energy and the primary energy from the SD signal into account. The fit results in a radiation energy at an SD energy of 10^{18} eV of $a = (1.14 \pm 0.03) \times 10^7$ eV and an index of $i = 1.91 \pm 0.04$, which differs from the energy dependency found in [118] of $a = (1.58 \pm 0.07) \times 10^7$ eV, $i = 1.98 \pm 0.04$. In Section 6.2.2 and Appendix C various reconstruction biases were found. However, they have no influence on the differences between the parameters derived in here and in [118], since both reconstruction were done with the same reconstruction strategy. Instead, the differences arise from the correction of the zenith angle dependence. The derived parameters are used to reconstruct the primary energy by

$$\frac{E_{\mathrm{RD}}}{10^{18}} = \left(\frac{S_{\mathrm{RD}}^{\rho_\theta}}{a} \right)^{1/i} \quad . \tag{7.1}$$

The absolute scale of the radiation energy is enlarged by 25 % to that of the proton showers and by 37 % to that of the iron showers of the simulations including the detector response in Section 6.2.2. The reconstruction biases found in Appendix C cause an underestimation of the radiation energy by 28 % in the simulations includ-

ing the detector response compared to the true values. However, this biases are introduced in steps during the analysis pipeline, which are applied to simulations and data in the same manner. Hence, no difference between the radiation energy reconstructed from simulations and from data is expected from this biases. However, in [185] it has been found, that the radiation energy is underestimated by CoREAS by 11 % when using the standard settings for CORSIKA simulations. In the standard settings, the step size of the electron multiple scattering length factor in the simulated particle cascade in CORSIKA (parameter "STEPFC") is chosen too large. Furthermore, the absolute scale of CoREAS has been validated to a scale of 15 – 20 % in amplitude [186], which corresponds to 30 – 40 % in radiation energy reconstructed from the energy fluence. Moreover, in AERA the LPDA antennas are calibrated with an overall uncertainty of the amplitude of 9.4 %, which corresponds to about 19 % uncertainty of the radiation energy. On the contrary, the calibration of the butterfly antennas is not yet finished and the currently used detector response has known deficits. An additional bias on the results from the data set might be arising from this, since the data set used here contains mostly radio signals measured by butterfly antennas.

7.3.2 Zenith angle dependence

The radiation energy is normalized using the SD energy and binned over the zenith angle in Fig. 7.8b. From the simulations, it is expected that the radiation energy increases with the zenith angle, despite the radiation energy is already corrected for the zenith angle dependence due to the atmospheric density. An additional zenith angle dependency arises from the different distances the showers travel until reaching the ground for the different zenith angles. More inclined showers travel a longer distance, on which more radiation energy is released. Moreover, the showers are 'clipped', i.e. not fully developed, when reaching the ground, which makes up 5 – 10 % of the radiation energy for a zenith angle of 0° and is negligible for showers above 50° zenith angle. However, within the uncertainties no conclusions can be drawn about the slope of the distribution over the zenith angle for the measured events.

7.4 Mass estimation by the ratio of the muon density and the radiation energy

The two observables are used in the following to investigate the mass sensitivity of the mass estimator built by the ratio $\rho_\mu^{600}/\sqrt{S_{\mathrm{RD}}^{\rho_\theta}}$. The measured muon density is plotted over the radiation energy in Fig. 7.9. For comparison, the correlation for proton and iron showers are shown in addition, as fitted from the simulations in Fig. 6.9a. To account for the known underestimation of the muon number in QGSJETII-04, the parameters a of the fits to the simulations are corrected by a factor of 1.61. For the data set measured with the uncalibrated Muon Detector, in addition, the muon density is corrected by a factor of 1.31. The distribution of the data shows a clear

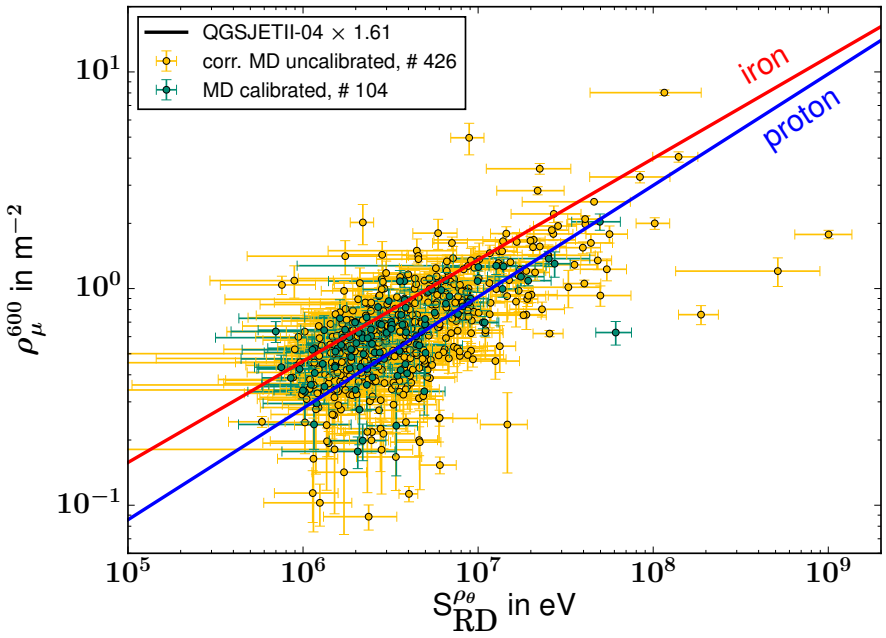

Figure 7.9: Correlation of the measured muon density and radiation energy of events measured in coincidence by AERA and the AMIGA MD in the time periods with uncalibrated and calibrated MD. For comparison, the correlation derived from air-shower simulations of proton and iron showers including detector responses of AERA and AMIGA are drawn. The measured events at the Pierre Auger Observatory contain on average 61 % more muons than predicted by the hadronic interaction model QGSJETII-04, which is corrected for in the fits shown here. The muon densities measured with the uncalibrated MD are corrected for the underestimation by 31 % compared to calibrated events.

correlation of ρ_μ^{600} and $S_{\mathrm{RD}}^{\rho_\theta}$. The average correlation is well within the simulated correlations for proton and iron, when taking the spread of the simulated data into account.

The ratio shows no dependency on the zenith angle, as shown in Fig. 7.10. However, the simulated ratio including the detector responses decreases with the zenith angle for proton and iron showers. This discrepancy indicates zenith angle dependent effects, which are not well understood, yet. This effects can be originated in the shower physics or the detector configuration, e.g. the calibration of the antennas and the muon detectors. However, no correlation of the zenith angle distribution with the primary energy was found and therefore, the following investigations of the mass composition over the energy is not affected by any zenith angle dependent effects.

To estimate the mean mass over the primary energy, the ratio is shown over the primary energy reconstructed from the Radio Detector signal in Fig. 7.11a. Only the calibrated data is shown, since the uncalibrated data was found to feature an energy bias, which influences the energy scale of the distribution. The mean ratio derived from the simulations in Fig. 6.9a for proton and iron showers, corrected for the offset of the hadronic interaction models, are shown in addition. The data shows a mean

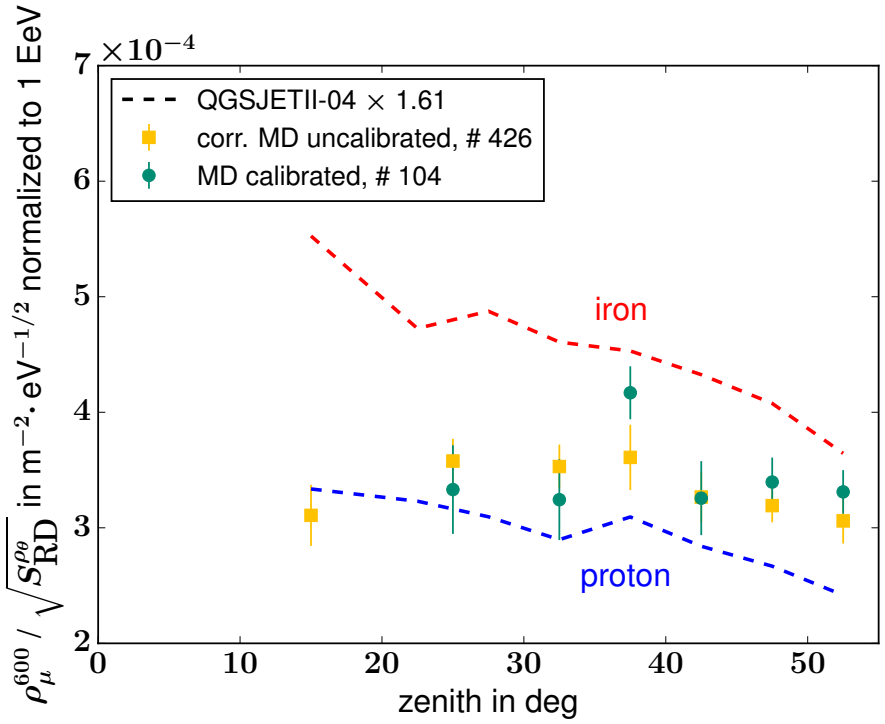

Figure 7.10: Zenith angle dependence The ratio $\rho_\mu^{600}/\sqrt{S_{\mathrm{RD}}^{\rho\theta}}$ shows no dependence on the zenith angle in the zenith angle range of the measurements. However, from simulations a decrease towards higher zenith angles is expected. This discrepancy indicates zenith angle dependent effects not considered in the air-shower simulations or in the simulated detector response. (Error bars depict the uncertainty on the mean $\sigma/\sqrt{N}$).

of the ratio close to the proton expectation. A slight trend towards a ligher composition can be observed. A linear fit to the logarithm of the energy results in a slope of $(-1.01 \pm 0.55) \times 10^{-4}\,\mathrm{m}^{-2}\,\mathrm{eV}^{-3/2}$, which validates the trend with a significance of $1.84\,\sigma$. The trend is in accordance to results from the Pierre Auger Collaboration at this energy range, derived from X_{max} measurements with the Fluorescence Detector including the HEAT telescopes, as shown in Fig. 7.11b, [187]. This result confirms the potential of the ratio $\rho_\mu^{600}/\sqrt{S_{\mathrm{RD}}^{\rho\theta}}$ for mass estimation.

Furthermore, the results of Fig. 7.11 confirms the average magnitude of the underestimation of the muon number by the hadronic interaction models to measurements. X_{max} is independent on the size of the muonic shower component, since it is dominated by the electromagnetic shower component, and therefore almost independent on the muon number. The measurements conducted here are shifted by the underestimation and show a composition relative to the expectation for pure proton/iron compatible with the X_{max} measurements. However,the absolute scale of the mass estimator for proton and iron showers cannot be derived exactly, since the discrepancy of the hadronic interaction models has been derived for a mixed composition measured by X_{max} in [65]. Hence, the proton and iron simulations

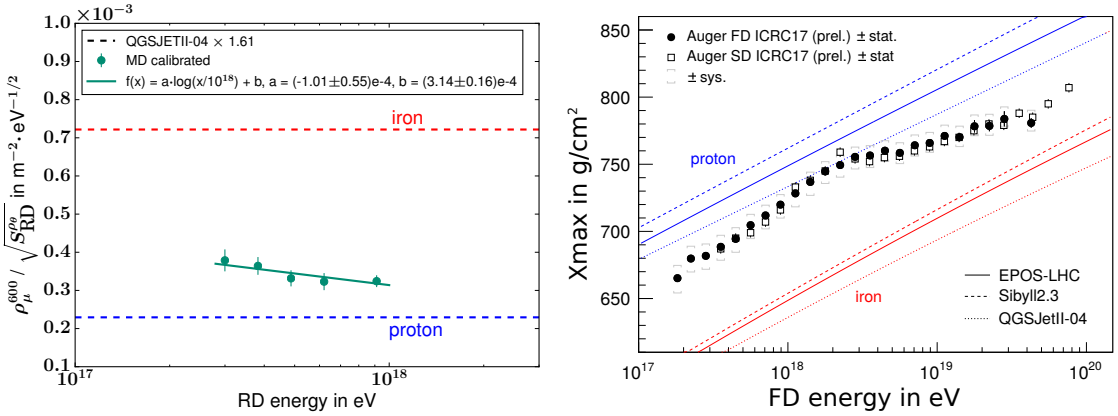

Figure 7.11: Mass composition of the calibrated data (a) The muon-radio ratio shows a light composition with a slight trend towards the expectation for pure proton for increasing energies, (error bars depict the uncertainty of the mean $\sigma/\sqrt{N}$). The linear fit to the logarithm of the energy reproduces the trend towards a ligher composition with a significance of $1.84\,\sigma$. **(b)** For comparison, measurements of the mass estimator X_{max} from fluorescence measurements are shown [187]. The distribution of X_{max} over the primary energy shows a trend compared to proton and iron showers compatible to the muon-radio ratio.

were corrected by a discrepancy corresponding to this mass composition and the discrepancy is likely to differ for a composition of pure protons or pure iron nuclei. Therefore, the scales for proton and iron in Fig. 7.11a are not independent on the corresponding scale in Fig. 7.11b.

In Fig. 7.12 the mass composition is shown for calibrated and the uncalibrated data set. Both data sets show a compatible distribution and the uncalibrated data set indicates a continuous trend towards a lighter composition with increasing energy. However, the uncalibrated data set showed a steeper dependency on the primary energy in Fig. 7.6a, which might result in a flattening of the distribution of $\rho_\mu^{600}/\sqrt{S_{\mathrm{RD}}^{\rho_\theta}}$ over the energy. Therefore, no conclusion on the mass composition should be drawn from this uncalibrated data set. In addition, the data set with calibrated muon data features a rather small statistics with 104 events. However, this events were measured in a short period of around 1 year and with only 7 AMIGA stations equipped with muon detectors. Currently, the complete AMIGA array is being equipped with muon detectors which will increase the number of events per year by an order of magnitude.

In summary, after more than 3 years of combined data taking, 530 coincident events of AMIGA and AERA were detected. In addition, for the first time 43 events were detected in all four detectors of the Pierre Auger Observatory - SD, MD, RD and FD. However, only 2 of these events contain high quality muon data, which is insufficient for a correlation study. In the future, the event rate of coincident events is expected to increase due to the increasing array covered with AMIGA muon

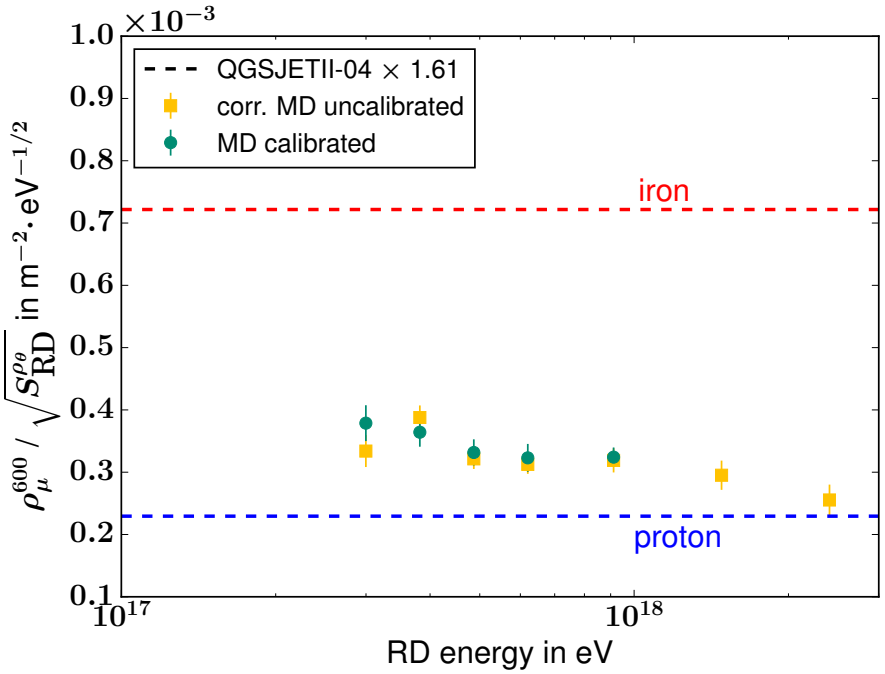

Figure 7.12: Mass composition For comparison, the mass composition of the data sets with uncalibrated and calibrated Muon Detector are shown. For both data sets, the muon-radio ratio shows a light composition with a slight trend towards an even lighter composition for increasing energies, (error bars depict the uncertainty of the mean $\sigma/\sqrt{N}$). However, no direct conclusion should be drawn from the uncalibrated data, since it features a small energy bias, which influences the energy scale. Nevertheless, this data set indicates that the trend continues towards higher energies as measured with the calibrated MD.

detectors. Furthermore, the quality of the data will be enhanced, since the AMIGA Muon Detector is now better understood and properly calibrated.

The large potential of the derived mass estimator $\rho_\mu^{600}/\sqrt{S_{\mathrm{RD}}^{\rho_\theta}}$ was demonstrated. Even with the small statistics, covering only a small energy range, the measured mass composition is compatible to observations of the Pierre Auger Collaboration using the Fluorescence Detector. With more coincident data of AMIGA and AERA in the future, the mass composition can be measured in the transition region from galactic to extragalactic cosmic rays with better accuracy. However, it is not clear, if a sufficient accuracy can be reached with, since AERA is an engineering array with irregular spacing between the antennas. Due to the insufficient hadronic interaction models, the absolute mass scale must be calibrated by the measured X_{max}, an independent mass estimator. By this, the method becomes almost independent from hadronic interaction models, since it is data driven. X_{max} can be derived from the Fluorescence Detector data, as soon as a higher statistics of 4-fold events is at hand. Alternatively, X_{max} can be reconstructed from the radio signal, which features a X_{max} resolution of about 39 g cm^{-2} [120] in comparison to a resolution of the FD HEAT of 20 – 30 g cm^{-2}

[188] in the energy range of AMIGA and AERA.

With the first combined analysis of AMIGA and AERA data, the new approach to combine muons with radio emission has been validated experimentally to feature mass sensitivity. Within the simulation study, the approach showed a great potential in particular for inclined showers. For this showers, only the muonic component reaches the ground and is measured by particle detectors, since the electromagnetic component is completely absorbed in the atmosphere. Hence, combined muon and radio measurements of inclined showers can be realized at the Pierre Auger Observatory by combining each Surface Detector with a radio antenna. In general, the new method can be applied to every cosmic-ray experiment featuring combined measurements of the muonic component and radio emission, such as TAIGA [86], or Ice-Top [69, 97], when equipped with radio antennas in addition to the ice-Cherenkov detectors. Therewith, the new method for mass estimation makes an important contribution to the general advance of the field of ultra-high energy cosmic rays.

CHAPTER 8

Summary and Conclusion

In this thesis, a new way for estimating the mass of ultra-high energy cosmic rays by combining the muon signal and the radio emission of extensive air showers is investigated. Recently, the Pierre Auger Collaboration discovered that cosmic rays above 8×10^{18} eV originate from outside our galaxy, by measuring an anisotropic distribution of their arrival directions [1]. However, it is not clear by which sources these extragalactic cosmic rays are accelerated. Separate measurements of the anisotropy and the energy spectrum of light and heavy cosmic rays can solve open questions regarding the sources, the acceleration and the propagation of cosmic rays. The novel method can provide additional accuracy for measurements of the mass of cosmic rays on a per-event basis over the whole zenith angle range.

A classical technique measures the mass of cosmic rays by combining the muonic and the electromagnetic shower component, using particle detectors. However, this technique fails for inclined showers, at which the electromagnetic component is mostly absorbed in the atmosphere and only the muonic component arrives at the ground. On the contrary, the electromagnetic component can be measured by its radio emission, which does not suffer absorption in the atmosphere. Moreover, the footprint of the radio emission covers a large area at the ground for inclined showers and can be measured with large spacing between the detectors. Hence, combining radio detectors with muon detectors enables measurements of the cosmic-ray mass in particular at large zenith angles, at which other techniques fail.

The Muon Detector of AMIGA and the Radio Detector AERA at the Pierre Auger Observatory represent an ideal environment to test the combination of muons and radio emission in the intermediate zenith angle range. First, the combination of muons and radio emission is studied on its mass sensitivity, using air-shower simulations. Then, an experimental scenario is simulated by adding detector responses of AMIGA and AERA and real radio background to these simulations. Finally, coincident measurements of AMIGA and AERA are analyzed.

Thereby, the size of the muonic shower component is represented by the muon density ρ_μ^{600} at a reference distance of 600 meter to the shower axis. The radiation energy $S_{\mathrm{RD}}^{\rho_\theta}$, i.e. the energy contained in the radio emission, is used as an observable of the size of the electromagnetic shower component. The ratio $\rho_\mu^{600}/\sqrt{S_{\mathrm{RD}}^{\rho_\theta}}$ then defines a mass estimator and is larger for showers initiated by an iron nuclei than by a proton.

Using the air-shower simulations, it is shown that the new mass estimator is,

with an average proton-iron merit factor of more than 2, comparably sensitive to established estimators based purely on particle measurements for showers with zenith angles below 40°, and clearly superior for more inclined showers. Moreover, its merit factor is larger by on average 0.5 to the mass estimator X_{max} for all zenith angles. These comparison of the mass estimators is not validated experimentally yet, since not enough coincident measurements of AMIGA, AERA and the Fluorescence detector are available, yet. Nevertheless, the results emphasize the potential of the new mass estimator in particular for inclined showers. When applying the detector responses to the simulations, the mass sensitivity is decreased due to measurement and reconstruction uncertainties compared to pure air-shower simulations, but is still sufficient to perform mass composition studies.

More than three years of combined measurements have been recorded by AMIGA and AERA. For a data period of 302 days, the Muon Detector of AMIGA was properly calibrated, yielding a high quality data set of 104 coincident events. Of these, only 2 events additionally feature calibrated measurements of the Fluorescence Detector of the Observatory. The measured observables ρ_{μ}^{600} and $S_{\mathrm{RD}}^{\rho_\theta}$ of this data set show the same correlation as for the air-shower simulations, which validates the capability of their ratio to serve as a mass estimator. However, the mean value of ρ_{μ}^{600} is larger than in simulations, which is caused by the known underestimation of the number of muons by hadronic interaction models [65]. When correcting for this discrepancy, the mass composition derived from $\rho_{\mu}^{600}/\sqrt{S_{\mathrm{RD}}^{\rho_\theta}}$ is compatible to measurements of X_{max} by the Fluorescence Detector of the Pierre Auger Observatory. This confirms the magnitude of the discrepancy between the hadronic interaction models and measurements. More importantly, it emphasizes the potential of the newly established mass estimator $\rho_{\mu}^{600}/\sqrt{S_{\mathrm{RD}}^{\rho_\theta}}$.

Thus, the experimental applicability is successfully shown for AMIGA and AERA. However, both detectors are built as engineering arrays, i.e. the detection techniques, the calibration of the detectors and the reconstruction methods are under continuous investigation and might suffer from unknown systematic uncertainties. Nevertheless, a higher rate of coincident events is expected in the future, since currently the instrumented area of the Muon Detector is being increased over the whole area of AERA and beyond. The number of events measured in coincidence with the Fluorescence Detector will grow with the time, which will enable an experimental comparison of the new mass estimator with X_{max} on a per-event level.

The novel method for mass estimation by combining muons and radio can further be applied at other cosmic-ray experiments, such as the TAIGA experiment [86], which as well combines muon detectors and radio antennas, or Ice-Top [69, 97], when equipped with radio antennas in addition to the ice-Cherenkov detectors. The upgraded Pierre Auger Observatory will measure the muonic and electromagnetic shower component with particle detectors on a per-event basis, which is essential for anisotropy studies [25]. However, in particular the electromagnetic component suffers from absorption in the atmosphere for inclined showers. In contrast, the water-Cherenkov detectors serve as detectors of the muonic component at these angles. Hence, equipping the water-Cherenkov detectors with radio antennas would enable mass estimation as well for inclined showers and increase the sky coverage for per-event measurements of the cosmic-ray mass.

APPENDIX A

Shower simulation input files

A.1 CORSIKA steering file example

```
RUNNR   438000
EVTNR   1
SEED    1314000 0       0
SEED    1314001 0       0
SEED    1314002 0       0
NSHOW   1
ERANGE  1e+09   1e+09
PRMPAR  14
THETAP  38.2424 38.2424
PHIP    92.3689 92.3689
ECUTS   1.000E-01       5.000E-02       2.500E-04       2.500E-04
ELMFLG  T       T
THIN    1.000E-06       1000    100E+02
THINH   1.000E+00       1.000E+02
OBSLEV  146679
ECTMAP  1.E11
STEPFC  1.0
MUADDI  T
MUMULT  T
HILOW   100
MAXPRT  1
MAGNET  19.79386        -14.15392
ATMOD   17
LONGI   T       5.      T       T
RADNKG  5.e5
DIRECT  ./
USER    holt-e
EXIT
```

This example of a steering file was taken from a simulation of the xx set. It reflects the common settings of all simulations used in this thesis. However, different run numbers (RUNNR) and seeds (SEED) for the random engines are chosen for each

simulation. The energy (ERANGE) and geometry (THETAP and PHIP correspond to the zenith and the azimuth angle, respectively) of the showers was varied in the different sets. Showers induced by protons (PRMPAR=14) and iron (PRMPAR=5626) as primary particles were calculated. The parameters for thin sampling are adjusted to the energy set in each simulation in line THIN, with the first parameter being the energy threshold $\varepsilon_{\mathrm{th}} = E/E_0$, the second parameter being the maximum weight factor and the third parameter being the maximum radial distance to the core to which the thin sampling takes place. The observation level (OBSLEV) is chosen to be 100 m below the altitute of the shower core reaching the ground at the Auger site. The Earth's magnetic field strength at the Pierre Auger Observatory is defined in MAGNET according to the timestamp of the event: the first parameter is the horizontal component pointing north and the second parameter is the vertical component pointing downwards, both in µT. The atmospheric model is set in ATMOD to the U.S. standard atmosphere after Keilhauer (17) is used.

A.2 CoREAS steering file example

```
# CoREAS V1.1 by Tim Huege <tim.huege@kit.edu> with contributions by
  Marianne Ludwig and Clancy James - parameter file

# parameters setting up the spatial observer configuration:

CoreCoordinateNorth = 0          ; in cm
CoreCoordinateWest = 0           ; in cm
CoreCoordinateVertical = 156679 ; in cm

# parameters setting up the temporal observer configuration:

TimeResolution = 5e-10           ; in s
AutomaticTimeBoundaries = 4e-07 ; 0: off, x: automatic boundaries with width x
                                  in s
TimeLowerBoundary = -1           ; in s, only if AutomaticTimeBoundaries set
                                  to 0
TimeUpperBoundary = 1            ; in s, only if AutomaticTimeBoundaries set
                                  to 0
ResolutionReductionScale = 0     ; 0: off, x: decrease time resolution linearly
                                  every x cm in radius

# parameters setting up the simulation functionality:
GroundLevelRefractiveIndex = 1.000292    ; specify refractive index at 0 m asl

# event information for Offline simulations:

EventNumber = 0
RunNumber = 0
GPSSecs = 1143507740
GPSNanoSecs = 438000
CoreEastingOffline = -26992                    ; in meters
```

```
CoreNorthingOffline = 15236.6                    ; in meters
CoreVerticalOffline = 91.4997                    ; in meters
RotationAngleForMagfieldDeclination = 2.714      ; in degrees
Comment = Event 438000 at 2016-04-01T01:02:03.000438000Z

# event information for your convenience and backwards compatibility with
# other software, these values are not used as input parameters for the
# simulation:

ShowerZenithAngle = 38.24239992          ; in degrees
ShowerAzimuthAngle = 92.36890335         ; in degrees, 0: shower propagates to
                                           north, 90: to west
PrimaryParticleEnergy = 1e+18            ; in eV
PrimaryParticleType = 14                 ; as defined in CORSIKA
DepthOfShowerMaximum = 695.2318014       ; slant depth in g/cm^2
DistanceOfShowerMaximum = 444847.9708    ; geometrical distance of shower
                                           maximum from core in cm
MagneticFieldStrength = 0.2433372823             ; in Gauss
MagneticFieldInclinationAngle = -35.56727834     ; in degrees, >0: in northern
                                                   hemisphere, <0: in southern
                                                   hemisphere
GeomagneticAngle = 118.5317502           ; in degrees
CorsikaFilePath = ./
CorsikaParameterFile = SIM438000.inp
```

APPENDIX B

Analysis pipeline of the combined analysis of AMIGA and AERA

The Offline release Dornröschen (v3r3, revision 31176) was used to run the analysis pipelines. Information about the AERA detector was fetched from the database AERA_3_A.

B.1 Air-shower simulations

Module sequence

```
<loop numTimes="unbounded" pushEventToStack="yes">
  <module> EventFileReaderOG </module>
  <loop numTimes="1" pushEventToStack="yes">
    <module> RdStationAssociator                    </module>
    <module> EventGeneratorOG                       </module>
    <!-- SD and MD combined Simulation -->
    <loop numTimes="unbounded" pushEventToStack="no">
      <module> CachedXShowerRegeneratorAG             </module>
      <module> G4XTankSimulatorAG                     </module>
    </loop>
    <module> SdSimulationCalibrationFillerOG        </module>
    <module> SdPMTSimulatorOG                       </module>
    <module> SdFilterFADCSimulatorMTU               </module>
    <module> SdBaselineSimulatorOG                  </module>
    <module> TankTriggerSimulatorOG                 </module>
    <module> TankGPSSimulatorOG                     </module>
    <module> UnderGrdInjectorAG                     </module>
    <module> EdepSimulatorAG                        </module>
    <module> MdCounterSimulatorAG                   </module>
    <module> CentralTriggerSimulatorXb              </module>
    <module> CentralTriggerEventBuilderOG           </module>
    <module> EventBuilderOG                         </module>
    <module> EventCheckerOG                         </module>
    <module> SdCalibratorOG                         </module>
```

```
    <module> SdEventSelectorOG                    </module>
    <module> SdMonteCarloEventSelectorOG          </module>
    <module> SdPlaneFitOG                         </module>
    <module> LDFFinderKG                          </module>
    <module> SdEventPosteriorSelectorOG           </module>
    <!-- MD Reconstruction -->
    <try>
      <module> MdMuonCounterAG                      </module>
      <module> MdModuleRejectorAG                   </module>
      <module> MdEventSelectorAG                    </module>
      <module> MdBiasCorrecterAG                    </module>
      <module> MdLDFFinderAG                        </module>
    </try>
    <!-- RD antenna simulation -->
    <module> RdAntennaStationToChannelConverter </module>
    <module> RdChannelResponseIncorporator      </module>
    <module> RdChannelResampler                 </module>
    <module> RdChannelTimeSeriesClipper         </module>
    <module> RdChannelVoltageToADCConverter     </module>
    <module> RdChannelNoiseImporter             </module>
    <!-- RD reconstruction -->
    <try>
      <module> RdEventInitializer                   </module>
      <module> RdTimeJitterAdder                    </module>
      <module> RdStationRejector                    </module>
      <module> RdChannelADCToVoltageConverter       </module>
      <module> RdChannelSelector                    </module>
      <module> RdChannelPedestalRemover             </module>
      <module> RdChannelResponseIncorporator        </module>
      <module> RdChannelBeaconSuppressor            </module>
      <module> RdChannelTimeSeriesTaperer           </module>
      <module> RdChannelBandstopFilter              </module>
      <module> RdChannelUpsampler                   </module>
      <module> RdAntennaChannelToStationConverter </module>
      <module> RdStationSignalReconstructor         </module>
      <module> RdStationEFieldVectorCalculator      </module>
      <loop numTimes="unbounded" pushEventToStack="no">
        <module> RdTopDownStationSelector             </module>
        <module> RdPlaneFit                           </module>
      </loop>
      <module> RdClusterFinder                      </module>
      <module> RdPlaneFit                           </module>
      <module> RdLDFMultiFitter                     </module>
      <module> Rd2dLDFFitter                        </module>
    </try>
    <module> RecDataWriterNG </module>
  </loop>
</loop>
```

Bootstrap

Only deviations from the RdSimulationObserver standard application of the v3r3 branch revision 31176 are listed here. The SD detector was set to simulate the real detector positions instead of the ideal positions. MD counter positions were associated to all real SD detector positions of the 750 m grid. At each counter position 3 modules with each 10 m^2 area were simulated, arranged in an L-shape and buried in 2.3 m depth (see Fig. 4.5). Parameters of the Offline modules overridden from the default or the setting in the RdSimulationObserver are listed in the following:

```
<configLink id="SdEventSelector">
  <SdEventSelector>
    <!-- bad periods only affect data, not simulations -->
    <EnableSdExcludedPeriods> 0 </EnableSdExcludedPeriods>
  </SdEventSelector>
</configLink>
<configLink id="MdEdepSimulator">
  <MdEdepSimulator>
    <globalPhysicsList> 1 </globalPhysicsList>
  </MdEdepSimulator>
</configLink>
<configLink id="MdMuonCounter">
  <MdMuonCounter>
    <!-- delays of modules to SD do not exist in simulations -->
    <setTimeStamps> 0 </setTimeStamps>
  </MdMuonCounter>
</configLink>
 <configLink id="MdEventSelector">
  <MdEventSelector>
    <selectEventByTheta> 1 </selectEventByTheta>
    <maxTheta> 55 </maxTheta> -> later cut to 55
  </MdEventSelector>
</configLink>
<configLink id="MdLDFFinder">
  <MdLDFFinder>
    <ldfType> KascadeGrande </ldfType>
    <referenceDistance unit='m'> 600 </referenceDistance>
    <fixBeta>0</fixBeta>
    <countersToFixBeta> 4 </countersToFixBeta>
    <fixCoreFromSd> 1 </fixCoreFromSd>
  </MdLDFFinder>
</configLink>
<configLink id="RdChannelNoiseImporter">
  <RdChannelNoiseImporter>
    <infoLevel> 2 </infoLevel>
    <NoiseFileSelection> Automatically </NoiseFileSelection>
    <NoiseFilePath> /path/to/noisefiles/dir </NoiseFilePath>
    <FilenamePrefix> rdp_ </FilenamePrefix>
    <TimeIntervalInFile> Day </TimeIntervalInFile>
```

```
      <ExpectSubDirectories> 1 </ExpectSubDirectories>
      <EvtSelInNoiseFile> ByTimestamp </EvtSelInNoiseFile>
      <MaxTimeDifference unit="minute"> 10 </MaxTimeDifference>
      <RejectStationsWithoutNoiseInformation> 0
                          </RejectStationsWithoutNoiseInformation>
    </RdChannelNoiseImporter>
  </configLink>
```

B.2 Data

Module sequence

```
<loop numTimes="unbounded">
  <module> EventFileReaderOG                  </module>
  <module> RdEventPreSelector                 </module>
  <module> EventCheckerOG                     </module>
  <!-- SD pre-selection -->
  <module> SdPMTQualityCheckerKG              </module>
  <module> TriggerTimeCorrection              </module>
  <module> SdCalibratorOG                     </module>
  <module> SdStationPositionCorrection        </module>
  <module> SdBadStationRejectorKG             </module>
  <module> SdSignalRecoveryKLT                </module>
  <module> SdEventSelectorOG                  </module>
  <!-- SD reconstruction -->
  <module> SdPlaneFitOG                       </module>
  <module> LDFFinderKG                        </module>
  <module> EnergyCalculationPG                </module>
  <module> DLECorrectionGG                    </module>
  <module> SdEventPosteriorSelectorOG         </module>
  <try>
    <module> SdHorizontalReconstruction         </module>
  </try>
  <!-- Rd reconstruction -->
  <module> RdEventInitializer                 </module>
  <module> RdStationPositionCorrection        </module>
  <module> RdStationRejector                  </module>
  <module> RdChannelADCToVoltageConverter     </module>
  <module> RdChannelSelector                  </module>
  <module> RdChannelPedestalRemover           </module>
  <module> RdChannelResponseIncorporator      </module>
  <module> RdChannelBeaconTimingCalibrator    </module>
  <module> RdChannelBeaconSuppressor          </module>
  <module> RdStationTimingCalibrator          </module>
  <module> RdStationTimeWindowConsolidator    </module>
  <module> RdChannelTimeSeriesTaperer         </module>
  <module> RdChannelBandstopFilter            </module>
```

```
  <module> RdChannelUpsampler                    </module>
  <module> RdAntennaChannelToStationConverter </module>
  <module> RdStationSignalReconstructor          </module>
  <module> RdStationEFieldVectorCalculator       </module>
  <loop numTimes="unbounded">
    <module> RdTopDownStationSelector              </module>
    <module> RdPlaneFit                            </module>
  </loop>
  <module> RdClusterFinder                       </module>
  <module> RdPlaneFit                            </module>
  <module> RdEventPostSelector                   </module>
  <module> RdLDFMultiFitter                      </module>
  <module> Rd2dLDFFitter                         </module>
  <!-- MD Recostruction -->
  <try>
    <module> MdMuonCounterAG                       </module>
    <module> MdModuleRejectorAG                    </module>
    <module> MdBiasCorrecterAG                     </module>
    <module> MdEventSelectorAG                     </module>
    <module> MdLDFFinderAG                         </module>
  </try>
  <!-- FD hybrid reconstruction -->
  <try>
    <module> FdCalibratorOG                        </module>
    <module> FdEyeMergerKG                         </module>
    <module> FdPulseFinderOG                       </module>
    <module> FdSDPFinderOG                         </module>
    <module> FdAxisFinderOG                        </module>
    <module> HybridGeometryFinderOG                </module>
    <module> HybridGeometryFinderWG                </module>
    <module> FdApertureLightKG                     </module>
    <module> FdEnergyDepositFinderKG               </module>
  </try>
  <module> RdStationTimeSeriesWindowCutter    </module>
  <module> RdStationTimeSeriesTaperer         </module>
  <module> RecDataWriterNG                    </module>
</loop>
```

Bootstrap

Only deviations from the RdObserver standard application of the v3r3 branch revision 31176 are listed here.

```
  <configLink id="RdEventPreSelector">
    <RdEventPreSelector>
      <MinNumberOfStations> 3 </MinNumberOfStations>
      <UseTriggerInformation> 1 </UseTriggerInformation>
      <UseSelfTriggeredEvent> 0 </UseSelfTriggeredEvent>
      <UseExternallyTriggeredEvent> 1 </UseExternallyTriggeredEvent>
      <UseCalibrationTriggeredEvent> 0 </UseCalibrationTriggeredEvent>
```

```
    <UseScintillatorTriggeredEvent> 0
                    </UseScintillatorTriggeredEvent>
    <UseSDTriggeredEvent> 1 </UseSDTriggeredEvent>
    <UseGUITriggeredEvent> 1 </UseGUITriggeredEvent>
    <UseFDTriggeredEvent> 1 </UseFDTriggeredEvent>
    <UseHEATTriggeredEvent> 1 </UseHEATTriggeredEvent>
    <UseAERAletTriggeredEvent> 1 </UseAERAletTriggeredEvent>
    <UseAIRPLANETriggeredEvent> 0 </UseAIRPLANETriggeredEvent>
    <UsePeriodicTriggeredEvent> 0 </UsePeriodicTriggeredEvent>
    <UsePassThroughTriggeredEvent> 0 </UsePassThroughTriggeredEvent>
  </RdEventPreSelector>
</configLink>
<configLink id="RdStationRejector">
  <RdStationRejector>
    <useBadPeriodDB> 1 </useBadPeriodDB>
  </RdStationRejector>
</configLink>
<configLink id="MdBiasCorrecter">
  <MdBiasCorrecter>
    <biasCorrection> 1 </biasCorrection>
  </MdBiasCorrecter>
</configLink>
<configLink id="MdMuonCounter">
  <MdMuonCounter>
    <strategy> Gap </strategy>
    <windowSize> 8 </windowSize>
    <nOnes> 2 </nOnes>
    <nGaps> 1 </nGaps>
  </MdMuonCounter>
</configLink>
<configLink id="MdLDFFinder">
  <MdLDFFinder>
    <ldfType> KascadeGrande </ldfType>
    <referenceDistance unit='m'> 600 </referenceDistance>
    <fixBeta>0</fixBeta>
    <countersToFixBeta> 4 </countersToFixBeta>
    <fixCoreFromSd> 1 </fixCoreFromSd>
  </MdLDFFinder>
</configLink>
```

APPENDIX C

Reconstruction biases on the radiation energy

In Section 6.2.2 an underestimation of about 28 % of the reconstructed radiation energy compared to the true radiation energy is observed. Thereby, the true radiation energy is calculated from the electromagnetic shower energy, using Eqs. (5.6) to (5.8) from [184]. The origin of this reconstruction bias is further investigated here.

It was found, that not only the radiation energy, but as well the energy fluence in the antennas, from which the radiation energy is calculated via a two-dimensional LDF fit, is underestimated in the reconstruction. To investigate the reason of this underestimation introduced in the reconstruction procedure performed with Offline, the pipeline is studied step-by-step.

Thereby, a set of CoREAS simulations is used, which includes observers at the antenna positions of AERA24 and in addition, observers on a star-shaped grid around the shower core. The simulation set comprises 65 events varying in primary energy and arrival direction, of which each is simulated once for a proton and once for an iron primary. Thereby, it is investigated, if the underestimation depends on the mass of the primary particle, which would influence the mass estimation, e.g., when combining muons and radio emission.

The true energy fluence of the observers and the true radiation energy of the events is derived directly from the CoREAS simulations. Therefore, the radio emission calculated for each observer position is filtered to a frequency range of 30 – 80 MHz, applying a rectangular bandpass filter. For each observer, the energy fluence is calculated by integrating over the filtered time trace in a time window of ±50 ns around the timestamp of the peak amplitude. Then, the radiation energy is directly calculated by interpolation of the energy fluences of the observers arranged in a star shaped grid. With this, the resulting radiation energy is independent of the model used in [184] and from the choice of the fit function to the radio footprint, which is model dependent, too. In addition, the energy fluences in the observers and the radiation energy is reconstructed, including a simulation of the AERA detector responses, as described in Sections 4.3.2 and 4.3.3. For this, the Offline release Dornröschen (v3r3, revision 31176) is used.

A comparison of the true (calculated from the CoREAS output directly) and the

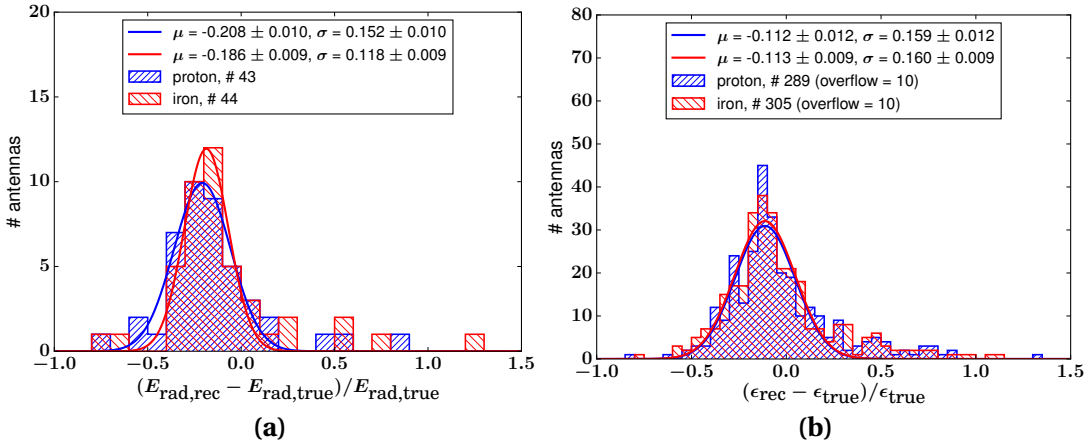

Figure C.1: Bias on the reconstruction using the full analysis pipeline of AERA The simulations include observers at the AERA24 station position and at positions on a star shaped grid. **(a)** Comparison of the reconstructed and true radiation energy. The mean value shows a large spread due to the small event number. **(b)** Comparison of the energy fluences in the antennas with signal (signal-to-noise ratio > 10).

reconstructed energy fluence in the antennas with a signal (signal-to-noise ratio > 10) as well as the true and the reconstructed radiation energy via a two-dimensional LDF fit is shown in Fig. C.1. A mean underestimation of the energy fluence in the antennas of about 11 % is observed. Thereby, no difference in the underestimation between proton and iron showers is observed. The reconstructed radiation energy features a larger bias of on average 19.7 %. The radiation energy is underestimated stronger for proton showers by 2 %, which is however not statistically significant.

The underestimation of the radiation energy is smaller than in Section 6.2.2. During the investigations to this bias, a technical problem was found in the application of the bandpass filter during the calculation of the energy fluences from the CoREAS output, i.e. in the calculations of the true values, and was solved. With this fix, the underestimation is reduced by 8 % in comparison to the results found in Section 6.2.2.

C.1 Step-by-step analysis of the reconstruction pipeline

To investigate the origin of the underestimation of the energy fluence, the reconstruction pipeline of Offline is performed step-by-step and after each step the energy fluences in the antennas are compared to the true values. This procedure is done for one proton and one iron example event[1]. Thereby, the steps causing an underestimation of the energy fluence can be identified and further studied to quantify the mean

[1] SIM100001 (proton) and SIM200001 (iron) of the "aeraPhaseI contained starShape" simulation library

Table C.1: Bias on the energy fluence observed after steps in the analysis pipeline in Offline. Steps causing a significant bias are marked in red.

step	modules added to the analysis pipeline	bias in % proton	bias in % iron
1.	RdStationBandpassFilter, 30 – 80 MHz, integration window ±50 ns	0.25	0.25
2.	RdAntennaStationToChannelConverter, RdChannelSelector, RdAntennaChannelToStationConverter, (from here exclude RdStationBandpassFilter)	–0.12	–0.13
3.	RdChannelResponseIncorporator forth and back	–0.12	–0.13
4.	RdChannelResampler	–0.35	0.27
5.	RdChannelUpsampler	–0.004	0.006
6.	RdChannelTimeSeriesClipper, RdChannelTimeSeriesTaperer	0.11	0.11
7.	RdChannelVoltageToADCConverter, RdChannelADCToVoltageConverter	0.07	0.04
8.	RdChannelPedestalRemover	1.20	1.06
9.	RdChannelBeaconSuppressor	–0.33	–1.73
10.	RdTimeJitterAdder	–0.33	–1.73
11.	RdStationRejector	–0.33	–1.73
12.	RdChannelBandstopFilter	–6.75	–7.56
13.	RdChannelNoiseImporter, MinSignalToNoise 10, noise event 1143595306 (GPS sec)	–17.39	–17.81
14.	RdChannelNoiseImporter, MinSignalToNoise 10, noise event 1143583006 (GPS sec)	–9.96	–10.35
15.	full analysis pipeline including SD, MD and RD, ref. distance SD, noise event 1143595306 (GPS sec)	–14.49	–17.42

underestimation due to each step. Furthermore, possible differences for proton and iron showers can be identified. A table of the analysis steps and their mean influence on the energy fluences in the antennas of the example events is shown in Table C.1.

In the first step, only a bandpass filter to 30 – 80 MHz is applied to the simulated time traces of the radio emission. Then, the energy fluences of the antennas are calculated using the *RdStationSignalReconstructor* module. Thereby, the size of the window around the peak amplitude in the time trace, which is integrated to calculate the energy fluence, is set to ±50 ns. This equals the procedure, which is performed to calculate the true values. A station is considered a signal station, if the peak amplitude is more than $1 \times 10^{-4}\,\mathrm{V\,m^{-1}}$. The corresponding module sequence of this step 1. is

```
<moduleControl>
  <loop numTimes="unbounded" pushEventToStack="yes">
    <module> EventFileReaderOG </module>
    <loop numTimes="1" pushEventToStack="yes">
      <module> RdStationAssociator          </module>
      <module> RdEventInitializer           </module>
      <module> RdStationBandpassFilter      </module>
      <module> RdStationSignalReconstructor </module>
      <module> RecDataWriterNG              </module>
    </loop>
  </loop>
</moduleControl>
```

After applying the *RdChannelPedestalRemover*, the mean energy fluence is slightly increased. A reduction of the mean energy fluence can be observed after applying the *RdChannelBeaconSuppressor* and the *RdChannelBandstopFilter*. Both modules cut a part of the frequency spectrum, which contains background. In the *RdChannelBeaconSuppressor* the power, which is cut by this, is approximated by assuming a flat spectrum and is added to the overall power of the signal to reduce the bias. However, is shows that this procedure does not recover the complete power, since the approximation of a flat spectrum is not valid for most of the antennas. In the *RdChannelBandstopFilter* frequencies featuring RFI peaks are set to the mean signal of all frequencies in the spectrum, which as well implies a flat spectrum. Furthermore, an increase in the underestimation is observed, when adding background to the time trace. This underestimation varies with the background event.

C.2 Study of reconstruction steps changing the absolute scale of the energy fluence

The reconstruction steps causing a change in the absolute scale of the energy fluence are further investigates. For the modules *RdChannelBeaconSuppressor* and *RdChannelBandstopFilter*, the full reconstruction pipeline is run with the respective module excluded and the results are compared to the full pipeline including the module in

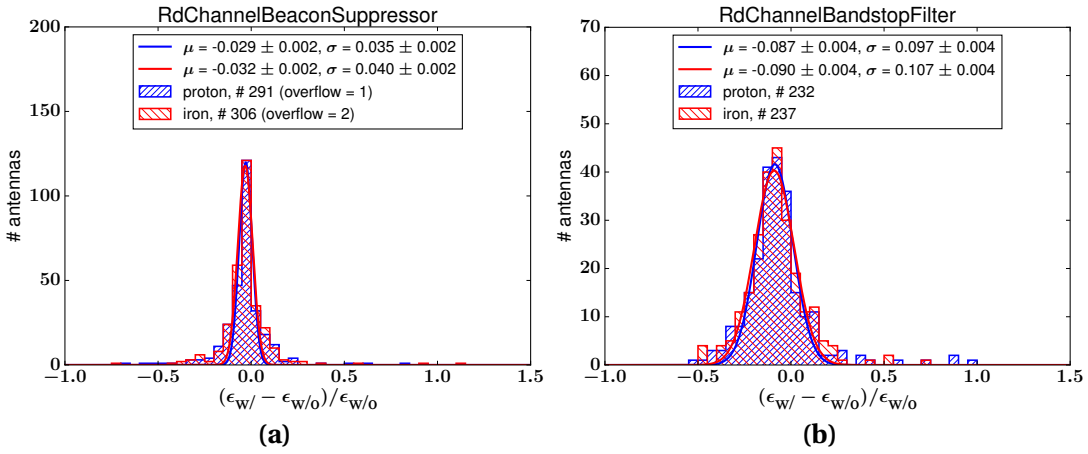

Figure C.2: Biases on the energy fluence by RFI cleaning by the *RdChannelBeaconSuppressor* and *RdChannelBandstopFilter* modules. The modules are separately excluded from the full reconstruction pipeline. The resulting energy fluence ($\epsilon_{\mathrm{w/o}}$) is then compared to the energy fluence of the full pipeline ($\epsilon_{\mathrm{w/}}$). The *RdChannelBeaconSuppressor* reduces the energy fluence by 3.1 % and the *RdChannelBandstopFilter* by 8.9 %

Figs. C.2a and C.2b. The *RdChannelBeaconSuppressor* reduces the energy fluence by 3.1 % and the *RdChannelBandstopFilter* by 8.9 %, which is larger than observed for the example event.

Furthermore, it was found that the underestimation due to background changed with the choice of the background event. To study the mean influence of the background and the spread of the energy fluence due to the background, the example event from Table C.1 is run 500 times with different background events. The resulting energy fluences in the antennas are compared to the energy fluences of the reconstruction of the event without background in Fig. C.3a. The mean bias is small with –1.5 %. However, the different background causes a spread on the energy fluence of 14.2 %.

In Fig. C.3b the relative difference of the pipeline including and excluding background is shown over the signal-to-noise ratio of the antennas. The spread of the energy fluence decreases with an increasing signal-to-noise ratio. This might explain the enlarged underestimation of the radiation energy compared to the energy fluence. The signal-to-noise ratio decreases on average with the distance to the shower axis. Hence, the energy fluence is underestimated stronger for more distant stations. This leads to a steeper lateral distribution in the reconstruction compared to the true lateral distribution. This influences the fit of the two-dimensional LDF. The radiation energy is reconstructed by integrating over the two-dimensional LDF and hence is smaller for a steeper LDF. This gives an additional bias on the radiation energy compared to the bias on the single-antenna energy fluence.

It was further found, that if the size of the integration window is set to the full trace length, the energy fluence increases by ≈ 5 % (not shown in the table). This is surpris-

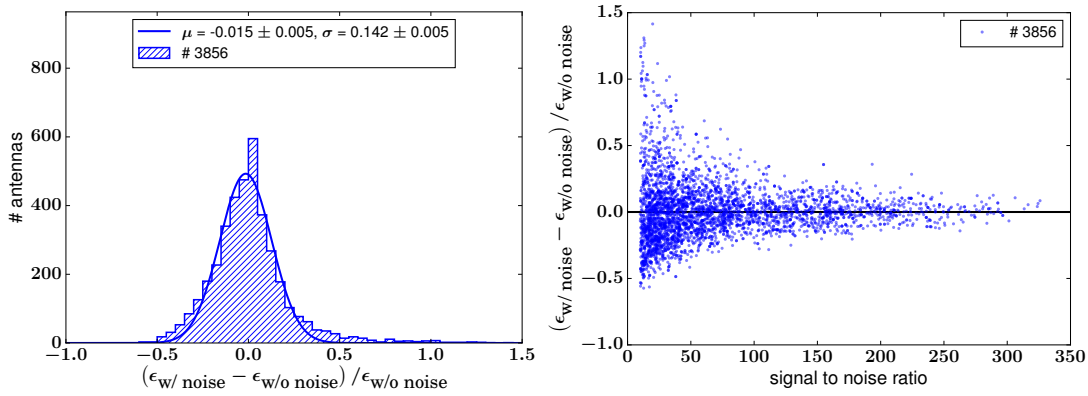

Figure C.3: Biases on the energy fluence by added background **(a)** The example event is combined with 500 different background events. The resulting energy fluences in the antennas is compared to the reconstruction of the event without background. A small bias of –1.5 % is observed, but a spread of 14.2 % is caused by the added background. **(b)** The relative difference of the energy fluences including and excluding background are shown over the signal-to-noise ratio. The spread decreases with increasing signal-to-noise ratio.

ing, since it was assumed that the size of the integration window has no influence on the energy fluence and that the majority of the signal is confined in ±50 ns around the peak amplitude. The signal energy fluence is calculated by integrating the time series of the radio signal over this window. Then it is corrected for the energy fluence arising from background radio signals. Therefore, the time series is integrated over a noise window of the same size as the signal window, in a region where presumably no cosmic-ray radio signal is present. The noise energy fluence is then subtracted from the energy fluence in the signal window to gain the signal energy fluence. This increase shows that the size of the integration window indeed influences the size of the energy fluence. However, when the radio signal includes background, the chance for RFI noise to be included in the signal window increases with its size. Therefore, the window has to be reduced to avoid a bias due to these RFI peaks.

The underestimation of the different steps in the reconstruction is summarized in Table C.2 The sum of all biases found is larger than the overall difference between the mean reconstructed and the mean true energy fluence in Fig. C.1b of 11 %. This indicates, that the single steps causing the underestimation are influencing each other, which has to be further investigated.

Table C.2: Summary of biases from different steps in the analysis pipeline

module	bias in %
RdChannelBeaconSuppressor	–3.1 %
RdChannelBandstopFilter	–8.9 %
RdChannelNoiseImporter	–1.5 %
overall on energy fluence	–11 %
overall on radiation energy	–19.7 %

APPENDIX D

Examples of coincident events of AMIGA and AERA

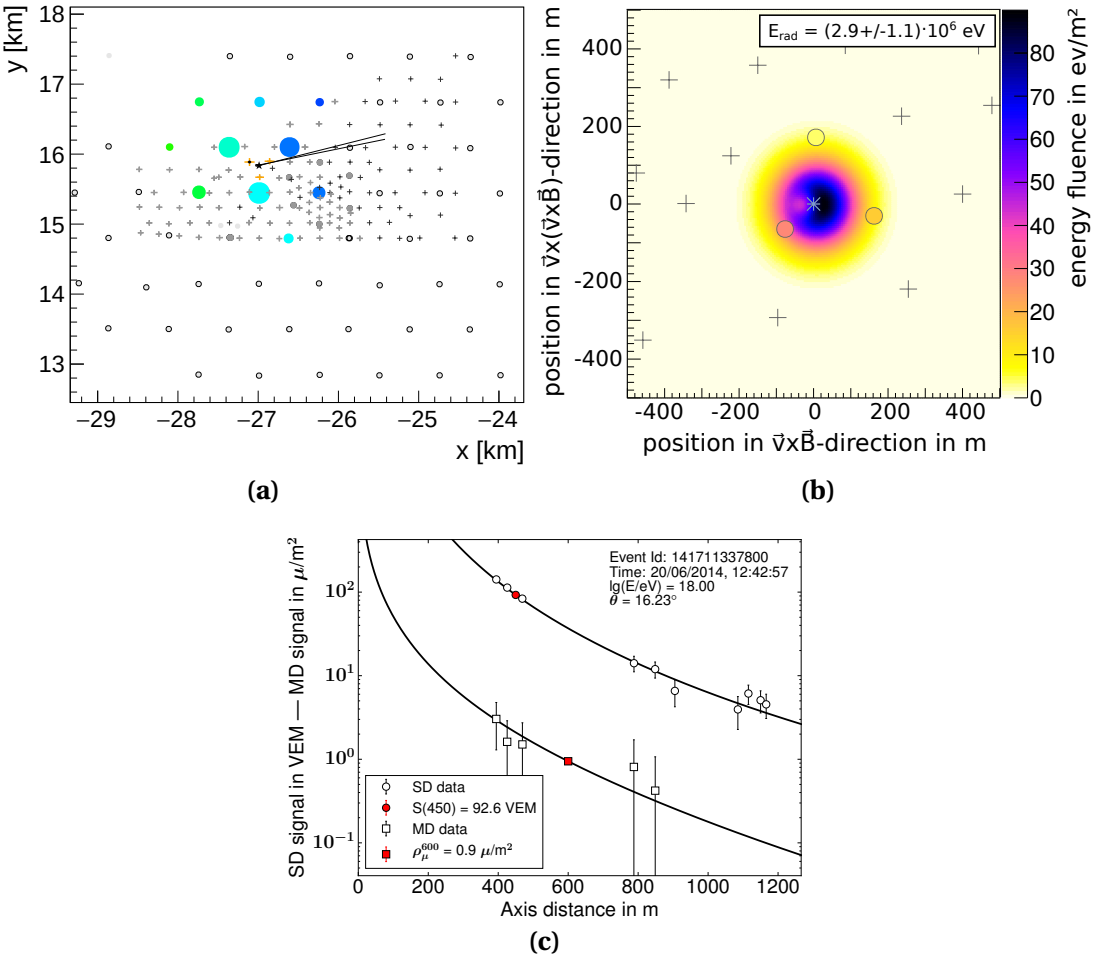

Figure D.1: Example event measured in the SD, MD and RD The event was detected in 10 Surface Detector stations, 5 Muon Detector stations and 3 Radio Detector stations. The arrival direction was reconstructed from the SD to a zenith angle of $\theta = (16.2 \pm 0.4)°$ and an azimuth angle of $\varphi = (13.2 \pm 1.2)°$, the primary energy to $(1.01 \pm 0.06) \times 10^{18}$ eV. The radiation energy released in the shower was reconstructed to $(2.9 \pm 1.1) \times 10^6$ eV. **(a)** SD and RD array **(b)** Reconstructed two-dimensional LDF of the RD signal. **(c)** Reconstructed one-dimensional LDFs to the SD and the MD signal.

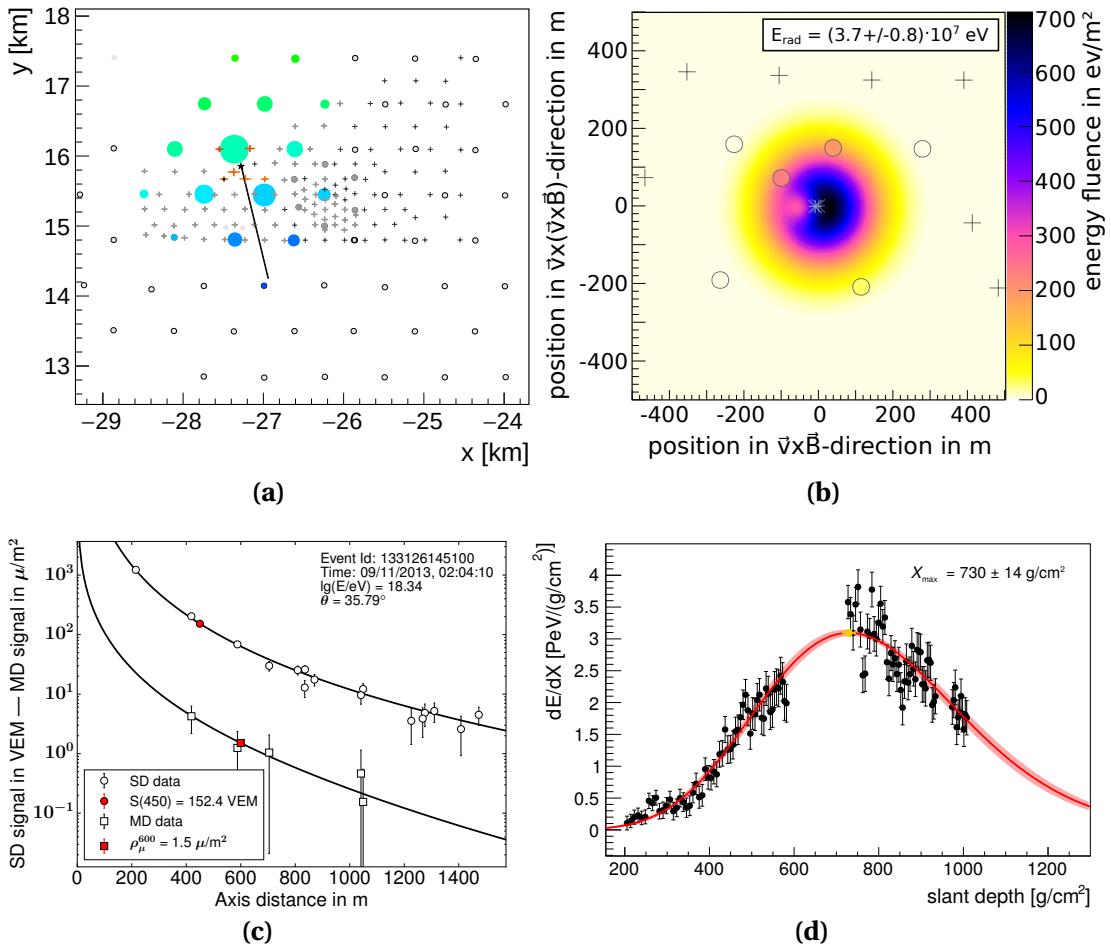

Figure D.2: 4-fold example event measured in Coihueco and HEAT The event was detected in 16 Surface Detector stations, 5 Muon Detector stations, 6 Radio Detector stations and 2 telescopes (Coihueco and HEAT). The arrival direction was reconstructed from the SD to a zenith angle of $\theta = (35.8 \pm 0.2)°$ and an azimuth angle of $\varphi = (281.8 \pm 0.4)°$, the primary energy to $(2.19 \pm 0.09) \times 10^{18}$ eV. The radiation energy released in the shower was reconstructed to $(3.7 \pm 0.8) \times 10^7$ eV from the RD signal. The shower maximum X_{max} was reconstructed to (730 ± 14) g cm^{-2} from the FD signal. **(a)** SD and RD array **(b)** Reconstructed two-dimensional LDF of the RD signal. **(c)** Reconstructed one-dimensional LDFs to the SD and the MD signal. **(d)** Reconstructed longitudinal profile of the energy deposit of the shower in the atmosphere.

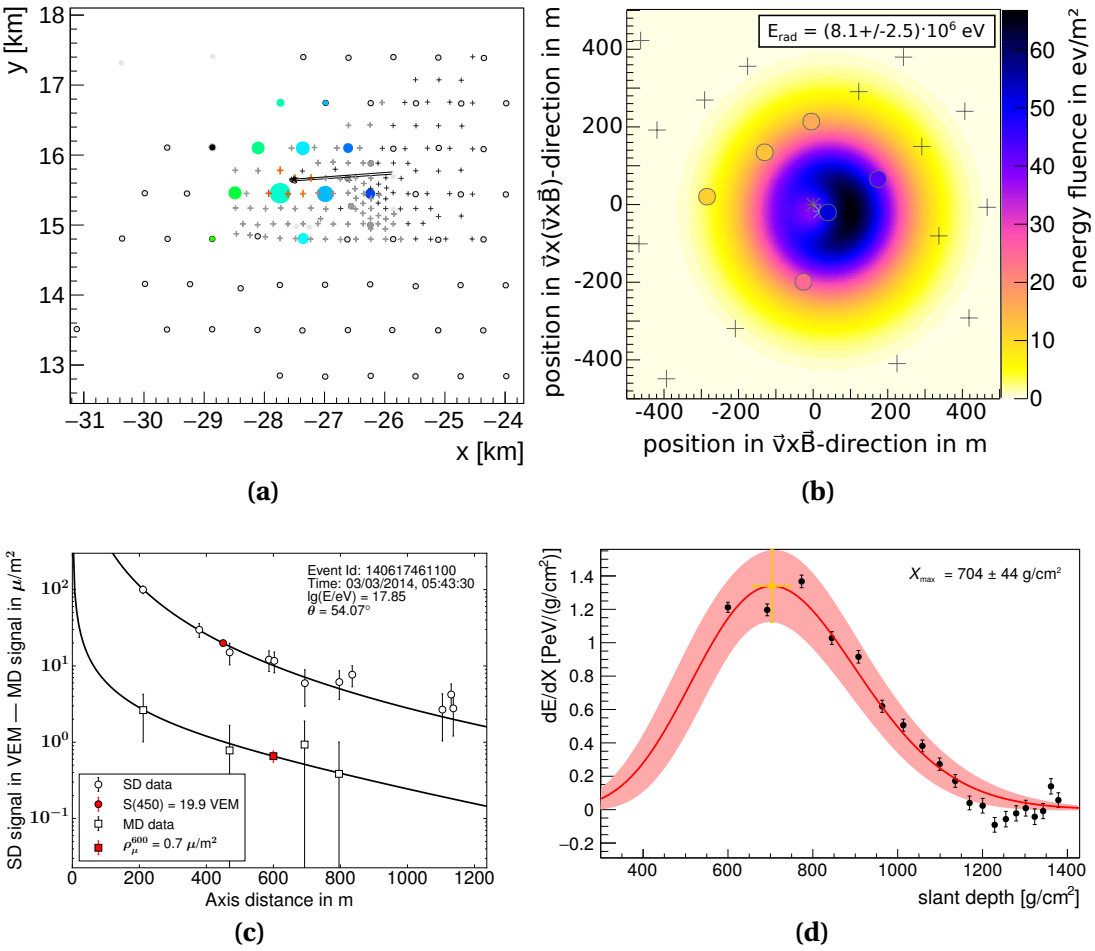

Figure D.3: 4-fold example event measured in Coihueco The event was detected in 11 Surface Detector stations, 4 Muon Detector stations, 6 Radio Detector stations and 1 telescope (Coihueco). The arrival direction was reconstructed from the SD to a zenith angle of $\theta = (54.1 \pm 0.3)°$ and an azimuth angle of $\varphi = (3.4 \pm 0.3)°$, the primary energy to $(7.16 \pm 1.10) \times 10^{17}$ eV. The radiation energy was reconstructed from the RD signal and is corrected for the zenith angle dependence to $(8.14 \pm 2.55) \times 10^6$ eV. The shower maximum X_{max} was reconstructed to (704 ± 44) g cm^{-2} from the FD signal. **(a)** SD and RD array **(b)** reconstructed two-dimensional LDF of the RD signal. **(c)** reconstructed one-dimensional LDFs to the SD and the MD signals. **(d)** Reconstructed longitudinal profile of the energy deposit of the shower in the atmosphere. The event was simulated for a proton and iron primary particle and successfully reconstructed, where the corresponding simulation is shown in Fig. 6.3.

Bibliography

[1] Pierre Auger Collaboration, A. Aab et al. "Observation of a Large-scale Anisotropy in the Arrival Directions of Cosmic Rays above 8×10^{18} eV". In: *Science* 357.6537 (2017), pp. 1266–1270. DOI: 10.1126/science.aan4338. arXiv: 1709.07321 [astro-ph.HE].

[2] T. Wulf. "Beobachtungen über Strahlung hoher Durchdringungsfähigkeit auf dem Eiffelturm". In: *Physikalische Zeitschrift* 11 (1910), pp. 811–813.

[3] V. F. Hess. "Über Beobachtungen der durchdringenden Strahlung bei sieben Freiballonfahrten". In: *Physikalische Zeitschrift* 13 (1912), p. 1084.

[4] J. R. Hörandel. "Early cosmic-ray work published in German". In: *American Institute of Physics Conference Series*. Ed. by J. F. Ormes. Vol. 1516. American Institute of Physics Conference Series, pp. 52–60. DOI: 10.1063/1.4792540. arXiv: 1212.0706.

[5] W. Kolhörster. "Messungen der durchdringenden Strahlung im Freiballon in grösseren Höhen". In: *Physikalische Zeitschrift* 14 (1913), pp. 1153–1155.

[6] W. Bothe and W. Kolhörster. "Das Wesen der Höhenstrahlung". In: *Physikalische Zeitschrift* 56 (1929), pp. 751–777.

[7] P. Auger et al. "Extensive cosmic ray showers". In: *Rev. Mod. Phys.* 11 (1939), pp. 288–291. DOI: 10.1103/RevModPhys.11.288.

[8] S. Mollerach and E. Roulet. "Progress in high-energy cosmic ray physics". In: *Prog. Part. Nucl. Phys.* 98 (2018), pp. 85–118. DOI: 10.1016/j.ppnp.2017.10.002. arXiv: 1710.11155 [astro-ph.HE].

[9] R. Engel, D. Heck, and T. Pierog. "Extensive air showers and hadronic interactions at high energy". In: *Ann. Rev. Nucl. Part. Sci.* 61 (2011), pp. 467–489. DOI: 10.1146/annurev.nucl.012809.104544.

[10] S.E.S. Ferreira and M.S. Potgieter. "Galactic cosmic rays in the heliosphere". In: *Advances in Space Research* 34.1 (2004). To the Edge of the Solar System and Beyond, pp. 115–125. ISSN: 0273-1177. DOI: http://dx.doi.org/10.1016/j.asr.2003.02.057.

[11] D. Kang. “Detection of cosmic rays in the PeV to EeV energy range”. In: *25th European Cosmic Ray Symposium (ECRS 2016) Turin, Italy, September 04-09, 2016*. 2017. arXiv: 1702.08743 [astro-ph.HE].

[12] KASCADE Collaboration, T. Antoni et al. “Muon density measurements with the KASCADE central detector”. In: *Astroparticle Physics* 16.4 (2002), pp. 373–386. ISSN: 0927-6505. DOI: http://dx.doi.org/10.1016/S0927-6505(01)00120-7.

[13] KASCADE Collaboration, T. Antoni et al. “KASCADE measurements of energy spectra for elemental groups of cosmic rays: Results and open problems”. In: *Astropart. Phys.* 24 (2005), pp. 1–25. DOI: 10.1016/j.astropartphys.2005.04.001. arXiv: astro-ph/0505413 [astro-ph].

[14] KASCADE-Grande Collaboration, W. D. Apel et al. “Kneelike structure in the spectrum of the heavy component of cosmic rays observed with KASCADE-Grande”. In: *Phys. Rev. Lett.* 107 (2011), p. 171104. DOI: 10.1103/PhysRevLett.107.171104. arXiv: 1107.5885 [astro-ph.HE].

[15] J. R. Hörandel. “Cosmic rays from the knee to the second knee: 10**4 to 10**18-eV”. In: *Mod. Phys. Lett.* A22 (2007). [,63(2006)], pp. 1533–1552. DOI: 10.1142/S0217732307024139. arXiv: astro-ph/0611387 [astro-ph].

[16] Tunka Collaboration, S. F. Berezhnev et al. “The Primary CR Spectrum by the Data of the Tunka-133 Array”. In: *JPS Conf. Proc.* 9 (2016), p. 010009. DOI: 10.7566/JPSCP.9.010009.

[17] HiRes Collaboration, R. U. Abbasi et al. “First observation of the Greisen-Zatsepin-Kuzmin suppression”. In: *Phys. Rev. Lett.* 100 (2008), p. 101101. DOI: 10.1103/PhysRevLett.100.101101. arXiv: astro-ph/0703099 [astro-ph].

[18] Pierre Auger Collaboration, I. Valino. “The flux of ultra-high energy cosmic rays after ten years of operation of the Pierre Auger Observatory”. In: *Proceedings, 34th International Cosmic Ray Conference (ICRC 2015): The Hague, The Netherlands, July 30-August 6, 2015*. Ed. by PoS. Vol. ICRC2015, p. 271.

[19] KASCADE-Grande Collaboration, W. D. Apel et al. “Ankle-like Feature in the Energy Spectrum of Light Elements of Cosmic Rays Observed with KASCADE-Grande”. In: *Phys. Rev.* D87 (2013), p. 081101. DOI: 10.1103/PhysRevD.87.081101. arXiv: 1304.7114 [astro-ph.HE].

[20] Pierre Auger Collaboration, J. Abraham et al. “Observation of the suppression of the flux of cosmic rays above 4×10^{19}eV”. In: *Phys. Rev. Lett.* 101 (2008), p. 061101. DOI: 10.1103/PhysRevLett.101.061101. arXiv: 0806.4302 [astro-ph].

[21] J. R. Hörandel. "Models of the knee in the energy spectrum of cosmic rays". In: *Astropart. Phys.* 21 (2004), pp. 241–265. DOI: 10.1016/j.astropartphys.2004.01.004. arXiv: astro-ph/0402356 [astro-ph].

[22] S. Thoudam et al. "Cosmic-ray energy spectrum and composition up to the ankle: the case for a second Galactic component". In: *Astron. Astrophys.* 595 (2016), A33. DOI: 10.1051/0004-6361/201628894. arXiv: 1605.03111 [astro-ph.HE].

[23] K. Greisen. "End to the Cosmic-Ray Spectrum?" In: *Phys. Rev. Lett.* 16 (17 04/1966), pp. 748–750. DOI: 10.1103/PhysRevLett.16.748.

[24] G. T. Zatsepin and V. A. Kuzmin. "Upper limit of the spectrum of cosmic rays". In: *JETP Lett.* 4 (1966). [Pisma Zh. Eksp. Teor. Fiz.4,114(1966)], pp. 78–80.

[25] Pierre Auger Collaboration, A. Aab et al. "The Pierre Auger Observatory Upgrade - Preliminary Design Report". In: *ArXiv e-prints* (04/2016). arXiv: 1604.03637 [astro-ph.IM].

[26] J. Blümer, R. Engel, and J. R. Hörandel. "Cosmic rays from the knee to the highest energies". In: *Progress in Particle and Nuclear Physics* 63 (10/2009), pp. 293–338. DOI: 10.1016/j.ppnp.2009.05.002. arXiv: 0904.0725 [astro-ph.HE].

[27] T. Pierog. *Xmax over cosmic ray energies*. personal communication. 21/12/2017.

[28] NA61 Collaboration, T2K Collaboration, N. Abgrall. "NA61-SHINE: Hadron Production Measurements for Cosmic Ray and Neutrino Experiments". In: 2010. arXiv: 1005.3692 [hep-ex].

[29] CMS CASTOR Collaboration, P. Gottlicher. "Design and test beam studies for the CASTOR calorimeter of the CMS experiment". In: *Nucl. Instrum. Meth.* A623 (2010), pp. 225–227. DOI: 10.1016/j.nima.2010.02.203.

[30] CMS CASTOR Collaboration, A. M. Sirunyan et al. "Measurement of the inclusive energy spectrum in the very forward direction in proton-proton collisions at $\sqrt{s}$ = 13 TeV". In: *JHEP* 08 (2017), p. 046. DOI: 10.1007/JHEP08(2017)046. arXiv: 1701.08695 [hep-ex].

[31] V. Berezinsky, A. Z. Gazizov, and S. I. Grigorieva. "Dip in UHECR spectrum as signature of proton interaction with CMB". In: *Phys. Lett.* B612 (2005), pp. 147–153. DOI: 10.1016/j.physletb.2005.02.058. arXiv: astro-ph/0502550 [astro-ph].

[32] V. Berezinsky, A. Z. Gazizov, and S. I. Grigorieva. "On astrophysical solution to ultrahigh-energy cosmic rays". In: *Phys. Rev.* D74 (2006), p. 043005. DOI: 10.1103/PhysRevD.74.043005. arXiv: hep-ph/0204357 [hep-ph].

[33] Pierre Auger Collaboration, A. Aab et al. "Evidence for a mixed mass composition at the 'ankle' in the cosmic-ray spectrum". In: *Phys. Lett.* B762 (2016), pp. 288–295. DOI: 10.1016/j.physletb.2016.09.039. arXiv: 1609.08567 [astro-ph.HE].

[34] "Pierre Auger Observatory and Telescope Array: Joint Contributions to the 35th International Cosmic Ray Conference (ICRC 2017)". In: *Proceedings, 35th International Cosmic Ray Conference (ICRC 2017): Bexco, Busan, Korea, July 12-20, 2017*. 2018. arXiv: 1801.01018 [astro-ph.HE].

[35] Pierre Auger Collaboration, A. Aab et al. "Indication of anisotropy in arrival directions of ultra-high-energy cosmic rays through comparison to the flux pattern of extragalactic gamma-ray sources". In: *Astrophys. J. Lett.* (2018). DOI: 10.3847/2041-8213/aaa66d. arXiv: 1801.06160 [astro-ph.HE].

[36] Telescope Array Collaboration, J. P. Lundquist, P. Sokolsky, and P. Tinyakov. "Evidence of Intermediate-Scale Energy Spectrum Anisotropy in the Northern Hemisphere from Telescope Array". In: *Proceedings, 35th International Cosmic Ray Conference (ICRC 2017): Bexco, Busan, Korea, July 12-20, 2017*. Ed. by PoS. Vol. ICRC2017. 513.

[37] E. Fermi. "On the Origin of the Cosmic Radiation". In: *Phys. Rev.* 75 (1949), pp. 1169–1174. DOI: 10.1103/PhysRev.75.1169.

[38] R. D. Blandford and J. P. Ostriker. "Particle Acceleration by Astrophysical Shocks". In: *Astrophys. J.* 221 (1978), pp. L29–L32. DOI: 10.1086/182658.

[39] R. D. Blandford and J. P. Ostriker. "SUPERNOVA SHOCK ACCELERATION OF COSMIC RAYS IN THE GALAXY". In: *Astrophys. J.* 237 (1980), pp. 793–808. DOI: 10.1086/157926.

[40] T. K. Gaisser, R. Engel, and E. Resconi. *Cosmic Rays and Particle Physics*. Cambridge University Press. ISBN: 9780521016469.

[41] M. T. Dova. "Ultra-High Energy Cosmic Rays". In: *Proceedings, 7th CERN-Latin-American School of High-Energy Physics (CLASHEP2013): Arequipa, Peru, March 6-19, 2013*, pp. 169–190. DOI: 10.5170/CERN-2015-001.169. arXiv: 1604.07584 [astro-ph.HE].

[42] A. M. Hillas. "The Origin of Ultra-High-Energy Cosmic Rays". In: ARA&A 22 (1984), pp. 425–444. DOI: 10.1146/annurev.aa.22.090184.002233.

[43] ESO/WFI (Optical); MPIfR/ESO/APEX/A.Weiss et al. (Submillimetre); NASA/CXC/CfA/R.Kraft et al. (X-ray). *Colour composite image of Centaurus A*. 17/01/2018. URL: https://www.eso.org/public/germany/images/eso0903a/.

[44] Pierre Auger Collaboration, A. Aab et al. "Combined fit of spectrum and composition data as measured by the Pierre Auger Observatory". In: *JCAP* 1704.04 (2017), p. 038. DOI: 10.1088/1475-7516/2017/04/038. arXiv: 1612.07155 [astro-ph.HE].

[45] GROND, SALT Group, OzGrav, DFN, INTEGRAL, Virgo, Insight-Hxmt, MAXI Team, Fermi-LAT, J-GEM, RATIR, IceCube, CAASTRO, LWA, ePESSTO, GRAWITA, RIMAS, SKA South Africa/MeerKAT, H.E.S.S., 1M2H Team, IKI-GW Follow-up, Fermi GBM, Pi of Sky, DWF (Deeper Wider Faster Program), Dark Energy Survey, MASTER, AstroSat Cadmium Zinc Telluride Imager Team, Swift, Pierre Auger, ASKAP, VINROUGE, JAGWAR, Chandra Team at McGill University, TTU-NRAO, GROWTH, AGILE Team, MWA, ATCA, AST3, TOROS, Pan-STARRS, NuSTAR, ATLAS Telescopes, BOOTES, CaltechNRAO, LIGO Scientific, High Time Resolution Universe Survey, Nordic Optical Telescope, Las Cumbres Observatory Group, TZAC Consortium, LOFAR, IPN, DLT40, Texas Tech University, HAWC, ANTARES, KU, Dark Energy Camera GW-EM, CALET, Euro VLBI Team, ALMA, B. P. Abbott et al. "Multi-messenger Observations of a Binary Neutron Star Merger". In: *Astrophys. J.* 848.2 (2017), p. L12. DOI: 10.3847/2041-8213/aa91c9. arXiv: 1710.05833 [astro-ph.HE].

[46] Virgo Collaboration, IceCube Collaboration, Pierre Auger Collaboration, ANTARES Collaboration, LIGO Scientific Collaboration, A. Albert et al. "Search for High-energy Neutrinos from Binary Neutron Star Merger GW170817 with ANTARES, IceCube, and the Pierre Auger Observatory". In: *Astrophys. J.* 850.2 (2017), p. L35. DOI: 10.3847/2041-8213/aa9aed. arXiv: 1710.05839 [astro-ph.HE].

[47] P. S. Marrocchesi. "Charged Cosmic Rays: a Review of Balloon and Space Borne Measurements". In: *25th European Cosmic Ray Symposium (ECRS 2016) Turin, Italy, September 04-09, 2016*. 2017. arXiv: 1704.00304 [astro-ph.HE].

[48] H. Yüksel, T. Stanev, M. D. Kistler, and P. P. Kronberg. "The Centaurus A Ultrahigh-energy Cosmic-Ray Excess and the Local Extragalactic Magnetic Field". In: ApJ 758, 16 (10/2012), p. 16. DOI: 10.1088/0004-637X/758/1/16. arXiv: 1203.3197 [astro-ph.HE].

[49] T. Stanev, D. Seckel, and R. Engel. "Propagation of ultrahigh-energy protons in regular extragalactic magnetic fields". In: *Phys. Rev.* D68 (2003), p. 103004. DOI: 10.1103/PhysRevD.68.103004. arXiv: astro-ph/0108338 [astro-ph].

[50] T. M. Kneiske, T. Bretz, K. Mannheim, and D. H. Hartmann. "Implications of cosmological gamma-ray absorption. 2. Modification of gamma-ray spectra". In: *Astron. Astrophys.* 413 (2004), pp. 807–815. DOI: 10.1051/0004-6361:20031542. arXiv: astro-ph/0309141 [astro-ph].

[51] R. Alves Batista et al. "CRPropa: a public framework to propagate UHECRs in the universe". In: *EPJ Web Conf.* 99 (2015), p. 13004. DOI: 10.1051/epjconf/20159913004. arXiv: 1411.2259 [astro-ph.IM].

[52] A.M. Hillas. "The energy spectrum of cosmic rays in an evolving universe". In: *Physics Letters A* 24.12 (1967), pp. 677–678. ISSN: 0375-9601. DOI: http://dx.doi.org/10.1016/0375-9601(67)91023-7.

[53] G. R. Blumenthal. "Energy loss of high-energy cosmic rays in pair-producing collisions with ambient photons". In: *Phys. Rev.* D1 (1970), pp. 1596–1602. DOI: 10.1103/PhysRevD.1.1596.

[54] D. Allard. "Extragalactic propagation of ultrahigh energy cosmic-rays". In: *Astroparticle Physics* 39-40 (2012). Cosmic Rays Topical Issue, pp. 33–43. ISSN: 0927-6505. DOI: http://doi.org/10.1016/j.astropartphys.2011.10.011.

[55] J. Matthews. "A Heitler model of extensive air showers". In: *Astropart. Phys.* 22 (2005), pp. 387–397. DOI: 10.1016/j.astropartphys.2004.09.003.

[56] J. F. Carlson and J. R. Oppenheimer. "On Multiplicative Showers". In: *Phys. Rev.* 51 (1937), pp. 220–231. DOI: 10.1103/PhysRev.51.220.

[57] W. Heitler. *The Quantum Theory of Radiation: Third Edition*. Oxford University Press, 1954, 368ff. ISBN: 0486645584.

[58] D. Heck, G. Schatz, T. Thouw, J. Knapp, and J. N. Capdevielle. "CORSIKA: A Monte Carlo code to simulate extensive air showers". In: *Forschungszentrum Karlsruhe Wissenschaftliche Berichte* FZKA-6019 (1998).

[59] J. Alvarez-Muniz, R. Engel, T. K. Gaisser, J. A. Ortiz, and T. Stanev. "Hybrid simulations of extensive air showers". In: *Phys. Rev.* D66 (2002), p. 033011. DOI: 10.1103/PhysRevD.66.033011. arXiv: astro-ph/0205302 [astro-ph].

[60] K.-H. Kampert and M. Unger. "Measurements of the Cosmic Ray Composition with Air Shower Experiments". In: *Astropart. Phys.* 35 (2012), pp. 660–678. DOI: 10.1016/j.astropartphys.2012.02.004. arXiv: 1201.0018 [astro-ph.HE].

[61] S. Ostapchenko. "Monte Carlo treatment of hadronic interactions in enhanced Pomeron scheme: I. QGSJET-II model". In: *Phys. Rev.* D83 (2011), p. 014018. DOI: 10.1103/PhysRevD.83.014018. arXiv: 1010.1869 [hep-ph].

[62] T. Pierog, Iu. Karpenko, J. M. Katzy, E. Yatsenko, and K. Werner. "EPOS LHC: Test of collective hadronization with data measured at the CERN Large Hadron Collider". In: *Phys. Rev.* C92.3 (2015), p. 034906. DOI: 10.1103/PhysRevC.92.034906. arXiv: 1306.0121 [hep-ph].

[63] F. Riehn et al. "The hadronic interaction model Sibyll 2.3c and Feynman scaling". In: *Proceedings, 35th International Cosmic Ray Conference (ICRC 2017): Bexco, Busan, Korea, July 12-20, 2017*. Ed. by PoS. Vol. ICRC2017, p. 301.

[64] T. Pierog. "Air Shower Simulation with a New Generation of post-LHC Hadronic Interaction Models in CORSIKA". In: *Proceedings, 35th International Cosmic Ray Conference (ICRC 2017): Bexco, Busan, Korea, July 12-20, 2017*. Ed. by PoS. Vol. ICRC2017, p. 1100.

[65] Pierre Auger Collaboration, A. Aab et al. "Testing Hadronic Interactions at Ultrahigh Energies with Air Showers Measured by the Pierre Auger Observatory". In: *Phys. Rev. Lett.* 117.19 (2016), p. 192001. DOI: 10.1103/PhysRevLett.117.192001. arXiv: 1610.08509 [hep-ex].

[66] A. Haungs. "Cosmic Rays from the Knee to the Ankle". In: *Proceedings, 13th International Conference on Topics in Astroparticle and Underground Physics (TAUP 2013): Asilomar, California, September 8-13, 2013* 61 (2015), pp. 425–434. DOI: 10.1016/j.phpro.2014.12.094. arXiv: 1504.01859 [astro-ph.HE].

[67] Pierre Auger Collaboration, A. Aab et al. "The Pierre Auger Cosmic Ray Observatory". In: *Nucl. Instrum. Meth.* A798 (2015), pp. 172–213. DOI: 10.1016/j.nima.2015.06.058. arXiv: 1502.01323 [astro-ph.IM].

[68] HAWC Collaboration, A. J. Smith. "HAWC: Design, Operation, Reconstruction and Analysis". In: *ArXiv e-prints* (08/2015). arXiv: 1508.05826 [astro-ph.IM].

[69] IceCube Collaboration, R. U. Abbasi et al. "IceTop: The surface component of IceCube". In: *Nucl. Instrum. Meth.* A700 (2013), pp. 188–220. DOI: 10.1016/j.nima.2012.10.067. arXiv: 1207.6326 [astro-ph.IM].

[70] Pierre Auger Collaboration, A. Aab et al. "Prototype muon detectors for the AMIGA component of the Pierre Auger Observatory". In: *JINST* 11.02 (2016), P02012. DOI: 10.1088/1748-0221/11/02/P02012. arXiv: 1605.01625 [physics.ins-det].

[71] KASCADE-Grande Collaboration, W. D. Apel et al. "The KASCADE-Grande experiment". In: *Nucl. Instrum. Meth.* A620 (2010), pp. 202–216. DOI: 10.1016/j.nima.2010.03.147.

[72] Tunka Collaboration, R. D. Monkhoev et al. "The Tunka-Grande experiment". In: *JINST* 12.06 (2017), p. C06019. DOI: 10.1088/1748-0221/12/06/C06019.

[73] AGASA Collaboration, N. Chiba et al. "Akeno giant air shower array (AGASA) covering 100-km^2 area". In: *Nucl. Instrum. Meth.* A311 (1992), pp. 338–349. DOI: 10.1016/0168-9002(92)90882-5.

[74] Telescope Array Collaboration, T. Abu-Zayyad et al. "The surface detector array of the Telescope Array experiment". In: *Nucl. Instrum. Meth.* A689 (2013), pp. 87–97. DOI: 10.1016/j.nima.2012.05.079. arXiv: 1201.4964 [astro-ph.IM].

[75] KASCADE-Grande Collaboration, D. Kang et al. "Sensitivity of KASCADE-Grande data to hadronic interaction models". In: *ArXiv e-prints* (09/2010). arXiv: 1009.4902 [astro-ph.HE].

[76] Pierre Auger Collaboration, A. Aab et al. "Inferences on mass composition and tests of hadronic interactions from 0.3 to 100 EeV using the water-Cherenkov detectors of the Pierre Auger Observatory". In: *Phys. Rev.* D96.12 (2017), p. 122003. DOI: 10.1103/PhysRevD.96.122003. arXiv: 1710.07249 [astro-ph.HE].

[77] HiRes Collaboration, G. Thomson. "New results from the HiRes experiment". In: *Nucl. Phys. Proc. Suppl.* 136 (2004). [,28(2004)], pp. 28–33. DOI: 10.1016/j.nuclphysbps.2004.10.061.

[78] Telescope Array Collaboration, H. Tokuno et al. "New air fluorescence detectors employed in the Telescope Array experiment". In: *Nucl. Instrum. Meth.* A676 (2012), pp. 54–65. DOI: 10.1016/j.nima.2012.02.044. arXiv: 1201.0002 [astro-ph.IM].

[79] JEM-EUSO Collaboration, M. Bertaina and E. Parizot. "The JEM-EUSO mission: a space observatory to study the origin of Ultra-High Energy Cosmic Rays". In: *Nuclear Physics B - Proceedings Supplements* 256 (2014), pp. 275–286. ISSN: 0920-5632. DOI: http://dx.doi.org/10.1016/j.nuclphysbps.2014.10.033.

[80] TUS Collaboration, B. A. Khrenov et al. "First results from the TUS orbital detector in the extensive air shower mode". In: *ArXiv e-prints* (04/2017). arXiv: 1704.07704 [astro-ph.IM].

[81] HESS Collaboration, R. Cornils et al. “The optical system of the HESS imaging atmospheric Cherenkov telescopes, Part 2: Mirror alignment and point spread function”. In: *Astropart. Phys.* 20 (2003), pp. 129–143. DOI: 10.1016/S0927-6505(03)00172-5. arXiv: astro-ph/0308247 [astro-ph].

[82] MAGIC Collaboration, D. Tescaro. “The upgraded MAGIC Cherenkov telescopes”. In: *Nucl. Instrum. Meth.* A766 (2014), pp. 65–68. DOI: 10.1016/j.nima.2014.04.037.

[83] VERITAS Collaboration, J. Holder. “Latest Results from VERITAS: Gamma 2016”. In: *AIP Conf. Proc.* 1792.1 (2017), p. 020013. DOI: 10.1063/1.4968898. arXiv: 1609.02881 [astro-ph.HE].

[84] CTA Consortium, C. Bigongiari. “The Cherenkov Telescope Array”. In: *Nucl. Part. Phys. Proc.* 279-281 (2016), pp. 174–181. DOI: 10.1016/j.nuclphysbps.2016.10.025. arXiv: 1606.08190 [astro-ph.IM].

[85] Tunka Collaboration, S. F. Berezhnev et al. “The Tunka - Multi-component EAS detector for high energy cosmic ray studies”. In: *Nucl. Instrum. Meth.* A732 (2013), pp. 281–285. DOI: 10.1016/j.nima.2013.05.180.

[86] TAIGA Collaboration, N. Budnev et al. “The TAIGA experiment: From cosmic-ray to gamma-ray astronomy in the Tunka valley”. In: *Nucl. Instrum. Meth.* A845 (2017), pp. 330–333. DOI: 10.1016/j.nima.2016.06.041.

[87] G. A. Askar’yan. “Excess negative charge of an electron-photon shower and its coherent radio emission”. In: *Sov. Phys. JETP* 14.2 (1962). [Zh. Eksp. Teor. Fiz.41,616(1961)], pp. 441–443.

[88] J.V. Jelley et al. “Radio pulses from extensive cosmic-ray air showers”. In: *Nature* 205.4969 (1965), pp. 327–328. DOI: 10.1038/205327a0.

[89] F. D. Kahn and I. Lerche. “Radiation from Cosmic Ray Air Showers”. In: *Proceedings of the Royal Society of London A: Mathematical, Physical and Engineering Sciences* 289.1417 (1966), pp. 206–213. ISSN: 0080-4630. DOI: 10.1098/rspa.1966.0007. eprint: http://rspa.royalsocietypublishing.org/content/289/1417/206.full.pdf.

[90] T. Huege. “Radio detection of cosmic ray air showers in the digital era”. In: *Phys. Rept.* 620 (2016), pp. 1–52. DOI: 10.1016/j.physrep.2016.02.001. arXiv: 1601.07426 [astro-ph.IM].

[91] F. G. Schröder. “Radio detection of Cosmic-Ray Air Showers and High-Energy Neutrinos”. In: *Prog. Part. Nucl. Phys.* 93 (2017), pp. 1–68. DOI: 10.1016/j.ppnp.2016.12.002. arXiv: 1607.08781 [astro-ph.IM].

[92] LOPES Collaboration, W. D. Apel et al. “Thunderstorm Observations by Air-Shower Radio Antenna Arrays”. In: *Adv. Space Res.* 48 (2011), pp. 1295–1303. DOI: 10.1016/j.asr.2011.06.003. arXiv: 1303.7068 [astro-ph.HE].

[93] J. Neuser. “Cosmic Rays and the Atmospheric Electric Field - Reconstruction and Data Analysis of Radio Emission from Air Showers at the Auger Engineering Radio Array”. PhD thesis. Bergische Universität Wuppertal, 2015.

[94] Pierre Auger Collaboration, P. Abreu et al. “Results of a Self-Triggered Prototype System for Radio-Detection of Extensive Air Showers at the Pierre Auger Observatory”. In: *JINST* 7 (2012), P11023. DOI: 10.1088/1748-0221/7/11/P11023. arXiv: 1211.0572 [astro-ph.HE].

[95] TREND Collaboration, T. Saugrin et al. “First Detection of Extensive Air Showers by the TREND Self-Triggering Radio Experiment”. In: *Proceedings, 32nd International Cosmic Ray Conference (ICRC 2011): Beijing, China, August 11-18, 2011*. Vol. 3. 2011, p. 274. DOI: 10.7529/ICRC2011/V03/1177.

[96] ARIANNA Collaboration, S. W. Barwick et al. “Radio detection of air showers with the ARIANNA experiment on the Ross Ice Shelf”. In: *Astropart. Phys.* 90 (2017), pp. 50–68. DOI: 10.1016/j.astropartphys.2017.02.003. arXiv: 1612.04473 [astro-ph.IM].

[97] A. Balagopal V., A. Haungs, T. Huege, and F. G. Schröder. “Search for PeVatrons at the Galactic Center using a radio air-shower array at the South Pole”. In: *Eur. Phys. J.* C78.2 (2018), p. 111. DOI: 10.1140/epjc/s10052-018-5537-2. arXiv: 1712.09042 [astro-ph.IM].

[98] LOPES Collaboration, H. Falcke et al. “Detection and imaging of atmospheric radio flashes from cosmic ray air showers”. In: *Nature* 435 (2005), pp. 313–316. DOI: 10.1038/nature03614. arXiv: astro-ph/0505383 [astro-ph].

[99] Tunka-Rex Collaboration, P. A. Bezyazeekov et al. “Measurement of cosmic-ray air showers with the Tunka Radio Extension (Tunka-Rex)”. In: *Nucl. Instrum. Meth.* A802 (2015), pp. 89–96. DOI: 10.1016/j.nima.2015.08.061. arXiv: 1509.08624 [astro-ph.IM].

[100] LOFAR Collaboration, M. P. van Haarlem et al. “LOFAR: The LOw-Frequency ARray”. In: *Astron. Astrophys.* 556 (2013), A2. DOI: 10.1051/0004-6361/201220873. arXiv: 1305.3550 [astro-ph.IM].

[101] ARA Collaboration, P. Allison et al. “Performance of two Askaryan Radio Array stations and first results in the search for ultrahigh energy neutrinos”. In: *Phys. Rev.* D93.8 (2016), p. 082003. DOI: 10.1103/PhysRevD.93.082003. arXiv: 1507.08991 [astro-ph.HE].

[102] GRAND Collaboration, K. Fang et al. "The Giant Radio Array for Neutrino Detection (GRAND): Present and Perspectives". In: *Proceedings, 35th International Cosmic Ray Conference (ICRC 2017): Bexco, Busan, Korea, July 12-20, 2017*. Ed. by PoS. Vol. ICRC2017. 996. arXiv: 1708.05128 [astro-ph.IM].

[103] I. S. Ohta et al. "Measurement of microwave radiation from electron beam in the atmosphere". In: *Nucl. Instrum. Meth.* A810 (2016), pp. 44–50. DOI: 10.1016/j.nima.2015.11.113.

[104] I. Al Samarai et al. "Molecular Bremsstrahlung Radiation at GHz Frequencies in Air". In: *Phys. Rev.* D93.5 (2016), p. 052004. DOI: 10.1103/PhysRevD.93.052004. arXiv: 1601.00551 [astro-ph.IM].

[105] CROME Collaboration, R. Smida et al. "First Experimental Characterization of Microwave Emission from Cosmic Ray Air Showers". In: *Phys. Rev. Lett.* 113.22 (2014), p. 221101. DOI: 10.1103/PhysRevLett.113.221101. arXiv: 1410.8291 [astro-ph.IM].

[106] B. Revenu and V. Marin. "Coherent radio emission from the cosmic ray air shower sudden death". In: *Proceedings, 33rd International Cosmic Ray Conference (ICRC2013): Rio de Janeiro, Brazil, July 2-9, 2013*. 2013, p. 0398. arXiv: 1307.5673 [astro-ph.HE].

[107] K. D. de Vries et al. "The cosmic-ray air-shower signal in Askaryan radio detectors". In: *Astropart. Phys.* 74 (2016), pp. 96–104. DOI: 10.1016/j.astropartphys.2015.10.003. arXiv: 1503.02808 [astro-ph.HE].

[108] S. A. Colgate. "The detection of high-energy cosmic-ray showers by the combined optical and electromagnetic pulse". In: *Journal of Geophysical Research* 72.19 (1967), pp. 4869–4879. ISSN: 2156-2202. DOI: 10.1029/JZ072i019p04869.

[109] CODALEMA Collaboration, D. Ardouin et al. "Geomagnetic origin of the radio emission from cosmic ray induced air showers observed by CODALEMA". In: *Astropart. Phys.* 31 (2009), pp. 192–200. DOI: 10.1016/j.astropartphys.2009.01.001. arXiv: 0901.4502 [astro-ph.HE].

[110] Pierre Auger Collaboration, A. Aab et al. "Probing the radio emission from air showers with polarization measurements". In: Phys. Rev. D 89.5, 052002 (03/2014), p. 052002. DOI: 10.1103/PhysRevD.89.052002. arXiv: 1402.3677 [astro-ph.HE].

[111] CODALEMA Collaboration, A. Bellétoile et al. "Evidence for the charge-excess contribution in air shower radio emission observed by the CODALEMA experiment". In: *Astropart. Phys.* 69 (2015), pp. 50–60. DOI: 10.1016/j.astropartphys.2015.03.007.

[112] D. Kostunin et al. “Reconstruction of air-shower parameters for large-scale radio detectors using the lateral distribution”. In: *Astropart. Phys.* 74 (2016), pp. 79–86. DOI: 10.1016/j.astropartphys.2015.10.004. arXiv: 1504.05083 [astro-ph.HE].

[113] LOFAR Collaboration, P. Schellart et al. “Polarized radio emission from extensive air showers measured with LOFAR”. In: *JCAP* 1410.10 (2014), p. 014. DOI: 10.1088/1475-7516/2014/10/014. arXiv: 1406.1355 [astro-ph.HE].

[114] LOFAR Collaboration, A. Corstanje et al. “The shape of the radio wavefront of extensive air showers as measured with LOFAR”. In: *Astropart. Phys.* 61 (2015), pp. 22–31. DOI: 10.1016/j.astropartphys.2014.06.001. arXiv: 1404.3907 [astro-ph.HE].

[115] LOPES Collaboration, W. D. Apel et al. “The wavefront of the radio signal emitted by cosmic ray air showers”. In: *JCAP* 1409.09 (2014), p. 025. DOI: 10.1088/1475-7516/2014/09/025. arXiv: 1404.3283 [hep-ex].

[116] LOPES Collaboration, F. G. Schröder et al. “Interferometric Radio Measurements of Air Showers with LOPES: Final Results”. In: *Proceedings, 35th International Cosmic Ray Conference (ICRC 2017): Bexco, Busan, Korea, July 12-20, 2017*. Ed. by PoS. Vol. ICRC2017. 458. arXiv: 1708.00626 [astro-ph.HE].

[117] LOFAR Collaboration, J. R. Hörandel et al. “Measurement of the properites of cosmic rays with the LOFAR radio telescope”. In: *25th European Cosmic Ray Symposium (ECRS 2016) Turin, Italy, September 04-09, 2016*. 2017. arXiv: 1705.04233 [astro-ph.HE].

[118] Pierre Auger Collaboration, A. Aab et al. “Energy Estimation of Cosmic Rays with the Engineering Radio Array of the Pierre Auger Observatory”. In: *Phys. Rev.* D93.12 (2016), p. 122005. DOI: 10.1103/PhysRevD.93.122005. arXiv: 1508.04267 [astro-ph.HE].

[119] Tunka-Rex Collaboration, P. A. Bezyazeekov et al. “Radio measurements of the energy and the depth of the shower maximum of cosmic-ray air showers by Tunka-Rex”. In: *JCAP* 1601.01 (2016), p. 052. DOI: 10.1088/1475-7516/2016/01/052. arXiv: 1509.05652 [hep-ex].

[120] Pierre Auger Collaboration, E. M. Holt. “Recent Results of the Auger Engineering Radio Array (AERA)”. In: *Proceedings, 35th International Cosmic Ray Conference (ICRC 2017): Bexco, Busan, Korea, July 12-20, 2017*. Ed. by PoS. Vol. ICRC2017. 492. arXiv: 1708.06592 [astro-ph.HE].

[121] S. Buitink et al. “Method for high precision reconstruction of air shower X_{max} using two-dimensional radio intensity profiles”. In: *Phys. Rev.* D90.8

(2014), p. 082003. DOI: 10.1103/PhysRevD.90.082003. arXiv: 1408.7001 [astro-ph.IM].

[122] Pierre Auger Collaboration, I. Allekotte et al. "The Surface Detector System of the Pierre Auger Observatory". In: *Nucl. Instrum. Meth.* A586 (2008), pp. 409–420. DOI: 10.1016/j.nima.2007.12.016. arXiv: 0712.2832 [astro-ph].

[123] Pierre Auger Collaboration, X. Bertou et al. "Calibration of the surface array of the Pierre Auger Observatory". In: *Nucl. Instrum. Meth.* A568 (2006), pp. 839–846. DOI: 10.1016/j.nima.2006.07.066.

[124] Pierre Auger Collaboration, J. Abraham et al. "The Fluorescence Detector of the Pierre Auger Observatory". In: *Nucl. Instrum. Meth.* A620 (2010), pp. 227–251. DOI: 10.1016/j.nima.2010.04.023. arXiv: 0907.4282 [astro-ph.IM].

[125] Pierre Auger Collaboration, P. Abreu et al. "Techniques for Measuring Aerosol Attenuation using the Central Laser Facility at the Pierre Auger Observatory". In: *JINST* 8 (2013), P04009. DOI: 10.1088/1748-0221/8/04/P04009. arXiv: 1303.5576 [astro-ph.IM].

[126] NOAA Air Resources Laboratory (ARL). *Global Data Assimilation System (GDAS1) Archive Information, Technical report.* http://ready.arl.noaa.gov/gdas1.php. Accessed: 2017-12-12.

[127] T. K. Gaisser and A. M. Hillas. "Reliability of the method of constant intensity cuts for reconstructing the average development of vertical showers". In: *International Cosmic Ray Conference* 8 (1977), pp. 353–357.

[128] Pierre Auger Collaboration, M. Tueros. "Estimate of the non-calorimetric energy of showers observed with the fluorescence and surface detectors of the Pierre Auger Observatory". In: *Proceedings, 33rd International Cosmic Ray Conference (ICRC2013): Rio de Janeiro, Brazil, July 2-9, 2013.* arXiv: 1307.5059 [astro-ph.HE].

[129] A. Schulz. "Measurement of the energy spectrum and mass composition of ultra-high energy cosmic rays". PhD thesis. Karlsruher Institut für Technologie (KIT), 2016. DOI: 10.5445/IR/1000053434.

[130] S. Müller and M. Roth. "A CORSIKA study on the influence of muon detector thresholds on the separability of primary cosmic rays at highest energies". In: *Proceedings, 34th International Cosmic Ray Conference (ICRC 2015): The Hague, The Netherlands, July 30-August 6, 2015.* Ed. by PoS. Vol. ICRC2015. 419.

[131] Pierre Auger Collaboration, A. Aab et al. “Muon counting using silicon photomultipliers in the AMIGA detector of the Pierre Auger observatory”. In: *JINST* 12.03 (2017), P03002. DOI: 10.1088/1748-0221/12/03/P03002. arXiv: 1703.06193 [astro-ph.IM].

[132] Pierre Auger Collaboration, B. Wundheiler. “The AMIGA muon counters of the Pierre Auger Observatory: Performance and first data”. In: *Proceedings, 32nd International Cosmic Ray Conference (ICRC 2011): Beijing, China, August 11-18, 2011*. Vol. 3. 2011, p. 84. DOI: 10.7529/ICRC2011/V03/0341.

[133] A. Lucero et al. “Analog multiplexer for testing multianode photomultipliers used in AMIGA project of the Pierre Auger Observatory”. In: *JINST* 10.09 (2015), T09004. DOI: 10.1088/1748-0221/10/09/T09004.

[134] Pierre Auger Collaboration, J. M. Figueira. “An improved reconstruction method for the AMIGA detectors”. In: *Proceedings, 35th International Cosmic Ray Conference (ICRC 2017): Bexco, Busan, Korea, July 12-20, 2017*. Ed. by PoS. Vol. ICRC2017. 396. arXiv: 1708.06592 [astro-ph.HE].

[135] S. Müller. “Measurement of the cosmic ray composition with air showers detected by the AMIGA extension at the Pierre Auger Observatory”. personal conversation, thesis in preparation. PhD thesis. Karlsruher Institut für Technologie (KIT), 2018.

[136] Pierre Auger Collaboration, P. Abreu et al. “Advanced functionality for radio analysis in the Offline software framework of the Pierre Auger Observatory”. In: *Nuclear Instruments and Methods in Physics Research A* 635 (04/2011), pp. 92–102. DOI: 10.1016/j.nima.2011.01.049. arXiv: 1101.4473 [astro-ph.IM].

[137] Pierre Auger Collaboration, P. Abreu et al. “Results of a self-triggered prototype system for radio-detection of extensive air showers at the Pierre Auger Observatory”. In: *Journal of Instrumentation* 7 (11/2012), P11023. DOI: 10.1088/1748-0221/7/11/P11023. arXiv: 1211.0572 [astro-ph.HE].

[138] LOFAR Collaboration, P. Schellart et al. “Probing Atmospheric Electric Fields in Thunderstorms through Radio Emission from Cosmic-Ray-Induced Air Showers”. In: *Phys. Rev. Lett.* 114.16 (2015), p. 165001. DOI: 10.1103/PhysRevLett.114.165001. arXiv: 1504.05742 [astro-ph.HE].

[139] Pierre Auger Collaboration, P. Abreu et al. “Antennas for the detection of radio emission pulses from cosmic-ray induced air showers at the Pierre Auger Observatory”. In: *Journal of Instrumentation* 7 (10/2012), P10011. DOI: 10.1088/1748-0221/7/10/P10011. arXiv: 1209.3840 [astro-ph.IM].

[140] CODALEMA Collaboration, D. Charrier. “Antenna development for astroparticle and radioastronomy experiments”. In: *Nucl. Instrum. Meth.* A662 (2012), S142–S145. DOI: 10.1016/j.nima.2010.10.141.

[141] O. Kambeitz. “Radio Detection of Horizontal Extensive Air Showers”. PhD thesis. Karlsruher Institut für Technologie (KIT), 2016. DOI: 10.5445/IR/1000055758.

[142] LOPES Collaboration, W. D. Apel et al. “LOPES-3D, an antenna array for full signal detection of air-shower radio emission”. In: *Nucl. Instrum. Meth.* A696 (2012), pp. 100–109. DOI: 10.1016/j.nima.2012.08.082. arXiv: 1303.6808 [astro-ph.IM].

[143] O. Krömer, H. Gemmeke, et al. “New Antenna for Radio Detection of UHECR”. In: *Contributions to the 31 st International Cosmic Ray Conference, Lodz, Poland.* Vol. FZKA 7516. 2009, pp. 77–80.

[144] Tunka-Rex Collaboration, F. G. Schröder et al. “Overview on the Tunka-Rex antenna array for cosmic-ray air showers”. In: *Proceedings, 35th International Cosmic Ray Conference (ICRC 2017): Bexco, Busan, Korea, July 12-20, 2017*. Ed. by PoS. Vol. ICRC2017. 459. arXiv: 1708.00627 [astro-ph.HE].

[145] CODALEMA Collaboration, O. Ravel. “The CODALEMA experiment”. In: *Nucl. Instrum. Meth.* A662 (2012), S89–S94. DOI: 10.1016/j.nima.2010.12.057.

[146] Pierre Auger Collaboration, A. Aab et al. “Nanosecond-level time synchronization of autonomous radio detector stations for extensive air showers”. In: *JINST* 11.01 (2016), P01018. DOI: 10.1088/1748-0221/11/01/P01018. arXiv: 1512.02216 [physics.ins-det].

[147] Pierre Auger Collaboration, A. Aab et al. “Calibration of the Logarithmic-Periodic Dipole Antenna (LPDA) Radio Stations at the Pierre Auger Observatory using an Octocopter”. In: *Submitted to: JINST* (2017). arXiv: 1702.01392 [astro-ph.IM].

[148] F. G. Schröder et al. “New method for the time calibration of an interferometric radio antenna array”. In: *Nucl. Instrum. Meth.* A615 (2010), pp. 277–284. DOI: 10.1016/j.nima.2010.01.072. arXiv: 1002.3775 [astro-ph.IM].

[149] A. Lang. “Time Calibration of the Auger Engineering Radio Array (AERA) Using Airplanes”. MA thesis. Karlsruhe Institute of Technology, 11/2014.

[150] Instituto Geográfico Nacional. *OGUA 18-086*. http://www.ign.gob.ar/descargas/posgar/red_posgar_2007/Monografias/OGUA.pdf. Accessed: 2018-01-25.

[151] *Instituto Geogràfico Nacional*. http://www.ign.gob.ar/NuestrasActividades/Geodesia/Posgar/RedPasma. Accessed: 2018-01-25.

[152] T. Huege, M. Ludwig, and C. W. James. "Simulating radio emission from air showers with CoREAS". In: *AIP Conf. Proc.* 1535 (2013), p. 128. DOI: 10.1063/1.4807534. arXiv: 1301.2132 [astro-ph.HE].

[153] S. Argiro et al. "The Offline Software Framework of the Pierre Auger Observatory". In: *Nucl. Instrum. Meth.* A580 (2007), pp. 1485–1496. DOI: 10.1016/j.nima.2007.07.010. arXiv: 0707.1652 [astro-ph].

[154] F. Schmidt. University of Leeds, UK. URL: https://www-zeuthen.desy.de/~jknapp/fs/iron-showers.html.

[155] A. Ferrari, P. R. Sala, A. Fasso, and J. Ranft. "FLUKA: A multi-particle transport code (Program version 2005)". In: *CERN-2005-010, SLAC-R-773, INFN-TC-05-11* (2005).

[156] T. T. Böhlen et al. "The FLUKA Code: Developments and Challenges for High Energy and Medical Applications". In: *Nuclear Data Sheets* 120 (06/2014), pp. 211–214. DOI: 10.1016/j.nds.2014.07.049.

[157] C. W. James, H. Falcke, T. Huege, and M. Ludwig. "General description of electromagnetic radiation processes based on instantaneous charge acceleration in "endpoints"". In: Phys. Rev. E 84.5, 056602 (11/2011), p. 056602. DOI: 10.1103/PhysRevE.84.056602. arXiv: 1007.4146 [physics.class-ph].

[158] K. D. de Vries, A. M. van den Berg, O. Scholten, and K. Werner. "Coherent Cherenkov Radiation from Cosmic-Ray-Induced Air Showers". In: *Phys. Rev. Lett.* 107 (2011), p. 061101. DOI: 10.1103/PhysRevLett.107.061101. arXiv: 1107.0665 [astro-ph.HE].

[159] LOPES Collaboration, W. D. Apel et al. "Improved absolute calibration of LOPES measurements and its impact on the comparison with REAS 3.11 and CoREAS simulations". In: *Astropart. Phys.* 75 (2016), pp. 72–74. DOI: 10.1016/j.astropartphys.2015.09.002. arXiv: 1507.07389 [astro-ph.HE].

[160] Tunka-Rex Collaboration, R. Hiller. "Calibration of the absolute amplitude scale of the Tunka Radio Extension (Tunka-Rex)". In: *Proceedings, 34th International Cosmic Ray Conference (ICRC 2015): The Hague, The Netherlands, July 30-August 6, 2015*. Ed. by PoS. Vol. ICRC2015. 573.

[161] LOFAR Collaboration, S. Buitink et al. "A large light-mass component of cosmic rays at 10^{17} - $10^{17.5}$ eV from radio observations". In: *Nature* 531 (2016), p. 70. DOI: 10.1038/nature16976. arXiv: 1603.01594 [astro-ph.HE].

[162] R. Brun and F. Rademakers. “ROOT - An object oriented data analysis framework”. In: *Nuclear Instruments and Methods in Physics Research Section A: Accelerators, Spectrometers, Detectors and Associated Equipment* 389.1 (1997). New Computing Techniques in Physics Research V, pp. 81–86. ISSN: 0168-9002. DOI: https://doi.org/10.1016/S0168-9002(97)00048-X.

[163] The AERA Group. “AERA proposal for the construction of the 20 km^2 Auger Engineering Radio Array at the Southern Auger Observatory”. In: *Auger internal note* GAP-2009-172 (2009).

[164] S. Mathys, J. Rautenberg, and J. Neuser. “Development and applications of a ROOT based IO library for AERA”. In: *Auger internal note* GAP-2015-011 (2015).

[165] A. Letessier-Selvon. “The Pierre Auger Project Central Data Acquisition System”. In: *Auger internal note* GAP-1999-003 (1999).

[166] B. Wundheiler, F. Sánchez, F. Contreras, A. Sedoski Croce, and A. Etchegoyen. “AMIGA muon data structure inside CDAS”. In: *Auger internal note* GAP-2012-086 (2012).

[167] F. Sánchez et al. “The AMIGA extension of Auger Offline Software”. In: *Auger internal note* GAP-2012-135 (2012).

[168] *MySQL*. https://www.mysql.com/. Accessed: 2017-08-01.

[169] E. Thébault et al. “International Geomagnetic Reference Field: the 12th generation”. In: *Earth, Planets and Space* 67.1 (05/2015), p. 79. ISSN: 1880-5981. DOI: 10.1186/s40623-015-0228-9.

[170] *Buildbot*. http://buildbot.net/. Accessed: 2017-08-01.

[171] *Boost*. http://www.boost.org/. Accessed: 2017-08-01.

[172] M. Frigo and S. G. Johnson. “The Design and Implementation of FFTW3”. In: *Proceedings of the IEEE* 93.2 (2005). Special issue on “Program Generation, Optimization, and Platform Adaptation”, pp. 216–231.

[173] GEANT4 Collaboration, S. Agostinelli et al. “GEANT4: A Simulation toolkit”. In: *Nucl. Instrum. Meth.* A506 (2003), pp. 250–303. DOI: 10.1016/S0168-9002(03)01368-8.

[174] G. J. Burke and A. J. Pogio. *Numerical Electromagnetics Code (NEC)-Method of Moments. Volume 1. A User-Oriented Computer Code for Analysis of the Electromagnetic Response of Antennas and Other Metal Structures.* Tech. rep.

Lawrence Livermore National Lab., CA.; Naval Ocean Systems Center, San Diego, CA., 1981.

[175] J. Abraham et al. "Trigger and aperture of the surface detector array of the Pierre Auger Observatory". In: *Nuclear Instruments and Methods in Physics Research A* 613 (01/2010), pp. 29–39. DOI: 10.1016/j.nima.2009.11.018. arXiv: 1111.6764 [astro-ph.IM].

[176] K. Kamata and J. Nishimura. "The Lateral and the Angular Structure Functions of Electron Showers". In: *Progress of Theoretical Physics Supplement* 6 (1958), pp. 93–155. DOI: 10.1143/PTPS.6.93. eprint: /oup/backfile/content_public/journal/ptps/6/10.1143/ptps.6.93/2/6-93.pdf.

[177] D. Ravignani and A. D. Supanitsky. "A new method for reconstructing the muon lateral distribution with an array of segmented counters". In: *Astropart. Phys.* 65 (2015), pp. 1–10. DOI: 10.1016/j.astropartphys.2014.11.007. arXiv: 1411.7649 [astro-ph.IM].

[178] J. Schulz. "Cosmic Radiation - Reconstruction of Cosmic-Ray Properties from Radio Emission of Extensive Air Showers". PhD thesis. Radboud Universiteit Nijmegen, 2016. ISBN: 9789402800173.

[179] Pierre Auger Collaboration, A. Aab et al. "Depth of maximum of air-shower profiles at the Pierre Auger Observatory. I. Measurements at energies above $10^{17.8}$ eV". In: *Phys. Rev.* D90.12 (2014), p. 122005. DOI: 10.1103/PhysRevD.90.122005. arXiv: 1409.4809 [astro-ph.HE].

[180] C. Welling. "Identification of Radio Signals from Cosmic Ray Induced Air Showers with the Auger Engineering Radio Array". MA thesis. Rheinisch-Westfälischen Technischen Hochschule Aachen, 2017.

[181] Pierre Auger Collaboration, C. Glaser, S. de Jong, M. Erdmann, J. R. Hörandel, and E. Willems. "Analytic description of the radio emission of air showers based on its emission mechanisms". In: *Proceedings, 35th International Cosmic Ray Conference (ICRC 2017): Busan, Korea, July 10-20, 2017*. Ed. by PoS. Vol. ICRC2017. 529.

[182] CASA Collaboration, K. G. Gibbs. "The Chicago Air Shower Array (CASA)". In: *Nucl. Instrum. Meth.* A264 (1988), pp. 67–73. DOI: 10.1016/0168-9002(88)91104-7.

[183] M. A. K. Glasmacher et al. "The cosmic ray composition between 10^{14} eV and 10^{16} eV". In: *Astropart. Phys.* 12 (1999), pp. 1–17. DOI: 10.1016/S0927-6505(99)00076-6.

[184] C. Glaser, M. Erdmann, J. R. Hörandel, T. Huege, and J. Schulz. "Simulation of Radiation Energy Release in Air Showers". In: *JCAP* 1609.09 (2016), p. 024. DOI: 10.1088/1475-7516/2016/09/024. arXiv: 1606.01641 [astro-ph.HE].

[185] M. Gottowik, C. Glaser, T. Huege, and J. Rautenberg. "Determination of the absolute energy scale of extensive air showers via radio emission: systematic uncertainty of underlying first-principle calculations". In: (2017). arXiv: 1712.07442 [astro-ph.HE].

[186] Tunka-Rex Collaboration, LOPES Collaboration, W. D. Apel et al. "A comparison of the cosmic-ray energy scales of Tunka-133 and KASCADE-Grande via their radio extensions Tunka-Rex and LOPES". In: *Phys. Lett.* B763 (2016), pp. 179–185. DOI: 10.1016/j.physletb.2016.10.031. arXiv: 1610.08343 [astro-ph.IM].

[187] Pierre Auger Collaboration, M. Unger. "Highlights from the Pierre Auger Observatory". In: *Proceedings, 35th International Cosmic Ray Conference (ICRC 2017): Busan, Korea, July 10-20, 2017*. Ed. by PoS. Vol. ICRC2017. 1102.

[188] A. Porcelli. "Measurement of the Depth of Shower Maximum in the Transition Region between Galactic and Extragalactic Cosmic Rays with the Pierre Auger Observatory". PhD thesis. Karlsruher Institut für Technologie (KIT), 2014.

List of Figures

List of Tables

List of Abbreviations

ADST	**A**dvanced **D**ata **S**ummary **T**ree
AERA	**A**uger **E**ngineering **R**adio **A**rray
AGN	**A**ctive **G**alactic **N**ucleus
AMIGA	**A**uger **M**uons and **I**nfill for the **G**round **A**rray
APE	**A**uger **P**ackage **E**nvironment
ASCII	**A**merican **S**tandard **C**ode for **I**nformation **I**nterchange
CDAS	**C**entral **D**ata **A**cquisition **S**ystem
CMB	**C**osmic **M**icrowave **B**ackground
CORSIKA	**CO**smic **R**ay **SI**mulations for **KA**scade
CPU	**C**entral **P**rocessing **U**nit
CoREAS	**Co**rsika-based **R**adio **E**mission from **A**ir **S**howers
CR	**C**osmic **R**ay
DAQ	**D**ata **A**c**Q**uisition
EAS	**E**xtensive **A**ir **S**howers
EBL	**E**xtragalactic **B**ackground **L**ight
EECR	**E**xtreme **E**nergy **C**osmic **R**ay
FADC	**F**lash **A**nalog-to-**D**igital **C**onverter
FD	**F**luorescence **D**etector
FFT	**F**ast **F**ourier **T**ransform
GRB	**G**amma-**R**ay **B**urst
HEAT	**H**igh **E**levation **A**uger **T**elescopes
LHC	**L**arge **H**adron **C**ollider
LPDA	**L**ogarithmic **P**eriodic **D**ipole **A**ntenna
MD	**M**uon **D**etector

PMT	**P**hoto**M**ultiplier **T**ube
RD	**R**adio **D**etector
RDS	**R**adio **D**etector **S**tation
RFI	**R**adio **F**requency **I**nterference
SBG	**S**tar**B**urst **G**alaxy
SD	**S**urface **D**etector
SNR	**S**uper**N**ova **R**emnant
UHECR	**U**ltra-**H**igh **E**nergy **C**osmic **R**ay
XML	E**X**tensible **M**arkup **L**anguage

Acknowledgments

This thesis would not have been possible without the support of many people and the great team-work at the IKP, the ITeDA/AMIGA group, the AERA group and the Pierre Auger Collaboration. In particular I owe special thanks to the following people.

First of all, I am very thankful to my referees Prof. Johannes Blümer from KIT and Prof. Alberto Etchegoyen from UNSAM, who offered me the opportunity to work on a topic combining AERA and AMIGA and to join the Double Doctoral Degree in Astrophysics. Your special support made the DDAp program possible.

I am especially grateful to my supervisor Frank Schröder for all his support during the whole time of my PhD. Frank, you always supported me more than I could ask for, be it with fruitful discussions about my analyses, with organizational things regarding the DDAp and my stays in Argentina, with thoroughly proofreading my thesis and manuscripts of all kinds, and with covering my back, whenever necessary. Thanks for always believing in me and my work.

Many thanks as well to Andreas Haungs as the leader of the Cosmic Ray Technologies group. Andy, your optimism and passion about everything you're doing is really infectious and contributes essentially to the great atmosphere in the group. In addition, I learned a lot about the politics of the scientific community from you.

At the IKP, I especially want to thank Sabine for taking great care of all kinds of organizational things. Thanks to the admin team Doris, Klaus, Dieter and Darko for keeping the computer system up and running, which was essential to get all the research done. Thanks to Jürgen for the great support regarding the CORSIKA and CoREAS simulations. Many thanks as well to all other colleagues at IKP. I really enjoyed the great atmosphere at the institute and that everyone is so supportive without asking for anything. Special thanks to Heike for the support during the GPS campaign and for all the fun we had during the deployment in Malargüe and for her friendship. Thanks to the whole WAB team for all the humorous conversations for a good start into the weekend.

I had a great time with all my office mates. In particular, Qader and Olga, thanks for your great humor, all the fun we had in the office and your friendship. David, you were a great support during the whole last year. You always helped me out, when I needed support, you cheered me up, when I was down, and you did all this with a lot of patience. This was worth a lot to me.

I would like to thank all my colleagues at the ITeDA for all the support and the great time during my stay in Buenos Aires. Special thanks to Federico Sanchez for the scientific support regarding all AMIGA related things of my work. Furthermore, thanks to Diego, Juan, Brian and Nico for all the help with Offline and fruitful scientific

discussions and all kinds of other humorous and interesting topics during the lunch times. Thanks a lot to Maria, Belen, Michelle and Florencia for the great support in organizational matters and to Adrián for the administrative support. Thanks to all colleagues at ITeDA for welcoming me so warmly and for all the great asados, mate teas and pizza nights. You all made my time in Argentina very special and give me a great intercultural experience. Christian, I really had a great time sharing my home with you in Buenos Aires. Thanks a lot for teaching me the real Spanish ;)

Within the DDAp, I especially want to thank Marie-Christine and Anibal for all the support in organizational matters. Many thanks to Frank again, to Markus and to Federico for giving all kinds of support to all us DDAp students. Special thanks as well to all DDAp students. We were a great community and all the support we gave each other made the program a very special experience to me. I'm especially thankful for the friendship with Nico and Ana, which grew out of the DDAp and which I hope will last a lifetime despite the distance between us.

Many thanks to all members of AERA and the radio Offline group for fruitful discussions during the weekly calls and the AERA meetings. In particular I owe special thanks to Tim and Julian, who led the AERA analysis group and who supported me with their expertise in my analysis. Thanks to the whole team of the AERA deployment, I had an exciting time with you in Malargüe. Thanks as well to the local staff in Malargüe, who supported us with all we needed to make the deployment, and in particular the GPS campaign happen in the short time we had.

I owe special gratitude to my family and friends, who always believed in me and supported me with a lot of encouragement, independent of how far away I was. Tobi, thank you for always being there for me and for all your support especially during the last year. Without all your encouragement and pragmatism I wouldn't have been able to finish this work.